

UCLA

UCLA Previously Published Works

Title

Engineering Reconnaissance following the October 2016 Central Italy Earthquakes - Version 2

Permalink

<https://escholarship.org/uc/item/2xh0z0xk>

Author

GEER Association

Publication Date

2017-05-08

Data Availability

The data associated with this publication are available at: http://www.geerassociation.org/index.php/component/geer_reports/?view=geerreports&layout=build&id=76



Engineering Reconnaissance Following the October 2016 Central Italy Earthquakes *Version 2*

GEER Team Leaders: Jonathan P. Stewart and Giuseppe Lanzo

Report Editors:
Paolo Zimmaro and Jonathan P. Stewart



DOI: 10.18118/G6HS39

Geotechnical Extreme Events Reconnaissance Association
Report No. GEER-050D
8 May 2017

GEER Team Members

**Leaders: Jonathan P Stewart, University of California Los Angeles (UCLA) and
Giuseppe Lanzo, Sapienza Università di Roma**

Ernesto Ausilio, Roberto Cairo, Università della Calabria

Francesca Bozzoni, Eucentre, Pavia

Maria Chiara Capatti, Università Politecnica delle Marche

Fernando della Pasqua, GNS Science

Francesca Dezi, Università degli Studi della Repubblica di San Marino

**Luigi Di Sarno, Armando Lucio Simonelli, Università degli studi del Sannio, Reluis
Consortium**

**Sebastiano Foti, Filiberto Chiabrando, Paolo Dabove, Vincenzo Di Pietra, Paolo Maschio,
Federico Passeri, Antonio Sgobio, Lorenzo Teppati Lose', Politecnico di Torino**

Kevin Franke, Brandon Reimschiissel, Brigham Young University

**Fabrizio Galadini, Emanuela Falcucci, Stefano Gori, Istituto Nazionale di Geofisica e
Vulcanologia (INGV)**

Robert E Kayen, US Geological Survey (USGS)

**Tadahiro Kishida, Pacific Earthquake Engineering Research Center (PEER), University of
California, Berkeley**

Bret Lingwall, South Dakota School of Mines and Technology

**Alessandro Pagliaroli, Silvia Giallini, Zurab Gogoladze, Giovanna Vessia, Alberto Pizzi,
Alessandra Di Domenica, Università degli Studi di Chieti-Pescara**

Panagiotis Pelekis, School of Pedagogical and Technological Education Athens

**Antonio Santo, Melania De Falco, Giovanni Forte Università degli Studi di Napoli
Federico II, Reluis Consortium**

**Giuseppe Scasserra, Filippo Santucci de Magistris, Massimina Castiglia, Tony Fierro,
Dipendra Gautam, Luciano Mignelli, Fiorenzo Staniscia, Università del Molise**

Anastasios Sextos, Raffaele De Risi, University of Bristol

Stefania Sica, Michele Mucciacciaro, Università degli Studi del Sannio

Paolo Tommasi, Anita Di Giulio, Istituto di Geologia Ambientale e Geoingegneria (IGAG), CNR

Giuseppe Tropeano, Università di Cagliari

Maria Giovanna Durante, Paolo Zimmaro, University of California Los Angeles (UCLA)

Acknowledgements

The GEER Association is supported by the National Science Foundation (NSF) through the Geotechnical Engineering Program under Grant No. CMMI-1266418. Any opinions, findings, and conclusions or recommendations expressed in this material are those of the authors and do not necessarily reflect the views of the NSF. The GEER Association is made possible by the vision and support of the NSF Geotechnical Engineering Program Directors: Dr. Richard Fragaszy and the late Dr. Cliff Astill. GEER members also donate their time, talent, and resources to collect time-sensitive field observations of the effects of extreme events.

Sponsorship of GEER activities was also provided by the B. John Garrick Institute for the Risk Sciences at UCLA and the NSF I/UCRC Center for Unmanned Aircraft Systems (C-UAS) at BYU under Project BYU13-03.

We thank Prof. Mauro Dolce and Engs. Paola Pagliara and Paola Bertuccioli from the Department of Civil Protection for their support and assistance. Matteo Francesco Stancato, master's student at Università della Calabria, contributed to data collection for building structures. We thank Giuseppe Riccioni (Ussita Municipality), Roberto Cantoni, and Raffaele Sorriento (Corpo Nazionale dei Vigili del Fuoco) for allowing surveys at Monte Bove northern flank and Valle di Panico. Eng. Monica Di Mattia (Teramo Province) supported survey activities in Crognaleto.

Organizations within Italy that supported the activities reported herein include the Italian Geotechnical Society; the Consortium ReLUIS (Network of Italian Laboratories of Earthquake Engineering), headquartered in the University of Naples Federico II; the Department of Engineering of University of Sannio, Benevento; Politecnico di Torino, which provided technical and financial support; EUcentre (European Centre for Training and Research in Earthquake Engineering; Pavia), which provided support for one team member; and LAGIC s.r.l., which performed laboratory tests on the material sampled at Monteleone di Fermo shown in Chapter 5 (Mud Volcanoes).

Contents

Acknowledgements.....	i
Contents.....	ii
List of Figures	vi
List of Tables	xxv
1 Introduction	1-1
1.1 Event Sequence Overview and Organization of Reconnaissance.....	1-1
1.2 Overview of Reconnaissance Activities.....	1-4
2 Seismic Source and Surface Rupture	2-1
2.1 Seismic Source.....	2-1
2.1.1 Moment tensors and aftershock patterns.....	2-1
2.1.2 Crustal deformations	2-3
2.1.3 Finite fault models and trimming	2-3
2.2 Surface Rupture	2-4
2.2.1 Observations of surface rupture following 26 October 2016 event	2-5
2.2.2 Surface rupture from 30 October 2016 event.....	2-6
2.3.3 Detailed results of GEER fault imaging and conventional fault mapping	2-9
3 Ground Motions.....	3-1
3.1 Available Recordings.....	3-1
3.2 Site Conditions	3-2
3.3 Near Source Ground Motions.....	3-6
3.3.1 Data quality issues	3-7

3.4 Comparison to Ground Motion Models	3-11
3.5 Spatial Interpolation for Estimating Ground Motions	3-14
4 Slope Displacements, Landslides, and Rockfalls	4-1
4.1 Introduction	4-1
4.2 Detailed Case Studies and Imaging	4-5
4.2.1 Nera Landslide	4-5
4.2.2 Monte Bove Rockfalls	4-8
4.2.3 Pescara del Tronto	4-11
4.2.4 Accumoli.....	4-25
4.2.5 Valle di Panico Landslide and Rockfall	4-30
4.2.6 Crognaletto Rockfall (Next to Cervaro Village)	4-35
4.2.7 Landslide near the village of Crognaletto	4-39
4.2.8 Pescia Rockfall.....	4-43
4.2.9 Rockfalls/Landslides along SP134 Visso – Castelsantangelo	4-48
4.2.10 Western flank of Mt. Vettore massif	4-53
4.2.11 Rockfall SP 477 Arquata-Castelluccio (reappraisal)	4-56
4.3 Quick checks (Visual inspections)	4-62
4.3.1 Rockfalls in Pontechiusita along SP209	4-62
4.3.2 Rockfalls between Piedipaterno and Cerreto	4-64
4.3.3 Landslide along SP746 road between Cittareale and Norcia	4-65
4.3.4 Landslide along road Ortolano-Campotosto	4-67
4.3.5 Rockfalls along SP476 (between Piedivalle and Preci)	4-71
4.3.6 Landslide below the village of Tino.....	4-72

4.3.7 SP477 Road embankment fill damage	4-74
5 Mud Volcanoes	5-1
5.1. Initial Report and Field Reconnaissance	5-1
5.2. Mud Volcanoes in Monteleone di Fermo	5-1
5.3. Mud Volcanoes in Santa Vittoria in Matenano.....	5-6
5.4. Earthquake-triggered eruptions and correlations between earthquake magnitude and distance.....	5-8
6 Performance of buildings and damage patterns	6-1
6.1 Revisits	6-3
6.1.1 Norcia.....	6-3
6.1.2 Accumoli.....	6-14
6.1.3 Amatrice.....	6-23
6.1.4 Arquata del Tronto.....	6-34
6.1.5 Pescara del Tronto	6-37
6.1.6 Tufo	6-43
6.1.7 Montegallo and surrounding hamlets	6-47
6-2 Newly inspected areas	6-53
6.2.1 Visso	6-53
6.2.2 Ussita.....	6-66
6.2.3 Tolentino	6-68
6.2.4 San Severino.....	6-76
6.2.5 Camerino.....	6-84
6.2.6 Pievebovigliana	6-99
6.2.7 Pieve Torina	6-110
6.2.8 Fiume	6-112

6.2.9 Casavecchia Alta	6-117
6.2.10 Sellano.....	6-121
6.2.11 Pié del Colle.....	6-124
6.2.12 Cessapalombo	6-128
6.2.13 Preci	6-133
6.2.14 Piedivalle	6-135
6.2.15 Caldarola	6-136
6.2.16 Castello di Campi.....	6-140
6.2.17 Colfiorito	6-141
6.2.18 San Lorenzo in Colpolina.....	6-142
6.2.19 Serravalle	6-146
6.2.20 Popoli	6-147
6.2.21 San Pellegrino	6-149
7 Performances of Bridges.....	7-1
8 High-Value Case Histories	8-1
References	R-1

List of Figures

Figure 1.1. Map of central Italy showing moment tensors of major earthquakes since 1997 and the intermediate gap areas. Finite fault models from Chiaraluce et al. (2004; 1997 Umbria-Marche event), Piatanesi and Cirella (2009; 2009 L’Aquila event), Tinti et al. (2016, 24 August event), and GdL INGV sul terremoto in centro Italia, 2016, 26 and 30 October events). Moment tensors for 26 and 30 October 2016 earthquakes are also shown 1-1

Figure 1.2. Regional map showing the active fault systems, finite fault models and epicenters of the 24 August, 26 and 30 October events, ground motion station locations and recorded peak ground accelerations (PGA) for the 30 October events, and locations of various earthquake effects discussed in this report 1-3

Figure 2.1. Map showing locations of hypocenters for three mainshock events in central Italy between 24 August and 30 October 2016. Also shown on selected finite fault models for each event and aftershock patterns for the 24-hour periods post-rupture 2-2

Figure 2.2. (a) horizontal, and (b) vertical GPS-based co-seismic displacement estimated after the 26 October event. Data used for producing the Figures were obtained from: ftp://gpsfree.gm.ingv.it/amatrice2016/static/Cosismico_26Oct2016_GPS_GdL_V1.dat, last accessed 4 April, 2017) 2-3

Figure 2.3. (a) horizontal, and (b) vertical GPS-based co-seismic displacement estimated after the 30 October event. Data used for producing the Figures were obtained from: ftp://gpsfree.gm.ingv.it/amatrice2016/static/Cosismico_30Oct2016_GPS_GdL_V1.dat, last accessed 4 April, 2017) 2-4

Figure 2.4. Detailed map of surface fault rupture, pre-event mapping of Mt. Vettore-Mt. Bove (green) fault system, and locations of 3D models 2-5

Figure 2.5. Comparative fault offset of 10cm. (a) Vertical offset from the August event, and (b) 30cm Vertical offset from the October 2016 events on the south face of Mt. Vettore near road SP477. Horizontal offsets were 0cm and 2cm. Lat = 42.79795, Long = 13.26607 2-7

Figure 2.6. Distribution of incremental and cumulative fault offsets for the southern half of the Mt. Vettore fault. All data in this Figure from hand measurements 2-7

Figure 2.7. Surface fault rupture displacements from August-October event sequence as evaluated from hand measurements in the field and UAV-based 3D model 2-9

Figure 2.8. Satellite image of the southern half of the Mt. Vettore Massif. The yellow box corresponds to the area shown in Figure 2.10 for the 3D model of the west face of Mt. Vettore, while the white box corresponds to the area shown in Figure 2.9 for the 3D models of the south face. The box to the west (orange) shows the location of the Piano Grande fault 3D model (Figure 2.11) 2-10

Figure 2.9. 3D digital terrain model from merged SfM and LiDAR data of the Mt Vettore fault on the southern flank of the Mt Vettore Massif. Approximate main fault trace indicated in yellow. Looking from the west to the east. The upper left of the image is the top of the slope. Area of soft sediments where the fault trace breaks into several (4 – 6) small scarps is indicated in white 2-11

Figure 2.10. 3D digital terrain model from merged SfM and LiDAR data of the Mt Vettore fault on the western flank of the Mt Vettore Massif. Approximate main fault trace(s) indicated in yellow, a second visible trace of the “Western Trace” shown in white (See Figure 2.11 for more details). Looking from the west. The left of the image is to the north. The slope moves from top to bottom of the image 2-12

Figure 2.11. 3D digital terrain model from merged SfM and LiDAR data of the Piano Grande fault on the western toe of the Mt Vettore Massif. Approximate fault trace(s) indicated in yellow. Looking from the west. The left of the image is to the north. Mt. Vettore on the top of the image 2-12

Figure 2.12. Fault offset measurements showing relative offset of August 2016 (0 cm) and October 2016 (70 cm) events on the lower or “western” fault trace in Figure 2.10 (shown in white). Lat = 42.812901, Long = 13.24626 2-13

Figure 2.13. Fault slip measurements showing multi-epoch offsets from August 2016 (upper white band, 16 cm) and October 2016 (130 cm) events. Lat = 42.81724, Long = 13.25449 2-13

Figure 2.14. Location of maximum fault offset of 210 cm following October 2016 events. The August event offset at this location is estimated as 20 cm, based on nearby data points. Lat = 42.81687, Long = 13.25503 2-14

Figure 2.15. Fault offset measurement across the footpath on the west face of Mt. Vettore. Offset measured as 80 cm following October events (a). This offset was 30 cm following August events (b). Lat = 42.807379, Long = 13.262966 2-14

Figure 2.16. Fault trace on the south face of Mt. Vettore, where the fault has ruptured along the path of buried polyethylene pipe supplying the pictured spring. Rupture partially hidden by long grass. Offset measured at 45 to 65cm. August offset data nearby is 0 to 15cm. Trace(s) above the spring indicated in red. Lat = 42.80474, Long = 13.26441 2-15

Figure 2.17. Fault offset measurement of one of several (4 to 6) small traces on the south face of Mt. Vettore in the area indicated in white in Figure 2.9. In this area surface soils are thick and ductile. Offset measured at 8 to 52cm on each trace. August offsets were 0 cm. Lat = 42.80483, Long = 13.26443	2-15
Figure 2.18. Fault offset measurement in gully on south face of Mt. Vettore. Offset measured at 80cm. August offset data nearby is 15cm, indicating October 2016 offset of 65cm.....	2-16
Figure 2.19. Fault offset measurement across SR477 on south face of Mt. Vettore. August offset data nearby is 2cm (a). Offset measured at 18cm to 20cm after October (b). Lat = 42.796829, Long = 13.265899	2-16
Figure 2.20. Secondary fault offset across a road on the Piano Grande at the base of the Mt. Vettore Massif. August 2016 event offset of 0cm. October 2016 event offset of 7 to 18 cm	2-17
Figure 2.21. Fault offset measurements along the south and west faces of the Mt. Vettore Massif showing differences in fault rupture offset through soil versus along the rock fault plane (where visible on the slope)	2-18
Figure 3.1. (a) Locations of instruments that recorded M6.1 , M5.3 and M4.8 August 2016 events; (b) close-up view of the instruments in the epicentral area.....	3-3
Figure 3.2. (a) Locations of instruments that recorded M6.5 , M5.9 and M5.4 October 2016 events; (b) close-up view of the instruments in the epicentral area.....	3-4
Figure 3.3. Spatial distribution of all events occurred in Central Italy between 24 August 2016 and 20 January 2017 with M ≥4.2	3-5
Figure 3.4: Data source types used for V_{S30} estimations for all considered recording stations	3-6
Figure 3.5. Pseudo acceleration response spectra (5% damping) for Amatrice (AMT) and Norcia (NRC, NOR) sites from the M6.1 24 August event	3-7
Figure 3.6. Pseudo acceleration response spectra (5% damping) for nine near source recording sites from the M6.5 30 October 2016 event.....	3-9
Figure 3.7. Original ground motion, extracted pulse, and residual ground motion for the M6.5 30 October 2016 event recorded at the (a) T1214, (b) CLO, and (c) CNE stations	3-10
Figure 3.8. Vertical component of acceleration, velocity, and displacement time-series for the M6.5 30 October 2016 event, processed using the Gregor et al. (2002) procedure for the (a) CLO, (b) T1214, (c) CNE, (d) T1216, (e) ACC, and (f) AMT station	3-10

Figure 3.9. Scheme of an earthquake source and distance measures using a vertical cross-section through a fault rupture plane (from Kaklamanos et al., 2011).....	3-12
Figure 3.10. Variation of PHA and PHV with R_{JB} for rock (NTC08: A), stiff (NTC08: B), soft soil (NTC08: C, D, E).....	3-13
Figure 3.11. Variation of PHA and PHV with R_{JB} for rock (NTC08: A), stiff (NTC08: B), soft soil (NTC08: C, D, E).....	3-14
Figure 3.12. Within-event residuals of PHA from recorded ground motions relative to predictions of the NGA2, NGA2-I and B11. Binned means shown with +/- one standard deviation.....	3-15
Figure 3.13. Within-event residuals of PHV from recorded ground motions relative to predictions of the NGA2, NGA2-I and B11. Binned means shown with +/- one standard deviation.....	3-16
Figure 3.14. Event terms for PGA and PSA oscillator periods of 0.1-2.0 sec for the three sets of models and six events. For context, the +/- one between-event standard deviation is shown: τ_2 for $M > 5.5$ from the Boore et al (2014) and σ_B from Bindi et al (2011)	3-17
Figure 3.15. Map of the spatial distribution of PGA Residuals for the M6.1 24 August 2016 earthquake.....	3-18
Figure 3.16. Map of the spatial distribution of PGA Residuals for the M5.9 26 October 2016 earthquake.....	3-19
Figure 3.17. Map of the spatial distribution of PGA Residuals for the M6.5 30 October 2016 earthquake.....	3-20
Figure 4.1. (a) Map of observed landslides (green diamonds), along with surface fault projections and moment tensors for the three mainshocks; (b) Observed landslides superimposed to the IFFI inventory.....	4-2
Figure 4.2. Location of reconnaissance sites, epicenter locations, and spatial distribution of PGA for the 30 October M6.5 earthquake.....	4-3
Figure 4.3. Daily rainfall (blue bars) and daily rainfall accumulated over one (black line) and two weeks (red line) recorded by (a) Visso, (b) Ponte Tavola (courtesy of Servizio Idrografico - Regione Marche), and (c) Nerito-Crognaleto (courtesy of Servizio Idrografico - Regione Abruzzo) rainfall gauges	4-4
Figure 4.4. Location of the Nera landslide	4-5

Figure 4.5. Nera rock avalanche photographed from the UCLA DJI Phantom 4 drone at an elevation of 400 meters above Route SS209. The primary rock-fall was a wedge that detached on the right side of the image and disintegrated into talus debris as it fell 330 meters to the river valley floor. The limestone bedding is visible in the scar of the wedge detachment 4-6

Figure 4.6. Headscarp of Nera rockfall..... 4-7

Figure 4.7. 3D Structure-from Motion (SfM) model of the Nera river valley at the rockfall. The Nera rock avalanche is seen here from the east (Visso) side of the rockfall. The light color on the midslope is from the setting sunlight on the SfM UAV imagery. Elevation difference from the crest of the headscarp to the river is 330m 4-8

Figure 4.8. Satellite overview image of Monte Bove and surrounding hamlets (courtesy of Google Earth) 4-9

Figure 4.9. Phantom 4 UAV image of Monte Bove. Suspected rockfall sources are circled in yellow..... 4-10

Figure 4.10. Photograph (300 mm) of the upper rockfall near the summit of Monte Bove 4-10

Figure 4.11. Screenshot of Monte Bove SfM meshed 3D model. Note the missing summit of the mountain in the model due to insufficient UAV imagery..... 4-11

Figure 4.12. Pescara del Tronto locality map. Specific locations referred to in the text shown 4-12

Figure 4.13. Pescara del Tronto aerial photograph taken from the Phantom 4 UAV..... 4-12

Figure 4.14. 3D SfM model of main damaged building area overlying talus deposits (Location 3a) 4-13

Figure 4.15. View of talus behind failed retaining wall by Strada Statale No. 4 (Location 3b)..... 4-14

Figure 4.16. Pavement and road base damage induced by underlying stability failure of fill material (Location 3c) 4-14

Figure 4.17. Road damage induced by slight rotation of the underlying retaining wall and/or settlement of the retaining wall backfill..... 4-15

Figure 4.18. Aerial photograph of landslide impacting Strada Statale No. 4 below Pescara del Tronto (Location 3d) 4-16

Figure 4.19. View of damaged rockfall netting caused by loose debris material from the landslide above Strada Statale No. 4 (Location 3d) 4-16

Figure 4.20. Failure of steepened talus gully wall material and crest area above (Location 3e) 4-17

Figure 4.21. Site vicinity map showing comparison locations of interest (after GEER, 2016)	4-18
Figure 4.22. 3D model comparison of the landslide below Pescara del Tronto between September 2016 (a) and December 2016 (b)	4-19
Figure 4.23. 3D model comparison of the smaller landslide below Pescara del Tronto between September 2016 (a) and December 2016 (b)	4-20
Figure 4.24. 3D model comparison of the failed retaining wall below Pescara del Tronto between September 2016 (a) and December 2016 (b)	4-21
Figure 4.25. 3D SfM model view of scarp linearity behind failed lower retaining wall in Pescara del Tronto	4-22
Figure 4.26. 3D model comparison of the landslide near the head of the gully in Pescara del Tronto between September 2016 (a) and December 2016 (b)	4-23
Figure 4.27. 3D model comparison of the landslide beneath the northern slope of Pescara del Tronto between September 2016 (a) and December 2016 (b)	4-24
Figure 4.28. 3D model comparison of the landslide near the gravel pit in Pescara del Tronto between September 2016 (a) and December 2016 (b)	4-25
Figure 4.29. Accumoli vicinity map	4-26
Figure 4.30. Failure of retaining wall due to shallow landslide (Point 4a, looking towards north)	4-27
Figure 4.31. Failure of retaining wall due to shallow landslide (Point 4a, looking towards south)	4-27
Figure 4.32. 3D model screenshot identifying objects of interest with the failed retaining wall and shallow slope failure at Point 4a	4-28
Figure 4.33. 3D model screenshot of the destroyed roadway Frazione Fonte del Campo (i.e., SP-18)	4-29
Figure 4.34. 3D model screenshots showing a retaining wall beneath the northeastern slope of Accumoli (a) undamaged in September 2016, and (b) damaged in December 2016.....	4-30
Figure 4.35. 3D model screenshots showing cracking from a shallow landslide (a) during the September GEER reconnaissance, and (b) during the December GEER reconnaissance	4-30
Figure 4.36. Site vicinity map for the Valle di Panico, located to the east of Ussita and to the north of Monte Bove	4-31

Figure 4.37. Landslide encountered along mountain road in the Valle di Panico (Point 5a)	4-32
Figure 4.38. 3D model of the eastern half of the Valle di Panico landslide headscarp	4-32
Figure 4.39. 3D model of the western half of the Valle di Panico landslide headscarp	4-33
Figure 4.40. 3D model of the Valle di Panico rockfall	4-34
Figure 4.41. Photograph of the largest observed boulder fragment in the Valle di Panico rockfall. The boulder measured approximately 3.0 meters in diameter.....	4-34
Figure 4.42. 3D model of the source of the Valle di Panico rockfall, located 90 meters above the mountain road.....	4-35
Figure 4.43. 3D model of the boulders and small power or pump house at the toe of the Valle di Panico rockfall.....	4-35
Figure 4.44. Location of rockfall site near Cervaro village (Crognaleto)	4-37
Figure 4.45. 3D SfM model of rockfall site near Cervaro village (Crognaleto). Primary rockfall source circled in yellow.....	4-37
Figure 4.46. Source and runout chute of rockfall site near Cervaro village (Crognaleto) as seen from road at base of slope. Primary rock source circled in white	4-38
Figure 4.47. UAV aerial image of rockfall path from source at top of slope to the road at bottom of slope. Red circles show boulder fragments larger than 1.5m. Last boulder fragment from rockfall near road at base of slope is circled in orange.....	4-38
Figure 4.48. Last boulder fragment (4 meter) from rockfall near road at base of slope. Also pictured are freshly toppled trees from the boulder’s roll to its final position.....	4-39
Figure 4.49. Location of rockfall site near Crognaleto village.....	4-39
Figure 4.50. 3D SfM model from UAV imagery of the rockfall site near Crognaleto village	4-40
Figure 4.51. UAV image of rockfall site near Crognaleto village from the source area at the top of slope looking down to road along runout chute. Note several large 1 to 3 meter boulder fragments in the drainage below the road (yellow circles)	4-41
Figure 4.52. Damaged segmented concrete block retaining wall at roadway. Blocks that fell on road have been removed by local officials prior to visit from GEER team.....	4-42
Figure 4.53. View upslope of damaged retaining wall, boulder fragments and runout chute from road at rockfall site near Crognaleto village	4-42
Figure 4.54. Location of Pescia rockfall sites	4-43

Figure 4.55. Pescia rockfall. Possible soil slope creep shown by tree trunks. (site 9a)	4-44
Figure 4.56. Pescia rockfall site 9a 3D SfM model from UAV data. Rock source and 2.5 meter boulders circled in yellow	4-45
Figure 4.57. 3D SfM orthophoto of the rockfall source at site 9a	4-45
Figure 4.58. Damage to road from 1-2.5 mm boulder impacts from rockfall between sites 9a and 9b	4-46
Figure 4.59. Pescia rockfall site 9b. 3D SfM model from UAV data. Boulders that have rolled into field below the road are circled in yellow. Source is indicated by white circle.....	4-47
Figure 4.60. Pescia rockfall site 9b. Source area at top with runout damage. Not pictured: runout boulders across road and into field, corresponding to approximate 30 degree Fahrboeschung angles	4-47
Figure 4.61. Frontal view of the rock monolith at km 3 of SP134 motorway.....	4-49
Figure 4.62. Lateral view from the drone of the rock column at km 3 of SP134 (right valley flank) (a). The left part of the column cap collapsed producing two small avalanches towards the column front and along the column free side. Scars left from two wedges on the adjacent cliff (b). Leftward tilting of the column cap is also visible in Figure 4.61.....	4-50
Figure 4.63. General oblique view of the rock slide and subsequent rock avalanche on the left flank of the Nera valley (km 3 of SP134 motorway) (a); detail of the detachment area (b). Images taken from the 3D model generated by BYU on the basis of drone surveys	4-51
Figure 4.64. General oblique view from the drone of the rock slide on the right flank of the Nera valley (km 4 of SP134 motorway); the rock avalanche invaded the motorway and the valley bottom below for a stretch of about 70 m spreading large blocks (b-c)	4-52
Figure 4.65. Close-range drone image of the detachment area (a) and detail of a bedding joint forming the sliding surface taken from the slide foot (b)	4-52
Figure 4.66. Drone image of a layer of cataclasized limestone located under the main slide scar(a) and detail of a pervasively fractured limestone block fallen from the slope (b)	4-53
Figure 4.67. Satellite image of Mt. Vettore Massive showing fault alignment and slope displacement sites 11 and 19	4-54

Figure 4.68. Excerpt from 3D SfM model from UAV data of the side of Mt. Vettore. The blue dashed line indicates the footpath. Red dashed line indicates scarps interpreted as the fault rupture trace(s). The yellow lines indicate scarps interpreted as minor slope instabilities. Looking from the west to the west face of Mt. Vettore. On the right of the image the slope descends on the south face towards road SR477	4-55
Figure 4.69. View of the east slope of Mt. Vettore showing talus slopes and fault rupture trace. Fault rupture displacements and strong ground shaking have caused densification and sliding of talus	4-55
Figure 4.70. Image of fault scarp and associated nearby slope instabilities (yellow)	4-56
Figure 4.71. Location of the rockfall on road SP 477 between Arquata and Castelluccio	4-56
Figure 4.72. Overlay of the UAV orthomosaic on top of the Google Earth image of SP477, the Castelluccio-Norcia highway. Isolated boulders descended from the outcrop NE trending ridge on the left down to a ravine on the right side of the ortho mosaic, a maximum distance of approximately 375 m as indicated by the blue line. No other area along this highway had intense rockfall	4-57
Figure 4.73. The most active area along Route SP 477 is below a large south facing ridge of limestone. The white areas near the top of the ridge are zones where fresh rock is exposed following collapse of blocks. This ortho mosaic is part of a three-dimensional model produced using a UAV phantom 4	4-57
Figure 4.74. Rockfalls with boulders on the road	4-58
Figure 4.75. Rockfalls with boulders on the road	4-59
Figure 4.76. Debris avalanche along the scarp of a previous landslide	4-59
Figure 4.77. Debris and boulders captured by the rockfall protection nets.....	4-60
Figure 4.78. Boulders supported by the vegetation	4-60
Figure 4.79. Fracture along the road, large vertical offset due to fracture and ultimate movement, damaged edge barriers and debris and boulders on the road surface	4-61
Figure 4.80. Telecommunication facility (a) over and (b) under the road.....	4-62
Figure 4.81. Location of the rockfalls in Pontechiusita along SP209	4-63
Figure 4.82. Rockfalls along the SP209 between Triponzi and Visso	4-63
Figure 4.83. Slope protection damaged by boulders and rock-blocks	4-63

Figure 4.84. Debris occurred on the right bank of the Nera river along SP209 (lat 42.9157N, lon 13.0456E)	4-64
Figure 4.85. Location of the rockfalls between Piedipaterno and Cerreto along highway SS685.....	4-64
Figure 4.86. Rockfalls between Piedipaterno and Cerreto along highway SS685	4-65
Figure 4.87. Location of the landslide between Cittareale and Norcia along the SP746	4-66
Figure 4.88. Landslide between Cittareale and Norcia along the SP746: (a) General view of the area; (b) Zoom on the crown and main body of the scarp.....	4-66
Figure 4.89. Failure in calcareous breccia between Cittareale and Norcia along the SP746: from (a) to (e) view of the all facade; (f) rockfall on the road.....	4-67
Figure 4.90. Location of the landslide along the road Ortolano-Campotosto.....	4-68
Figure 4.91. (a) Overview of the whole longitudinal extent of the landslide area; (b) close up view of the landslide-related features from the road Ortolano-Campotosto.....	4-68
Figure 4.92. Cracks along the road	4-69
Figure 4.93. A slide observed on the fill slope	4-69
Figure 4.94. Fractures on the cut slope	4-70
Figure 4.95. Damages along the road	4-70
Figure 4.96. Minor scarps observed on the cut slope side of the road	4-71
Figure 4.97. Rock-net protection with captured debris.....	4-71
Figure 4.98. Location of the rockfalls along SP476 (between Piedivalle and Preci)	4-72
Figure 4.99. Observed rockfalls along SP476 (between Piedivalle and Preci)	4-72
Figure 4.100. Location of the Landslide below the village of Tino on small road parallel to highway SS4	4-73
Figure 4.101. Landslide debris covering the roadway. Boulders range in size up to 2 meters. Also pictured is rockfall netting used by local officials for minor rockfall control on the slope.....	4-74
Figure 4.102. Landslide debris and head scarp. Also pictured is rockfall netting.....	4-74
Figure 4.103. Location embankment fill damage area next to fault trace zone along SP477 road, Mt Vettore.....	4-75

Figure 4.104. 3D SfM model of embankment fill damage area next to fault trace zone along SP477 road, Mt Vettore. Fill that has experienced 15 to 20cm lateral displacement circled in yellow. Observed fault rupture trace shown in red	4-75
Figure 4.105. Road embankment damage along SP477 road, Mt Vettore (Location 19, viewing North). Note fault trace across road and black (new) bitumen repairs following previous (24 August 2016) earthquake	4-76
Figure 4.106. Road embankment damage along SP477 road, Mt Vettore (Location 19, viewing west)	4-76
Figure 5.1. Location of the observed mud volcanoes	5-2
Figure 5.2. Tour sign indicating mud volcanoes sited in Monteleone di Fermo.....	5-3
Figure 5.3. Location of the observed mud volcanoes in Monteleone di Fermo.....	5-3
Figure 5.4. (a) overview of the mud volcano in Santa Maria in Paganico; (b) sampling activities in in Santa Maria in Paganico; (c) crack originated by the mud volcano in Valle Corvone, (d) mud volcano in Valle Corvone, (e) details of a crack in Valle Corvone, (f) close-up view of the material ejected in the Ete Vivo river (Valle Corvone)	5-5
Figure 5.5. (a) and (b) photos of the mud volcano in Valle Corvone taken by INGV in November 2016 (INGV, 2016); (c) and (d) photos of the mud volcano in Valle Corvone taken from a common perspective by GEER in December 2016	5-5
Figure 5.6. Particle size distributions of the mud volcano soils in Monteleone di Fermo and Santa Vittoria in Matenano.....	5-6
Figure 5.7. (a) Plasticity chart and (b) activity chart of the mud volcano soils in Monteleone di Fermo and Santa Vittoria in Matenano	5-7
Figure 5.8. Location of the inspected mud new volcano in Santa Vittoria in Matenano	5-7
Figure 5.9. Overview of the mud new volcano in Santa Vittoria in Matenano	5-8
Figure 5.10. Earthquake magnitude versus epicentral distance for earthquake-triggered mud volcanoes, along with limiting curves from Delle Donne et al (2010, blue dashed curve), and Manga et al. (2009, black dashed curve). Red dots represent data collected in this study, blue dots are data points from Delle Donne et al. (2010), black dots are data points from Manga et al. (2009)	5-9
Figure 6.1. Evolution of damage after (a) the 24 August earthquake, and (b) the October events.....	6-3

Figure 6.2. Percentage of damaged structures (a) in the aftermath of first event and (b) after the whole sequence.....	6-4
Figure 6.3. Structures shown in detail in the following. (M stands for Masonry).	6-5
Figure 6.4. Building M1.	6-5
Figure 6.5. Building M2.	6-6
Figure 6.6. Building M3.	6-6
Figure 6.7. Building M4.	6-7
Figure 6.8. Visual angles investigated during UAV flights.....	6-7
Figure 6.9. UAV image V1.	6-8
Figure 6.10. UAV image V2.	6-8
Figure 6.11. UAV image V3.	6-9
Figure 6.12. UAV image V4.	6-9
Figure 6.13. UAV image V5.	6-9
Figure 6.14. UAV image V6.	6-10
Figure 6.15. Damage proxy map of Norcia, along with all structures with assigned damage level D5, and selected structures with assigned damage level D4.....	6-11
Figure 6.16. Zoom-in of the damage proxy map of Norcia, along with the identification numbers of all structures with assigned damage level D5 from field inspections and available high-quality on-site information and photos.	6-12
Figure 6.17. Pictures of all structures with assigned damage level D5 in the city center of Norcia, along with their identification numbers.....	6-14
Figure 6.18. Evolution of damage after (a) the first seismic event and (b) the sequence of events.....	6-15
Figure 6.19. Percentage of damaged structures (a) after the first event and (b) after the whole sequence.	6-16
Figure 6.20. (a) Access route to the lowest (easternmost) portion village (V1). (b) Piazza San Francesco (V2).	6-16
Figure 6.21. Aerial view, east-west direction (V3).....	6-17

Figure 6.22. Aerial view, west-east direction (V4).....	6-17
Figure 6.23. Aerial view, south-north direction (V5).	6-18
Figure 6.24. Ortho-images captured on December: (a) overview; (b) zoom on Piazza San Francesco.	6-19
Figure 6.25. Representative pictures taken in Accumoli during the GEER survey (see Table 6.2).	6-22
Figure 6.26. Representative pictures of landslide in eastern part of village (September 2016).	6-22
Figure 6.27. Representative pictures of landslide in the eastern part of village (December 2016).	6-22
Figure 6.28. Evolution of damage after (a) the first seismic event and (b) the sequence of events.....	6-23
Figure 6.29. Percentage of damaged structures (a) in the aftermath of first event and (b) after the whole sequence.	6-24
Figure 6.30. Overview of the location and structural system of the buildings that are documented in the following. (RC: Reinforced Concrete, M: Masonry, and S: Steel buildings).....	6-24
Figure 6.31. Visual angles investigated during the UAV flight.	6-25
Figure 6.32. UAV image V1.	6-25
Figure 6.33. UAV image V2.	6-26
Figure 6.34. UAV image V3.	6-26
Figure 6.35. UAV image V4.	6-27
Figure 6.36. UAV image V5.	6-27
Figure 6.37. Building RC1.	6-28
Figure 6.38. Building RC2.	6-29
Figure 6.39. Building RC3.	6-29
Figure 6.40. Building RC4.	6-30
Figure 6.41. Building S1.....	6-31
Figure 6.42. Building M1.	6-32

Figure 6.43. Building M2.	6-32
Figure 6.44. Building M3.	6-33
Figure 6.45. Building M4.	6-33
Figure 6.46. Building M5.	6-34
Figure 6.47. Location of representative pictures taken in Arquata del Tronto/Borgo after the 24 August 2016 earthquake (yellow dots), and after the October events (red dots).	6-35
Figure 6.48. Overview of Arquata del Tronto (a) after the 24 August earthquake, and (b) after the October events.	6-35
Figure 6.49. A reinforced masonry building in Borgo (a) after the 24 August earthquake, and (b) after the October events.	6-36
Figure 6.50. A building in Borgo (a) after the 24 August earthquake, and (b) after the October events.	6-36
Figure 6.51. Access road to Arquata del Tronto after the October events.	6-36
Figure 6.52. Overview of the damage level in Arquata del Tronto after October events.	6-37
Figure 6.53. Mapped damage levels in Pescara del Tronto: (a) after the 24 August, and (b) the October events.	6-38
Figure 6.54. Histogram of damage levels in Pescara del Tronto: (a) after the 24 August, and (b) the October events.	6-38
Figure 6.55. Location of representative pictures taken in the village after the 24 August (yellow dots) and locations for which we have multi-epoch photos of the same structures (red dots).	6-39
Figure 6.56. Comparative pictures of selected structures in Pescara del Tronto after the 24 August event, and after the October events.	6-40
Figure 6.57. Overview of Pescara del Tronto from a common perspective (a) after the 24 August earthquake, and (b) after the October events.	6-41
Figure 6.58. 3D-model overview of Pescara del Tronto from a common perspective (a) after the 24 August earthquake, and (b) after the October events.	6-42
Figure 6.59. Mapped damage levels in Tufo: (a) after the 24 August, and (b) the October events.	6-43

Figure 6.60. Histograms of damage levels in Tufo: (a) after the 24 August, and (b) the October events.	6-44
Figure 6.61. Map of the selected representative structures in Tufo.	6-44
Figure 6.62. Comparative pictures of selected structures in Tufo after the 24 August event, and after the October events.	6-46
Figure 6.63. Representative pictures taken in Montegalloy during the GEER survey (see Table 6.6 and Table 6.7).	6-53
Figure 6.64. Geological map (a) and cross-sections (b) of the Visso village area (Regione Marche, 2012).	6-56
Figure 6.65. Locations of representative structures inspected in the Visso village (see Table 6.8 for details).	6-56
Figure 6.66. Representative pictures taken in Visso during the survey (see Table 6.8).	6-64
Figure 6.67. Damage zonation within the villages of Visso village.	6-65
Figure 6.68. Noise measurement T01 results in terms of H/V spectral ratio (up) and H/V polar plots (bottom).	6-66
Figure 6.69. Locations of representative structures inspected in Ussita, and damage zonation within the village.	6-67
Figure 6.70. Representative pictures taken in Ussita (P13)	6-68
Figure 6.71. San Nicola da Tolentino church, façade (left) and interior part (right) (before earthquake events).	6-70
Figure 6.72. Geological map of the Tolentino area.	6-71
Figure 6.73. Tolentino reconnaissance map: in green the most damaged zones.	6-71
Figure 6.74. Representative pictures taken in Tolentino during the GEER survey (see Table 6.9).	6-75
Figure 6.75. Relative position and distance between San Severino Marche and Tolentino.	6-77
Figure 6.76. Piazza del Popolo, San Severino Marche (before seismic events).	6-78
Figure 6.77. Geological map of the San Severino area.	6-78
Figure 6.78. Summary reconnaissance map for San Severino Marche.	6-79

Figure 6.79. Summary reconnaissance map for San Severino Marche (zoom on the Uvaiolo neighborhood).....	6-79
Figure 6.80. Representative pictures taken in San Severino Marche during the GEER survey (see Table 6.10).....	6-83
Figure 6.81. Geological map of Camerino (a) and cross section BB' (b) (Regione Marche, 2012).....	6-85
Figure 6.82. Historical earthquakes occurred in Camerino (CPTI- INGV).	6-86
Figure 6.83. Locations of the representative structures inspected in Camerino (including red zone) (see Table 6.11 for details).....	6-86
Figure 6.84. Representative pictures taken in Camerino (see Table 6.11 for details).....	6-99
Figure 6.85. (a) Geological map of Pievebovigliana village and (b) geological section showing the main stratigraphical relationships (Regione Marche, 2014).	6-101
Figure 6.86. Locations of representative structures inspected in Pievebovigliana (see Table 6.12 for details).....	6-102
Figure 6.87. Representative pictures in Pievebovigliana during the survey (see Table 6.12).	6-107
Figure 6.88. Damage zonation within the villages of Pievebovigliana village.	6-109
Figure 6.89. Noise measurements results in terms of H/V spectral ratio (on the left column) and H/V polar plots (on the right).	6-110
Figure 6.90. Locations of representative structures inspected in Pieve Torina, and damage zonation within the village.....	6-111
Figure 6.91. Representative pictures taken in Pieve Torina.	6-111
Figure 6.92. Noise measurements results in terms of H/V spectral ratio (on the left column) and H/V polar plots (on the right)	6-112
Figure 6.93. (a) Geological map of Fiume (Pieve Torina) village and (b) EW Geological cross-section (Regione Marche, 2012).....	6-113
Figure 6.94. Locations of representative structures inspected in Fiume (Pieve Torina) and damage zonation (see Table 6.13 for details).....	6-114
Figure 6.95. Representative pictures taken in Fiume (Pieve Torina) during the survey (see Table 6.13).	6-116

Figure 6.96. Noise measurements results in terms of H/V spectral ratio (on the left column) and H/V polar plots (on the right).	6-117
Figure 6.97. (a) Geological map of Casavecchia Alta village, and (b) Geological cross-section (Regione Marche, 2012b).	6-118
Figure 6.98. Locations of representative structures inspected in Casavecchia (see Table 6.14 for details).....	6-119
Figure 6.99. Representative pictures taken in Casavecchia during the survey (see Table 6.14).....	6-120
Figure 6.100. Noise measurement T01 results in terms of H/V spectral ratio (up) and H/V polar plots (bottom).....	6-120
Figure 6.101. Locations of representative structures inspected in Sellano and surrounding hamlets (see Table 6.15 for details).....	6-121
Figure 6.102. Representative pictures taken in Sellano and surroundings during the survey (see Table 6.15).....	6-123
Figure 6.103. Noise measurement results in terms of H/V spectral ratio (top) and H/V polar plots (bottom) (Sellano, Municipio square, 42.888828°- 12.926805°).....	6-124
Figure 6.104. Locations of the representative structures inspected in Ancarani pié del colle (see Table 6.16 for details).	6-1125
Figure 6.105. Representative pictures taken at Ancarani pié del Colle (see Table 6.16 for details).	6-128
Figure 6.106. Geological map of Cessapalombo main centre (Regione Marche, 2012).....	6-129
Figure 6.107. Historical earthquakes felt in Cessapalombo (CPTI- INGV).....	6-130
Figure 6.108. Locations of the representative structures inspected in Cessapalombo (see Table 6.17 for details).	6-130
Figure 6.109. Representative pictures taken at Cessapalombo (see Table 6.17 for details).....	6-133
Figure 6.110. Locations of the representative structures inspected in Preci.	6-134
Figure 6.111. Representative pictures of church in Preci (Lat = 42.881418, Lon = 13.036290).	6-135
Figure 6.112. Locations of the representative structures inspected in Piedivalle.....	6-135
Figure 6.113. Representative pictures taken at Piedivalle.	6-136

Figure 6.114. Locations of the representative structures inspected in Caldarola (see Table 6.18 for details).....	6-137
Figure 6.115. Representative pictures taken at Caldarola (see Table 6.18 for details).....	6-140
Figure 6.116. Locations of the representative structures inspected in Castello di Campi (see Table 6.19 for details).....	6-140
Figure 6.117. Representative pictures taken at Castello di Campi (see Table 6.19 for details).....	6-141
Figure 6.118. Representative pictures taken in Colfiorito during the survey (see Table 6.20).....	6-142
Figure 6.119. (a) Geological map of San Lorenzo in Colpolina village, and (b) Geological cross-section (Regione Marche, 2012).....	6-144
Figure 6.120. Locations of representative structures inspected in San Lorenzo in Colpolina (see Table 6.21 for details).....	6-144
Figure 6.121. Representative pictures taken in San Lorenzo in Colpolina during the survey (see Table 6.21).....	6-145
Figure 6.122. Noise measurements results in terms of H/V spectral ratio (top) and H/V polar plots (bottom).....	6-146
Figure 6.123. Representative pictures taken in Serravalle during the GEER reconnaissance (see Table 6.22).....	6-147
Figure 6.124. Damage proxy map of Popoli (http://aria-share.jpl.nasa.gov/events/20161030-Italy_EQ/DPM/ , last accessed 21 April, 2017).....	6-148
Figure 6.125. Representative pictures taken in Popoli during the GEER reconnaissance (see Table 6.23).....	6-149
Figure 6.126. Damage proxy map of San Pellegrino (http://aria-share.jpl.nasa.gov/events/20161030-Italy_EQ/DPM/) along with the identification numbers of the structures with assigned damage level D5.....	6-150
Figure 6.127. Damaged constructions in the oldest part of San Pellegrino (http://video.repubblica.it/dossier/terremoto-30-ottobre/terremoto-centro-italia-la-distruzione-a-san-pellegrino-di-norcia-dal-drone/257495/257761).....	6-151
Figure 6.128. Pictures of the structures with assigned damage level D5 in San Pellegrino, before and after the October earthquake, along with their identification numbers.....	6-152
Figure 7.1. Map of epicentral region showing locations of bridge sites visited by the GEER team following the October 2016 seismic sequence.....	7-1

Figure 7.2. Bridge along SP477 (42.782073 deg, 13.142383 deg): road surface cracks (a); longitudinal cracks along the road side (b); cracks between the bridge arch and the main structure (c-d); view of the bridge on December 2011 (e) 7-4

Figure 7.3. Roman-era bridge along the Trisungo route (1 span bridge - Tufo area – Arquata del Tronto - N42.735981, E13.254862): view of the arch (a, b) and the road cracks (c, d) after the 24 August event (photo on September 7 2016 (a, c)) and after the 30 October event (photo on December 13 2016 (b, d)) 7-5

Figure 7.4. Roman-era bridge along the Trisungo route (3 spans bridge - Tufo area – Arquata del Tronto - N42.73538, E13.25365): (c) after the 24 August event (photo on September 7 2016) and (d) after the 30 October event (photo on December 13 2016) 7-6

Figure 7.5. Ponte a Tre Occhi (42.620668 deg, 13.290176deg): (a) after the 24 August event (photo on September 7 2016) and (b,c,d) after the 30 October event (photo on December 13 2016), repairing works (c) and bridge masonry collapse (d) 7-7

Figure 7.6. Ponte a Cinque Occhi (42.623178 deg, 13.250428deg): increased sub-vertical cracks to the piers after the 30 October event at the top (a) and bottom (b) of the piers (photo on November 20 2016) and structural retrofitting of the bridge (c and d) (photo on December 15 2016) 7-8

List of Tables

Table 2.1.	Summary of the six main events occurred in Central Italy between 24 August and 30 October 2016	2-1
Table 3.1.	Attributes of the six earthquake events analyzed.....	3-1
Table 3.2.	Measured VS30 and details of the newly characterized recording station sites.....	3-6
Table 4.1.	Reconnaissance landslide site locations (Case studies and Imaging).....	4-4
Table 4.2.	Reconnaissance landslide site locations (Visual inspection sites)	4-5
Table 4.3.	Landslide abundance as a function of little logic unit (from Guzzetti et al, 2004).....	4-7
Table 6.1.	Inspected villages/hamlets and estimated ground motions.	6-2
Table 6.2.	Summary of pictures and structures inspected in Accumoli. (*pictures that show the comparison between September (left) and December (right) inspection).	6-18
Table 6.3.	Locations of representative pictures with description of reported damage.....	6-37
Table 6.4.	Locations of representative pictures with description of reported damage.....	6-43
Table 6.5.	Summary of selected representative structures in Tufo (all pictures show the comparison between September (left) and December (right) inspection).	6-47
Table 6.6.	Summary of reconnaissance results for Montegallo hamlets.	6-48
Table 6.7.	Summary of pictures and structures inspected in Montegallo hamlets.	6-48
Table 6.8.	Locations of representative structures with damage descriptions.	6-57
Table 6.9.	Summary of pictures and structures inspected in Tolentino.....	6-75
Table 6.10.	Summary of pictures and structures inspected in San Severino Marche.....	6-84
Table 6.11.	Locations of representative structures with damage descriptions.	6-87
Table 6.12.	Locations of representative structures with damage descriptions	6-108
Table 6.13.	Locations of representative structures with damage descriptions.	6-114
Table 6.14.	Locations of representative structures with damage descriptions.	6-119

Table 6.15.	Locations of representative structures with damage descriptions	6-122
Table 6.16.	Locations of representative structures with damage descriptions.	6-125
Table 6.17.	Locations of representative structures with damage descriptions.	6-131
Table 6.18.	Locations of representative structures with damage descriptions.	6-138
Table 6.19.	Locations of representative structures with damage descriptions.	6-141
Table 6.20.	Locations of representative structures with damage descriptions	6-142
Table 6.21.	Locations of representative structures with damage descriptions.	6-145
Table 6.22.	Locations of representative structures with damage descriptions	6-147
Table 6.23.	Locations of representative structures with damage descriptions	6-149
Table 6.24.	Locations of representative structures with damage descriptions.	6-152
Table 7.1.	Details of bridges inspected following October 2016 seismic sequence.	7-2

1 Introduction

Jonathan P. Stewart, Paolo Zimmaro

1.1 Event Sequence Overview and Organization of Reconnaissance

Between August and November 2016, three major earthquake events occurred in Central Italy. The first event, with **M6.1**, took place on 24 August 2016, the second (**M5.9**) on 26 October, and the third (**M6.5**) on 30 October 2016. Each event was followed by numerous aftershocks.

As shown in Figure 1.1, this earthquake sequence occurred in a gap between two earlier damaging events, the 1997 **M6.1** Umbria-Marche earthquake to the north-west and the 2009 **M6.1** L'Aquila earthquake to the south-east. This gap had been previously recognized as a zone of elevated risk (GdL INGV sul terremoto di Amatrice, 2016). These events occurred along the spine of the Apennine Mountain range on normal faults and had rake angles ranging from -80 to -100 deg, which corresponds to normal faulting. Each of these events produced substantial damage to local towns and villages. The 24 August event caused massive damages to the following villages: Arquata del Tronto, Accumoli, Amatrice, and Pescara del Tronto. In total, there were 299 fatalities (www.ilgiornale.it), generally from collapses of unreinforced masonry dwellings. The October events caused significant new damage in the villages of Visso, Ussita, and Norcia, although they did not produce fatalities, since the area had largely been evacuated.

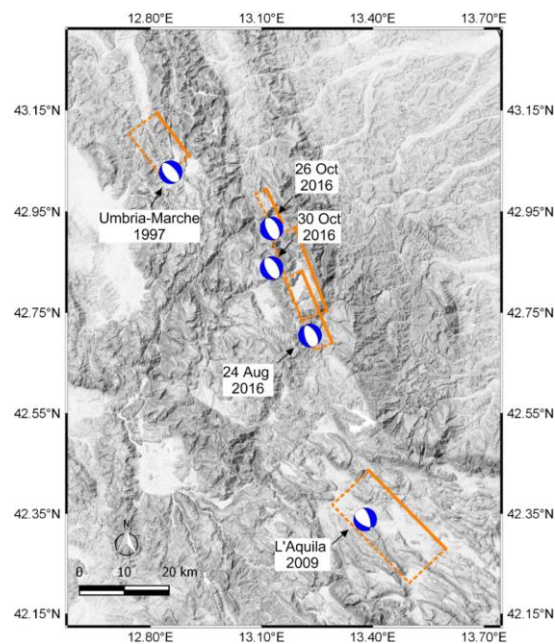


Figure 1.1. Map of central Italy showing moment tensors of major earthquakes since 1997 and the intermediate gap areas. Finite fault models from Chiaraluce et al. (2004; 1997 Umbria-Marche event), Piatanesi and Cirella (2009; 2009 L'Aquila event), Tinti et al. (2016, 24 August event), and GdL INGV sul terremoto in centro Italia, 2016, 26 and 30 October events). Moment tensors for 26 and 30 October 2016 earthquakes are also shown.

The NSF-funded Geotechnical Extreme Events Reconnaissance (GEER) association, with co-funding from the B. John Garrick Institute for the Risk Sciences at UCLA and the NSF I/UCRC Center for Unmanned Aircraft Systems (C-UAS) at BYU, mobilized a US-based team to the area in two main phases: (1) following the 24 August event, from early September to early October 2016, and (2) following the October events, between the end of November and the beginning of December 2016. The US team worked in close collaboration with Italian researchers organized under the auspices of the Italian Geotechnical Society, the [Italian Center for Seismic Microzonation and its Applications](#), the Consortium ReLUIS, Centre of Competence of Department of Civil Protection and the Disaster REcovery Team of Politecnico di Torino. The objective of the Italy-US GEER team was to collect and document perishable data that is essential to advance knowledge of earthquake effects, which ultimately leads to improved procedures for characterization and mitigation of seismic risk.

The Italy-US GEER team was multi-disciplinary, with expertise in geology, seismology, geomatics, geotechnical engineering, and structural engineering. The composition of the team was largely the same for the two mobilizations, particularly on the Italian side. Our approach was to combine traditional reconnaissance activities of on-ground recording and mapping of field conditions, with advanced imaging and damage detection routines enabled by state-of-the-art geomatics technology. GEER coordinated its reconnaissance activities with those of the Earthquake Engineering Research Institute (EERI), although the EERI mobilization to the October events was delayed and remains pending as of this writing (April 2017). For the August event reconnaissance, EERI focused on emergency response and recovery, in combination with documenting the effectiveness of public policies related to seismic retrofit. As such, GEER had responsibility for documenting structural damage patterns in addition to geotechnical effects.

This report is focused on the reconnaissance activities performed following the October 2016 events. More information about the GEER reconnaissance activities and main findings following the 24 August 2016 event, can be found in GEER (2016). The objective of this document is to provide a summary of our findings, with an emphasis of documentation of data. In general, we do not seek to interpret data, but rather to present it as thoroughly as practical. Moreover, we minimize the presentation of background information already given in GEER (2016), so that the focus is on the effects of the October events. As such, this report and GEER (2016) are inseparable companion documents.

Similar to reconnaissance activities following the 24 August 2016 event, the GEER team investigated earthquake effects on slopes, villages, and major infrastructure. Figure 1.2 shows the most strongly affected region and locations described subsequently pertaining to:

1. Surface fault rupture;
2. Recorded ground motions;
3. Landslides and rockfalls;
4. Mud volcanoes;
5. Investigated bridge structures;
6. Villages and hamlets for which mapping of building performance was performed;

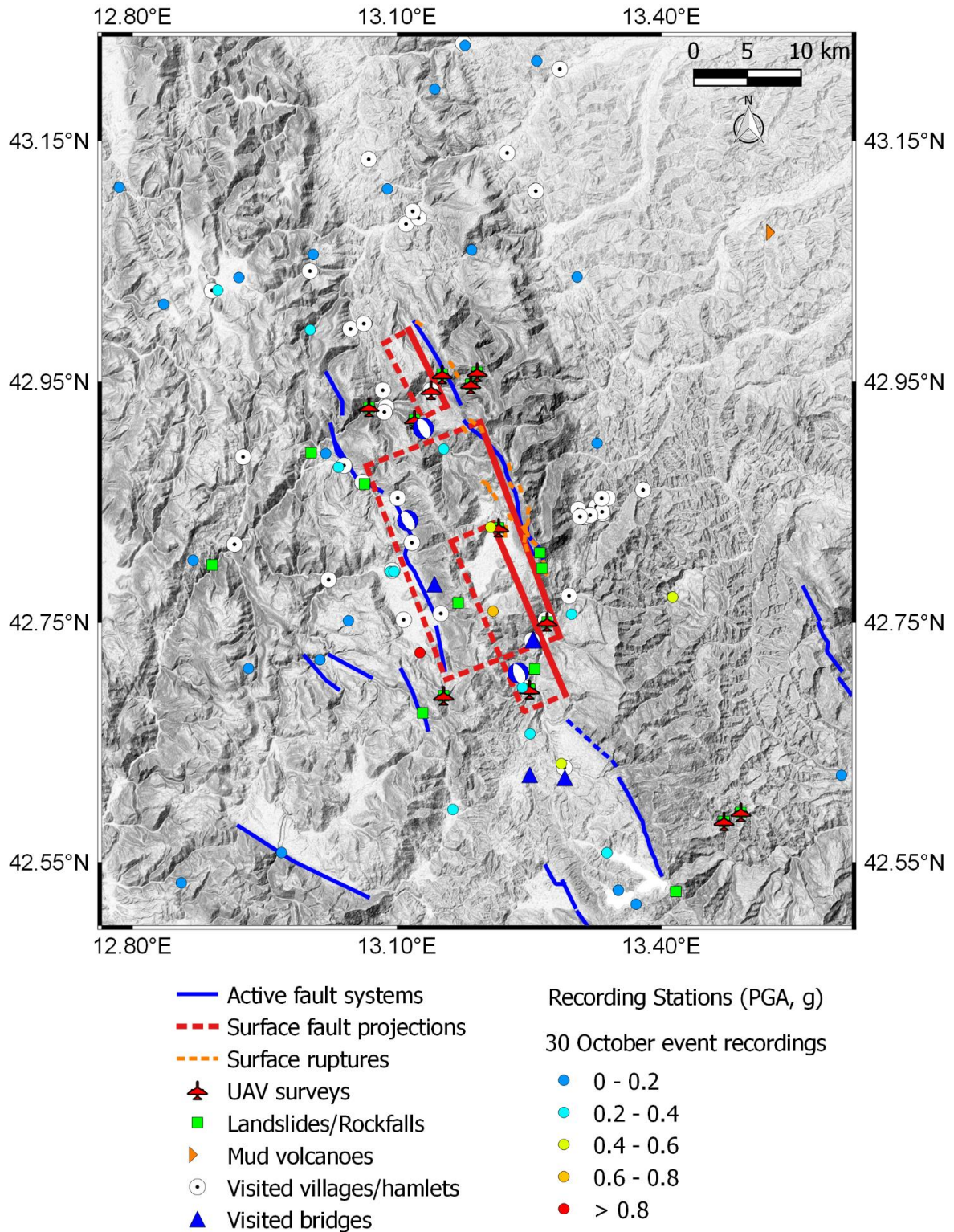


Figure 1.2. Regional map showing the active fault systems, finite fault models and epicenters of the 24 August, 26 and 30 October events, ground motion station locations and recorded peak ground accelerations (PGA) for the 30 October events, and locations of various earthquake effects discussed in this report.

1.2 Overview of Reconnaissance Activities

The approach followed by the GEER team was to combine traditional reconnaissance activities of on-ground recording and mapping of field conditions, with advanced imaging and damage detection routines enabled by state-of-the-art geomatics technology. This combination of reconnaissance techniques provides opportunities for innovative future study.

GEER reconnaissance occurred in two principal phases. The first focused on landslides and surface rupture, the second on mapping of structural damage patterns in villages and hamlets of interest. Phase 1 took place principally from 30 November - 7 December, 2017, and Phase 2 from 10-13 December 2016. As with the September reconnaissance we completed extensive three-dimensional imaging from UAVs (Unmanned Aerial Vehicles) of landslide features, surface faulting, and structural damage patterns. Three-dimensional models resulting from this work are available at the following links (last accessed 5 May, 2017):

- [GEER website – 2016 Central Italy earthquakes event page \(three-dimensional interactive PDF models; A1-A11\);](#)
- [BYU-PRISM website – 2016 Central Italy earthquakes event page \(interactive on-line three-dimensional models\).](#)

Following this introduction, Chapter 2 describes the seismic source (moment tensor, finite faulting) and observations of surface faulting from the October events. Background information on tectonic setting, regional geology, and historic earthquakes in the region can be found in GEER (2016). Chapter 3 describes strong ground motions from the October events, including near-fault ground motion characteristics and how the observations compare to available ground motion models. Chapter 4 presents our reconnaissance of earthquake-induced landslides, which were much more severe in the October events than in the earlier August events. Chapter 5 describes several mud volcanoes observed following the event sequence, which is an effect not encountered following the August events.

Chapter 6 is concerned with the performance of building structures in the villages and hamlets within the strongly shaken areas. Chapter 6 has two major sub-sections, one on 're-visits' to areas previously visited following the August events, and the second only newly visited areas. The re-visit documentation is relatively brief, focusing on the new data. For large newly visited areas, we present further information on historical seismicity, geological conditions, and the results of our mapping work. Chapter 7 documents the performance of bridge structures, with an emphasis on changes in damage levels resulting from the October events relative to earlier inspections. In the last chapter, significant case histories that can serve as subjects for future research are identified and discussed.

2 Seismic Source and Surface Rupture

Fabrizio Galadini, Emanuela Falcucci, Stefano Gori, Robert E. Kayen, Bret Lingwall, Alberto Pizzi, Alessandra Di Domenica, Paolo Zimmaro, Jonathan P. Stewart

2.1 Seismic Source

The August-October 2016 earthquake sequence occurred on mapped normal faults in the Apennine Mountain range in central Italy. This is a region with a long history of destructive earthquakes. The locations of faults have been well studied and the effects of past earthquakes on villages and towns in the region is well documented. Chapter 2 of GEER (2016) describes this background information and provides specific historical and technical information for the major fault systems in the vicinity of this earthquake sequence. Here we focus our remarks on source models for the October 2016 events and mapping of surface ruptures from those events.

2.1.1 Moment tensors and aftershock patterns

Between 24 August and 30 October 2016, 17 events with $M > 4.2$ were recorded by the Italian National Seismic Network (Rete Sismica Nazionale, RSN; www.gm.ingv.it/index.php/rete-sismica-nazionale/, last accessed 3 April, 2017) owned by the Italian Institute of Geophysics and Vulcanology (Istituto Nazionale di Geofisica e Vulcanologia, INGV). Table 2.1 shows parameters and locations of the six largest- M events from that sequence. The information in Table 2.1 are provided by INGV (<http://cnt.rm.ingv.it>, last accessed 3 April, 2017). Using event-type identification procedures discussed in Section 3.1, we identified three mainshocks: (1) 24 August $M6.1$, (2) 26 October $M5.9$, and (3) 30 October $M6.5$ (bold entries in Table 2.1).

Table 2.1. Summary of the six main events occurred in Central Italy between 24 August and 30 October 2016

Date	Hour (UTC)	Latitude (N)	Longitude (E)	Depth (km)	M	Strike (deg)	Dip (deg)
08/24/2016	01:36:32	42.70	13.23	8	6.1	156	50
08/24/2016	02:33:28	42.79	13.15	8	5.3	134	56
08/26/2016	04:28:25	42.60	13.29	9	4.8	165	36
10/26/2016	17:10:36	42.88	13.13	9	5.4	160	38
10/26/2016	19:18:05	42.92	13.13	8	5.9	328	43
10/30/2016	06:40:17	42.84	13.11	5	6.5	162	27

Figure 2.1 shows focal mechanisms for each mainshock event, along with other information to be discussed subsequently. Each event involved normal slip on faults striking NW-SE and dipping to the SW. Specifics for each event are given in Table 2.1. The hypocenter locations, slip directions, and surface rupture suggest that the 26 and 30 October events occurred on segments of the Mt. Vettore fault. As described in GEER (2016), this fault and the neighboring Laga mountain fault to the south experienced rupture during the 24 August event.

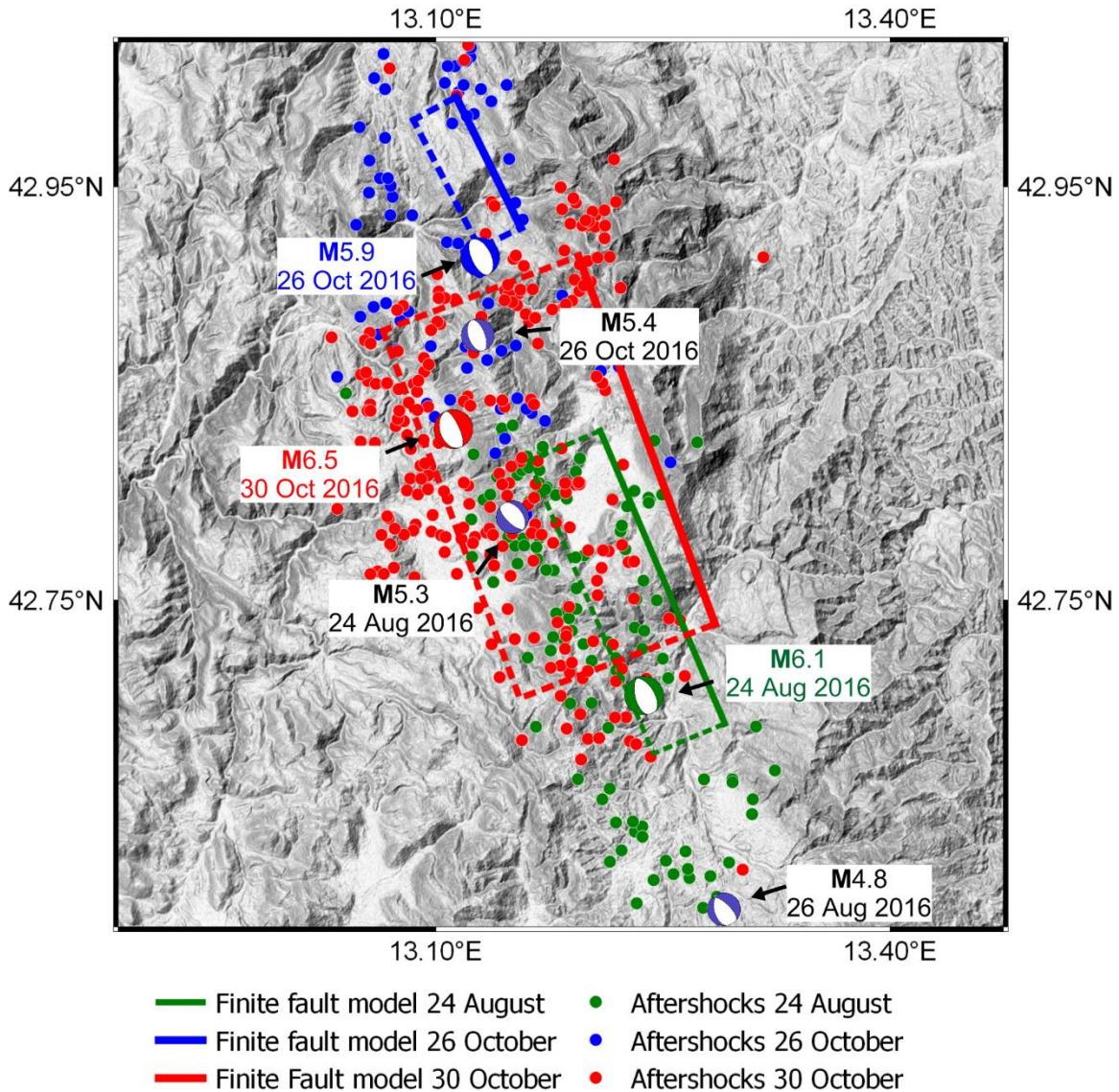


Figure 2.1. Map showing locations of hypocenters for three mainshock events in central Italy between 24 August and 30 October 2016. Also shown on selected finite fault models for each event and aftershock patterns for the 24-hour periods post-rupture.

The number of aftershocks within 24 hour periods following each mainshock were 121 (24 August), 75 (26 October), and 258 (30 October). Aftershocks following the three considered mainshocks have clear spatial patterns. For the 24 August event, most of the aftershock epicenters are not within the surface projection of the hanging wall above the finite fault model, with many south and west of the rupture. This pattern holds for the 26 October event as well, although in this case very few aftershocks epicenters actually occur within the surface projection of the rupture. The aftershocks pattern for the largest event (30 October) follows the expected pattern in which most epicenters occur within the surface projection of the rupture.

2.1.2 Crustal deformations

Crustal deformations associated with the 24 August 2016 event are described in Section 2.3.3 of GEER (2016). As with that event, crustal deformation data is available from GPS sensors for the two October events. Figures 2.2-2.3 show GPS-based deformation results for the two events. GPS data were obtained from INGV working group (2016). Crustal displacements would be expected to involve downward vertical displacement and horizontal displacement approximately to the southwest on the hanging walls of the fault. This is indeed the case for the 30 October event (Figure 2.3), for which the levels of displacement are large relative to the resolution of these measurement techniques. In the case of the 26 October event, the horizontal displacements are relatively randomly oriented, and may reflect the effects of noise in the measurements (Figure 2.2). The data in Figures 2.2 shows peak horizontal and vertical crustal displacements of about 0 – 3 and -2 – +0.7 cm, respectively for the 26 October event. The corresponding values for the 30 October event, shown in Figures 2.3, are 0 – 38 and -45 – +5 cm.

2.1.3 Finite fault models and trimming

Finite fault models for the 26 and 30 Oct events are presented by INGV (2016). These models are based on inversion of GPS data. As of this writing, we have not seen inversions that include both GPS and broadband ground motion data. The surface projection of the models, with some adjustment, are shown in Figure 2.1.

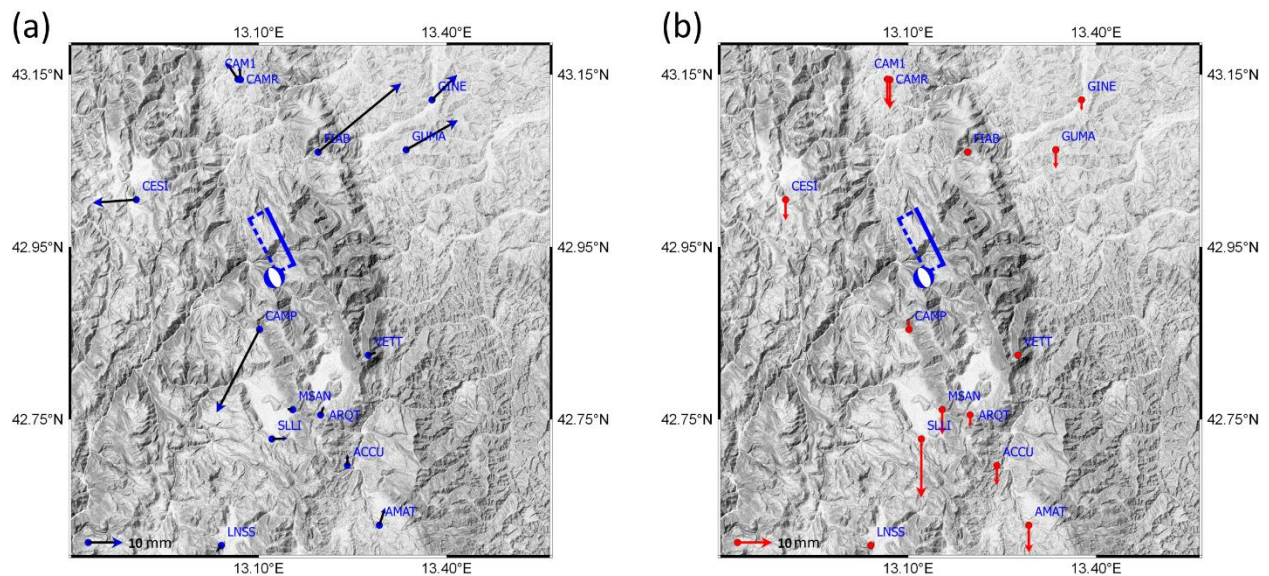


Figure 2.2. (a) horizontal, and (b) vertical GPS-based co-seismic displacement estimated after the 26 October event. Data used for producing the Figures were obtained from: ftp://gpsfree.gm.ingv.it/amatrice2016/static/Cosismico_26Oct2016_GPS_GdL_V1.dat, last accessed 4 April, 2017).

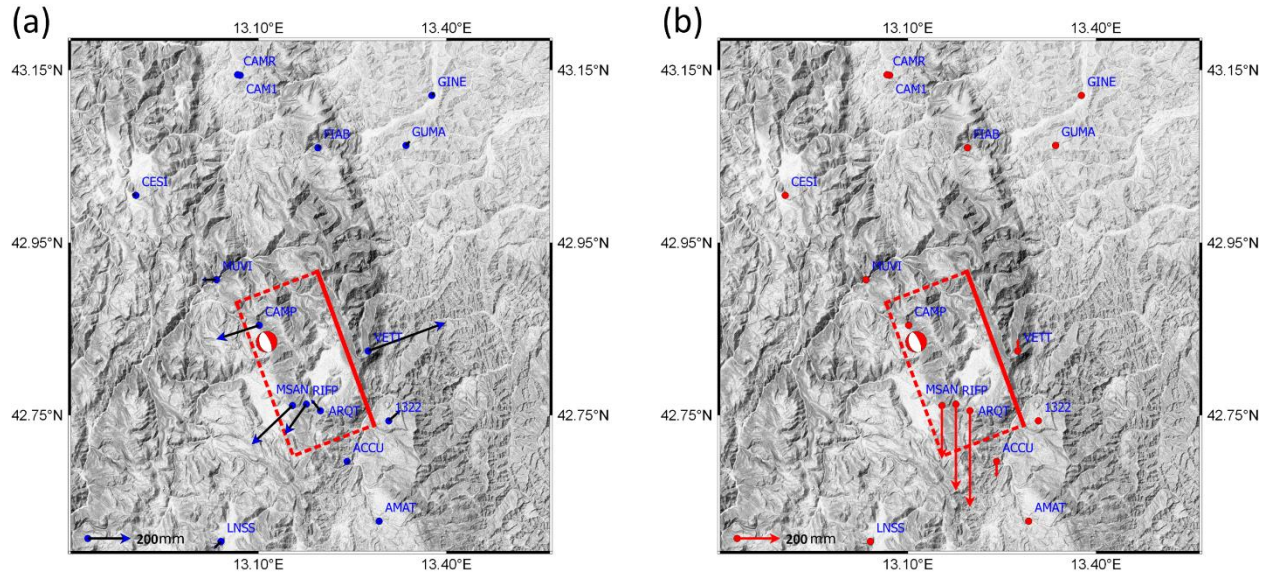


Figure 2.3. (a) horizontal, and (b) vertical GPS-based co-seismic displacement estimated after the 30 October event. Data used for producing the Figures were obtained from: ftp://gpsfree.gm.ingv.it/amatrice2016/static/Cosismico_30Oct2016_GPS_GdL_V1.dat, last accessed 4 April, 2017).

The 26 October event has an along-strike length of 8 km and down-dip width of 4 km. We adopt the trimmed model from INGV (2016), despite the lack of information in that document on how the trimming was performed. Details of this process are of nominal importance given the relatively small dimensions of this rupture (because the fault dimensions do not have a large effect on distances to sites of interest). The INGV model does not include a slip pattern.

The 30 October event has an along-strike length of 21 km and down-dip width of 16 km. The model presented by INGV (2016) is untrimmed, but includes a slip pattern. We trim by-eye the fault into a rectangular shape, removing parts of the rupture surface with slip < 50 cm (17% of the maximum slip of 300 cm). The trimmed version is shown in Figure 2.1. The largest slip on the fault is concentrated in the middle of the fault (along-strike) and near its deepest extent.

2.2 Surface Rupture

Surface rupture for the 24 August event is described in Section 2.4 of GEER (2016). The level of documentation of surface rupture effects is mixed for the October events classified as mainshocks (26 and 30 October). For the 26 October event, limited field observations are described from the short time window between this event and the subsequent 30 October event, which produced substantial additional slip on fault features. The limited observations following the 26 October event do not include detailed mapping, but do include observations that establish the presence of surface rupture.

For the 30 October event, several phases of reconnaissance were performed that establish the fault segments on which rupture was and was not observed, and which provide relatively

detailed pictures of the amounts and distribution of slip in some areas. The full length of the fault rupture was not mapped due to inclement weather that made mapping impossible beyond a certain date. Further mapping is expected following the Spring 2017 thaw.

The following sections summarize available information from the two events. Figure 2.4 shows the areas where surface rupture was observed in the two event, and locations of detail maps. The third section below explains in more details the method and results of GEER reconnaissance in early December 2016.

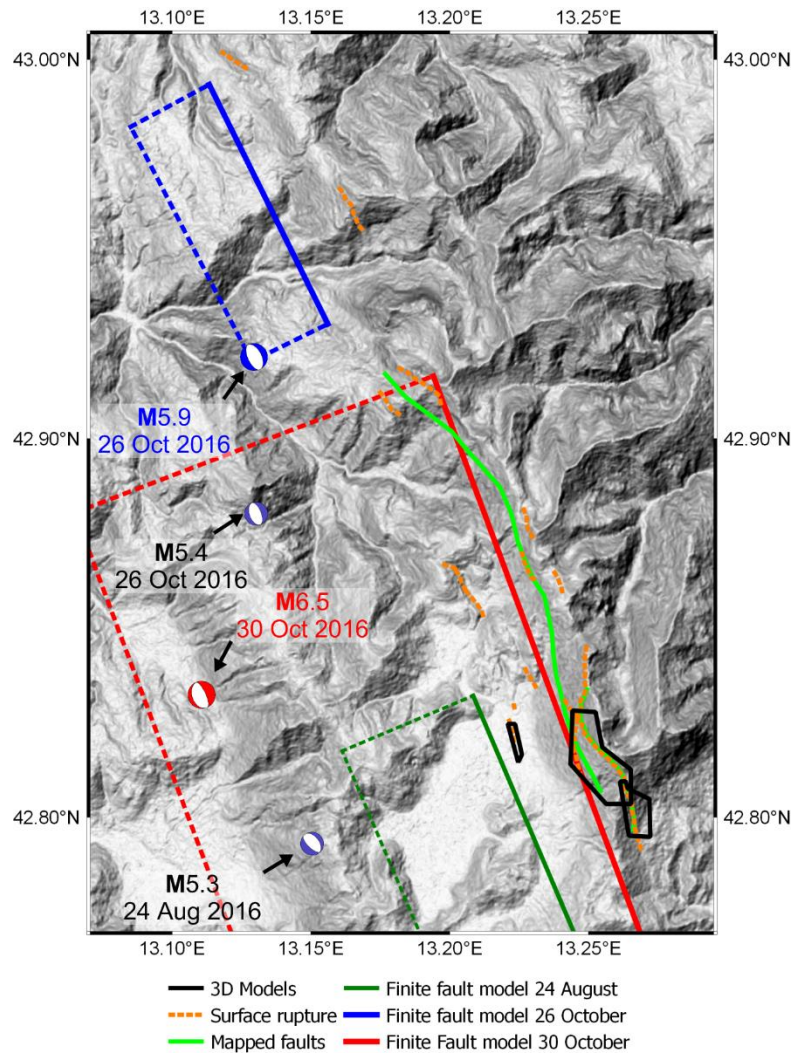


Figure 2.4. Detailed map of surface fault rupture, pre-event mapping of Mt. Vettore-Mt. Bove (green) fault system, and locations of 3D models.

2.2.1 Observations of surface rupture following 26 October 2016 event

Field surveys by INGV geologists performed in the epicentral area of the 26 October event revealed surface rupture features at the locations shown in Figure 2.4. Figure 2.7 shows

photographs of several of these features. No formal and systematic measurements of slip occurred, but these features suggest amounts ranging from 5 to 18 cm.

As shown on Figure 2.4, the locations of the observed surface ruptures coincide with a segment of the Mt. Vettore fault as mapped by Falcucci et al. (2016). This segment of the fault did not rupture in the 24 August event. No information about the last known rupture of this fault segment is available. It has likely ruptured during past events on the Mt. Vettore fault as identified by Galadini and Gali (2003) through paleoseismological studies.

2.2.2 Surface rupture from 30 October 2016 event

Overview of activities and findings

Reconnaissance of surface fault rupture following the 30 October event consisted of three principle elements:

- Observations of fault segments with and without surface rupture. Similar to the field work following the 26 October event, these observations are useful to establish locations of rupture. For approximately the northern half of the rupture, these are the only surface rupture data currently available.
- Two phases of detailed mapping of surface rupture locations and direct measurement of displacements using rulers and tape measures (by GEER).
- Imaging of the deformed ground surface at and near the fault through the use of unmanned aerial vehicles (UAV) and terrestrial Lidar (by GEER).

Figure 2.4 shows the broad area in which both observations of rupture locations, and detailed mapping/imaging, were undertaken. A comparison of deformations obtained from these two methods is discussed further below.

An important point to make here is that surface rupture observations at any point in time represent the cumulative slip from all prior events. Hence, the only way to evaluate slip from any particular event is through the differencing of multi-epoch displacement measurements. Detailed, by hand, mapping was conducted following the 24 August event (GEER 2016) for the southern portion of the Mt Vettore fault, shown in Figure 2.4. Because such areas did not experience slip in the 26 October event, but were observed to have additional displacements in our December 2016 reconnaissance, such differentials can be attributed to the 30 October event. As an example, Figure 2.5 shows a location near the south end of the fault rupture close to road SP477 where multi-epoch photographs and measurements are available, showing the much larger slip in these areas from the second (30 October) event. Figure 2.6 compares cumulative displacements (total displacement measured in December reconnaissance) with the September-to-December differential, which is attributed to the 30 October event. These results were measured along the southern portion of the Mt. Vettore fault rupture.

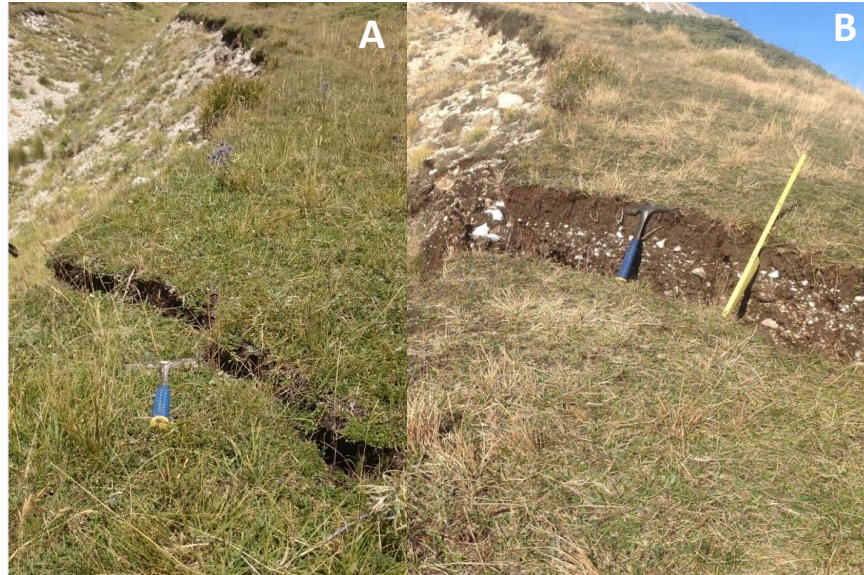


Figure 2.5. Comparative fault offset of 10cm. (a) Vertical offset from the August event, and (b) 30cm Vertical offset from the October 2016 events on the south face of Mt. Vettore near road SP477. Horizontal offsets were 0cm and 2cm. Lat = 42.79795, Long = 13.26607.

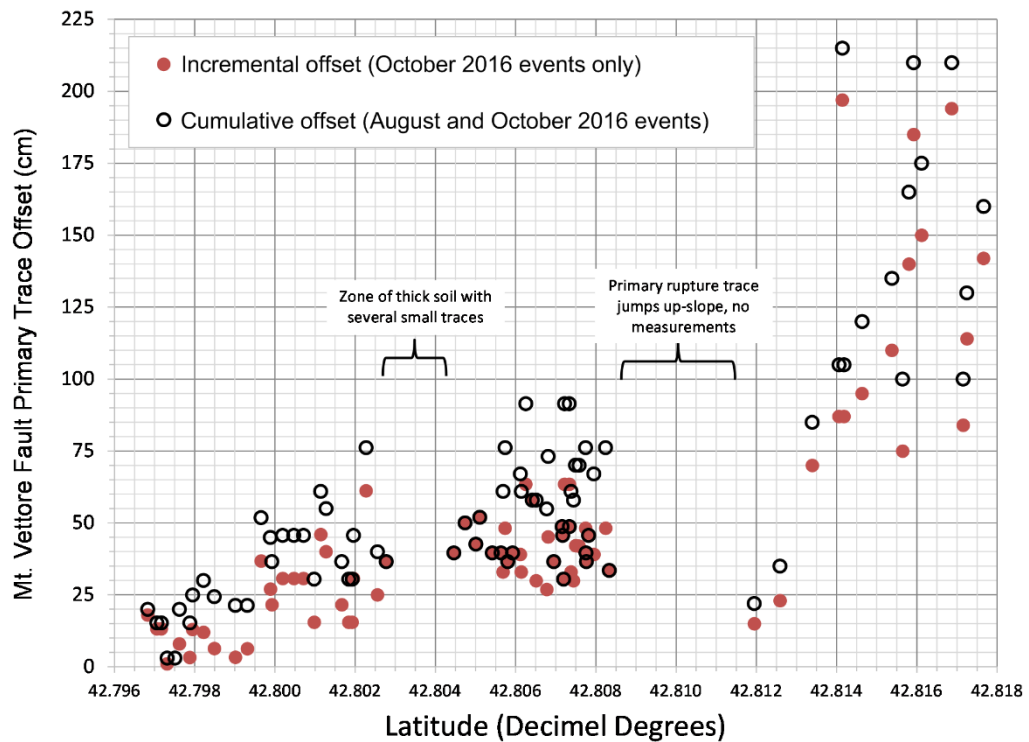


Figure 2.6. Distribution of incremental and cumulative fault offsets for the southern half of the Mt. Vettore fault. All data in this Figure from hand measurements.

In the southern portion of Mt Vettore fault, slip occurred on three segments. The primary segment is on the ridge of Monte Vettore at the contact between bedrock and thin overburden talus and alpine deposits. An apparently secondary segment occurs lower on the ridge, which ruptured in the 30 October event but not in the earlier events. Another secondary segment is in the lower-lying basin, Piano Grande, in lacustrine and alluvial deposits that have infilled the basin. Rupture on this segment was only observed following the 30 October event.

Fault imaging

Figure 2.4 shows areas along the fault where detailed imaging was performed using UAVs and LiDAR; further details on this work is described in the next section. A method was developed to merge point cloud data from UAV imagery and the 3-D terrestrial laser scanner to record the offsets along the Mt Vettore fault. At some sites, Lidar data was collected using the terrestrial laser scanning method. The scanner was placed on a tripod, and its GPS location was recorded. A point cloud of coordinates visible to the scanner is collected and registered with the other scans in the same area where overlapping data exists.

Point cloud data from the UAV are processed through a computationally intensive multi-stage process. First, a flight plan is established to overfly the fault and collect downward looking photographs using a Phantom 4 UAV quad-copter. These images were collected with a minimum of 80% overlap and 80% side-lap coverage to ensure that there are common features in adjacent images. Using cloud computing software from 'Dronedeploy,' and workstation-based software from 'Agisoft,' all of the downward-looking images were aligned using hard features that were common to multiple photographs. Images were first aligned crudely, and then a sequence of higher level alignments improved the model and established a tight relationship between adjacent images. The structure-from-motion method computes angular separations between objects visible in overlapping images. The scale and location of the objects are determined by knowing the location of each photograph from the photo metadata GPS-location. That is, the GPS-tagged photographs from the drone provided the scale for the model.

Aligned drone imagery was used to process a dense point cloud and a 3-D mesh triangular irregular network surface. The same aligned imagery was used to construct a precise orthomosaic of the scanned area. Once the UAV model was constructed, the point cloud from the UAV data can be merged with the point cloud from the Lidar scanner. UAV and LiDAR datasets are merged using the software ISITE-Studio (Maptek company). The advantage of merging data is that the Lidar data-set is presumably more precise regarding pixel location, whereas the UAV data have a more accurate color representation for each pixel because of the direct relationship between the point cloud and the orthomosaic image.

Comparison of displacements from 3D models and hand measurements

In Figure 2.7 we compare displacements along the primary (highest elevation) segment of the Mt. Vettore fault as measured by hand and from the 3D terrain model. These displacements were made along the portions of Mt. Vettore that are on the west face of the ridge and on the branch descending the ridge towards SP477. Figure 2.7 shows cumulative displacements across

all events, which for this portion of the fault arise from the 24 August and 30 October events. The 3D model in these areas is based on UAV point cloud data, and the displacements were measured from the model using the program Dronedeploy. The comparison is considered quite good, with no clear evidence of bias. Further comparisons in other areas will be undertaken in future work.

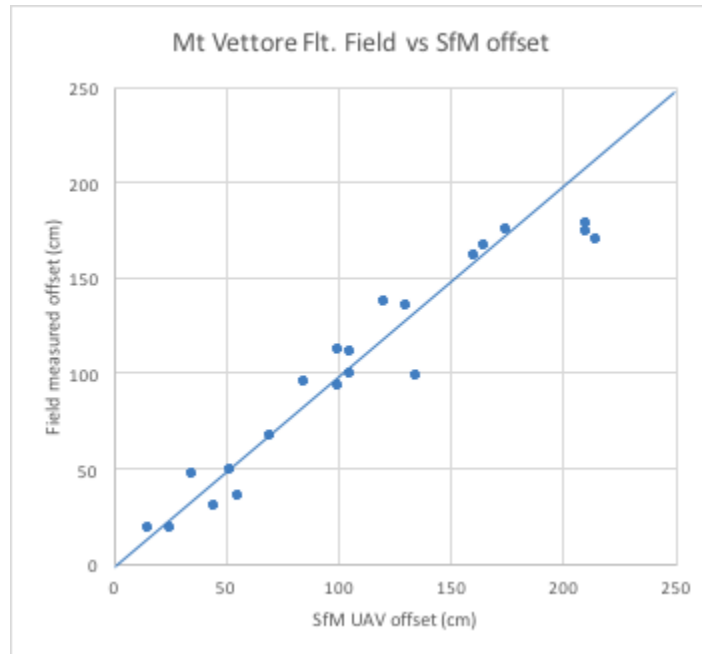


Figure 2.7. Surface fault rupture displacements from August-October event sequence as evaluated from hand measurements in the field and UAV-based 3D model.

2.3.3 Detailed results of GEER fault imaging and conventional fault mapping

An overview of the GEER findings from December 2016 reconnaissance is provided in Section 2.3.2. The work summarized there includes hand measurement by GEER team members from INGV and additional hand measurements and imaging by a Phase 2 team. This section provides further details of the activities of the Phase 2 GEER team.

The Phase 2 GEER team was onsite at Mt. Vettore 1-4 December 2016. 3D models were generated for the south face of Mt. Vettore in the area of surface fault rupture using a combination of both UAV SfM and LiDAR point cloud modeling. Figure 2.8 shows the area of the south face of the Mt. Vettore Massif where these 2 data collection activities occurred. UAV data collection was continuous over the area, while LiDAR data collection was made from a single location on road SP477 at the base of the slope leading up the south slope of Mt. Vettore. The surface fault rupture southern terminus was slightly down-slope and south of the location of the LiDAR data collection and the southern extent of UAV data collection. Figure 2.8 also shows the area of the west face of the Mt. Vettore Massif where UAV point cloud data was collected and a SfM 3D point cloud model was generated. A second LiDAR point cloud model was obtained for the secondary fault rupture surface on the Piano Grande (also shown on Figure 2.8

to the west of Mt. Vettore). In parallel with UAV and LiDAR data collection, the GEER team performed conventional fault mapping activities using GPS and measuring sticks to locate and measure fault dip and strike offsets.

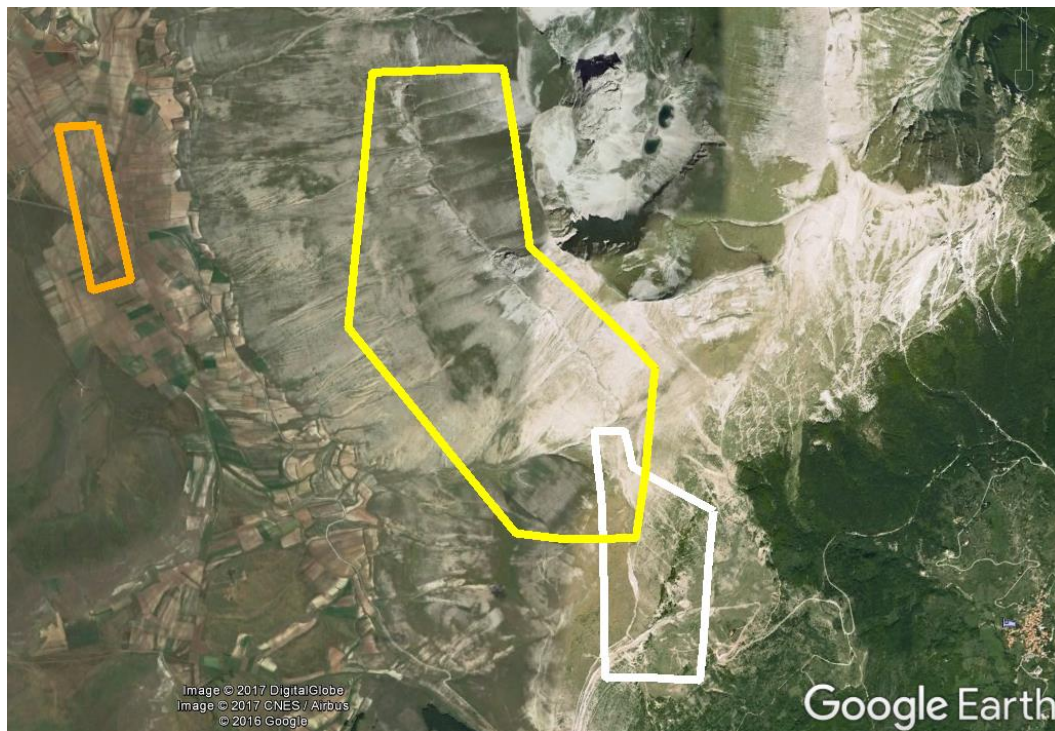


Figure 2.8. Satellite image of the southern half of the Mt. Vettore Massif. The yellow box corresponds to the area shown in Figure 2.10 for the 3D model of the west face of Mt. Vettore, while the white box corresponds to the area shown in Figure 2.9 for the 3D models of the south face. The box to the west (orange) shows the location of the Piano Grande fault 3D model (Figure 2.11).

The 3D point cloud model, generated using both UAV SfM and LiDAR point cloud modeling, for the south face of Mt. Vettore is shown in Figure 2.9. Due to the large area and low color contrast of fault scarps compared to the native ground surface, lines have been added to this image to show approximate surface fault rupture traces. Figure 2.9 shows that the fault rupture alignment climbs the slope from south to north. In general, larger fault offsets were measured to the north. The southern terminus of observed fault rupture is down slope of road SP477 which is at bottom of Figure 2.9. Most of the mapping effort was performed north of SP477, as the fault dip offsets observed south of SP477 were minimal.

An interesting observation from both 3D point cloud and conventional mapping is that there is a zone of apparently thick and soft (ductile) soil sediment overburden on the slope where the distinct single fault rupture surface is defrayed into several smaller scarps. This area is shown in Figure 2.9. Above and below this area, the fault trace is singular and well defined. Within the

area, the fault splinters into 4 to 6 distinct, short, small displacement traces roughly parallel to one another.



Figure 2.9. 3D digital terrain model from merged SfM and LiDAR data of the Mt Vettore fault on the southern flank of the Mt Vettore Massif. Approximate main fault trace indicated in yellow. Looking from the west to the east. The upper left of the image is the top of the slope. Area of soft sediments where the fault trace breaks into several (4 – 6) small scarps is indicated in white.

Similarly to Figure 2.9, the image in Figure 2.10 depicts a 3D model of the west face of the Mt. Vettore Massif that was generated from combined UAV images and LiDAR scans. Figure 2.10 shows an area that is located north of the area depicted in Figure 2.9, and covers the northern extent of the fault mapping. Figure 2.10 shows an approximate fault trace location for the main trace and the aforementioned western trace. We performed field mapping on both the main trace and the western trace, though mapping activities were more extensive on the main trace.

Rupture displacements increase as the fault extends to the north. Also, the rupture becomes more centralized to a single surface as the fault moves north between Figures 2.9 and 2.10. On the south (right) of Figure 2.10, the fault has several distinct rupture scarps that we have interpreted as fault scarps. Several other scarps were measured, mapped, and are shown in the 3D model. These other scarps are interpreted as minor slope instability scarps and are discussed in Chapter 4 (Section 4.2.10).

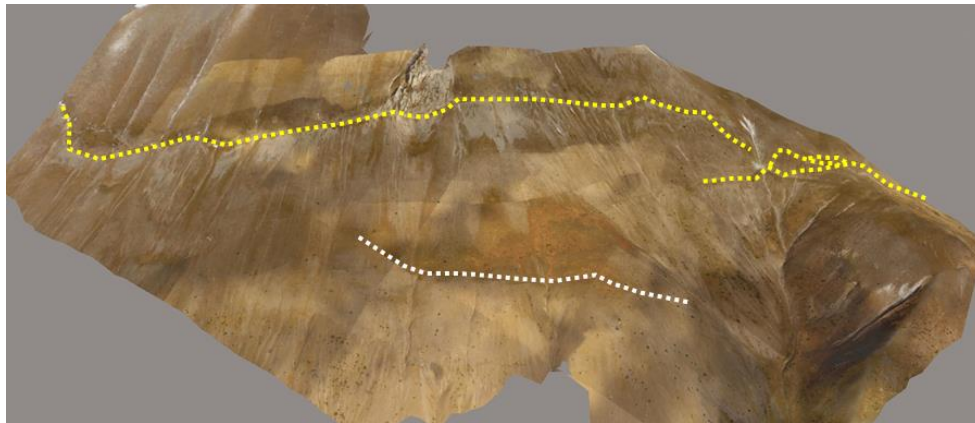


Figure 2.10. 3D digital terrain model from merged SfM and LiDAR data of the Mt Vettore fault on the western flank of the Mt Vettore Massif. Approximate main fault trace(s) indicated in yellow, a second visible trace of the “Western Trace” shown in white (See Figure 2.11 for more details). Looking from the west. The left of the image is to the north. The slope moves from top to bottom of the image.

The final 3D point cloud model is from LiDAR imaging of the Piano Grande fault at the western foot of the Mt. Vettore Massif (location shown by the orange rectangle on left side of Figure 2.8). The Piano Grande fault has been interpreted as a secondary rupture surface. This fault was not observed after the August 2016 event. Figure 2.11 presents an image of this 3D model.



Figure 2.11. 3D digital terrain model from merged SfM and LiDAR data of the Piano Grande fault on the western toe of the Mt Vettore Massif. Approximate fault trace(s) indicated in yellow. Looking from the west. The left of the image is to the north. Mt. Vettore on the top of the image

A comparison of offset measurements from the August 2016 and 30 October 2016 earthquakes from conventional mapping was performed and is illustrated in the following Figures. In these comparisons, we use co-located measurements when possible, and otherwise show initial displacements (measured in September) from adjacent locations for comparison to the offsets measured following the 30 October 2016 event. Figures 2.12 through 2.21 show a selection of fault measurement locations and recorded offsets for this comparison.



Figure 2.12. Fault offset measurements showing relative offset of August 2016 (0 cm) and October 2016 (70 cm) events on the lower or “western” fault trace in Figure 2.10 (shown in white). Lat = 42.812901, Long = 13.24626.



Figure 2.13. Fault slip measurements showing multi-epoch offsets from August 2016 (upper white band, 16 cm) and October 2016 (130 cm) events. Lat = 42.81724, Long = 13.25449.



Figure 2.14. Location of maximum fault offset of 210 cm following October 2016 events. The August event offset at this location is estimated as 20 cm, based on nearby data points. Lat = 42.81687, Long = 13.25503.

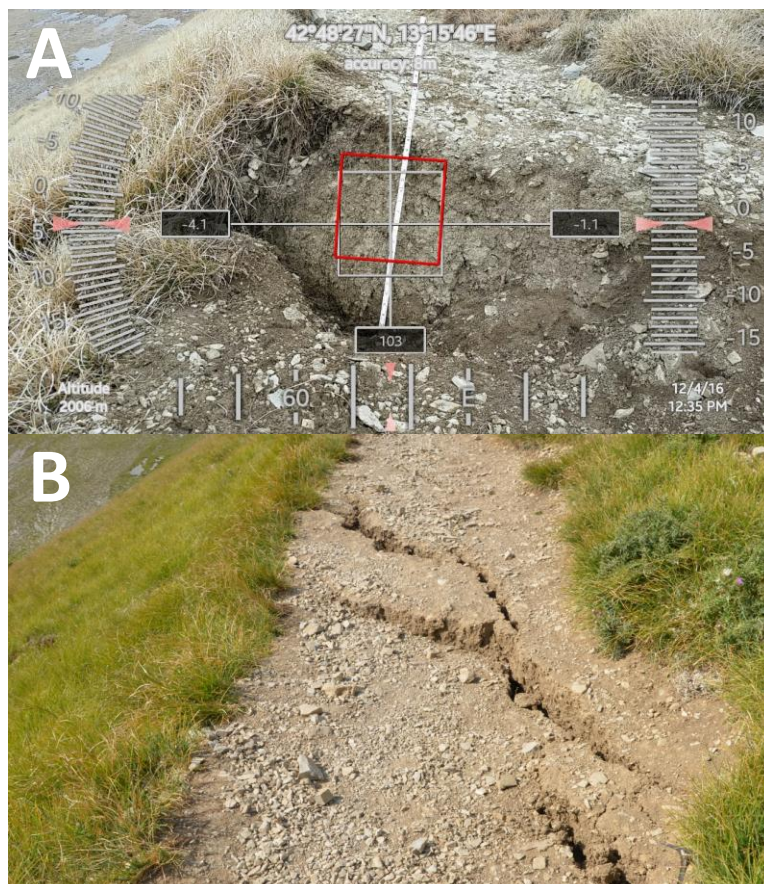


Figure 2.15. Fault offset measurement across the footpath on the west face of Mt. Vettore. Offset measured as 80 cm following October events (a). This offset was 30 cm following August events (b). Lat = 42.807379, Long = 13.262966.



Figure 2.16. Fault trace on the south face of Mt. Vettore, where the fault has ruptured along the path of buried polyethylene pipe supplying the pictured spring. Rupture partially hidden by long grass. Offset measured at 45 to 65cm. August offset data nearby is 0 to 15cm. Trace(s) above the spring indicated in red. Lat = 42.80474, Long = 13.26441.



Figure 2.17. Fault offset measurement of one of several (4 to 6) small traces on the south face of Mt. Vettore in the area indicated in white in Figure 2.9. In this area surface soils are thick and ductile. Offset measured at 8 to 52cm on each trace. August offsets were 0 cm. Lat = 42.80483, Long = 13.26443.

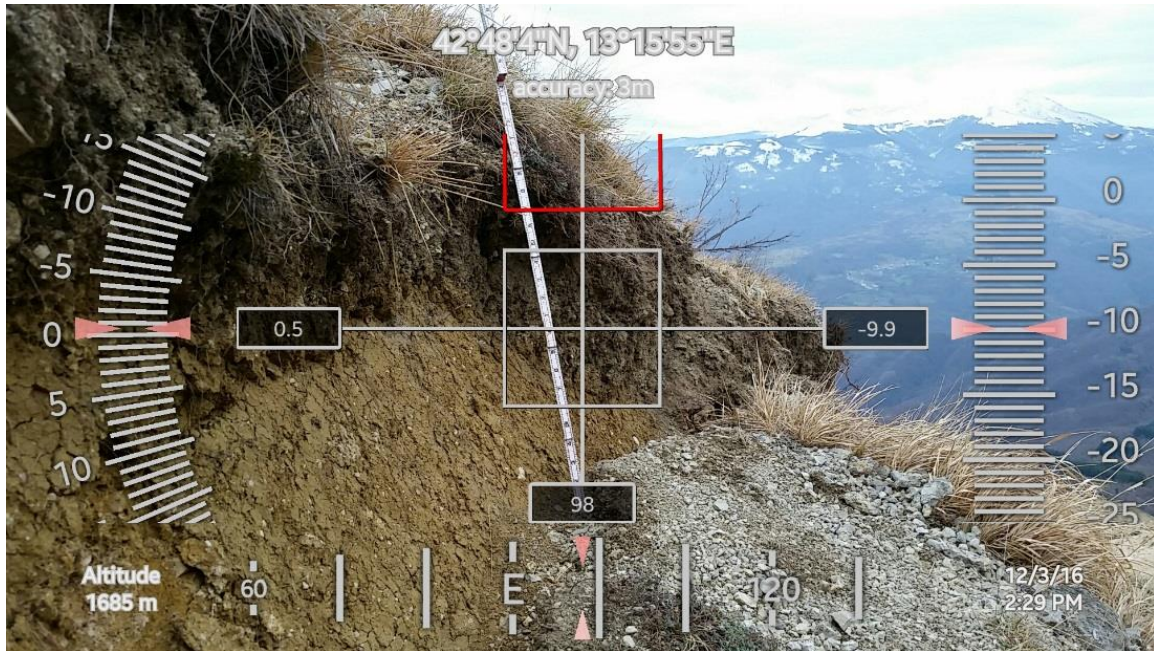


Figure 2.18. Fault offset measurement in gulley on south face of Mt. Vettore. Offset measured at 80cm. August offset data nearby is 15cm, indicating October 2016 offset of 65cm.

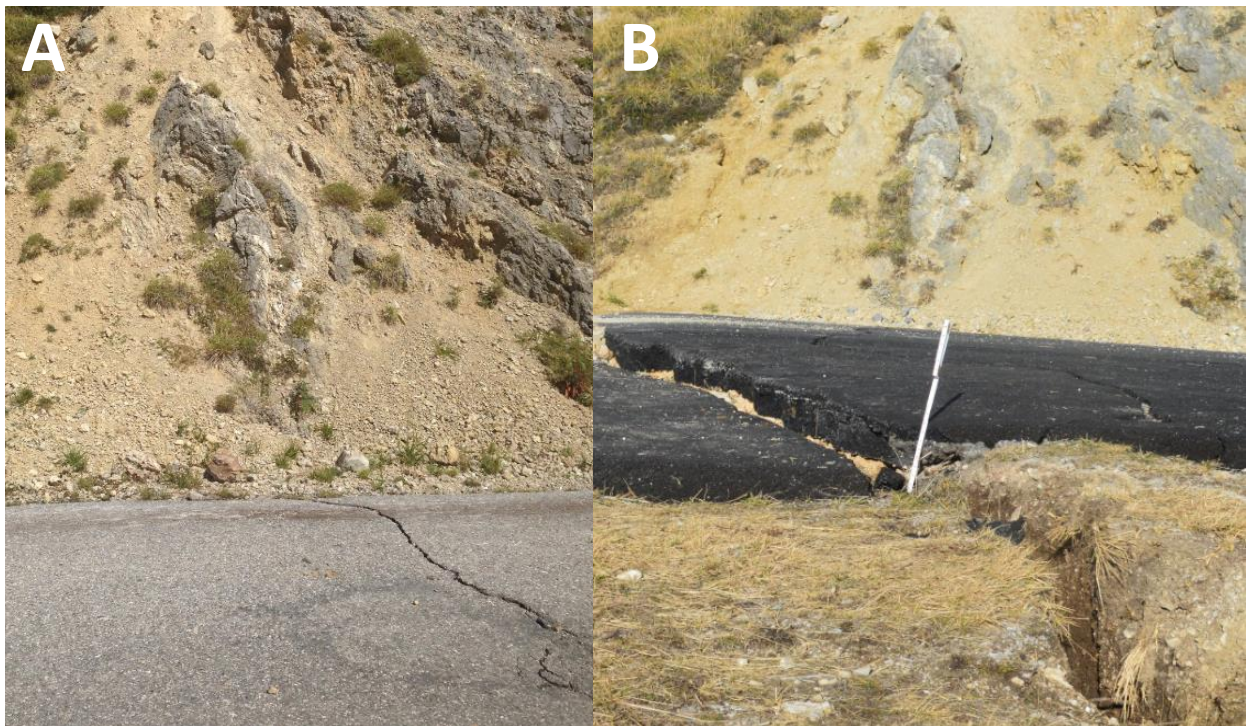


Figure 2.19. Fault offset measurement across SR477 on south face of Mt. Vettore. August offset data nearby is 2cm (a). Offset measured at 18cm to 20cm after October (b). Lat = 42.796829, Long = 13.265899.



Figure 2.20. Secondary fault offset across a road on the Piano Grande at the base of the Mt. Vettore Massif. August 2016 event offset of 0cm. October 2016 event offset of 7 to 18 cm.

The Mt. Vettore fault crosses variable surficial geologies, with differences in fault rupture manifestation for each surface material type. Figure 2.21 presents three different images of the fault rupture. The fault occasionally followed a well-defined limestone fault plane. This was especially true in the “gulley” on the south face of Mt. Vettore and along much of the west face of the Massif for both the main and western splays of the fault. Measurements are relatively straightforward in these areas. In areas where a near-surface limestone fault plane was not present (i.e. thick soil sediment cover), the fault rupture often appears as shown in Figures 2.21a and 2.21b, with lateral gapping developing and the fault trace occasionally splitting into two or more traces. Displacements across these individual traces often sum to be as much as the displacement in adjacent areas with shallow or exposed limestone. For example, between latitudes 42.806 and 42.808, the fault trace splits into several traces, converges, and then diverges again before becoming a single distinct surface north of Latitude 42.808. In the locations of a single trace, the measured offset is 92 cm. In the nearby locations with 2 or 3 traces, the individual traces measure 30 to 40 cm, but the sum is very close to 90 cm.

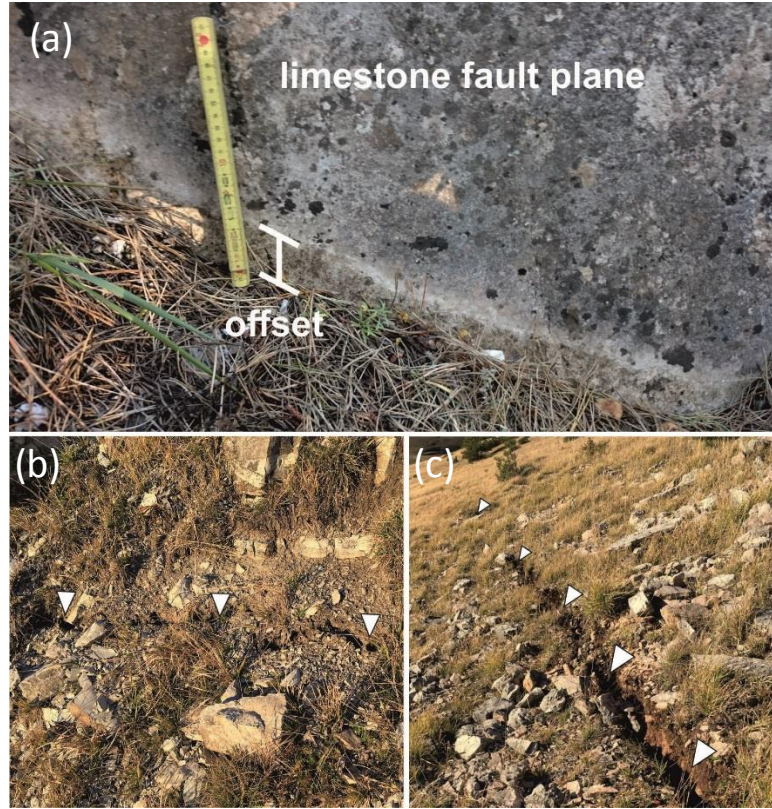


Figure 2.21. Fault offset measurements along the south and west faces of the Mt. Vettore Massif showing differences in fault rupture offset through soil versus along the rock fault plane (where visible on the slope).

3 Ground Motions

Principal authors: Paolo Zimmaro, Giuseppe Scasserra, Tadahiro Kishida, Jonathan P. Stewart

Contributing authors: Massimina Castiglia, Tony Fierro, Luciano Mignelli, Panagiotis Pelekis, Filippo Santucci de Magistris, Giuseppe Tropeano

3.1 Available Recordings

In this section, we analyze recordings obtained from the ESM database (Luzi et al., 2016; <http://esm.mi.ingv.it>, last accessed 16 March, 2017), for six earthquake events that occurred between 24 August and 30 October 2016. This chapter serves as an update to Chapter 3 of GEER (2016), which summarized ground motions from the first three of these events from August 2016. In this chapter, we provide a collective overview of the ground motions from this event sequence; the chapter is not merely an update to the prior one but supersedes it.

The selected database contains recordings from 298 recording stations. Each station recorded at least one of the considered events. The majority of the recordings are from the Italian Accelerometric Network (Rete Accelerometrica Nazionale, RAN; ran.protezionecivile.it/, last accessed 16 March, 2017), owned by the Italian Civil Protection Department (Dipartimento della Protezione Civile, DPC). Data from other networks are also considered – a list of all the considered networks (and their urls) is provided in GEER (2016).

Table 3.1 shows key characteristics of the six events. Based on spatial and temporal attributes, we have classified aftershocks using both: (1) a traditional approach based on time and distance windows, with the latter evaluated as the radial distance from the mainshock epicenter (Gardner and Knopoff, 1974), and (2) an approach developed during the NGA-West2 project (Bozorgnia et al., 2014) that uses the Gardner-Knopoff time window in combination with a new distance metric based on the closest distance to the horizontal projection of the rupture plane (Joyner and Boore distance, R_{JB}) (Wooddell and Abrahamson, 2012). Both approaches provide similar results. In Table 3.1, events classified as CL1 are either mainshocks or foreshocks, while events classified as CL2 are aftershocks. Table 3.1 also shows the number of we consider to be usable. For all events, additional recordings beyond those identified as usable were made, but were either flagged by the data owners as ‘bad-quality’ (these records are generally available, and we have confirmed the quality problems) or as ‘restricted’ in the ESM database (these data have not been made publically available).

Table 3.1. Attributes of the six earthquake events analyzed.

Date	M	Number of recordings ¹	Aftershock flag	Description
24 August 2016	6.1	235	CL1	Mainshock
24 August 2016	5.3	180	CL2	Aftershock
26 August 2016	4.8	132	CL2	Aftershock
26 October 2016	5.4	178	CL1	Foreshock
26 October 2016	5.9	224	CL1	Mainshock
30 October 2016	6.5	212	CL1	Mainshock

¹ Number of recordings available for ground motion characterization purposes

Table S1 (available in the electronic supplement to this report) shows main attributes of the 298 digital accelerometer stations, including location, surface geology, V_{S30} , and instrument housing type. Among them, 15 are temporary stations. In Chapter 3 of GEER (2016), we described temporary station arrays deployed by multiple agencies after the August 24 2016 mainshock, although at that time we did not have any recordings from those arrays. We now have recordings for the 15 sites in Table S1. GEER (2016) lists 87 additional temporary stations for which we do not have data. Moreover, we do not have information at this time on additional deployments and removals of prior deployments since August 2016.

Figures 3.1 and 3.2 show the spatial distribution of all permanent recording stations, along with epicenters of recorded events during August (Figure 3.1) and October 2016 (Figure 3.2). Figure 3.3 shows the spatial distribution of all events occurred in Central Italy between 24 August 2016 and 20 January 2017 with $M \geq 4.2$. Events analyzed in this report (and summarized in Table 3.1) are highlighted in red.

3.2 Site Conditions

We identify surface geology using local, larger-scale maps (from 1:10,000 to 1:25,000 scale) when available, documentation from ad-hoc site-specific microzonation studies, or technical papers (details on this approach are provided in GEER, 2016). Information sources for each site are listed in Table S1. The assignment of a V_{S30} value to each site followed the protocols of Scasserra et al. (2009): (1) Type A utilizes on-site measured velocities from established geophysical techniques; (2) Type B utilizes velocity measurements from nearby sites having the same surface geology as the subject station; (3) Type C estimates V_{S30} using proxy-based relationships for Italy (i.e. Scasserra et al., 2009); and (4) Type D estimates V_{S30} based on the midpoint value of the Italian Code subsoil category indicated in the ESM database (Norme Tecniche per le Costruzioni, 2008; NTC08). Figure 3.4 shows data source type for each of all digital stations that produced recordings considered in this chapter.

During the reconnaissance activities performed after the August 2016 events, T. Pelekis of the GEER team performed spectral analysis of surface waves (SASW) testing for six station locations for which only Type D estimates had previously been available. As a result, the following six sites are now classified as Type A in Table S1: (1) Foligno (FOC), (2) Poggio Cancelli (PCB), (3) Selle Pedicate, Campotosto (SPD), (4) Mascioni, Campotosto (MSC), (5) Norcia (NRCA), and (6) Montereale (MTR). Table 3.2 shows station codes, location, measured V_{S30} and number of recorded events (among those analyzed in this chapter) of these newly characterized recording station sites. Figures S1-S6 (available in the electronic supplement to this report) show measurement details and instrumentation deployment layouts. Figures S7-S24 show dispersion curves and inverted V_S profiles for these sites.

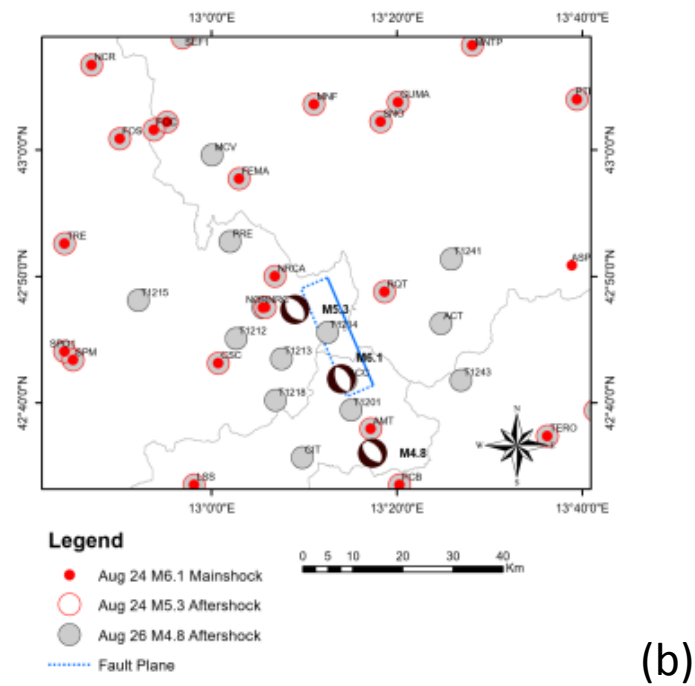
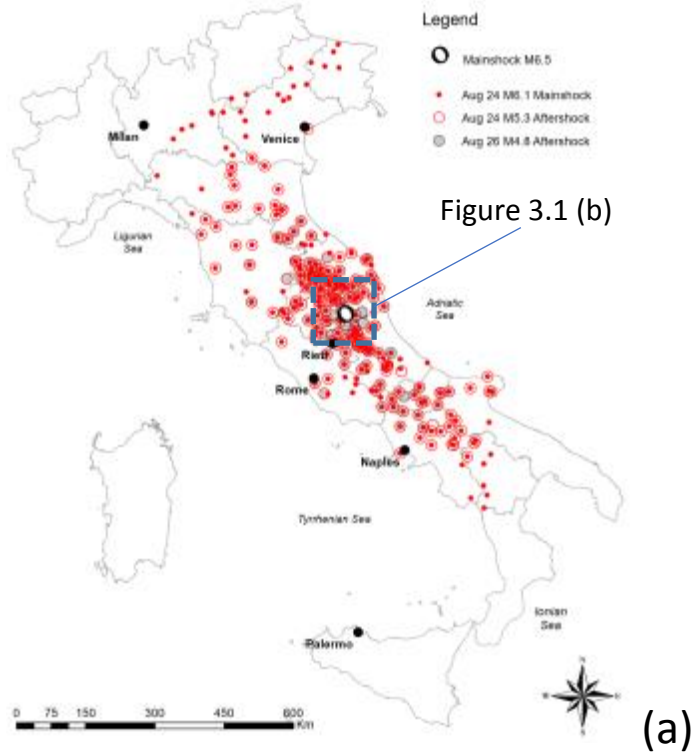


Figure 3.1. (a) Locations of instruments that recorded M6.1, M5.3 and M4.8 August 2016 events; (b) close-up view of the instruments in the epicentral area.

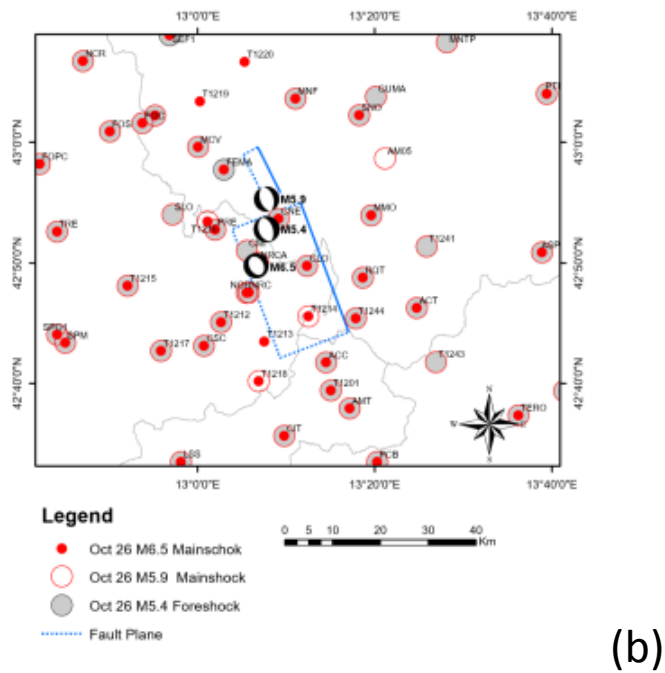
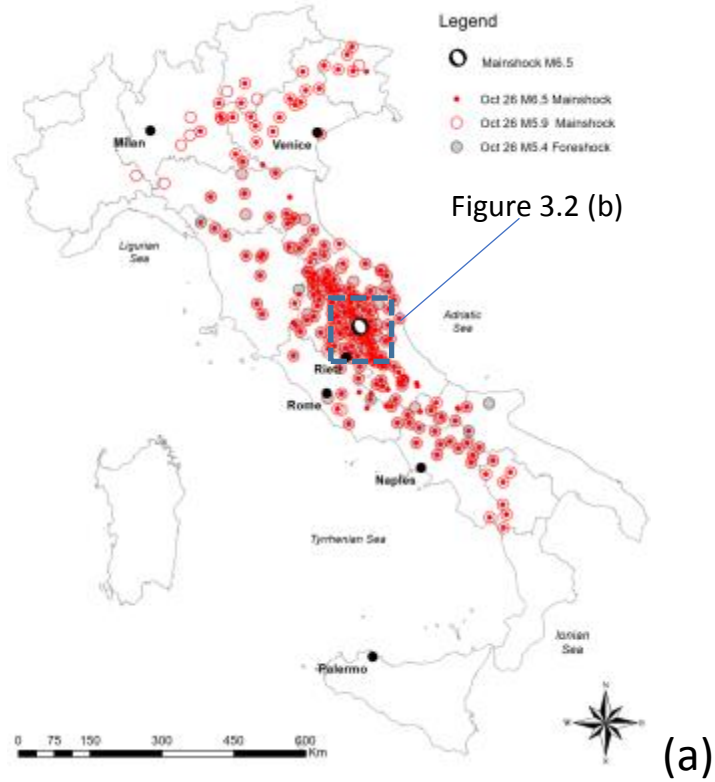


Figure 3.2. (a) Locations of instruments that recorded M6.5, M5.9 and M5.4 October 2016 events; (b) close-up view of the instruments in the epicentral area.

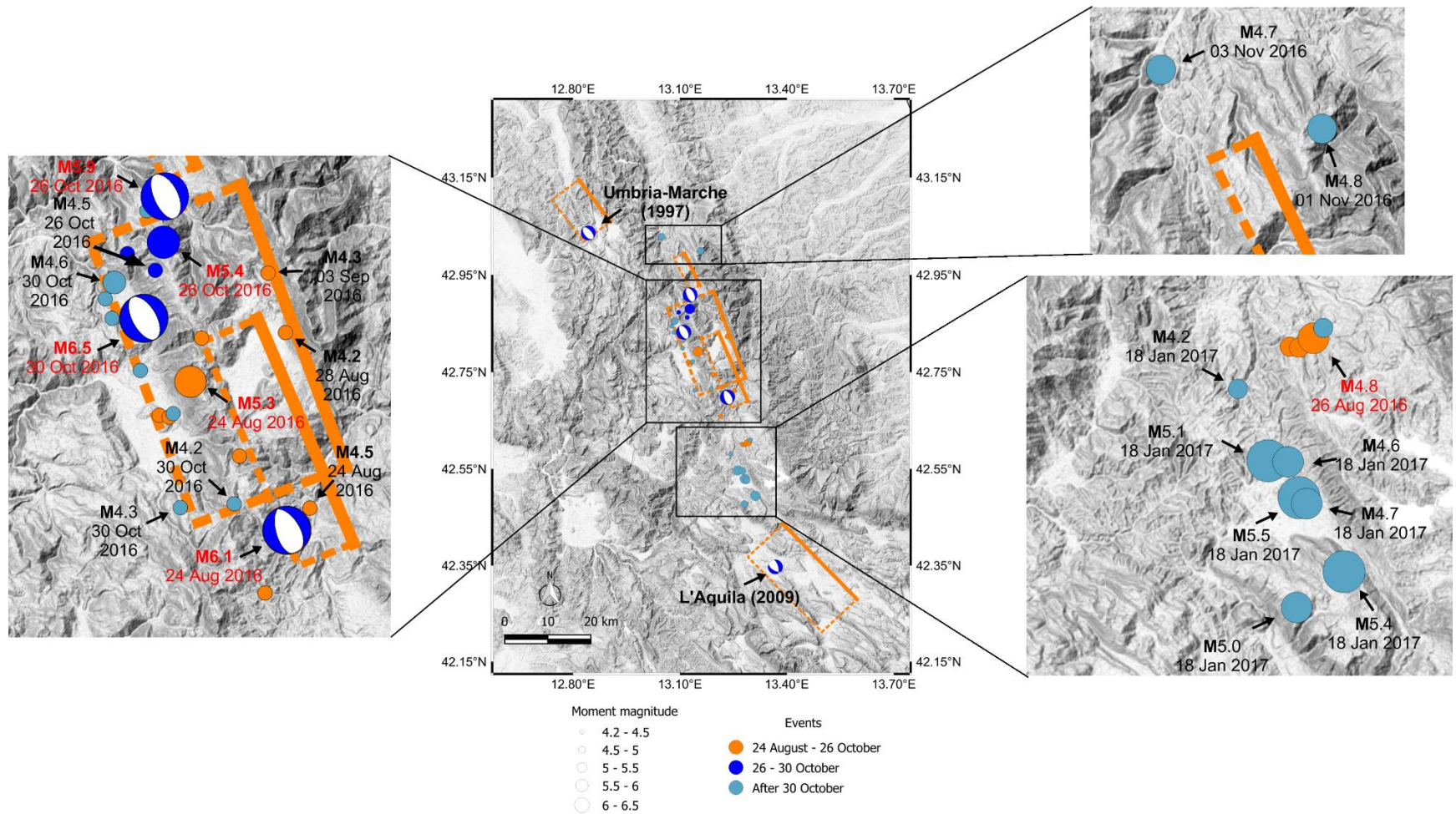


Figure 3.3. Spatial distribution of all events occurred in Central Italy between 24 August 2016 and 20 January 2017 with $M \geq 4.2$.

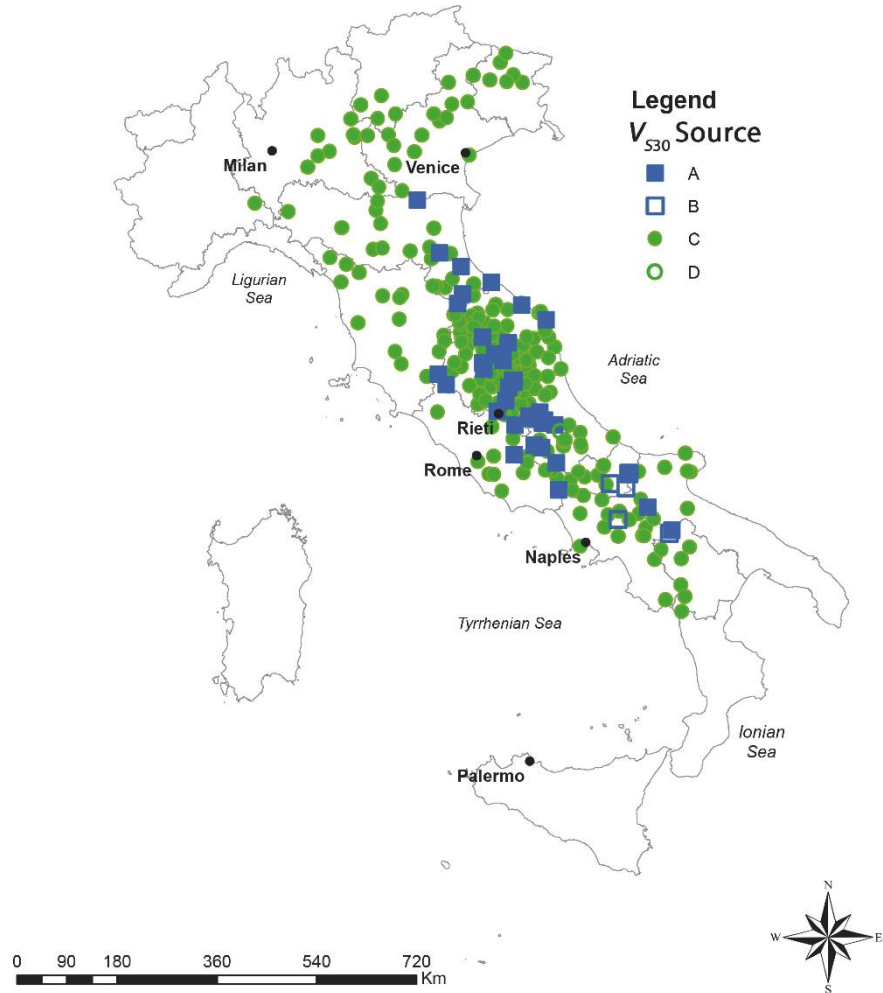


Figure 3.4: Data source types used for V_{530} estimations for all considered recording stations.

Table 3.2. Measured V_{530} and details of the newly characterized recording station sites.

Station code	Lat. (deg)	Lon. (deg)	Measured V_{530}	# of recorded events
FOC	43.02630	12.89651	285	6
PCB	42.55802	13.33799	366	6
SPD	42.51514	13.37104	521	6
MSC	42.52676	13.35084	540	6
NRCA	42.83355	13.11427	491	1
MTR	42.52402	13.24480	1130	5

3.3 Near Source Ground Motions

In the ESM database, both raw unprocessed and processed accelerograms are available. We downloaded raw unprocessed ground motion data, which was then processed using standard Pacific Earthquake Engineering Research (PEER) center procedures (Ancheta et al., 2014). Details on the application of the PEER procedures are available in GEER (2016).

3.3.1 Data Quality Issues

Several potentially important recording stations in the near-field did not record properly one or more earthquake events during the period 24 August to 30 October 2016. The NRCA station, located in the town of Norcia, did not record any mainshock. The NRCA station only recorded the **M4.8** 26 August aftershock. This results from a sudden power outage during the earthquakes and lack of auxiliary power. The RQT station, in Arquata del Tronto, recorded all six events. One of the components (NS) appears to be unusable (signal is essentially zero) in five of the six recordings. The only usable record produced by the RQT station (in the analyzed period) is from the **M5.4** 26 October 2016 foreshock. RQT is of special interest because it is among the few instruments located on the footwall (for all events) in the near-field area.

Data from six recording stations (AQA, FCC, PRE, RQT, NOR, and AMT) published on the ESM database after the 24 August 2016 mainshock, became unavailable from the database and flagged as ‘restricted’ on 11 November 2016. The recordings from these stations have been reviewed, corrected, and re-published on 23 December 2016. These updates are particularly relevant because the recording of the **M6.1** 24 August event from the AMT station changed significantly.

Figure 3.5 shows 5% damped pseudo-acceleration response spectra (PSA) for the **M6.1** 24 August 2016 event, from three stations in the near field (AMT, NRC and NOR). The corrected ground motions have been rotated into fault normal (FN) and fault parallel (FP) orientations. The AMT ground motion has higher amplitudes in the FN direction at short oscillator periods (< 1.0 sec), whereas the two components are practically equivalent beyond about 0.6 sec. The NRC and NOR motions have higher amplitudes in the FN direction at long periods (> 1.0 sec). Figure 3.5 also compares for AMT median-component (RotD50) spectra for the original (available from the database before 11 November 2016, labelled as ‘previous version’) and the reviewed recordings (published on 23 December 2016). There is no discernable difference between previous and reviewed recordings for NRC and NOR. There is approximately a factor of 2.0 difference for the AMT station.

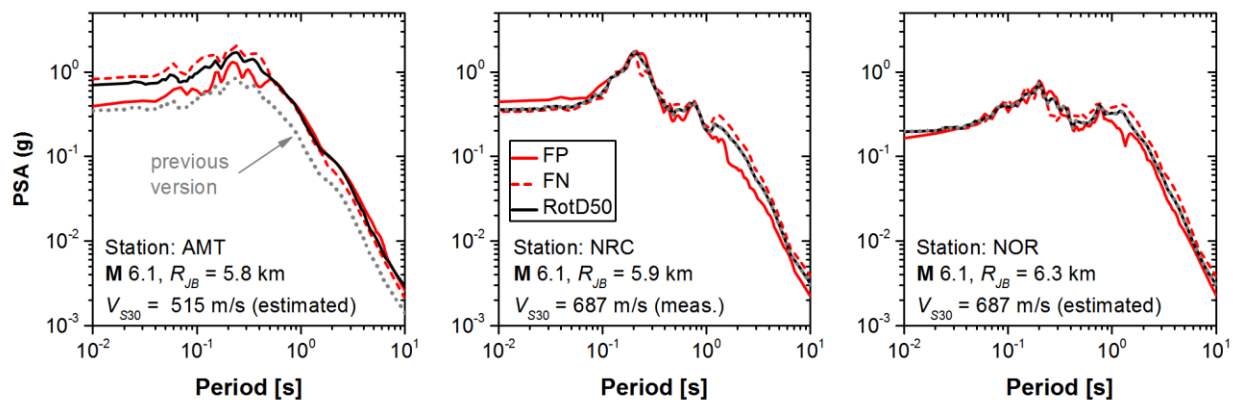


Figure 3.5. Pseudo acceleration response spectra (5% damping) for Amatrice (AMT) and Norcia (NRC, NOR) sites from the **M6.1** 24 August event.

Figure 3.6 shows 5% damped pseudo-acceleration response spectra (PSA) from nine stations at various locations in the near field zone for the **M**6.5 30 October event. The locations of these stations are shown in Figure 3.2b. Three of these stations are on the hanging wall of the fault (T1214, CLO, CNE) and one other is located on the footwall near the surface expression (T1244). These four stations would be the most likely to show an effect of rupture directivity, but no such effect is apparent from the comparison of FN and FP spectra (FN would be expected to be higher). The other spectra shown in Figure 3.6 are in locations of interest due to their proximity to villages and other features discussed in this report.

Another way to examine possible near-fault effects is the presence of pulse-like features in the ground motions velocity time series. These characteristics were checked for stations T1214, CNE, and CLO using the Baker (2007) pulse identification procedure, with the results shown in Figure 3.7. Our interpretation, based on visual inspection of the extracted pulses, is that the pulse effects are weak, which is consistent with the lack of polarization in the FN direction for these records.

We also investigate the presence of fling-step effects (i.e. earthquake-related static ground displacements, resulting from fault rupture). These effects can be present in near-source recordings, especially on the hanging wall of dip-slip faults. Figure 3.8a-c show vertical displacement time series for the three hanging walls records from the **M**6.5 30 October 2016 earthquake. These records have been reprocessed using a procedure developed to preserve static (permanent or tectonic) displacements (Gregor et al., 2002). The amount of vertical-component fling-step in these records ranges from 15-83 cm.

For one of the three recordings on the hanging wall of the trimmed fault model (T1214), co-seismic displacements from GPS measurements are available for the **M**6.5 30 October 2016 earthquake at a nearly co-located station (ARQT). The displacements from these two sensors were independently processed by P Zimmaro (GPS data) and G Tropeano (T1214 accelerogram), and were found to be -45 cm (GPS) and -46 cm (double-integrated accelerogram). The ACC, AMT, and T1216 recording stations (not on hanging wall) also have nearly co-located GPS stations (ACCU, AMAT, and MUVI, respectively). Figure 3.8d-f show the lack of fling step for these stations, which was also confirmed by the GPS data. The observed co-seismic displacements for the stations on the hanging wall are similar to those observed during the 2009 L'Aquila earthquake (i.e. Stewart et al., 2012).

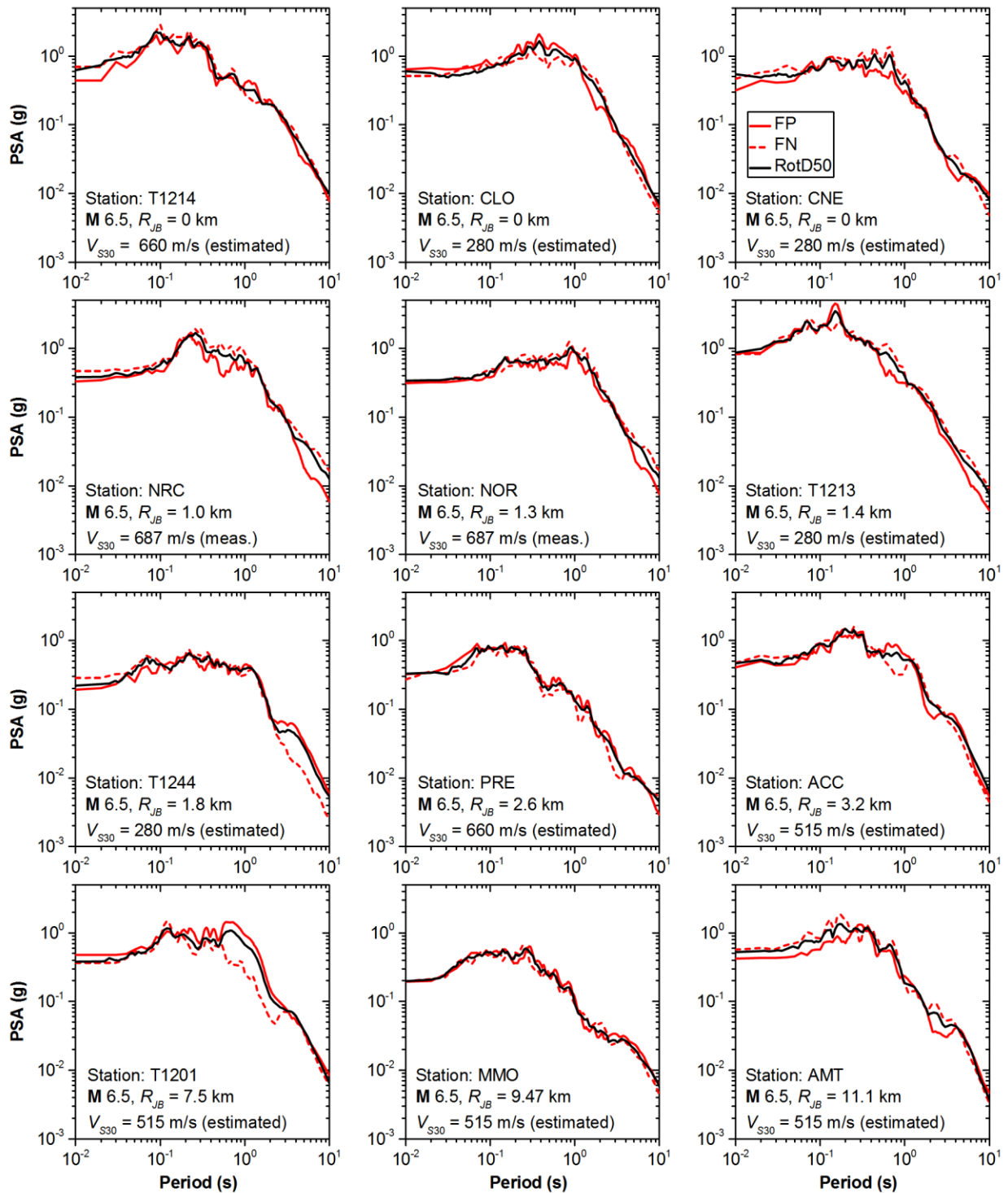


Figure 3.6. Pseudo acceleration response spectra (5% damping) for nine near source recording sites from the M6.5 30 October 2016 event.

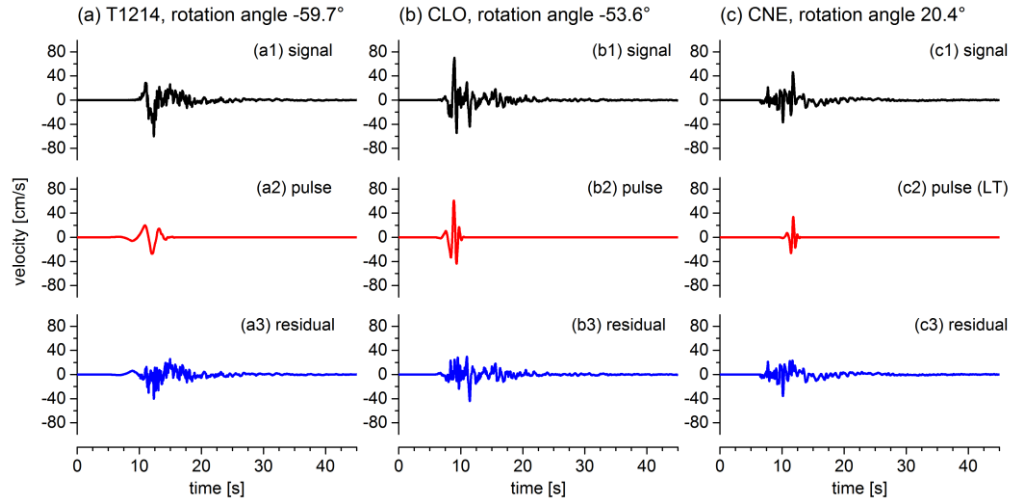


Figure 3.7. Original ground motion, extracted pulse, and residual ground motion for the M6.5 30 October 2016 event recorded at the (a) T1214, (b) CLO, and (c) CNE stations.

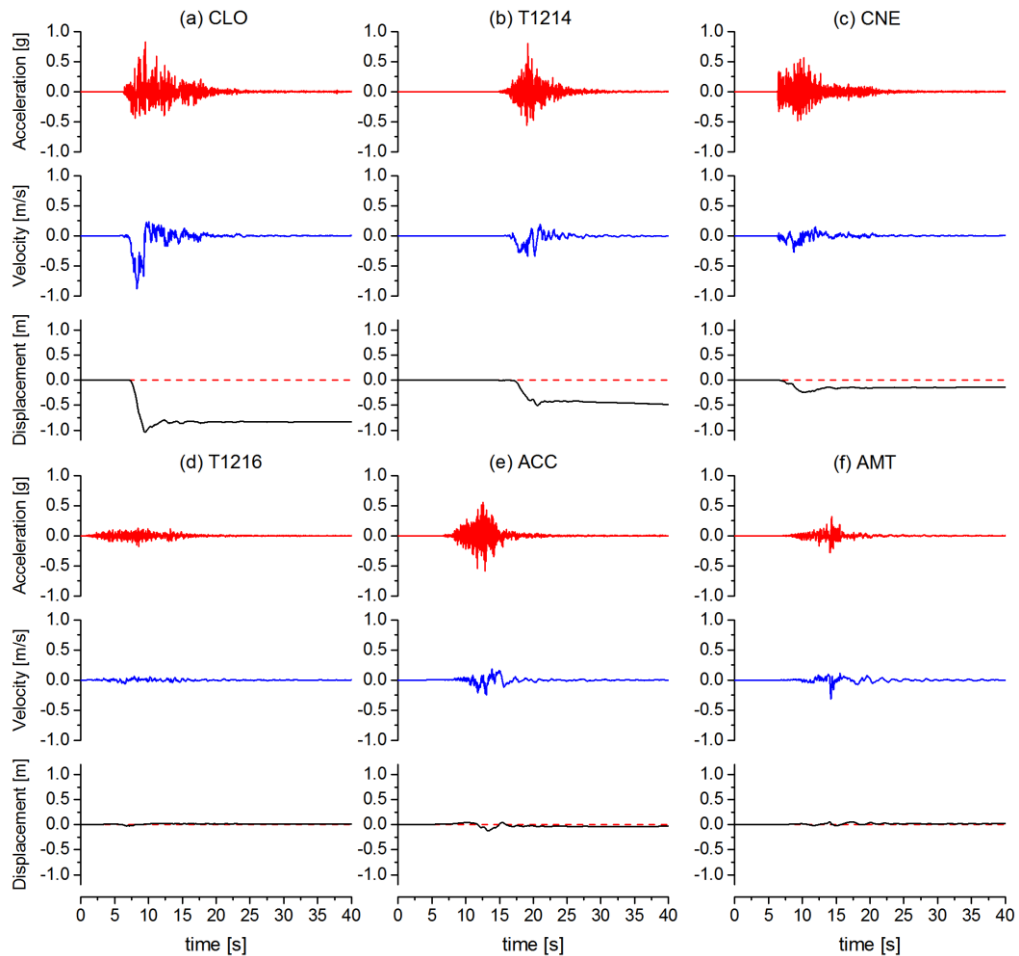


Figure 3.8. Vertical component of acceleration, velocity, and displacement time-series for the M6.5 30 October 2016 event, processed using the Gregor et al. (2002) procedure for the (a) CLO, (b) T1214, (c) CNE, (d) T1216, (e) ACC, and (f) AMT station.

3.4 Comparison to Ground Motion Models

Ground motion models (GMMs) are typically used within seismic hazard assessment frameworks for predicting expected levels of shaking given magnitude, source-to-site distance, site condition, and/or other additional factors. In this section, we compare GMM predictions to observed data. The objective of these comparisons is not to identify a preferred model. Rather, the aim is to facilitate visualization and identification of the main features of the recorded data (e.g. attenuation with distance, near-source ground motions).

In recent years, several studies focused on the selection of suitable GMMs to use in global (Stewart et al., 2015), regional (Delavaud et al., 2012), or site specific applications in Italy (Zimmaro and Stewart, 2017). These selections are often performed comparing GMM predictions over a parameter space of engineering interest. While local models can reflect local geologic and tectonic conditions, which may differ from those represented by global models, the limited database size used to develop local models may be inadequate to constrain GMMs for conditions often critical for application (large magnitudes and small distances). Global models are more effective for such conditions, because they are typically based on much larger databases, but may contain bias with respect to local effects. Regional adjustment factors are typically used to reduce the bias of global models, as in the NGA West-2 project (Bozorgnia et al., 2014). Those factors relate to anelastic attenuation and/or site effects, applicable to various tectonic regions (i.e. California, Turkey, Taiwan, Japan and Italy).

We compare recorded data with the following GMMs for shallow crustal regions: (1) an Italy-specific model by Bindi et al. (2011; hereafter B11), (2) the average of four NGA West-2 GMMs, without regional adjustments (Abrahamson et al., 2014; Boore et al., 2014; Campbell and Bozorgnia, 2014; and Chiou and Youngs, 2014; hereafter NGA2), and (3) the average of three NGA West-2 models containing regional adjustments applicable to Italy (Boore et al., 2014; Campbell and Bozorgnia, 2014; and Chiou and Youngs, 2014; hereafter NGA2-I).

The selected GMMs, use different distance metrics. The B11 and Boore et al. (2014) models use closest distance to the horizontal projection of the rupture plane, or Joyner and Boore distance (R_{JB}). The Abrahamson et al. (2014), Campbell and Bozorgnia (2014), and Chiou and Youngs (2014) models use the closest distance to the rupture plane (R_{RUP}) as the primary distance metric (Figure 3.9). All distances are calculated using the trimmed finite-fault models for the three mainshocks (**M6.1** 24 August 2016 event – GEER, 2016; **M5.9** 26 October and **M6.5** 30 October 2016 earthquakes - Section 2.1.3. For the other events analyzed in this study (**M5.3** 24 August, **M4.8** 26 August, and **M5.4** 26 October 2016 events), we calculate distances considering these earthquakes to be point sources.

Figures 3.10 and 3.11 shows the distance-dependence of RotD50 peak horizontal acceleration (PHA), and peak horizontal velocity (PHV) for all six events. Recorded data are divided into three categories: (1) rock ($V_{S30} > 800$ m/s), (2) stiff soil ($360 < V_{S30} < 800$ m/s), and (3) soft soil ($V_{S30} < 360$ m/s). Also shown in Figures 3.10 and 3.11 are median predictions from the

B11 model, the average of the four NGA2 models, and the average of the NGA2-I models. The model predictions have been calculated using a constant $V_{S30}=580$ m/s. This V_{S30} value falls into subsoil class B of the Italian building code (NTC08) and is considered to be a typical value for the region (GEER, 2016).

Figures 3.10 and 3.11 show that all models fit the data reasonably well in the range $R_{JB} = 0-100$ km. Beyond this distance, there is a relatively fast attenuation of ground motions in all six events. This feature, captured only by the NGA2-I models (with regional adjustment for Italy) is characteristic of Italian data. It has been observed in previous studies (e.g., Scasserra et al., 2009 using Italian data up to 2005; and Stewart et al. 2012 using data from the 2009 L’Aquila event sequence). These fast attenuation features are observed in the aftershock data as well, although none of the considered models appear to be unbiased for aftershock data beyond about 80-100 km. At short distances (i.e. 1-10 km), data are sparse, but there are differences between models. In particular, B11 has a wider flat-attenuation region at close distance, likely due to a larger ‘fictitious depth term’ in the function.

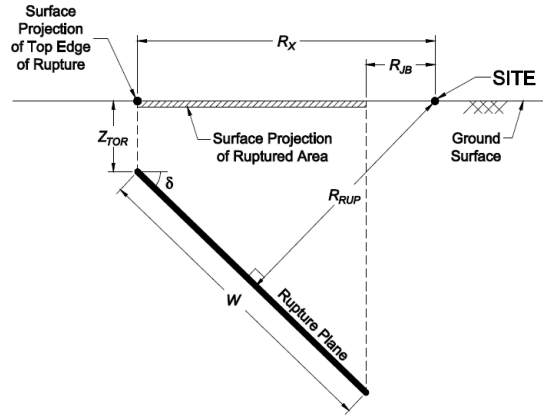


Figure 3.9. Scheme of an earthquake source and distance measures using a vertical cross-section through a fault rupture plane (from Kakkamanos et al., 2011).

The performance of multiple GMMs relative to the data is also analyzed using residuals analysis. We calculate total residuals for each data point considering the appropriate source-to-site distance and site condition as follows:

$$R_i = \ln(IM_i)_{rec} - \overline{\ln(IM_i)_{GMM}} \quad (3.1)$$

where $(IM_i)_{rec}$ is the value of ground motion intensity measure from recording i and $(IM_i)_{GMM}$ is the value of that same IM from ground motion models. For the NGA West-2 models, $\overline{\ln(IM_i)_{GMM}}$ indicates the average of the natural log means from all four GMMs (NGA2) or the average of the natural log means from the three with regional adjustment (NGA2-I). For B11, the median prediction is used. Total residuals are then partitioned into random effect (or event term, η) and the remaining residual (ϵ) using procedures given in Stafford (2012).

We show within-event residuals for peak horizontal acceleration in Figure 3.12 and for peak horizontal velocity in Figure 3.13 for all six events. All data are compared in each plot with

binned means of the within-event residuals, along with their standard deviations, using five intervals for each log-cycle (due to paucity of data, a unique bin is assumed for R_{JB} between 0-10 km).

The results for PHA in Figure 3.12 suggest good consistency between the models and mainshock data for distances up to 100 km. The non-zero residuals of B11 for large distances may result from sparse data (especially from old events) for distances greater than 100 km in their data set. The B11 model includes an anelastic attenuation term, but the effect is smaller than suggested by the data from this event sequence.

The event terms are shown in Figure 3.14 as a function oscillator period for the six considered earthquakes. Also shown are plus/minus one between-event standard deviations from the Boore et al. (2014) GMM. For short periods (PGA to 0.5s), the Central Italy event terms for the NGA2-I range from zero to -1, whereas they are nearly zero for greater periods. This trend is consistent with what was observed for the 2009 L’Aquila event ground motions using NGA-West1 GMMs with an Italy adjustment (Stewart et al., 2012).

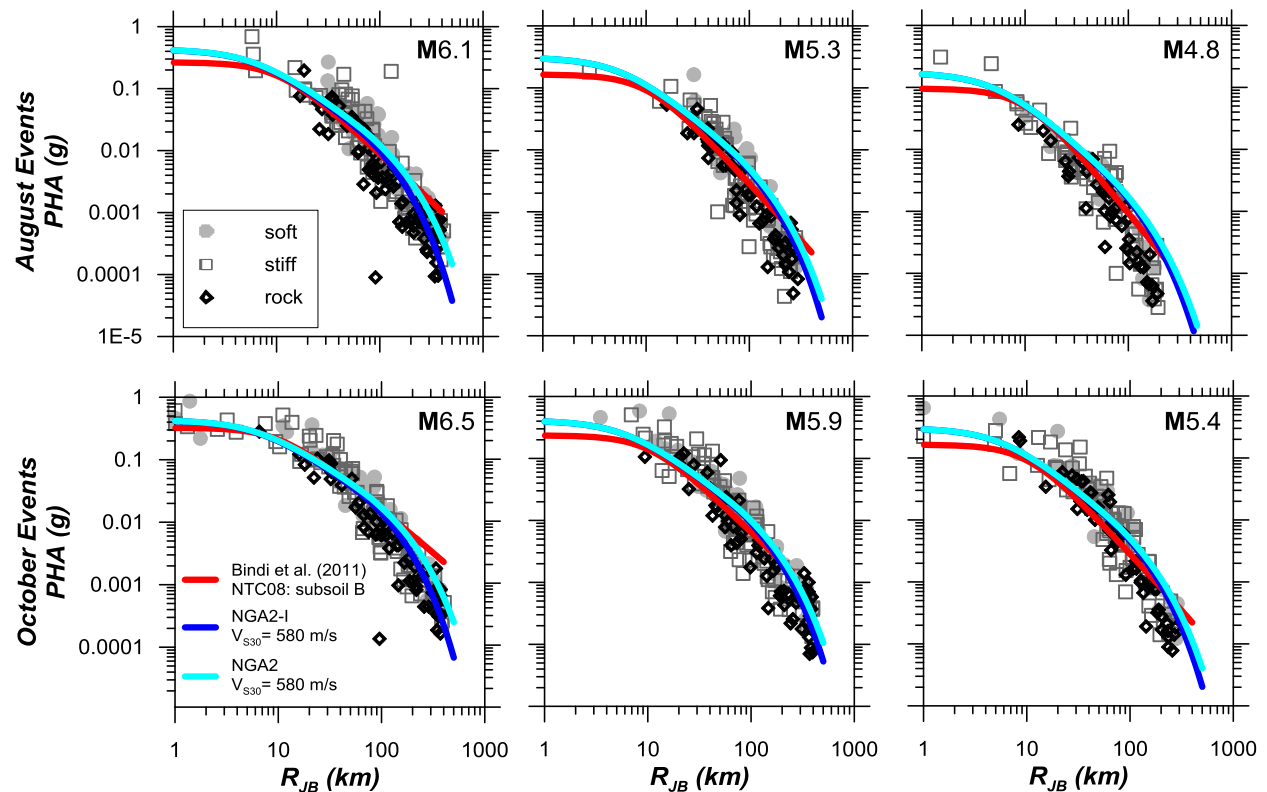


Figure 3.10. Variation of PHA and PHV with R_{JB} for rock (NTC08: A), stiff (NTC08: B), soft soil (NTC08: C, D, E).

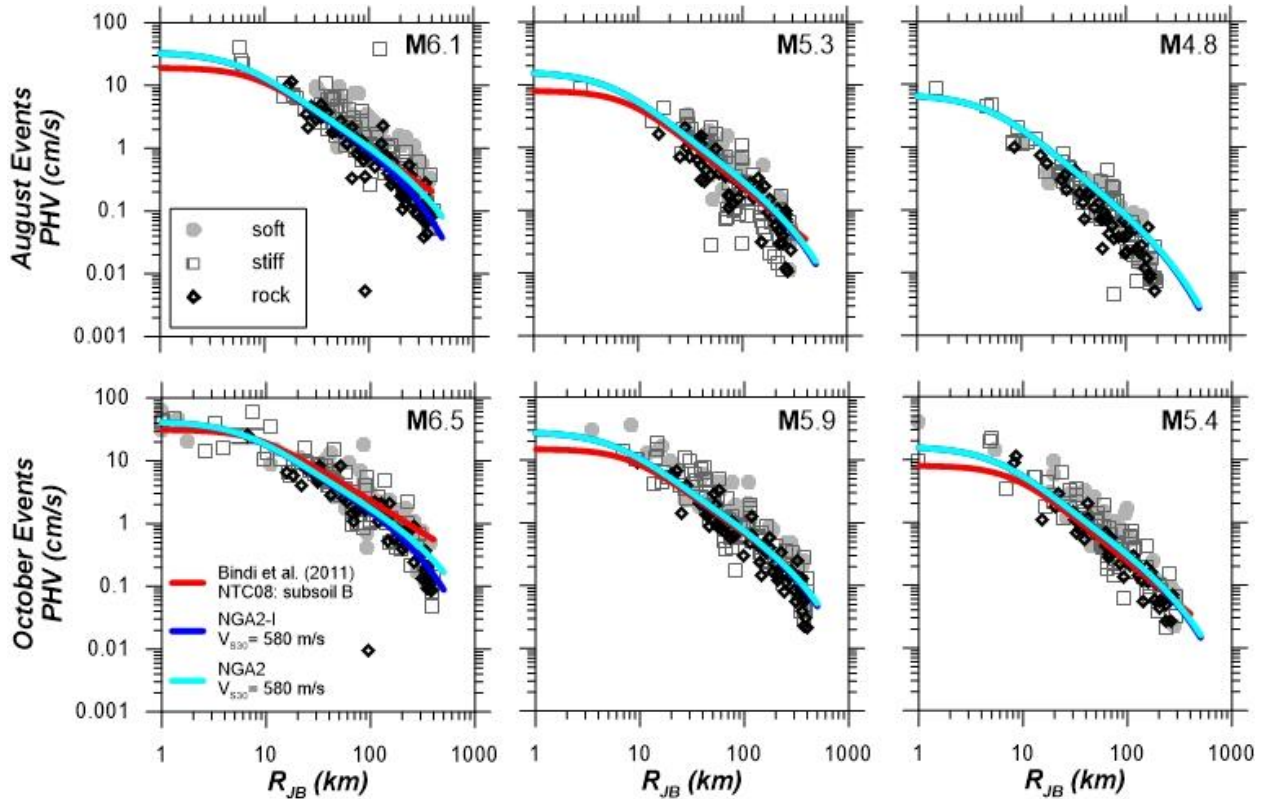


Figure 3.11. Variation of PHA and PHV with R_{JB} for rock (NTC08: A), stiff (NTC08: B), soft soil (NTC08: C, D, E).

3.5 Spatial Interpolation for Estimating Ground Motions

Chapters 4-7 of this report describe observations of ground deformation and/or structural damage induced by strong ground motion. As such, it is of interest to estimate ground shaking at these sites, which generally do not have recording instruments.

We adopt the approach of Kwak et al. (2012, 2016) for ground motion interpolation. In this approach, within-event residuals (ε), calculated as the difference between total residuals and event terms ($R-\eta$), are plotted in space for a given event (each value of ε is plotted at the location of the accelerometer that produced it). We then use apply Kriging techniques with a semi-variogram model from Jayaram and Baker (2009). Figures 3.15-3.17 show the spatial pattern of ε computed in this manner (using residuals from the NGA2-I models).

Armed with the maps from Figures 3.15-3.17, ground motion intensity measures for any given location can then be computed as:

$$\ln(IM)_k = \overline{\ln(IM_k)_{GMM}} + \eta + \varepsilon_k \quad (3.2)$$

where $\ln(IM)_k$ is the desired ground motion intensity measure for arbitrary location k , $\overline{\ln(IM_k)_{GMM}}$ is the average of natural log means from NGA2-I models as applied for site k (note

that this requires the use of a site-specific site-source distance and a site parameter, typically V_{S30} , η is the event term for the event of interest (Figure 3.14), and ε_k is the location-specific within-event residual (Figures 3.15-3.17). Results of these calculations for sites of interest are given in tables near the beginning of Chapters 4 and 6.

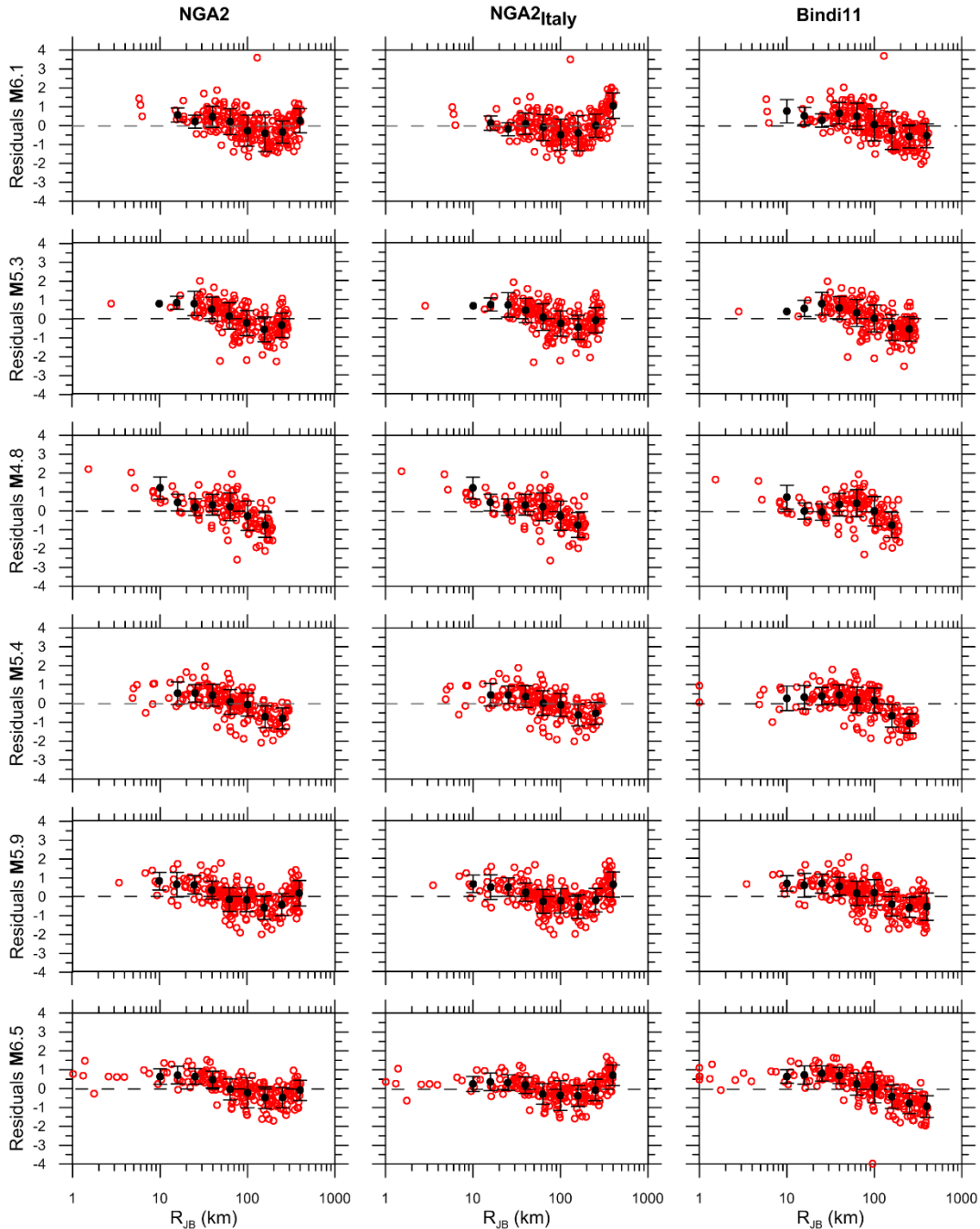


Figure 3.12. Within-event residuals of PHA from recorded ground motions relative to predictions of the NGA2, NGA2-I and B11. Binned means shown with +/- one standard deviation.

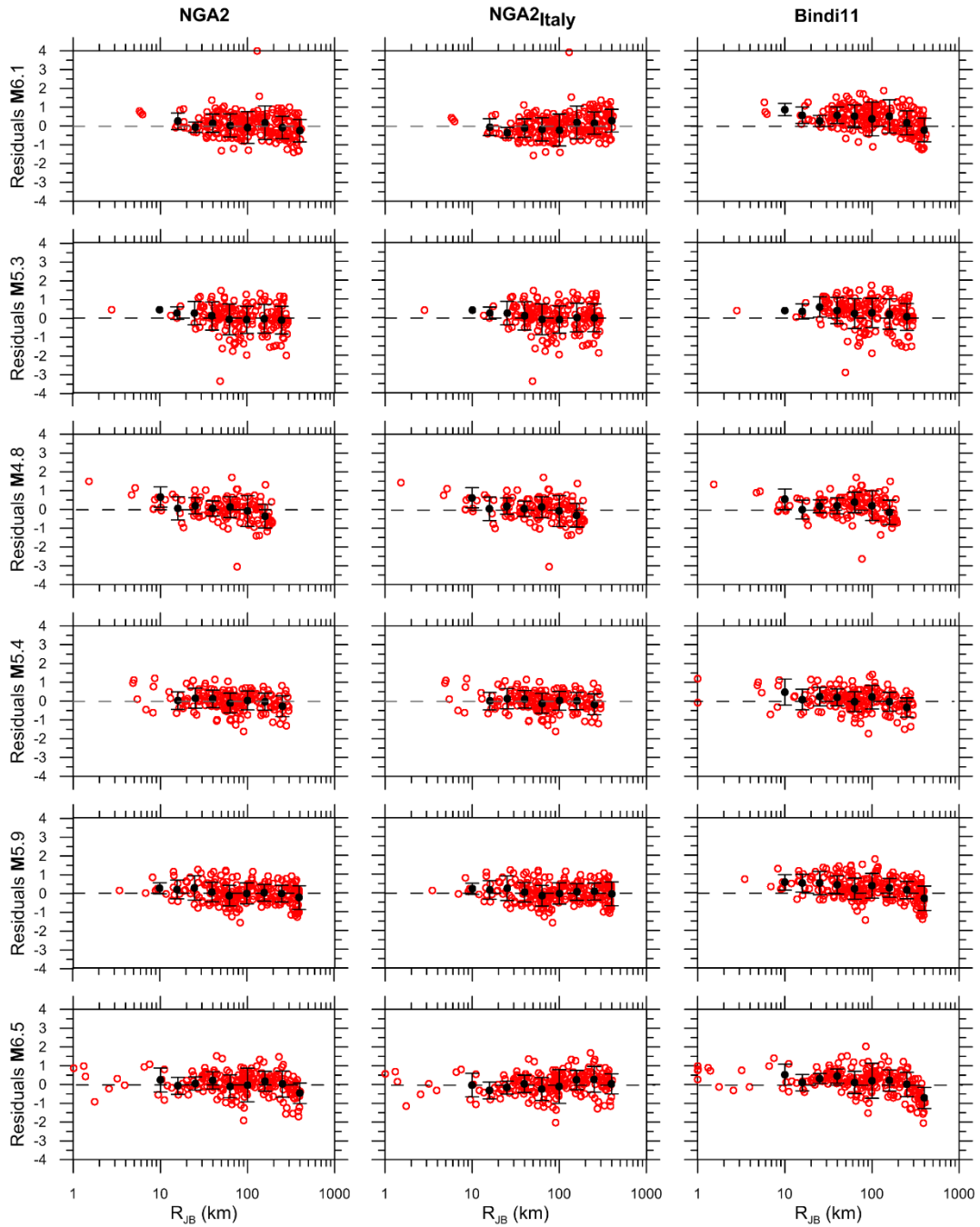


Figure 3.13. Within-event residuals of PHV from recorded ground motions relative to predictions of the NGA2, NGA2-I and B11. Binned means shown with \pm one standard deviation.

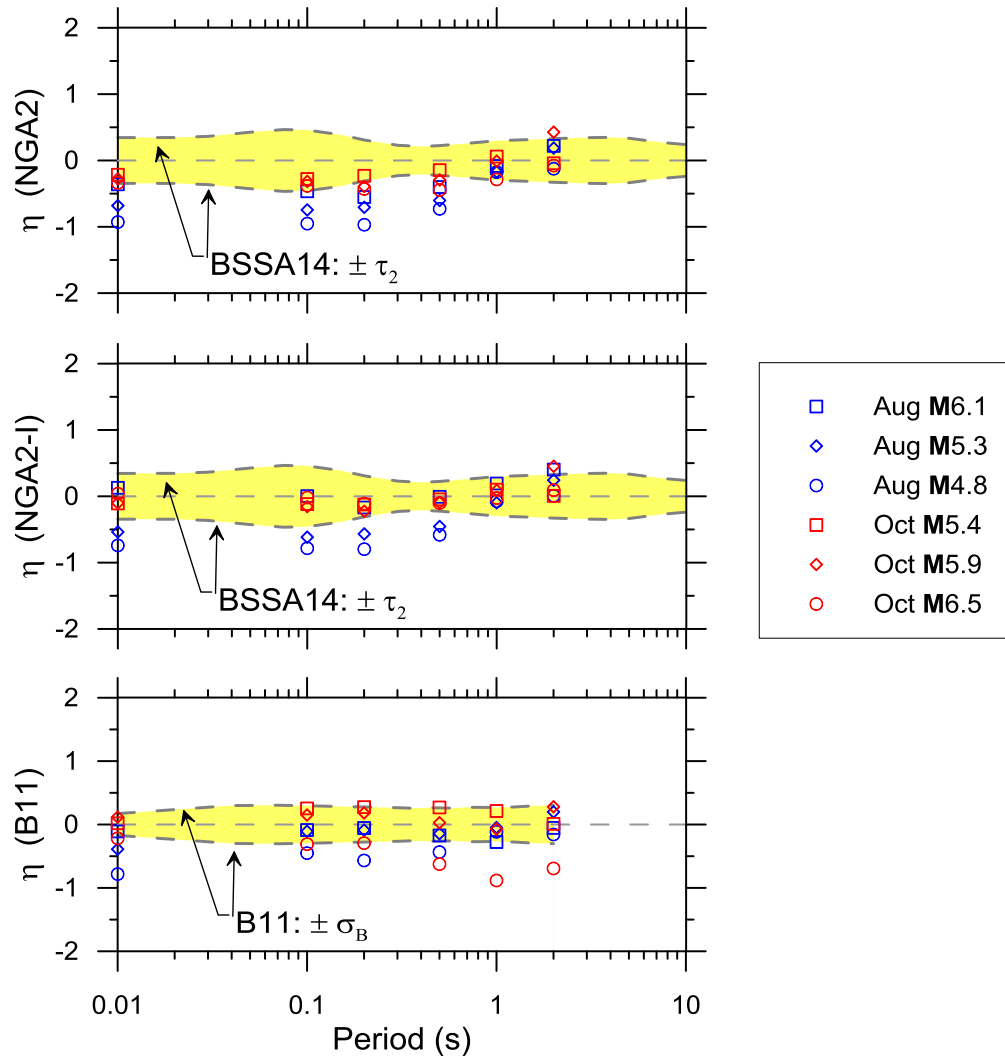


Figure 3.14. Event terms for PGA and PSA oscillator periods of 0.1-2.0 sec for the three sets of models and six events. For context, the +/- one between-event standard deviation is shown: τ_2 for $M_{\geq 5.5}$ from the Boore et al (2014) and σ_B from Bindi et al (2011).

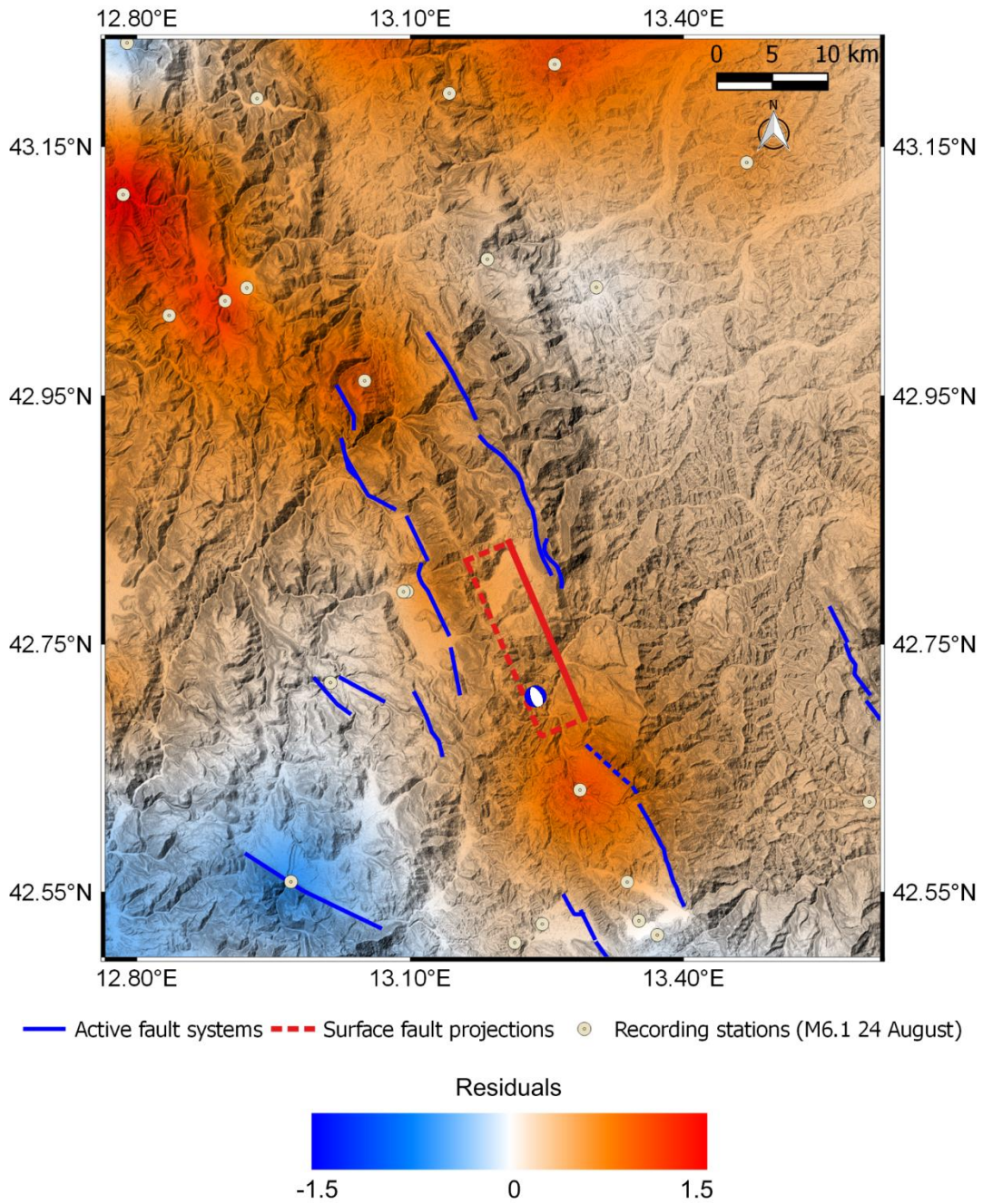


Figure 3.15. Map of the spatial distribution of PGA Residuals for the **M6.1 24 August 2016** earthquake.

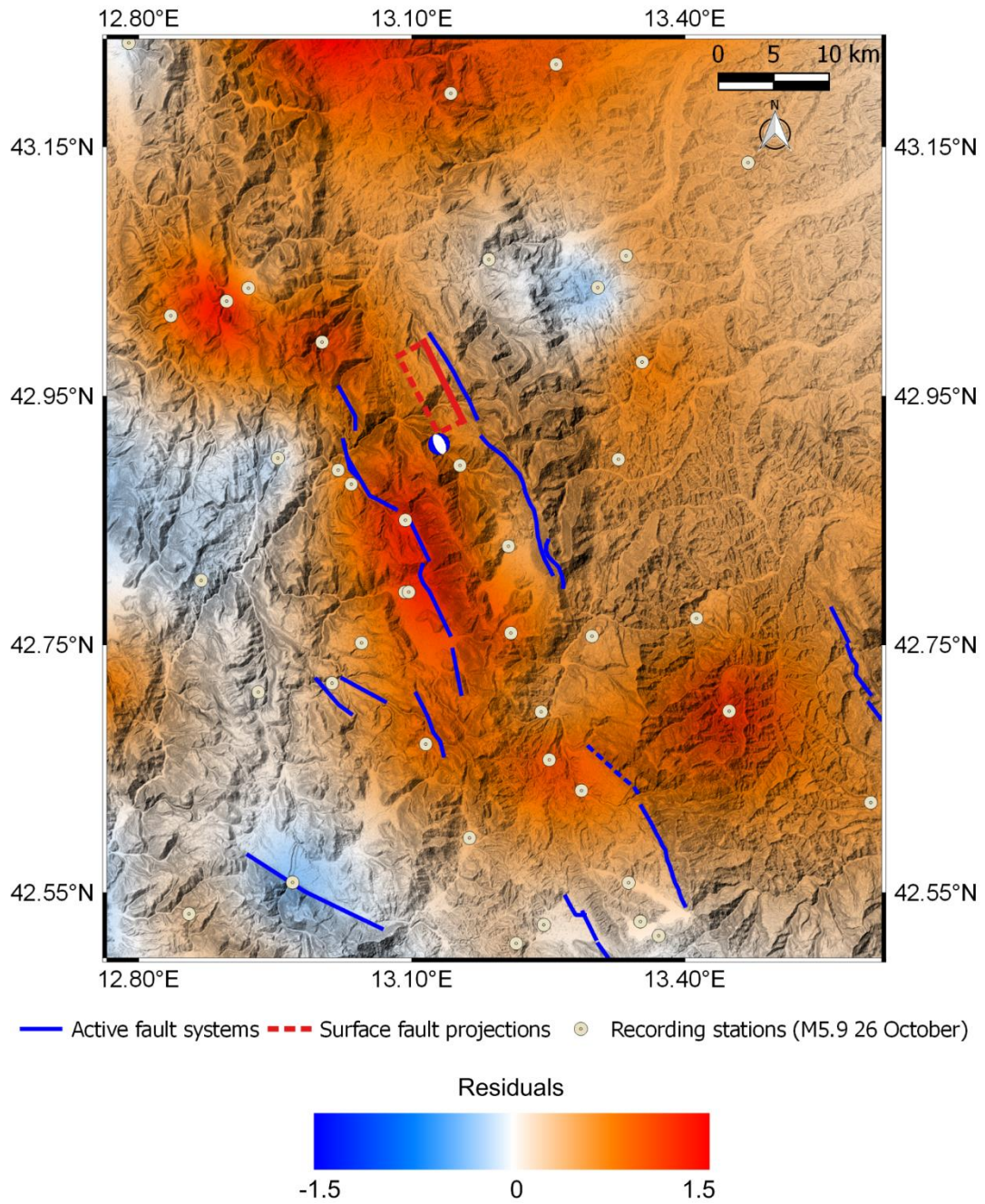


Figure 3.16. Map of the spatial distribution of PGA Residuals for the **M5.9 26 October 2016** earthquake.

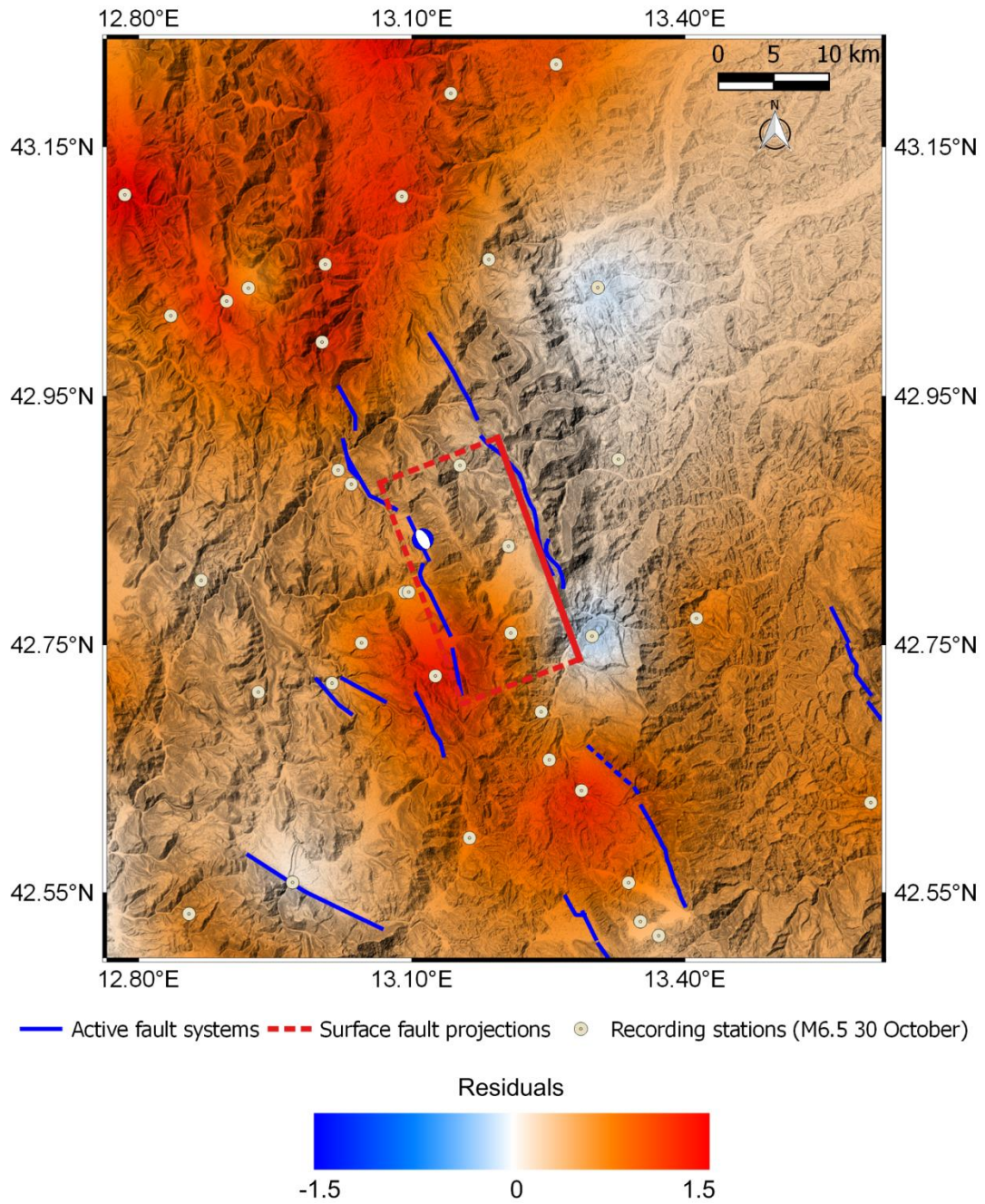


Figure 3.17. Map of the spatial distribution of PGA Residuals for the **M6.5 30 October 2016** earthquake.

4 Slope Displacements, Landslides, and Rockfalls

Principal authors: Kevin Franke, Robert E. Kayen, Bret Lingwall, Paolo Tommasi, Fernando della Pasqua, Paolo Zimmaro

Contributing authors: Ernesto Ausilio, Francesca Bozzoni, Roberto Cairo, Massimina Castiglia, Filiberto Chiabrande, Paolo Dabove, Melania De Falco, Anita Di Giulio, Vincenzo Di Pietra, Tony Fierro, Giovanni Forte, Sebastiano Foti, Dipendra Gautam, Giuseppe Lanzo, Paolo Maschio, Luciano Mignelli, Federico Passeri, Brandon Reimschiessel, Antonio Santo, Filippo Santucci de Magistris, Antonio Sgobio, Lorenzo Teppati Lose, Giuseppe Tropeano

4.1 Introduction

The number and significance of landslides and rockfalls was far greater from the October 2016 event sequence than the earlier August events. Locations of landslides presented in this chapter are provided in Figure 4.1a. As a result, our reconnaissance was organized to emphasize documentation of these important case histories. Because our field work occurred only three to four weeks after the 30 October event, during a period when the government and local authorities were still in an emergency response phase, transportation was challenging and access to sites was limited. Nonetheless, we organized the reconnaissance to:

- Revisit landslide areas inspected following the August events, to assess possible landslide reactivation, and
- Document major new earthquake triggered landslide events.

As in the reconnaissance for the August events (GEER, 2016), we utilized data on landslide susceptibility and risk as derived from pre-earthquake studies, which are reported in two databases: (1) the Italian landslide inventory (Inventario dei Fenomeni Franosi in Italia, IFFI project, ISPRA - Dipartimento Difesa del Suolo-Servizio Geologico d'Italia, available at: <http://www.progettoiffi.isprambiente.it>, last accessed 22 March 2017), and (2) the plans for landslide and flood risk management (PAI), which are both prepared at the basin scale. Figure 4.1b shows a map that combines IFFI and PAI pre-earthquake landslide areas. Not surprisingly, most of the observed landslides were in locations of known landslide risk, although it should be noted that many of the observed features were associated with local features such as road cuts or road embankment failures.

Using the procedure described in Section 3.5, we have estimated ground motions (PGA, PGV) at each of the locations discussed in this chapter during the 24 August, 26 October, and 30 October 2016 mainshocks with the results shown in Table 4.1-4.2. The ground motions were estimated for a representative site condition of $V_{s30} = 580$ m/s. These ground motions do not include topography-related site effects, which likely affected ground motions at landslide sites to varying degrees. Figure 4.2 shows a map of anticipated peak accelerations across the study region from the 30 October event, based on the procedure in Section 3.5.

Three rain gauges are operated in the area affected by landslides: Visso and Ponte Tavola operated by Servizio Idrografico - Regione Marche, and Nerito-Crognaleto operated by Servizio Idrografico - Regione Abruzzo. Figure 4.3 shows the precipitation recordings in these gauges over the time period of the event sequence (August to December 2016).

The following sections present case histories with detailed documentation (4.2) and those with relatively rapid and less detailed characterization of the features (4.3).

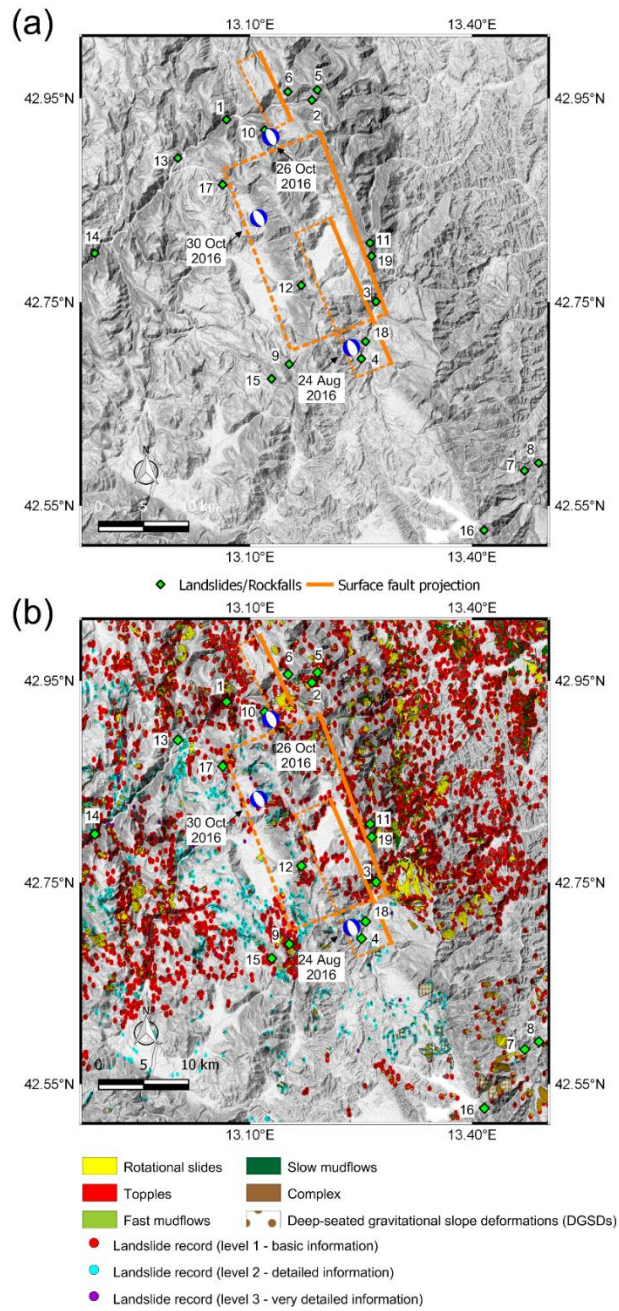


Figure 4.1. (a) Map of observed landslides (green diamonds), along with surface fault projections and moment tensors for the three mainshocks; (b) Observed landslides superimposed to the IFFI inventory.

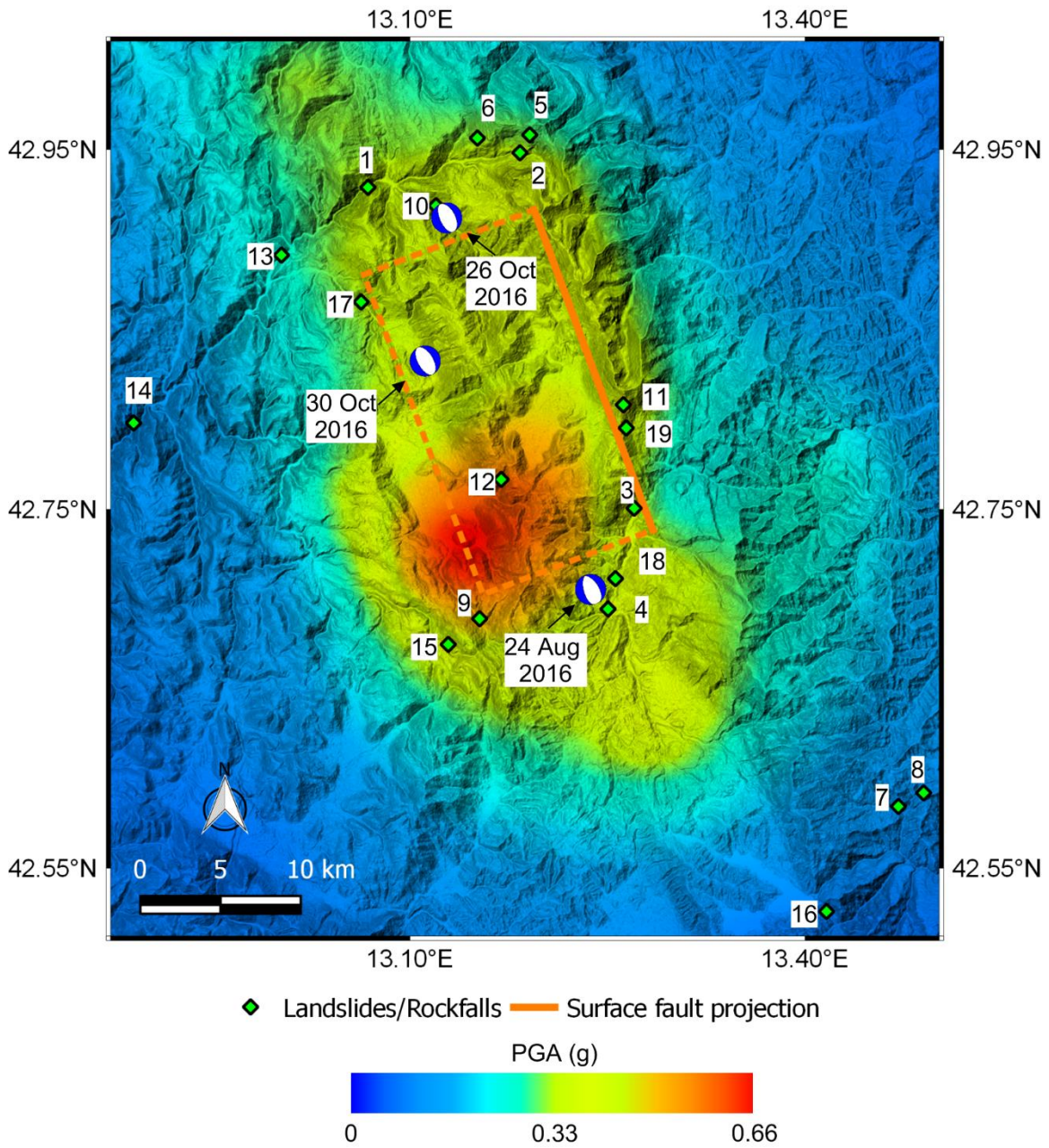


Figure 4.2. Location of reconnaissance sites, epicenter locations, and spatial distribution of PGA for the 30 October M6.5 earthquake.

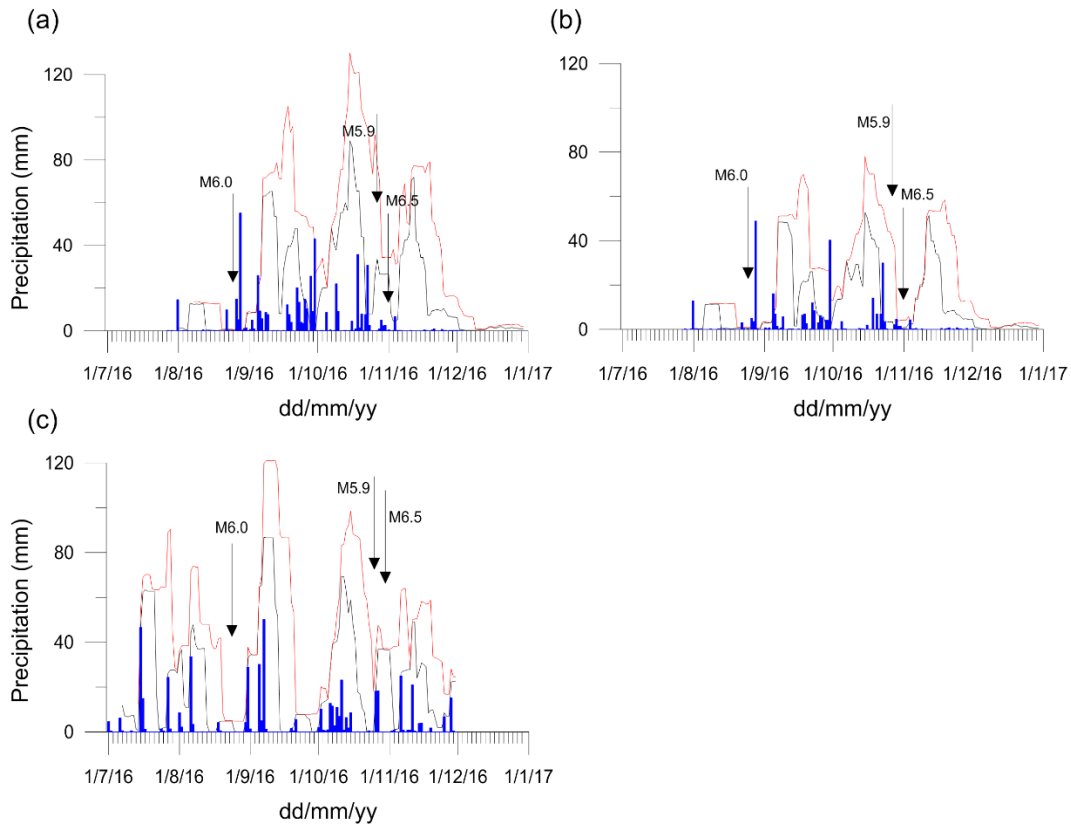


Figure 4.3. Daily rainfall (blue bars) and daily rainfall accumulated over one (black line) and two weeks (red line) recorded by (a) Visso, (b) Ponte Tavola (courtesy of Servizio Idrografico - Regione Marche), and (c) Nerito-Crognaleto (courtesy of Servizio Idrografico -Regione Abruzzo) rainfall gauges.

Table 4.1. Reconnaissance landslide site locations (Case studies and Imaging).

No.	Lat	Lon	PGA (g)			Location Summary
			M6.1 24 August	M5.9 26 October	M6.5 30 October	
1	42.92900	13.06800	0.25	0.40	0.37	Nera Landslide
2	42.93570	13.19010	0.20	0.36	0.38	Monte Bove Rockfalls
3	42.75057	13.27010	0.51	0.10	0.38	Pescara del Tronto
4	42.69442	13.25029	0.57	0.07	0.44	Accumoli
5	42.94923	13.18799	0.18	0.32	0.35	Valle di Panico Rockfall
6	42.94717	13.14364	0.20	0.42	0.36	Valle di Panico Landslide
7	42.58433	13.47075	0.12	0.04	0.13	Crognaleto Rockfall (Next to Cervaro Village)
8	42.59190	13.48990	0.12	0.04	0.13	Landslide near the village of Crognaleto
9	42.68901	13.15276	0.27	0.11	0.57	Pescia Landslide
10	42.91877	13.11964	0.26	0.49	0.41	Rockfalls/Landslides along SP134 Visso - Castelsantangelo
11	42.80816	13.26192	0.44	0.14	0.43	Western flank of Mt. Vettore massif
12	42.76658	13.16915	0.45	0.20	0.64	Rockfall SP 477 Arquata-Castelluccio (reappraisal)

Table 4.2. Reconnaissance landslide site locations (Visual inspection sites).

No.	Lat	Lon	PGA (g)			Location Summary
			M6.1 24 August	M5.9 26 October	M6.5 30 October	
13	42.891342	13.002303	0.19	0.18	0.29	Rockfalls in Pontechiusita along SP209
14	42.798017	12.890086	0.10	0.05	0.13	Rockfalls between Piedipaterno and Cerreto
15	42.674714	13.128963	0.21	0.11	0.46	Landslide along SP746 road between Cittareale and Norcia
16	42.525667	13.416131	0.09	0.25	0.10	Landslide along road Ortolano-Campotosto
17	42.865321	13.062843	0.25	0.38	0.36	Rockfalls along SP476 (between Piedivalle and Preci)
18	42.71114	13.2559	0.56	0.08	0.46	Landslide below the village of Tino
19	42.795242	13.264144	0.45	0.13	0.42	SP477 road embankment fill damage

4.2 Detailed Case Studies and Imaging

The locations of sites described in this section are shown in Figure 4.1 and listed in Tables 4.1 and 4.2. A total of 19 sites with observed rockfalls and/or landslides have been documented.

4.2.1 Nera Landslide

Field Observations

A large rockfall above the Nera River, a tributary of the Tiber River, occurred just downstream and 1 kilometer west of the town of Visso (Figure 4.4 and Table 4.1). No reports of slope instability at this location were made following the 24 Aug 2017 event nor the 26 October 2017 event. The landslide was witnessed by a passing car during the 30 October 2017 event (Visso resident), who had just passed through the Strade Provinciale 209 tunnel west of the site and saw the slide debris pass over the roadway in his rear-view mirror.

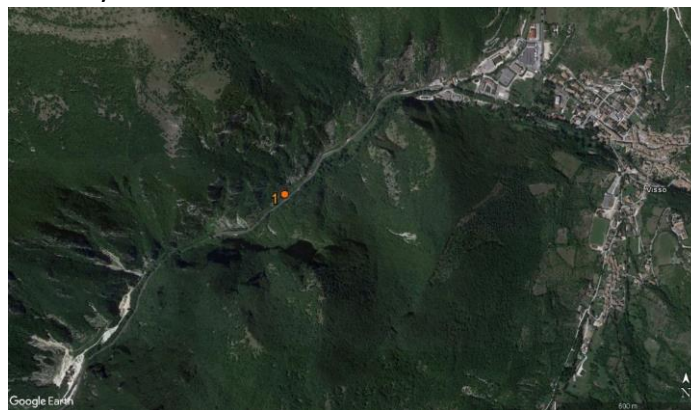


Figure 4.4. Location of the Nera landslide.

Estimated level-site ground motions at this location during all three events are shown in Table 4.1; the largest ground motions are expected to have occurred in the 30 October event. Pre-event precipitation in the local region, as recorded at the Visso rain gauge, is shown in Figure 4.3(a).

This large rock fall damaged national road SS-209 and formed a small landslide lake as shown in Figure 4.5. The rockfall severed road transportation between Visso and the Spoleto Valley. Access to Visso, the Nera river valley and the landslide was from the eastern Adriatic coast.

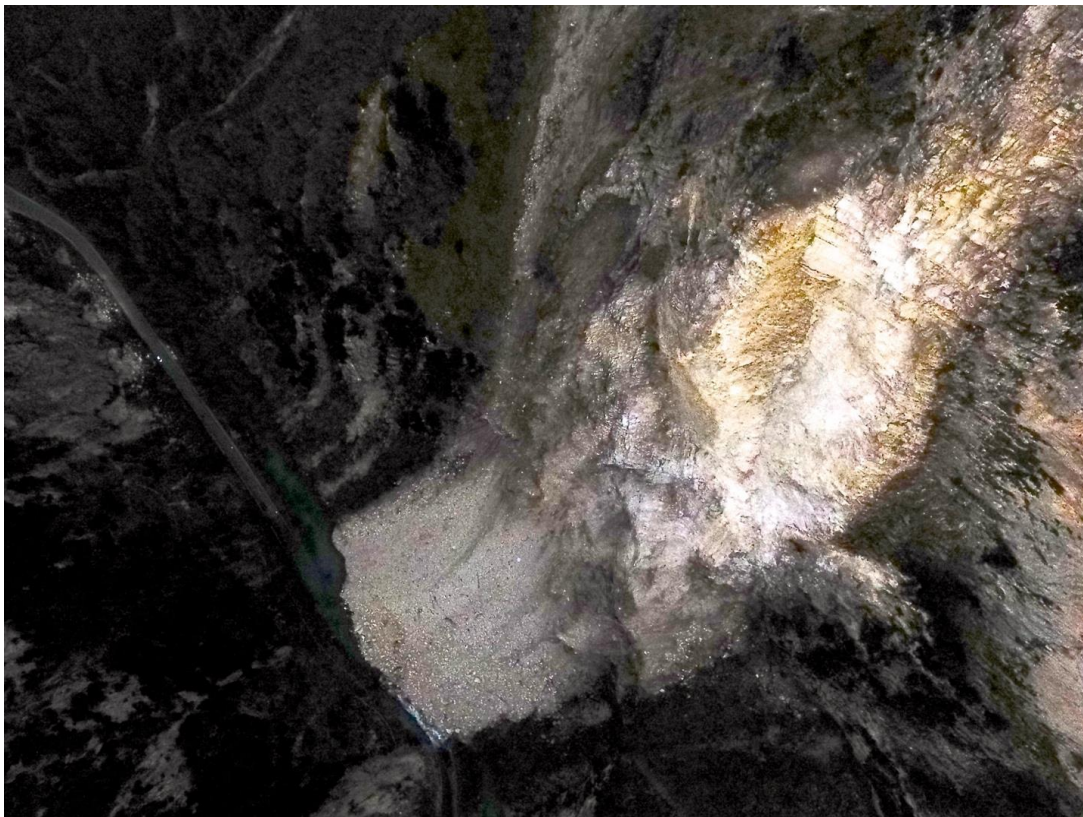


Figure 4.5. Nera rock avalanche photographed from the UCLA DJI Phantom 4 drone at an elevation of 400 meters above Route SS209. The primary rock-fall was a wedge that detached on the right side of the image and disintegrated into talus debris as it fell 330 meters to the river valley floor. The limestone bedding is visible in the scar of the wedge detachment

Geology

The landslide occurred in the sedimentary rocks of the Umbria-Marche stratigraphic sequence, an early Jurassic to Eocene age formation. The sequence at Nera is a well-layered limestone. The geomorphological landslide inventory map for the Umbria Region by Antonini et al. (2002) shows that mapped landslides in the Nera River valley cumulatively cover more than 65 km², or 6.3% of the ground area within the valley. This ratio is similar to the overall ratio for landslides about the area of the Umbria-Marche stratigraphic sequence that comprises almost the entire extent of the valley (Unit G, Table 4.3). The source of the Nera landslide was not mapped as a landslide in the Antonini et al. (2002) inventory. Compared with other geologic units in Umbria, the Umbria-Marche stratigraphic carbonate sequence has one of the lowest landslide-to-geologic unit area ratios (Table 4.3 from Guzzetti, et al. 2004).

This unit was also subject to rockfall during the Umbria-Marche earthquake sequence of September to October 1997 that affected the central Apennines. That earthquake swarm of two

decades prior produced abundant rock falls along the Nera River valley in the vicinity of the 30 October 2016, event (Guzzetti et al., 2004).

Table 4.3. Landslide abundance as a function of lithological unit (from Guzzetti et al, 2004).

Lithological complex	Group of rock units	Rock unit area		Landslide area (A_L)		A_L/A_{LT}
		km ²	%	km ²	%	
	Post-orogenic complex	3242.1	38.34	198.5	6.12	27.8
A	Alluvial deposits	1394.8	16.49	–	–	–
B	Lake, continental and marine deposits	1847.3	21.85	198.5	6.12	27.8
C	Volcanic complex	151.3	1.79	5.4	3.60	0.8
	Flysch complex	2445.6	28.92	360.8	14.75	50.7
D	Marly flysch (Marnoso Arenacea Fm.)	1729.5	20.45	232.4	13.44	32.7
E	Sandy flysch (Cervarola Fm.)	676.8	8.00	111.1	16.42	15.6
F	Ligurian sequence	39.3	0.46	17.3	43.95	2.4
G	Carbonate complex Umbria-Marche stratigraphic sequence	2617.0	30.95	147.4	5.63	20.7
	Umbria Region	8465.0		712.6	8.38	

Geometry of slope failure

During the 30 October 2016 earthquake, the rock avalanche at Nera separated from the steep rock-face in a brittle detachment. The fall was fast-moving and disintegrative. Quantitative measurements from the rockfall were made from photogrammetric reconstruction of imagery captured from the UCA DJI Phantom drone quad copter. Reconstruction was performed using the Structure-from Motion method. The crest of the valley wall at the top of the detachment is approximately 330 meters above SS209. The slope at the detachment area is between 75° and 80°. The slope of the debris apron SS209 is about 27°. The entire talus field covers about 20,000 m².

The upper detachment zone can be seen in the SFM imagery of Figure 4.6-4.7. In these images, the bedding is seen with an apparent dip towards the east of 20°-30°, and the wedge is apparently a double joint set orthogonal to the bedding. The failure occurred along the joint sets. Further analysis of the SFM data may resolve the strike and dip of the bedding and the joint sets that resulted in the detachment.



Figure 4.6. Headscarp of Nera rockfall.

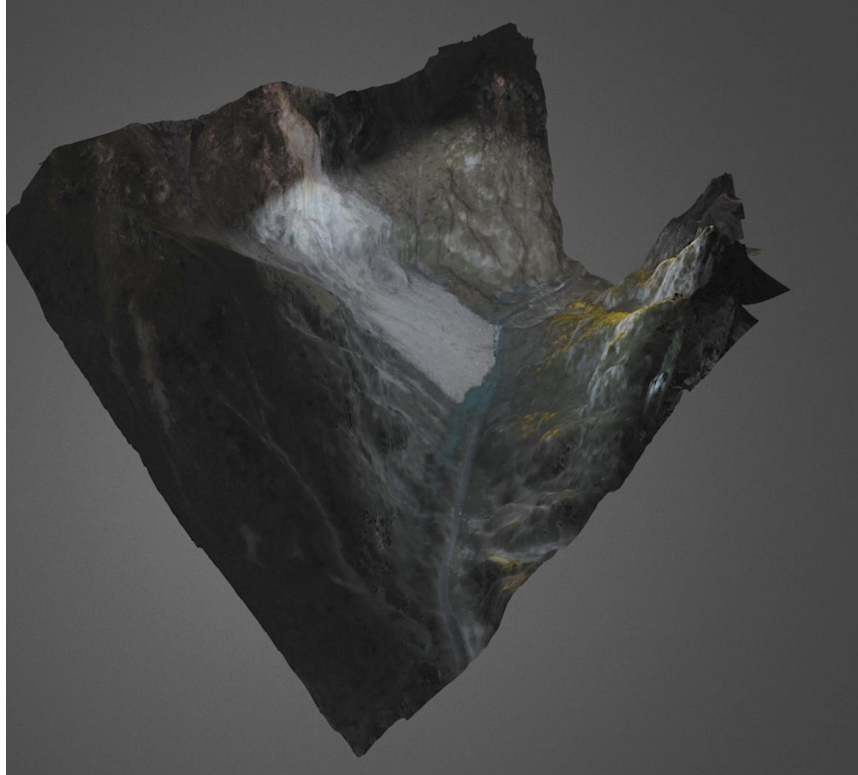


Figure 4.7. 3D Structure-from Motion (SfM) model of the Nera river valley at the rockfall. The Nera rock avalanche is seen here from the east (Visso) side of the rockfall. The light color on the midslope is from the setting sunlight on the SfM UAV imagery. Elevation difference from the crest of the headscarp to the river is 330m.

4.2.2 Monte Bove Rockfalls

A series of rockfalls was observed along the northern face of Monte Bove, which is prominent mountain peak in the Appenine range that is located approximately 4 km east-southeast of the hamlet of Ussita. A satellite view image of Monte Bove and surrounding hamlets is presented in Figure 4.8. Personal communication with the City Engineer of Ussita revealed that no instabilities or rockfalls were observed following the **M6.1**, 24 August event, but all of the visible rockfalls had occurred after the **M5.9**, 26 October event. Interestingly, he mentioned that no new rockfalls on Monte Bove were observed following the **M6.5**, 30 October event. Estimated level-site ground motions at Monte Bove during all three events are shown in Table 4.1.

Most of the northern flank of Monte Bove is formed by massive or coarsely bedded Jurassic limestones of the Calcare Massiccio Formation (MAS). At the top of the mountain the MAS formation is overlaid by limestones (Bugarone Formation) with more regular bedding (medium to thick beds). The M.te Bove massif has been involved in intense quaternary and ancient tectonics which has produced faults trending in a strike range from ESE-WNW to N-S. As a result, the rock mass is characterized by both closely spaced joints and persistent joints belonging to the major joint sets. However, when looking to the irregular shape of failure surfaces, pervasive jointing is evident. In particular, severe loosening of thick outer parts of the intensely fractured mountain flank could have favored the detachment of large irregular slices under seismic loading.



Figure 4.8. Satellite overview image of Monte Bove and surrounding hamlets (courtesy of Google Earth)

Numerous talus fields were visible along the base of Monte Bove, some of which are visible in Figure 4.9. These talus fields were located more than two kilometers from where the GEER reconnaissance team members were deployed, and could only be imaged from a distance. Suspected source areas for these talus fields were visible on Monte Bove by the lighter coloration of the freshly-exposed unweathered limestone (many circled in Figure 4.9). Two particularly large rockfalls were observed near the summit of Monte Bove, and are labeled in Figure 4.9. The upper rockfall was photographed using a 300 mm telephoto lens (Figure 4.10). The BYU Phantom 4 UAV was used to image as much of Monte Bove as possible, but flight altitude and distance-from-controller limitations prevented the UAV from clearly imaging the large rockfalls near the summit. Nevertheless, the captured UAV video was processed using SfM computer vision to develop a non-scaled 3D meshed surface model of the most of the mountain minus its summit. A screenshot of this model is presented in Figure 4.11. Links to the three-dimensional models resulting from this work are available at the [GEER web site \(Appendices A1-A11\)](#), and at the [BYU-PRISM website](#) (last accessed 5 May, 2017).

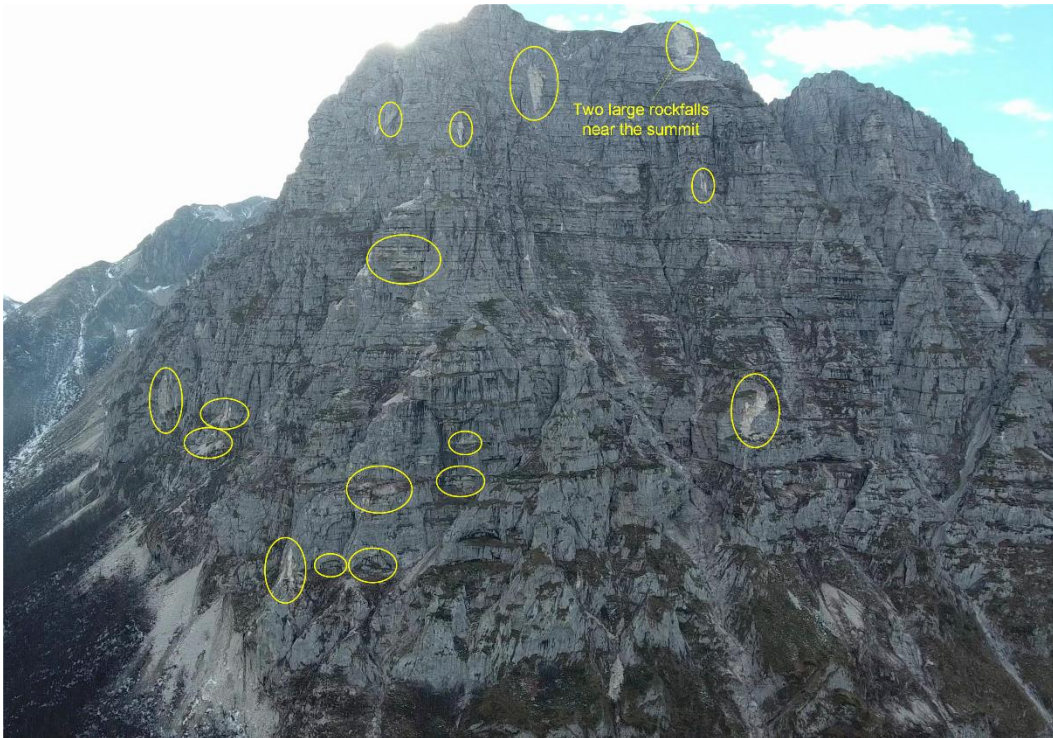


Figure 4.9. Phantom 4 UAV image of Monte Bove. Suspected rockfall sources are circled in yellow.



Figure 4.10. Photograph (300 mm) of the upper rockfall near the summit of Monte Bove.



Figure 4.11. Screenshot of Monte Bove SfM meshed 3D model. Note the missing summit of the mountain in the model due to insufficient UAV imagery

4.2.3 Pescara del Tronto

Significant ground deformations were observed in Pescara del Tronto following the August events (GEER 2016), and additional ground deformations were observed following the October events. GEER investigators explored the village both manually (where feasible and safe) and using UAVs (with the BYU Phantom 4 and the Politecnico eBee). UAV-based photographs were used to develop orthophotos and SfM 3D points clouds and meshed models of the village. GEER (2016) describe in detail the regional geology and observed ground deformations following the 24 August event. Overall, we observed that the October events caused considerably more damage and landslide movements that will be described in this section. Discussion will focus on five principal observation areas in Pescara del Tronto, all labeled in the overview image presented in Figure 4.12. An aerial image of Pescara del Tronto taken from the BYU Phantom 4 UAV is presented in Figure 4.13.

Structural Damage Area (Location 3a)

Area 3(a) shown in Figure 4.12 identifies the region of Pescara del Tronto characterized by completely collapsed residential structures built upon talus deposits (Figure 4.14). Structural damage in this area is described in Section 6.1.5. Structural debris was so complete and widespread that it was difficult (if not impossible) to investigate ground deformations in this zone from the UAV. Any attempt to manually investigate this zone was infeasible due to the dangerous and unstable nature of the debris field.



Figure 4.12. Pescara del Tronto locality map. Specific locations referred to in the text shown.



Figure 4.13. Pescara del Tronto aerial photograph taken from the Phantom 4 UAV.



Figure 4.14. 3D SfM model of main damaged building area overlying talus deposits (Location 3a).

Failed Retaining Wall Surrounding Village (Location 3b)

The lower portion of Pescara del Tronto was partially supported by a 24 m-tall masonry retaining wall that surrounded much of the village. Portions of that retaining were observed to have failed following the **M6.1** event on 24 August. However, *all* of these retaining walls were observed to have collapsed following the October events. Figure 4.15 presents an aerial photograph of the exposed talus/fill remaining following the retaining wall failure. Details of the construction of these retaining walls is not currently available, but it is suspected that only the walls and the fill placed behind the walls failed. The angle of repose for the native talus slope behind the failed wall was measured in the SfM 3D model of the village to be 53 degrees.

Failure of Road Base and Retaining Wall/Fill (Location 3c)

Moderate to severe damage was observed in most of the roads located adjacent to slopes and/or above retaining walls throughout Pescara del Tronto. An example of the typical damage that was observed is presented in Figures 4.16 and 4.17. Most of the damaged observed in the roads appears to be due to horizontal deformations in the fill material placed on the slopes (Figure 4.16) or behind the retaining walls (Figure 4.17). Observed damage typically consisted of long cracks in the pavement running parallel with the face of the slope or retaining wall, often with variable amounts of vertical offsets due to rotation of the retaining wall and/or settlement of the underlying fill.

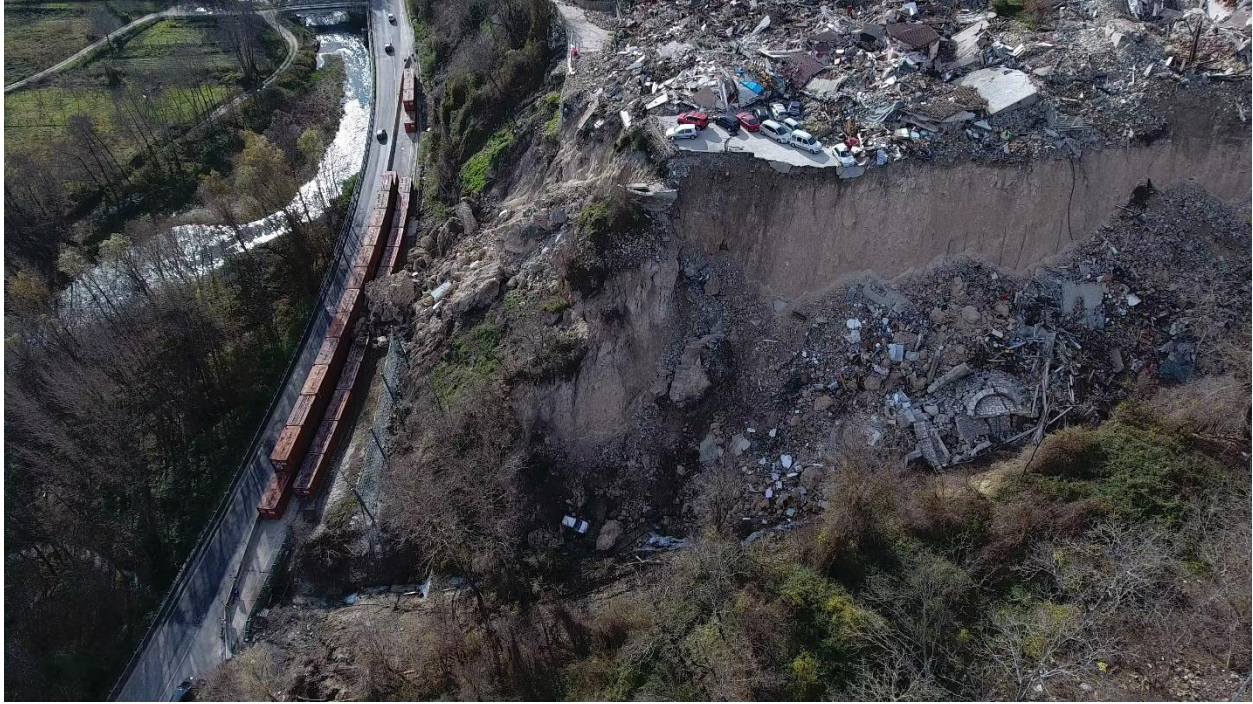


Figure 4.15. View of talus behind failed retaining wall by Strada Statale No. 4 (Location 3b).



Figure 4.16. Pavement and road base damage induced by underlying stability failure of fill material (Location 3c).



Figure 4.17. Road damage induced by slight rotation of the underlying retaining wall and/or settlement of the retaining wall backfill.

Landslide Impacting Strada Statale No. 4 (Location 3d)

Following the 24 August event, the GEER team observed and documented a large landslide below Pescara del Tronto that had impacted Strada Statale No. 4, which is the main highway through the region and connects cities such as Ascoli Piceno to Rome. Following the October 2 events, significantly more movement was observed on this landslide. An aerial image of the landslide captured from the BYU Phantom 4 UAV is presented in Figure 4.18. Limestone boulders in excess of 6 m in diameter were dislodged from the slope and rolled onto the highway. It is not clear which subsequent earthquake event (or perhaps both) caused the boulders to move. However, prior to the movement, a line of rockfall netting had been installed above the highway to prevent smaller boulders from bouncing onto the highway. Unfortunately, the massive boulders from the landslide overwhelmed the netting (Figure 4.19). In attempt to protect the highway and passing cars from any potentially large boulders that could have toppled or slid, it appears that a makeshift barrier wall comprised of cargo shipping containers stacked two containers high and a concrete barrier was erected along Strada Statale No. 4 (visible in both Figures 4.18 and 4.18). Debris from the landslide was resting against this barricade wall, suggesting that the wall had been erected before the landslide occurred. It was not clear if the cargo containers were empty or filled with some material like sand to provide additional mass to the barrier. Regardless, the barrier wall appeared to have worked effectively by keeping the landslide debris out of the single remaining travel lane on the highway.



Figure 4.18. Aerial photograph of landslide impacting Strada Statale No. 4 below Pescara del Tronto (Location 3d).



Figure 4.19. View of damaged rockfall netting caused by loose debris material from the landslide above Strada Statale No. 4 (Location 3d).

Localized Landslides along Gulley Wall (Location 3e)

Within the village of Pescara del Tronto, there exists a natural creek that flows down a gulley located in the middle of the village. The presence of the gulley gives Pescara del Tronto the appearance of an inverted horseshoe shape or upside-down “U” when observed from the air (see Figure 4.12). During the December reconnaissance mission, GEER team members observed that portions of the gulley wall had failed in localized landslides, causing any overlying structures to fall into the gulley (Figure 4.20). The exposed scarps revealed talus comprised of heavily weathered limestone.

Comparing Points of Interest from September 2016 to December 2016

In Chapter 4 of the GEER (2016) report, several points of interest were observed and noted in Pescara del Tronto (Figure 4.21). This section will now compare those same points of interest from the September reconnaissance mission with the December reconnaissance mission to evaluate the presence of incremental ground deformations. We lack details regarding the origin of these changes between the 26 October and 30 October events. Ongoing change detection analyses using SfM point clouds is already underway to detect where slopes may have moved and to estimate how much movement occurred between the two GEER reconnaissance missions.



Figure 4.20. Failure of steepened talus gully wall material and crest area above (Location 3e).



Figure 4.21. Site vicinity map showing comparison locations of interest (after GEER, 2016).

Area 1: Landslide above Strada Statale No. 4: As mentioned above, significant movement occurred on the landslide below Pescara del Tronto, directly above Strada Statale No. 4. This significant movement is apparent when comparing the landslide from September (Figure 4.22a) with the landslide from December (Figure 4.22b). Large portions of the road and supporting retaining wall that were standing in September collapsed with the landslide in December. It appears that the majority of the very large limestone boulders visible in December were dislodged from beneath the road.



Figure 4.22. 3D model comparison of the landslide below Pescara del Tronto between September 2016 (a) and December 2016 (b).

Area 2: Smaller landslide above Strada Statale No. 4: The smaller landslide just to the south of the landslide described as Area 1 was not observed to change significantly between September (Figure 4.23a) and December (Figure 4.23b). In this section, even the retaining wall supporting the road appeared to maintain its stability. However, significantly more structural debris from collapsed residences was observed at this location in December.



Figure 4.23. 3D model comparison of the smaller landslide below Pescara del Tronto between September 2016 (a) and December 2016 (b).

Areas 3 and 4: Failed Retaining Wall below Pescara del Tronto: Portions of the 12-25 m-tall retaining wall below Pescara del Tronto were observed to have failed in September 2016 following the 24 August event (Figure 4.24a). All remaining retaining walls were observed to have failed by December 2016 following the October events (Figure 4.24b). In addition, another 6 m or more of the soil behind the wall also failed and collapsed by December based on measurements from the 3D SfM model. Overlying infrastructure and debris (including at least

one car) tumbled 12-25 m into the gulley as a result. Interestingly, the remaining side slope is nearly linear as it follows the gulley up the creek (Figure 4.25), with a uniform dip angle of about 53 degrees. This observed linearity of the remaining slope suggests that the failures involved anthropogenic soil fills and retaining walls failures, whereas the remaining soil/rock remained intact.



Figure 4.24. 3D model comparison of the failed retaining wall below Pescara del Tronto between September 2016 (a) and December 2016 (b).

Area 5: Landslide near the Head of the Gully: Following the 24 August event, a minor sloughing of the gully wall was observed from the UAV imaging (Figure 4.26a). However, similar UAV imaging performed in December after the October earthquake events revealed that a section of the slope nearly 9 m thick and 20 m wide failed and slid into the gully (Figure 4.26b). The remaining scarp is nearly 12 m in height and stands with at an angle of 52 degrees, remarkably similar to the same scarp angle that remains behind the failed lower retaining wall (i.e., Areas 3 and 4). A small residential structure that was observed to rest on top of the slope in September had plummeted into the gully by December.

Area 6: Landslide on the Northern Slope of the Village: A shallow landslide was observed on the northern slope of the city following the 24 August event (Figure 4.27a). This landslide was observed to have exposed some tree roots and undermined a few residential structures. Investigation of the same slope in December following the October events revealed that the depth of the landslide remained relatively unchanged, but the width of the landslide appears to have expanded from 17 m in September to more than 36 m in December (Figure 4.27b). However, it is difficult to discern from the UAV images and 3D model whether the flattened trees along the slope are due to an expansion of the shallow landslide or due to structural debris from above the slope.



Figure 4.25. 3D SfM model view of scarp linearity behind failed lower retaining wall in Pescara del Tronto.

Area 7: Haul Road and Exposed Pipeline near the Gravel Pit: A small landslide was observed on the slope bounding the gravel pit on the southern portion of the village of Pescara del Tronto, adjacent to SP129, following the 24 August event (Figure 4.28a). This landslide was caused by the unraveling of weathered limestone and calcareous soils that were underlying a dirt haul road for the gravel pit. The landslide exposed approximately 15 m of a 50 cm-diameter pipeline. The

condition of the landslide remained largely unchanged following the October earthquake events (Figure 4.28b). The slope beneath the haul road degraded slightly more, causing nearly half of the haul road above the landslide to disappear. Additionally, approximately 8 more meters of the pipeline became exposed from the additional slope movements, causing the pipeline to apparently sag and bow slightly. Another smaller pipe of a few centimeters' diameter was also exposed and sagging substantially along the scarp.



Figure 4.26. 3D model comparison of the landslide near the head of the gully in Pescara del Tronto between September 2016 (a) and December 2016 (b).



Figure 4.27. 3D model comparison of the landslide beneath the northern slope of Pescara del Tronto between September 2016 (a) and December 2016 (b).



Figure 4.28. 3D model comparison of the landslide near the gravel pit in Pescara del Tronto between September 2016 (a) and December 2016 (b).

4.2.4 Accumoli

Significantly more structural and landslide-related damage was observed by the GEER team in December following the October events than was observed following the August event and documented in GEER (2016). This section will summarize several of the important observations made in Accumoli by the GEER team. Figure 4.29 presents a vicinity map that shows the village

of Accumoli and highlights three areas of observed damage that will be discussed below. Section 6.1.2 discussed the distribution of structural damage in Accumoli.



Figure 4.29. Accumoli vicinity map.

Point 4a: Failed Retaining Wall and Shallow Slope Failure on Eastern side of Village

Point 4a (42.69442 N 13.25029 E) identifies the location of a rotated retaining wall described in GEER (2016). Following the 24 August event, the 4.8 m-tall retaining wall was observed to be rotated outwards 3.5 degrees with horizontal movements of 57 cm and downward vertical movements of nearly 18 cm. A soil graben nearly 2.7 m wide was observed behind the rotated wall, with soil settlements of 45-50 cm.

During the December GEER deployment, much more damage was observed. It appeared that a shallow landslide developed beneath the retaining wall and caused the entire structure to slide several meters down the slope. Figures 4.30 and 4.31 present photographs of the head of the shallow landslide showing the retaining wall's former location. Figure 4.32 presents an aerial screenshot of the 3D model developed from Phantom 4 UAV imagery of the site. Several features of interest are identified in Figure 4.32, and will be discussed below.



Figure 4.30. Failure of retaining wall due to shallow landslide (Point 4a, looking towards north).



Figure 4.31. Failure of retaining wall due to shallow landslide (Point 4a, looking towards south).

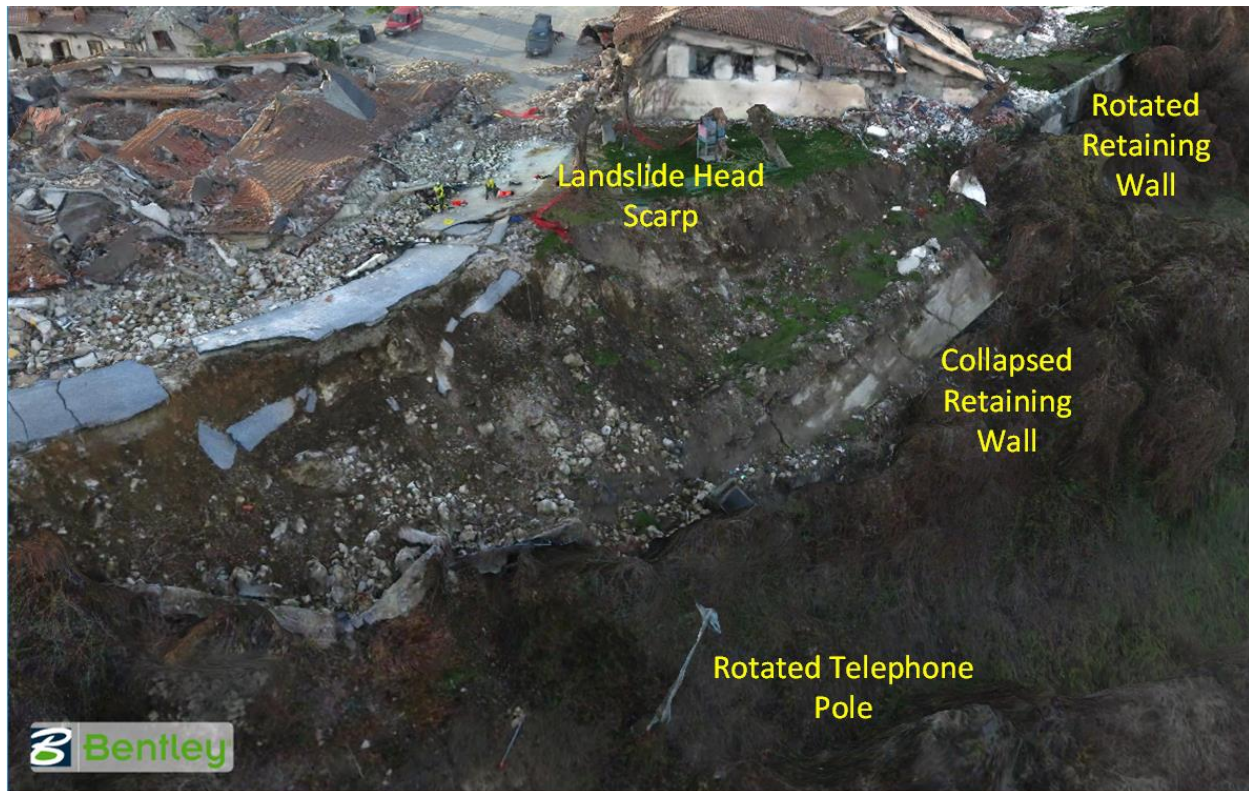


Figure 4.32. 3D model screenshot identifying objects of interest with the failed retaining wall and shallow slope failure at Point 4a.

The shallow landslide appeared to be limited to the upper corner of the slope, near the crown. The slide therefore likely occurred in the non-native fill slopes placed during the construction of the village. The scarp of the landslide appeared to follow the scarp of the soil graben observed behind the wall in September, suggesting that the graben may have been caused by more than just the rotation of the retaining wall. The landslide displaced the top of the wall between 5 to 6 m horizontally and between 3 to 4 m vertically downward. In total, approximately 50 m of the retaining wall below Accumoli failed and slid 5 to 6 m downslope. This loss of confinement resulted in significant horizontal and vertical deformations in the overlying roadway Frazione Fonte del Campo (SP18), as shown in Figure 4.33. The road was measured to have displaced horizontally between 0.1–1.6 m, and vertically downward 9–50 cm. Vegetation remained intact below the collapsed retaining wall, again suggesting that the landslide was likely shallow and limited to the upper limits of the slope. However, the rotated telephone pole located further down the slope, which was observed to have rotated 13 degrees in September, was observed to have rotated a total of 27 degrees in December. However, it is not clear whether this rotation was due to displacements of the heavily-vegetated soil slope or due to inertial effects on the pole from the earthquake.

Figure 4.32 also shows a second damaged retaining wall located approximately 60 m to the northwest of the collapsed wall (42.6948 N 13.2496 E). 3D model screenshots of the wall in September 2016 and December 2016 are presented in Figure 4.34. In September, no rotation of

the wall or cracking in the soil were observed. The structure adjacent to the wall was damaged, but still standing. In December, the wall was observed to have rotated outward 3.6 degrees, with a 1.8 m-wide graben forming behind the wall. The soil in the graben was measured to have settled approximately 29 cm. The structure adjacent to the wall was completely collapsed. The similarities in the observed damages with this wall with the observed damages of the now-collapsed wall in September are remarkable, and suggest that another shallow landslide may have formed beneath this damaged wall.



Figure 4.33. 3D model screenshot of the destroyed roadway Frazione Fonte del Campo (i.e., SP-18).

Point 4b: Shallow Landslide below Southeast Portion of the Village

During the September 2016 reconnaissance, the GEER team observed a series of shallow cracks approximately 5–14 cm in width in the soil below the southeastern slope of the village (42.69406 N 13.25019 E). These cracks were believed to have been caused by shallow landslide displacements in the soft silty-sand located near the surface of the fillslope.

Much more deformation was observed by the GEER team in December 2016. Figure 4.35 presents 3D model images of the headscarp cracks in both September (Figure 4.35a) and December (Figure 4.35b). In general, the GEER team observed that the cracks developed in the 24 August event opened further from 5-14 cm to 0.8-1.9 m. The depth of the crack was measured from the 3D model as approximately 55 cm. However, beyond the widening of the cracks from the shallow landslide, no other significant damage was observed at this point.



Figure 4.34. 3D model screenshots showing a retaining wall beneath the northeastern slope of Accumoli (a) undamaged in September 2016, and (b) damaged in December 2016.



Figure 4.35. 3D model screenshots showing cracking from a shallow landslide (a) during the September GEER reconnaissance, and (b) during the December GEER reconnaissance.

4.2.5 Valle di Panico Landslide and Rockfall

Monte Bove represents the southern flank of a narrow valley called the Valle di Panico. The northern flank of the valley is formed by a succession of limestone and marly units from Jurassic to Cretaceous in age. While traveling to investigate the reported rockfalls observed on Monte Bove (described in Section 4.2.2), the GEER team encountered two landslide locations along the mountain road that winds along the northern flank of Valle di Panico. These two sites are marked the site vicinity map presented in Figure 4.36 as Points 5 and 6, and their latitude/longitude

coordinates are reported in Table 4.1. The road is cut into thinly-bedded marly limestones (Scaglia Bianca Formation) whose bedding joints frequently have a clay/bituminous infilling. This structural/lithologic feature together with an intense fracturing gives the rock mass quality a low quality. The source area of the rock fall at the second site is located in a marly-limestone unit featured by thicker layers. In this area the bedrock is extensively covered by slope debris some meter thick.

The first site encountered (Point 5a) was a landslide in the soil slope through and beneath the road. An aerial photograph of the landslide is shown in Figure 4.37 (note the fire fighter in the upper left corner for scale). The landslide was measured to be 55-60 m in width. While the head of the landslide was easily seen in the road pavement, no toe or side scarp of the landslide could be traced on the heavily vegetated slope below the road. On the road, the vertical offset measured in the pavement ranged from 10-70 cm, and the horizontal deformation ranged from 2-40 cm. The GEER team observed that the eastern portion of the landslide headscarp showed a distinct crack and displacement (Figure 4.38), while the western portion of the landslide headscarp appeared more gradual and showed more pavement cracking (Figure 4.39). This landslide was believed to have occurred in the shallow soils along the side of the mountain slope, and appeared limited in its extent.

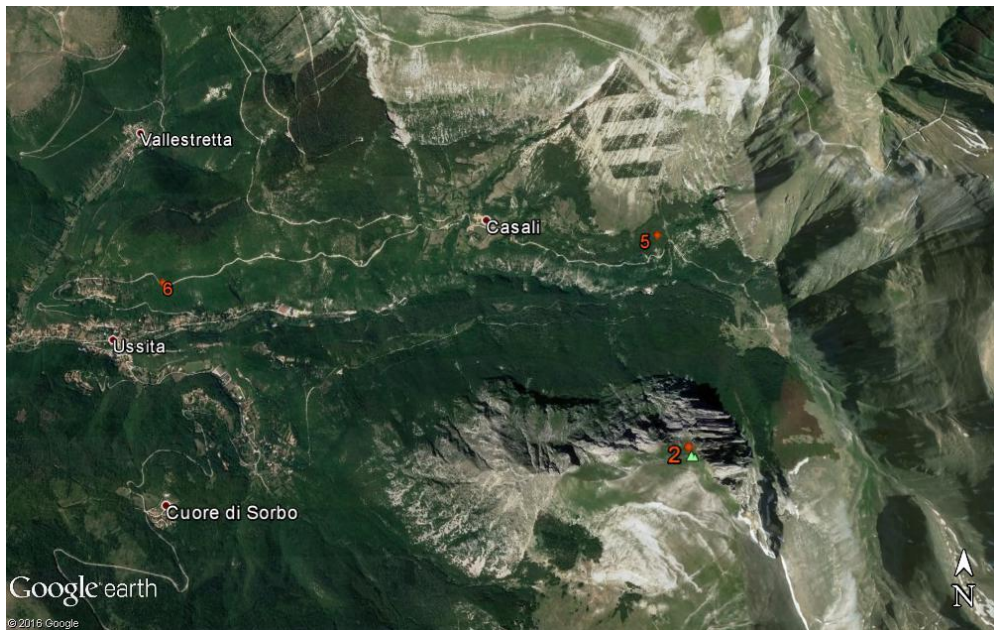


Figure 4.36. Site vicinity map for the Valle di Panico, located to the east of Ussita and to the north of Monte Bove.



Figure 4.37. Landslide encountered along mountain road in the Valle di Panico (Point 5a).



Figure 4.38. 3D model of the eastern half of the Valle di Panico landslide headscarp.



Figure 4.39. 3D model of the western half of the Valle di Panico landslide headscarp.

The second site encountered (Point 5b) was a rockfall nearly 419 m in length along the mountain road in the Valle di Panico. A 3D model of the entire rockfall is presented in Figure 4.40. The total change in elevation from the source of the boulder to the final resting place on the bottom of the valley is approximately 235 m. The sideslope of the valley was measured to rest at an angle of 34 degrees from the horizontal (1.5H:1V). Numerous boulder fragments ranging in diameter from gravel-size to over 3 m were observed and photographed along the entire rockfall length. The largest boulder fragment was observed to rest adjacent to the mountain road, and is pictured in Figure 4.41. The source boulder appeared to be approximately 11.2 m in length and to have broken free from a formation of heavily weathered and fractured limestone located 91 m above the mountain road (Figure 4.42). Much of the limestone boulder exploded into gravel-sized fragments in the first 90 m of the rockfall. The remaining parts of the boulder broke in larger fragments while tumbling to the bottom of the valley. At the bottom of the valley, over ten large boulder fragments ranging in diameter from 0.8-2.9 m were observed to rest at the valley floor just 13 m from what appeared to be a small pump or power house (Figure 4.43). Amazingly, none of the boulders appeared to damage this small structure.



Figure 4.40. 3D model of the Valle di Panico rockfall.



Figure 4.41. Photograph of the largest observed boulder fragment in the Valle di Panico rockfall. The boulder measured approximately 3.0 meters in diameter.



Figure 4.42. 3D model of the source of the Valle di Panico rockfall, located 90 meters above the mountain road.

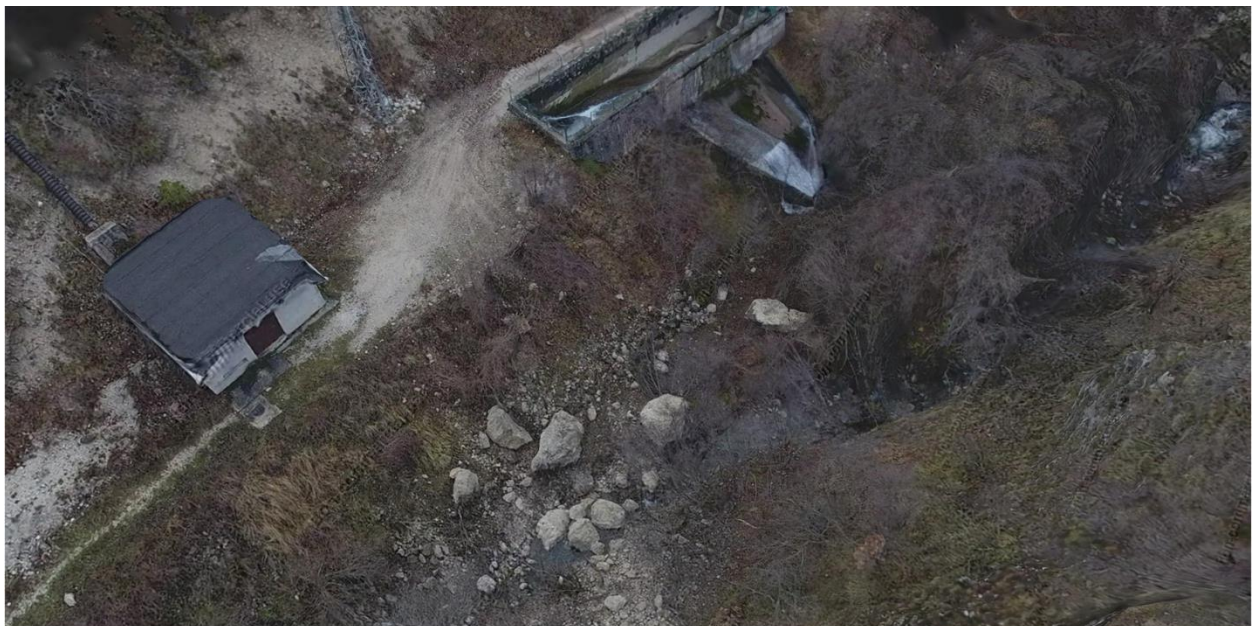


Figure 4.43. 3D model of the boulders and small power or pump house at the toe of the Valle di Panico rockfall.

4.2.6 Crognaleto Rockfall (Next to Cervaro Village)

The GEER team visited Teramo Province at the request of the provincial engineers who recorded a large rockfall near the village of Cervaro along road Via Treiste, a small mountain road that loops from highway SP45a through several hamlets north and east of Crognaleto to the Village of Cervaro. Figure 4.44 shows the location on the Via Treiste where we began reconnaissance

activities. Due to the steep terrain and the long distances involved in the runout of the boulders from this rockfall event, we relied primarily on UAV and LiDAR sensing technologies to collect data. The distance between rock source and final position is so large that the rock source is not actually captured in Figure 4.44. Figure 4.45 shows an orthophoto from the UAV SfM model developed from UAV imagery at the Cervaro rockfall. A LiDAR point cloud model was generated but is not shown here. The distance from the rock source to the final position of the last large boulder is approximately 530 m with an elevation change of 250 m. Just below the rock face, the slope is 31° until about mid slope, when a second massive limestone exposure face adds a 12 m vertical face. Below this mid-slope face, the slope flattens to 18° to 20°.

The Laga flysch formation outcrops extensively in the area and forms high and steep slopes. In the Crognaleto area the formation is characterized by a regular structural setting with sub-horizontal or gently-dipping bedding. The Sandstone (S) to Marl (M) ratio and bedding joint spacing are highly variable in the area, depending on their palaeo-environmental location. In both Crognaleto and Cervaro areas sandstones prevail and sequences with sandstone layers up to 10m thick and thin marly layers are rather frequent.

Observations conducted on several ledges indicate that spacing of vertical joints normal to the slope face (having tectonic origin) is high and can reach 8-9 m. From observation of rockslide scars left by failed blocks, spacing of joints parallel to the slope face is lower due to the superimposition of tectonic joints to fractures induced by stress-release and stiffness contrast between the sandstone layers and the underlying mudstone layers. As a consequence, block volume can easily reach tens of cubic meters. This value is definitely high if compared to that observed in other areas hit by the seismic sequence (i.e. Amatrice area). Usually persistence of vertical joints is sufficient to crosscut the whole sandstone layer. The lower spacing of joints parallel to the slope face produces tabular blocks which can fragment more easily thus reducing runout. Ledges with large blocks are often located at the crest of very high and steep slopes as in the two sites involved in the rockfalls so that blocks have high potential energy.

No evidence of major rockfalls were noticed in the subject region, near Cervaro village, after the 24 August and 26 October events. Nevertheless, these events may have loosened the rock mass, especially by weakening the sandstone-mudstone contact and decreasing block interlocking. Similarly, there is no evidence of rockfalls caused by the 2009 L'Aquila seismic sequence (29 km to the south). However, the finding of large old blocks at both sites indicates the two slopes have experienced past rockfalls. Neither site is marked in the official hazard maps (<http://autoritabacini.regione.abruzzo.it/index.php/carta-delle-pericolosita-pai>). Rainfall data recorded at Nerito Crognaleto station are reported in Figure 4.3c. Both daily rainfall and rainfall accumulated over one and two weeks were not appreciable prior to the 30 October event.

The rock source itself is an 8 m-thick massive arenaceous limestone exposure that sits at the top of the slope like a rim. The primary source area of the rockfall was measured using 3D point cloud models to be 8 m tall (the entire thickness of the exposure) and 10.5 m wide, and at least 3 m deep. Several other, smaller, source areas on the rim-rock exposure were identified and on

the mid-slope rock face. However, our data indicates that most of the boulders that reached near to the road came from the primary source area at the top of the slope. From the perspective of the Via Trieste, the photo in Figure 4.46 shows the mid-slope rock face and the source at the top of the slope from the rim-rock limestone exposure.

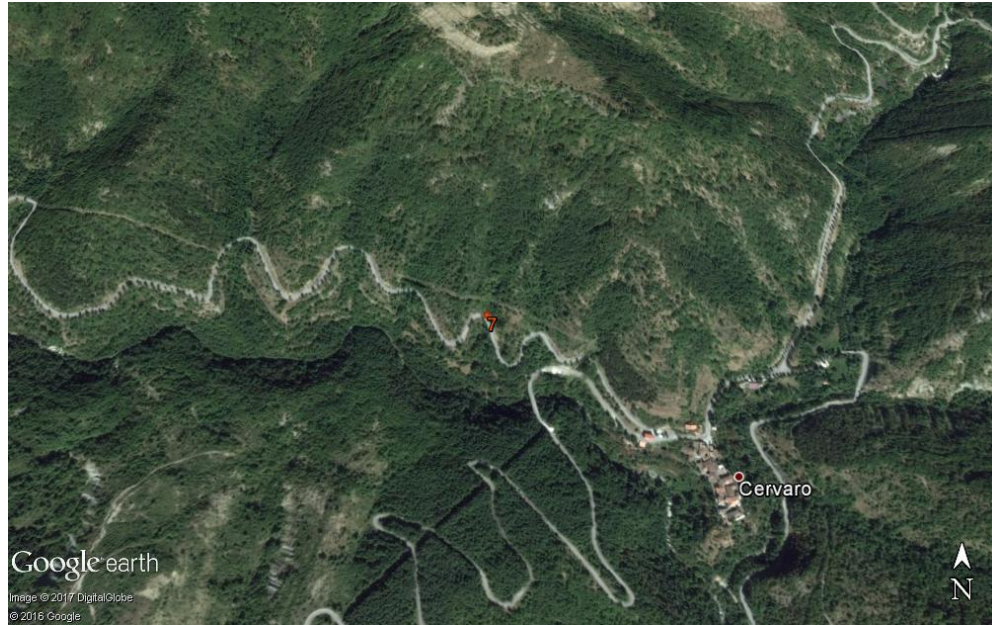


Figure 4.44. Location of rockfall site near Cervaro village (Crognaleto).



Figure 4.45. 3D SfM model of rockfall site near Cervaro village (Crognaleto). Primary rockfall source circled in yellow.



Figure 4.46. Source and runout chute of rockfall site near Cervaro village (Crognaleto) as seen from road at base of slope. Primary rock source circled in white.

Below the primary rock source, the large rock mass(es) followed the path of a drainage feature to the bottom of the slope just above the Via Trieste where the final large boulder came to rest. Figure 4.47 shows an overhead photo from the UAV with large boulder fragments identified. It may have been that the source rock was already fractured prior to the earthquake into 1 to 4 m blocks that dislodged. It may also be that the rock dislodged in one or two large masses that broke apart on the runout down the slope towards the road. The final boulder is 4 m and is shown in Figure 4.48, with a 1.7 m tall GEER team member next to the boulder for size perspective.



Figure 4.47. UAV aerial image of rockfall path from source at top of slope to the road at bottom of slope. Red circles show boulder fragments larger than 1.5m. Last boulder fragment from rockfall near road at base of slope is circled in orange.



Figure 4.48. Last boulder fragment (4 meter) from rockfall near road at base of slope. Also pictured are freshly toppled trees from the boulder’s roll to its final position.

4.2.7 Landslide near the village of Crognaleto

The GEER team visited Teramo Province at the request of provincial engineers who recorded a large rockfall near the village of Crognaleto along road SP45a north of Crognaleto. Large blocks detached from a 3.5 m thick sandstone seam located at an elevation of 1200 m a.s.l., i.e. about 100 m and 150 m above the upper and lower stretch of the SP45A motorway respectively, and 250 m above the valley bottom. The rockfall location is shown in Figure 4.49, about 0.5 km from the village. The road SP45a winds along the mountainside at about mid-slope. The rockfall occurred at the top of the slope and boulders ran-out across SP45a down the slope. At Site 7, the GEER team performed both LiDAR and UAV data collection of the rockfall. 3D point cloud models were developed from both datasets. Figure 4.50 presents the SfM model from UAV data.

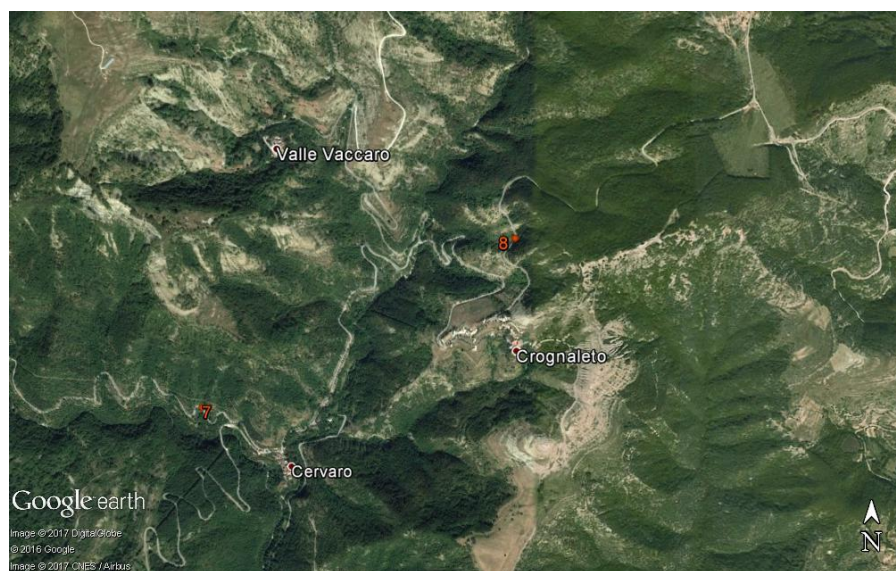


Figure 4.49. Location of rockfall site near Crognaleto village.

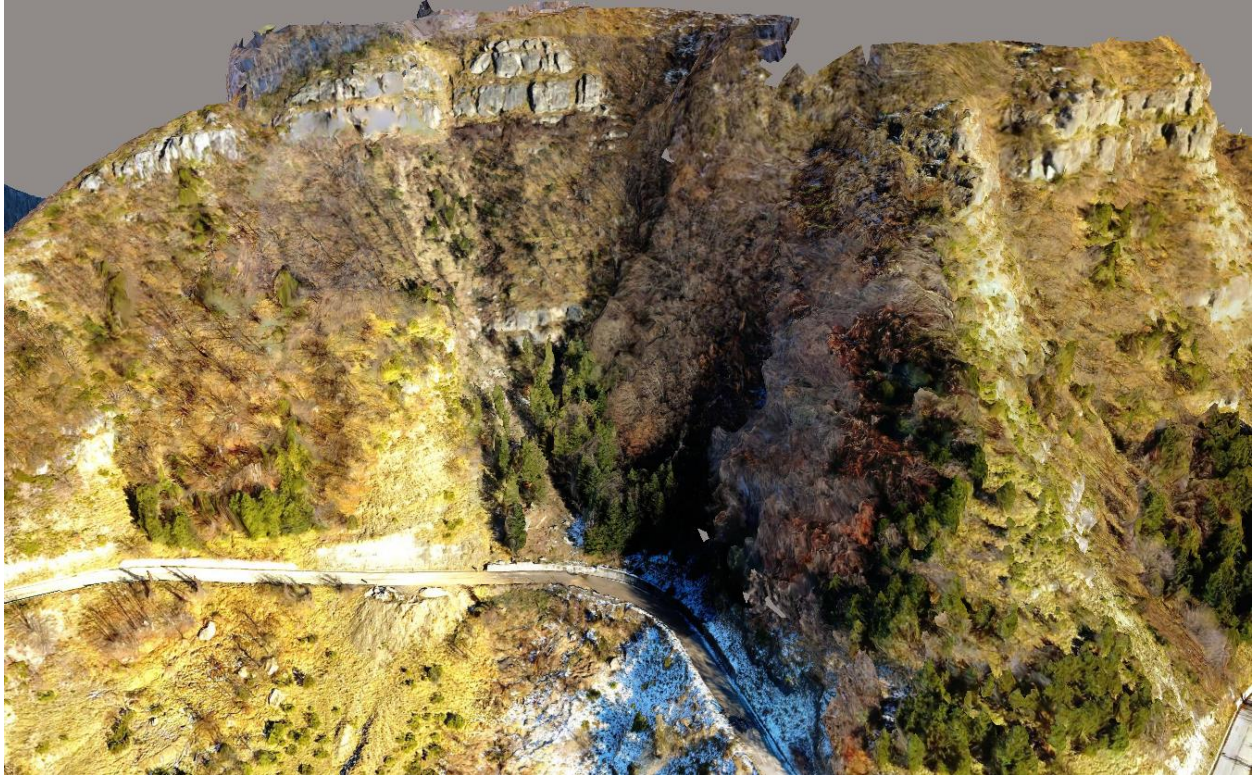


Figure 4.50. 3D SfM model from UAV imagery of the rockfall site near Crognaleto village.

We did not examine closely the rock source at the top of the slope due to the steepness of the terrain. However, mapped geology and observations of the boulders both indicate that the rock source is massive arenaceous limestone and limestone breccia. The rock in the boulders was very strong and hard. Boulders ranged from 1 to 3 m in size. The provincial highway officials had blasted apart and cleared several of the larger boulders off of the SP45a roadway, so our observations of some boulders are post-blasting. It is possible that several of the boulders may have been 6-8 m during the rockfall event. The rock source is a sheer face of two massive layers of rock at the top of the slope, each layer approximately 8 m thick. Below of the vertical faces, the slope is 30° to 34° and rises 84 m above SP45a. Below SP45a, the slope is approximately 20°.

One of the UAV images from the perspective of the top of the rock face looking down slope across SP45a to the bottom of the slope is shown in Figure 4.51. Several of the large boulders are indicated in the Figure below road SP45a. Several of these are “undisturbed” boulders that lay as they ended after runout, and several were pushed off of the road by local officials for safety precautions and to clear the road. The GEER team observed two large impact craters on the slope, indicative of high energy impact by large boulders, so at least two of the large boulders below the slope ran-out under their own energy during the rockfall event. The highway officials also had to clear the road of at least three large trees that rockfall boulders had toppled across the road.



Figure 4.51. UAV image of rockfall site near Crognaleto village from the source area at the top of slope looking down to road along runout chute. Note several large 1 to 3 meter boulder fragments in the drainage below the road (yellow circles).

The local highway officials also cleared 9 pre-cast concrete retaining wall blocks off of the road after the earthquake. These large pre-cast concrete retaining wall blocks can be seen in Figure 4.52. Each block is 75cmx100cmx200cm and has some small amount of internal steel reinforcement. Two small steel bars connect the blocks in the wall as shear pins. Concrete blocks not damaged appeared to be in good condition, with minor surface weathering but no cracking. The wall is formed by stacking the blocks with shear pins in place and a thin mortar. The retaining wall runs along SP45a for several hundred meters with no damage from strong ground shaking or dynamic lateral earth pressures. Only at the location of the rockfall and boulder run-out does that wall have any damage. At the location of the boulder runout, it is clear that the boulders impacted the back of the retaining wall, dislodged or shattered the top blocks, and then fell onto or over the road. Figure 4.53 is a photo taken from SP45a looking up the runout chute towards the top of the slope over the damaged wall. A number of boulders are seen in this photo, two of which are the remains of a larger boulder blasted by local officials due to an unsafe resting position. Other, older rockfall boulders can be seen in Figure 4.53 covered in vegetation. This

shows that the area has regular rockfall, and that strong ground shaking from the October 30, 2016 earthquake has merely accelerated the rate of rockfall at the site.



Figure 4.52. Damaged segmented concrete block retaining wall at roadway. Blocks that fell on road have been removed by local officials prior to visit from GEER team.



Figure 4.53. View upslope of damaged retaining wall, boulder fragments and runout chute from road at rockfall site near Crognaleto village.

4.2.8 Pescia Rockfall

During the August 2016 earthquake, the mountain slopes high above Via del Passero, just north of the town of Pescia, experienced rockfall (site 9a in Figure 4.54). The August 2016 earthquake GEER team visited Pescia and collected UAV based imagery and developed a SfM 3D model. During the 30 October 2016 earthquake, the mountain slopes experienced much more rockfall, so we visited Via del Passero and Pescia for a reappraisal of the rockfall. When we arrived at site 9a, the team also identified a larger landslide (a rock avalanche) at nearby site 9b. UAV flights were performed for both sites 9a and 9b. The 3D SfM model at site 9a serves as the reappraisal, while the 3D SfM model at site 9b is new data for the new landslide.

The August 2016 rockfall was relatively minor compared to that in October 2016. In August 2016, few boulders that detached from the rock face reached the Via del Passero roadway. In the 30 October 2016 earthquake, many boulders reached the roadway, with some large boulders reaching the valley floor and the stream below the road. The mountain slopes in the area have long been creeping under gravity loads (as seen in Figure 4.55), but when the GEER team visited the site, the team also observed displacements of the roadway embankment fills for Via del Passero. These slope displacements were not observed after the August 2016 earthquake.

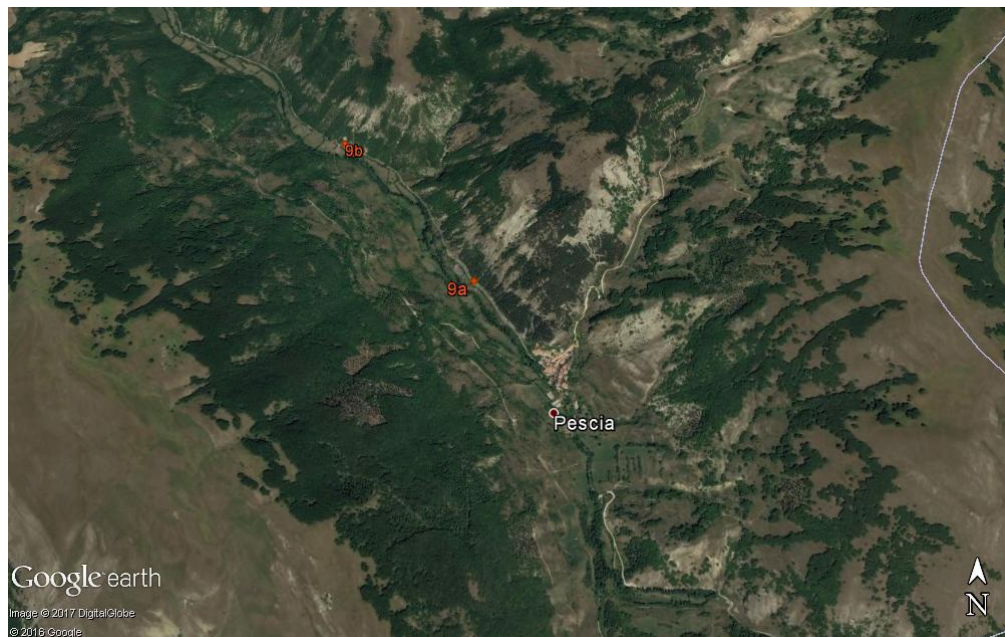


Figure 4.54. Location of Pescia rockfall sites.



Figure 4.55. Pescia rockfall. Possible soil slope creep shown by tree trunks. (site 9a).

The 3D SfM model for site 9a is shown in Figure 4.56, while an orthophoto of the rock face and source of the rockfall are shown in greater detail in Figure 4.57. The rock face is approximately 90 m wide and 60 m high. The rock material that composes the face is a combination of limestone, argillaceous limestone, and Marlstone. The GEER team climbed the slope above Via del Passero and examined the intact rock at the rock face. The GEER team determined that the rock was at times laminated and at times massive. The limestone tended to be massive (and produce large boulders), while the Marlstone and argillaceous limestone was laminated to thinly bedded. All of the rock species were moderately weathered. The limestone was strong and resisted a geologist's hammer, while the other species of rock crumbled under a blow from a geologic hammer, but could not be peeled via a pocketknife. The limestone was hard, while the other species were moderately hard. Discontinuities were narrow joints with little infilling and spaced widely. Our assessment of the intact rock are that the conditions are ideal for rockfall with boulders up to 2.5 m. Boulders of this size were indeed observed on the slope, on Via del Passero itself, and at the bottom of the slope. Indicated on Figure 4.56 are two boulders of at least 2.5 m that reached the valley floor below Via del Passero. Boulder diameters were measured by hand, and compare well with the measurements performed via 3D SfM models. The boulders encountered below the tree line, on the road, and on the valley floor were all limestone. Boulders above the tree line were mostly the argillaceous limestone and marlstone.



Figure 4.56. Pescia rockfall site 9a 3D SfM model from UAV data. Rock source and 2.5 meter boulders circled in yellow.

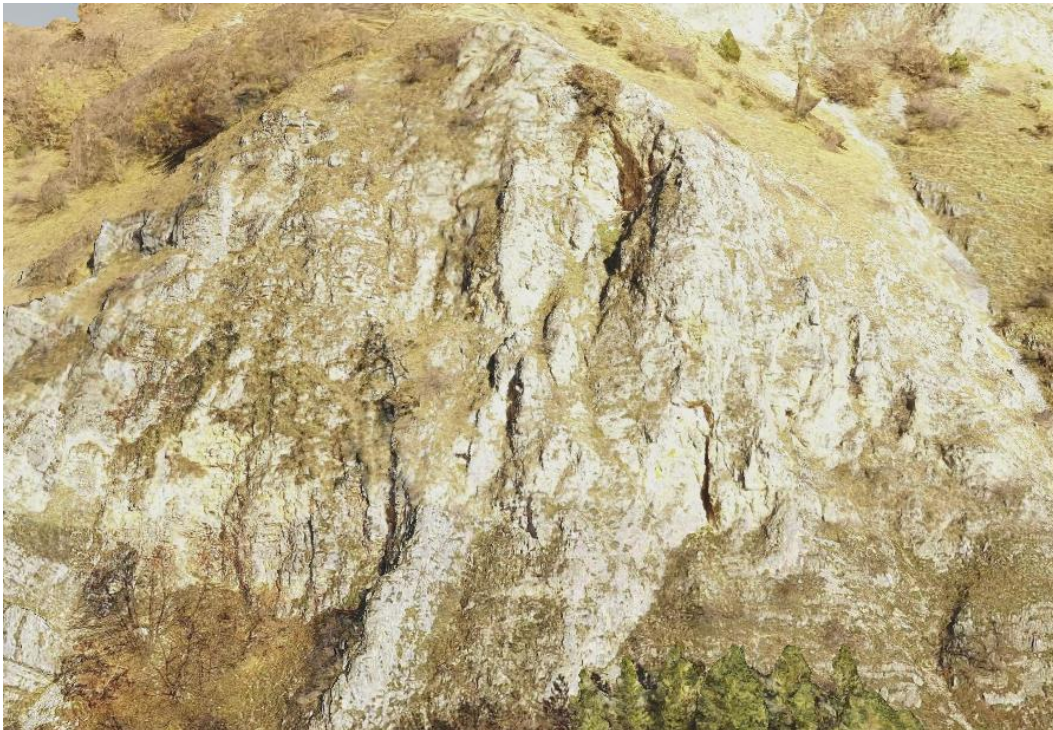


Figure 4.57. 3D SfM orthophoto of the rockfall source at site 9a.

Damage to the pavements occurred between Sites 9a and 9b from boulder impacts. Figure 4.58 shows one such example. This photo was taken directly up-slope of the large 2.5 m boulders

shown in Figure 4.56. Still visible in Figure 4.58 is a smaller 1 m limestone boulder and several smaller 150-250cm boulders. The pavement was heavily damaged from multiple boulder impacts at this and several other locations.



Figure 4.58. Damage to road from 1-2.5 m boulder impacts from rockfall between sites 9a and 9b.

The larger landslide that occurred during the 30 October 2016 earthquake at site 9b was a rock avalanche. The site is shown in Figure 4.59 using a 3D SfM model orthophoto developed from UAV imaging. The source rock face is massive but weathered and jointed limestone is at least 50 m high. The source of the rock avalanche itself is 16 m wide and 32 m high. The slope below the rock face varies from 28° to 32° and is around 57 m from the rock face to the road. A flat field and Via del Passero lay at the bottom of the slope. The source is shown in Figure 4.59 as the light colored part of the rock face. We did not climb the slope to perform a close-up assessment of the rock at Site 9b. However, the limestone boulders that travelled to the base of the slope and out into the field below Via del Passero indicate the geology and rock type. These boulders were 0.75-1.25 m. Figure 4.60 shows the perspective of the rock avalanche from the field, where the runout down the slope is seen through the trees.



Figure 4.59. Pescia rockfall site 9b. 3D SfM model from UAV data. Boulders that have rolled into field below the road are circled in yellow. Source is indicated by white circle.



Figure 4.60. Pescia rockfall site 9b. Source area at top with runout damage. Not pictured: runout boulders across road and into field, corresponding to approximate 30 degree Fahrboeschung angles.

4.2.9 Rockfalls/Landslides along SP134 Visso – Castelsantangelo

The slopes on both flanks of the Nera River valley in the section between Visso and Castelsantangelo experienced a number of slope failures. The epicenter of the 26 October event is near this area. Even though landslide events are reported in the inventory map of landslides (IFFI) none of the observed landslides were in areas characterized as having landslide hazard (PAI hazard maps).

Rock exposures within the valley are cretaceous units of the *Umbro-Marchigiana* succession, which are essentially limestones (*Maiolica* formation) and marly limestones (*Scaglia Rossa*, *Scaglia Bianca* and *Marne a Fucoidi* formations). All units are well stratified; bedding joints are spaced down to 0.1 m in the Scaglia rossa formation where they are often tight and cemented. The Maiolica is characterized by larger spacing but the bedding joints are more continuous and have higher loosening (weathering of material in the joints). The structural setting is rather regular and is controlled by relatively gentle folding with NW-SE oriented axes (i.e., parallel to the valley). Major failures/rockfalls occurred in the Maiolica limestone formation which form the lower part of the valley flanks along most of the considered valley stretch.

On both valley flanks failures have induced rockfalls or small rock avalanches that often reached the SP134 motorway and caused partial damming of the Nera River. Source areas are not always recognizable thus compromising knowledge of structure and lithology of the slope and hence failure mechanisms. However, a number of unstable slopes were well exposed and are described below.

Daily antecedent rainfall histories (cumulated over one and two weeks) recorded at Ponte Tavola meteo station, along the SP134 (Figure 4.3b) do not support the contribution of water pressures in the rock mass to failure triggering (Figure 4.61).

Two drone surveys were carried out: i) at km 3 of the SP134 (42.919°, 13.117°), where two landslides on opposite flanks of the valley face each other; ii) at km 4 (42.9095°, 13.1308°), where a rock slide on the right flank produced a large rockfall that crossed the motorway and the valley bottom below.

At km 3, a 23-m-high rock column consisting of regular sub-horizontal layers of *Maiolica* limestone experienced toppling of the prism cap (9 m high) and falls of blocks from the column walls and the cap itself (Fig. 4.61). The prism is isolated by very persistent joints belonging to two nearly-orthogonal sets, at about 45° with respect to the direction of the valley and its cap was intensely fractured and split in two parts by an opened joint before the 2016 seismic sequence.

UAV surveys (Figure 4.62) suggest that one half of the cap collapsed and the other was damaged as a consequence of the shaking. Similarly, a 4-m-high hanging wedge (center-left of Figure 4.62b) and a 5-m-high wedge high (upper-left in Figure 4.62b) failed along a bedding joints and slid along two vertical joints, respectively.

Drone surveys and pictures at high-zoom also indicate that fracturing of the rock mass is not homogeneous. The rock mass above the bedding joint at delimiting the cap bottom is more fractured. Similarly, the rock forming the cap and the cliff at its left is more fractured than the rock mass at the right of the cap.

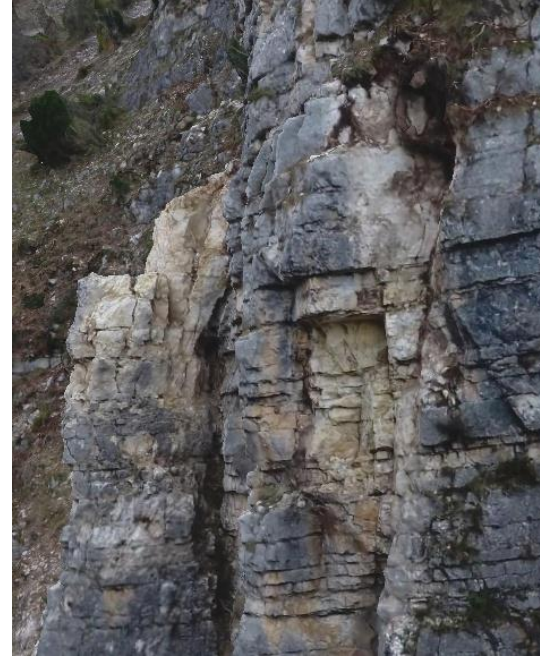
On the opposite valley flank a rock slide occurred at a height of about 100 m above the valley bottom and evolved into a small rock avalanche that fell into the Nera River (some blocks reached the opposite riverside). UAV drone surveys were instrumental in understanding landslide geometry, rock mass quality and failure mechanism. The oblique view in Figure 4.63a shows that the failed mass suffered intense fragmentation and eroded the slope with significant entraining of debris overlying the bedrock. Figure 4.63b indicates that sliding involved an intensely fractured wedge of Maiolica limestone delimited by two persistent joints.



Figure 4.61. Frontal view of the rock monolith at km 3 of SP134 motorway.



(a)



(b)

Figure 4.62. Lateral view from the drone of the rock column at km 3 of SP134 (right valley flank) (a). The left part of the column cap collapsed producing two small avalanches towards the column front and along the column free side. Scars left from two wedges on the adjacent cliff (b). Leftward tilting of the column cap is also visible in figure 4.61.



(a)



Figure 4.63. General oblique view of the rock slide and subsequent rock avalanche on the left flank of the Nera valley (km 3 of SP134 motorway) (a); detail of the detachment area (b). Images taken from the 3D model generated by BYU on the basis of drone surveys.

The left joint (observing the slide from the opposite flank) was a sub-vertical, persistent, relatively smooth and striated fault plane, whilst the right joint seems a relatively planar joint dipping at low angle toward the valley. It is not clear if the mechanism was planar or three-dimensional. The wedge is sector-shaped with a height of 19 m and maximum transversal dimensions of 8m and 4 m respectively.

A major failure occurred on the northeast flank of the valley at km 4 of SP 134 within the Maiolica limestone formation (Figure 4.64a). The subsequent rock avalanche invaded the motorway and the valley bottom below for a stretch of about 70 m with large blocks (Figure 4.64b and Figure 4.64c). The main slide scar, located on a rock spur, suggests that the slide was planar and occurred along a surface composed of a number of bedding joints dipping parallel to the slope. Bedding dip progressively increases from top to bottom of the slide scar (about 15°). The sliding surface is stepped both longitudinally and transversally (Figure 4.65a) due to well-spaced joints of two sets roughly striking parallel and normal to the slope. On the left side (viewing from the opposite, southwest, valley flank) the slide had no confinement. Bedding joints are relatively planar and smooth with apparent signs of weathering and oxidation (Figure 4.65b). Weathering seems to affect also the sub-vertical joints. The rock mass appears to be loosened and the rock material intensely fractured.

The height of the main slide scar is estimated from the 3D model as 20m. A layer of pervasively fractured rock below the main scar (Figure 4.66a), visible on close-range drone images, and the general ravinement of the lower half of the slope, suggest that the slide mass might extend downward and movement could be more complex. Apparent loosening of the rock mass, the pervasive fracturing of the rock at small scale (Figure 4.66b) indicate that the zone is tectonically disturbed and the slope underlying the slid rock spur was involved in the failure.

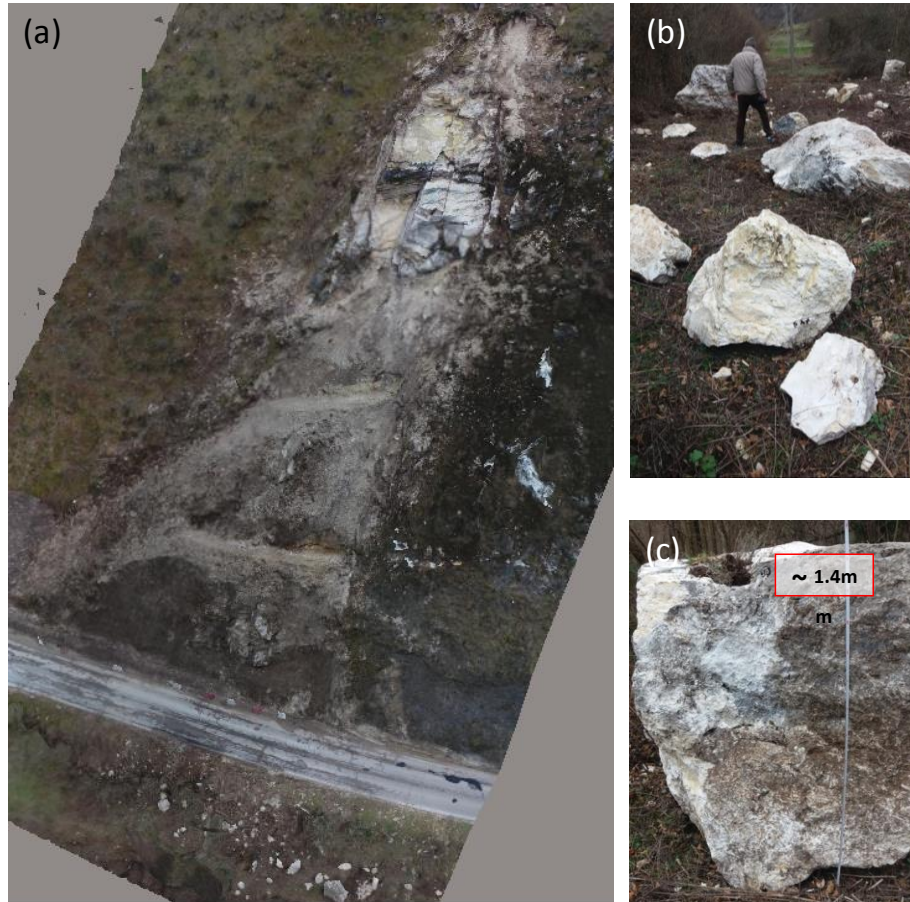


Figure 4.64. General oblique view from the drone of the rock slide on the right flank of the Nera valley (km 4 of SP134 motorway); the rock avalanche invaded the motorway and the valley bottom below for a stretch of about 70 m spreading large blocks (b-c).

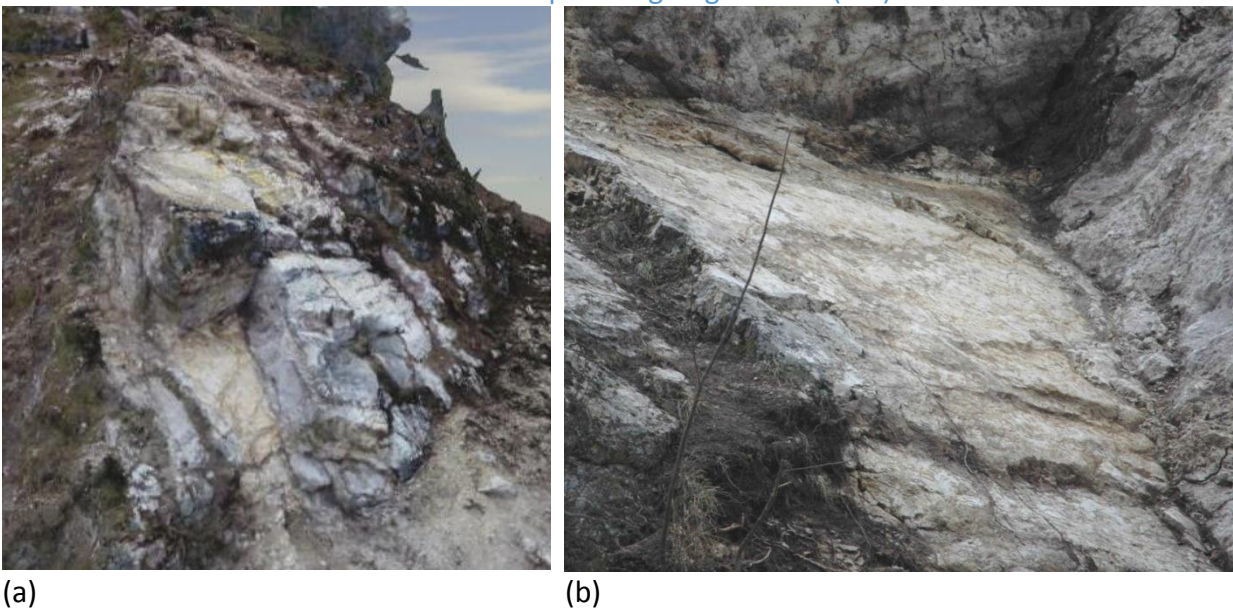


Figure 4.65. Close-range drone image of the detachment area (a) and detail of a bedding joint forming the sliding surface taken from the slide foot (b).

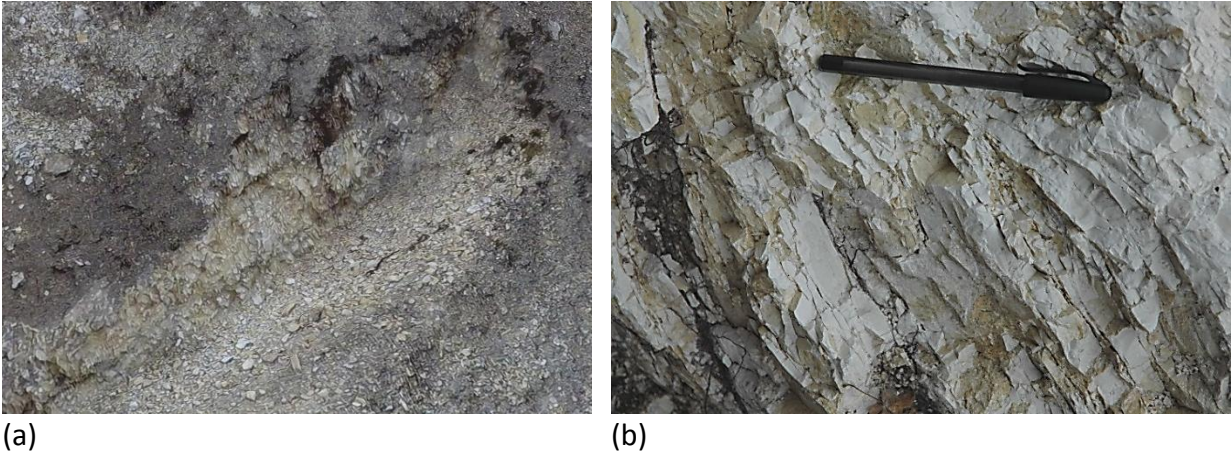


Figure 4.66. Drone image of a layer of cataclasized limestone located under the main slide scar(a) and detail of a pervasively fractured limestone block fallen from the slope (b).

4.2.10 Western flank of Mt. Vettore massif

During fault rupture mapping of the west face of the Mt Vettore Massif, we observed many fissures, cracks, and scarps not directly associated with the primary fault rupture trace along the side of the mountain. These fissures, cracks and scarps complicated fault offset mapping and required careful interpretation to ascertain which scarps were faulting and which were from slope instabilities. These additional fissures, cracks, and scarps were limited to the west face of the Massif. None of these were observed on the south face, above road SR477. Figure 4.67 shows the location of these slope instabilities on the Massif (point 11), while the location of road SR477 is shown in Figure 4.67 as point 19.

These features occurred on a steep slope (21° to 31° based on SfM 3D model and hand clinometer with isolated slopes steeper than 40°) on the west face of Mt. Vettore. We mapped the cracks, fissures, and scarps in detail in the area of fault crossing the footpath that climbs Mt. Vettore. The footpath provided excellent access for the team to the upper portions of the west face of the Massif. UAV imaging data was also collected in the area to assist in the interpretation of fault rupture scarps versus slope instabilities. Figure 4.68 shows an excerpt from the 3D SfM model derived from the UAV image data. The footpath is indicated Figure 4.68 along with the fault rupture surface (see Section 2.2), and a number of other fissures, cracks, and scarps that are roughly parallel to the fault trace, but are generally lower on the slope. Not all cracks and fissures are represented in Figure 4.68, but all scarps with vertical offset of at least 10cm are. In the area of Figure 4.68, there are few exposed rock outcrops. The fault tends to run along the base of rock outcrops and between those rock outcrops. Other fissures, cracks and scarps tended to be well away from rock outcrops in thick soil overburden or at the top of talus slopes. In thick, soft, soil overburden, minor slope instabilities have occurred, while in talus slopes the loose rock has compacted during shaking. Thin talus over thick soil overburden further complicates mapping and identification as thin talus tends to shift and distribute over fissures, cracks, and scarps in the underlying soil if the vertical offset is less than 20cm.

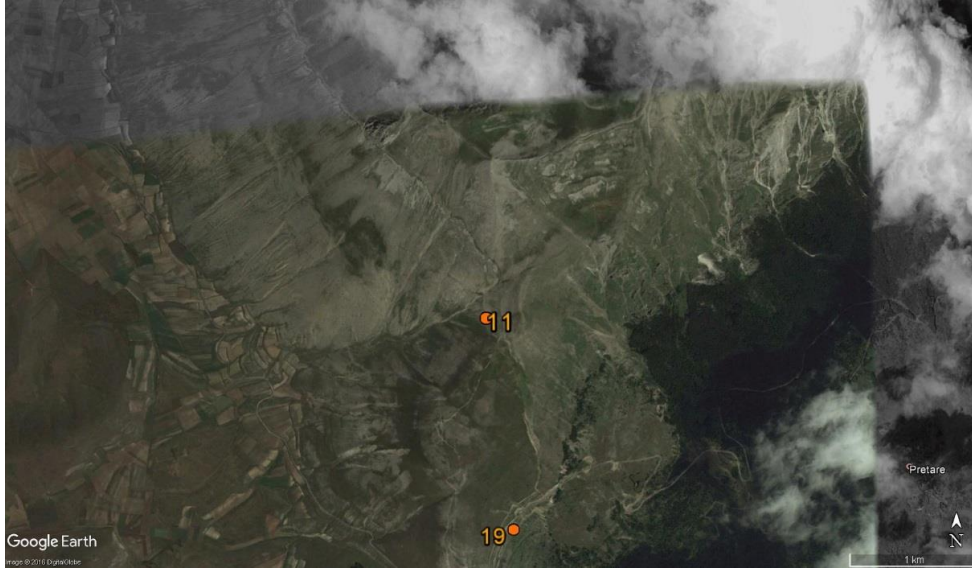


Figure 4.67. Satellite image of Mt. Vettore Massive showing fault alignment and slope displacement sites 11 and 19.

One means of identifying fault versus slope instability deformations or compaction of talus was lateral movement. Scarps with lateral (strike) offset were interpreted as related to the fault, while scarps with no lateral offset were interpreted as caused by slope instability or compaction of talus. Thus, two main factors were used to determine fault versus slope instability: 1) rock outcrop proximity and 2) lateral offset. When examining 3D SfM or LiDAR based point-cloud models, it is impossible to differentiate between the slope instabilities and fault movement since rock outcrops can be difficult to discern due to tall grass and low coniferous shrub vegetation and the inability to see lateral displacements over such a large area. Conventional field mapping thus still plays an important role in determining fault movements.

Figure 4.69 shows an image of the west flank of Mt. Vettore from the footpath. The fault can be seen as the linear feature that runs along the slope towards the large rock outcropping of Cima del Lago at the top left of the Massif in the image. Also seen are thick talus slopes below the fault. One of the key features that enables the distinction between faulting versus slope instability or talus compaction as the cause of the linear feature is the large fault offsets recorded at Cima del Lago. At Cima del Lago, limestone bedrock rises steeply to exposure at the surface. Below the limestone exposure is thick sediments without thick talus. At this location very few fissures, cracks, or scarps were identified aside from the fault trace. The only scarp lower on the slope at this location is the western trace of the Mt. Vettore fault, approximately half way down the face of the Massif to the Piano Grande plain below. No indications of slope instability, landsliding, or talus compaction were observed at Cima del Lago.

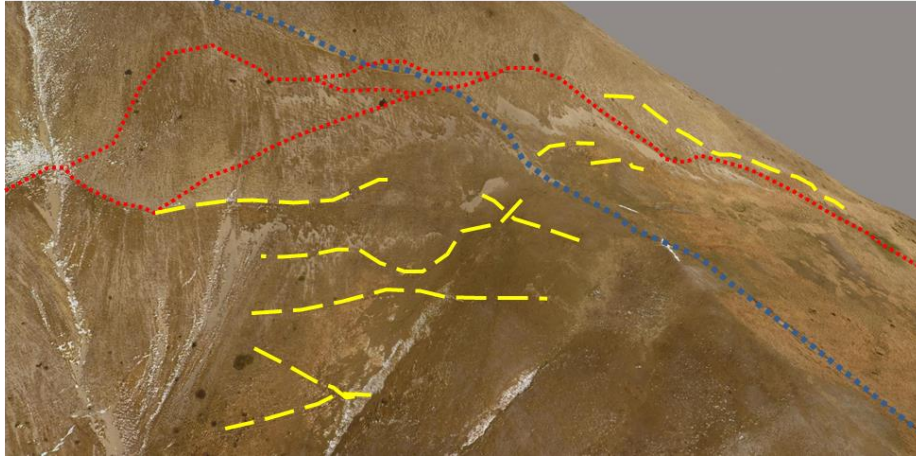


Figure 4.68. Excerpt from 3D SfM model from UAV data of the side of Mt. Vettore. The blue dashed line indicates the footpath. Red dashed line indicates scarps interpreted as the fault rupture trace(s). The yellow lines indicate scarps interpreted as minor slope instabilities. Looking from the west to the west face of Mt. Vettore. On the right of the image the slope descends on the south face towards road SR477.



Figure 4.69. View of the east slope of Mt. Vettore showing talus slopes and fault rupture trace. Fault rupture displacements and strong ground shaking have caused densification and sliding of talus.

In very steep areas of the west flank of the Mt. Vettore Massif, fault rupture and slope instability were occasionally present together. Figure 4.70 shows an example, where the fault offset is being measured but above and below of the fault, blocks of soil have displaced. In some instances, the blocks that tumbled across the fault making measurements of the fault offset impossible. The slope in Figure 4.70 was approximately 40°.



Figure 4.70. Image of fault scarp and associated nearby slope instabilities (yellow).

4.2.11 Rockfall SP 477 Arquata-Castelluccio (reappraisal)

Rockfall in a layered limestone unit occurred along the SP477 route between Castelluccio and Norcia (Figure 4.71), showering the road with large blocks. The rockfall was observed following the 24 August event and again after the October events. All of the rockfalls were apparently the result of isolated blocks of limestone that detached from the outcropping bedrock above the highway. As with the August event, most of these blocks came to rest on the road, but individual boulders crossed the highway and descended a steep ravine. A UAV phantom4 was used to fly the outcrop bridge (Figures 4.72-4.73). Maximum block run out distances were on the order of 375 m, descending a net elevation change of 190-210 m.

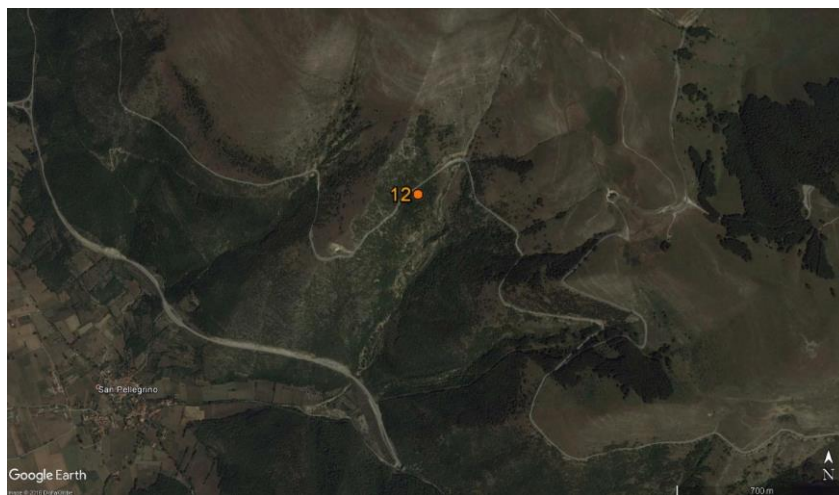


Figure 4.71. Location of the rockfall on road SP 477 between Arquata and Castelluccio.

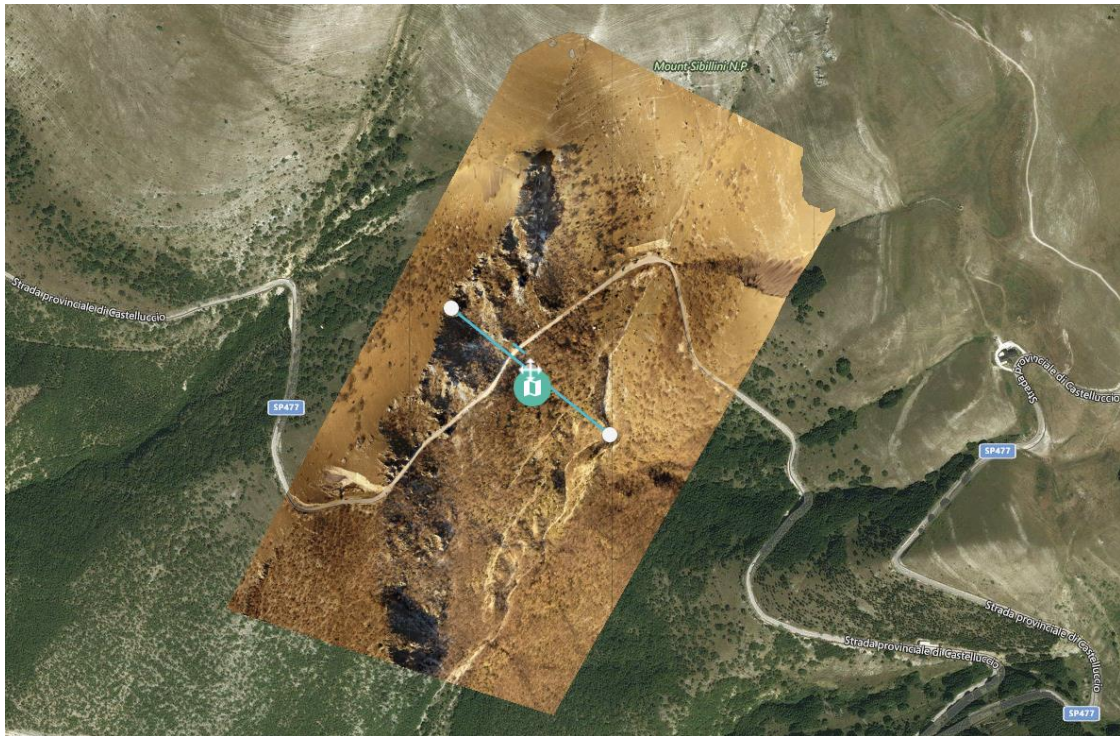


Figure 4.72. Overlay of the UAV orthomosaic on top of the Google Earth image of SP477, the Castelluccio-Norcia highway. Isolated boulders descended from the outcrop NE trending ridge on the left down to a ravine on the right side of the ortho mosaic, a maximum distance of approximately 375 m as indicated by the blue line. No other area along this highway had intense rockfall.

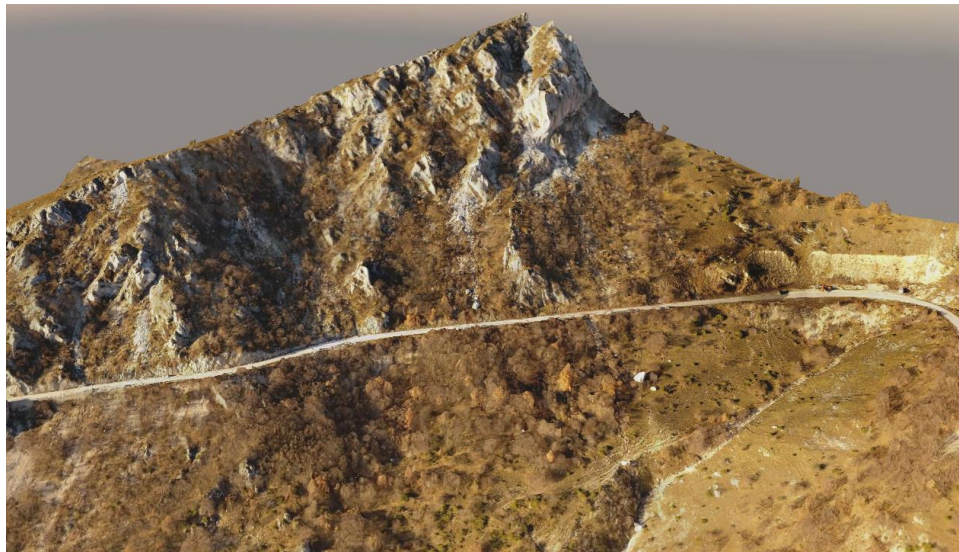


Figure 4.73. The most active area along Route SP 477 is below a large south facing ridge of limestone. The white areas near the top of the ridge are zones where fresh rock is exposed following collapse of blocks. This ortho mosaic is part of a three-dimensional model produced using a UAV phantom 4.

We performed a field reconnaissance along the SP 477 (indicated in Figure 4.71). During our visit (December 10, 2016), public vehicular movement along the road was not possible because of pavement fissures, embankment failures and rock obstructions. Indeed, several rock fall sites and mass movements along SP477 were observed between 42.776881N 13.143958E and 42.770243N 13.151854E. Roadway damage mainly consisted of cracks along the road, uneven track trails, edge barriers destroyed by rock falls, and damaged rock protection nets. Several boulders were unstably supported by vegetation on the steep mountain slopes. Due to steep slopes, most of the falls should have run down, however countable debris was still present on road pavement during our visit. Generally, boulder sized rocks were present in debris and the same sized were found in the unstably supported condition. A systematic overview of the various damage features is presented in Figures 4.74-4.79. Minor damage in culvert was observed across the road section. A telecommunication facility near the road pavement was found to be not damaged due to rockfall (see Figure 4.80).



Figure 4.74. Rockfalls with boulders on the road.



Figure 4.75. Rockfalls with boulders on the road.



Figure 4.76. Debris avalanche along the scarp of a previous landslide.



Figure 4.77. Debris and boulders captured by the rockfall protection nets.



Figure 4.78. Boulders supported by the vegetation.



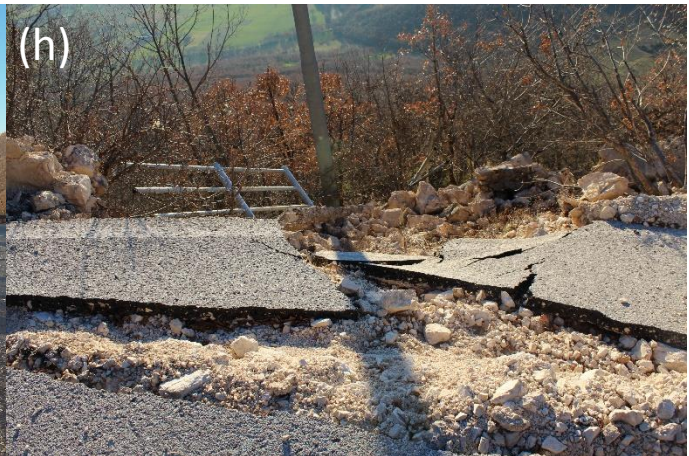


Figure 4.79. Fracture along the road, large vertical offset due to fracture and ultimate movement, damaged edge barriers and debris and boulders on the road surface.

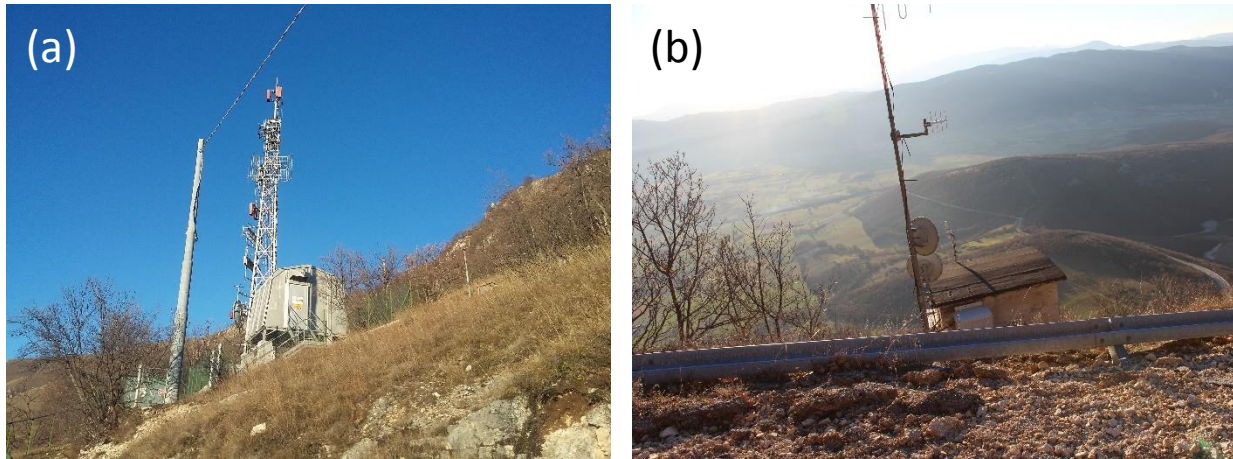


Figure 4.80. Telecommunication facility (a) over and (b) under the road.

4.3 Quick checks (Visual inspections)

4.3.1 Rockfalls in Pontechiusita along SP209

Along the provincial road SP209 between Triponzi and Visso southwest of the Nera landslide (Figure 4.81), we identify several evidences of rockfalls and debris-flows. This stretch of road runs along the Nera river. The geology of the area is characterized by the presence of scree inside the local carbonatic formations. The IFFI landslide inventory (Figure 4.1b) classifies this area as subjected to widespread rock falls and slumps.

Figure 4.82 shows some of the rockfalls in the calcareous formations located on the left bank of the Nera river that we have identified after the 30 October 2016 earthquake. Many blocks, having a volume ranging from a dozen of cubic centimeters to a few of cubic meters, have been found on the shoulder or across the road. At the time of our reconnaissance, slide debris remained on the road and the highway was still closed.

The area has been subjected to slump failures in the past. As a result, slope protections (i.e. rockfall nets, dynamic rockfall barriers or catch fences) are present along the road. Figure 4.83 shows many cases in which rock-nets have been passed over or damaged by boulders and rock-blocks. The slope located on the right bank of the Nera river has been interested by various slope instability events. They consisted of gravel debris. These features (Figure 4.84) are similar to those observed for the Nera landslide (Section 4.2.1) but very limited spatially and in volume.

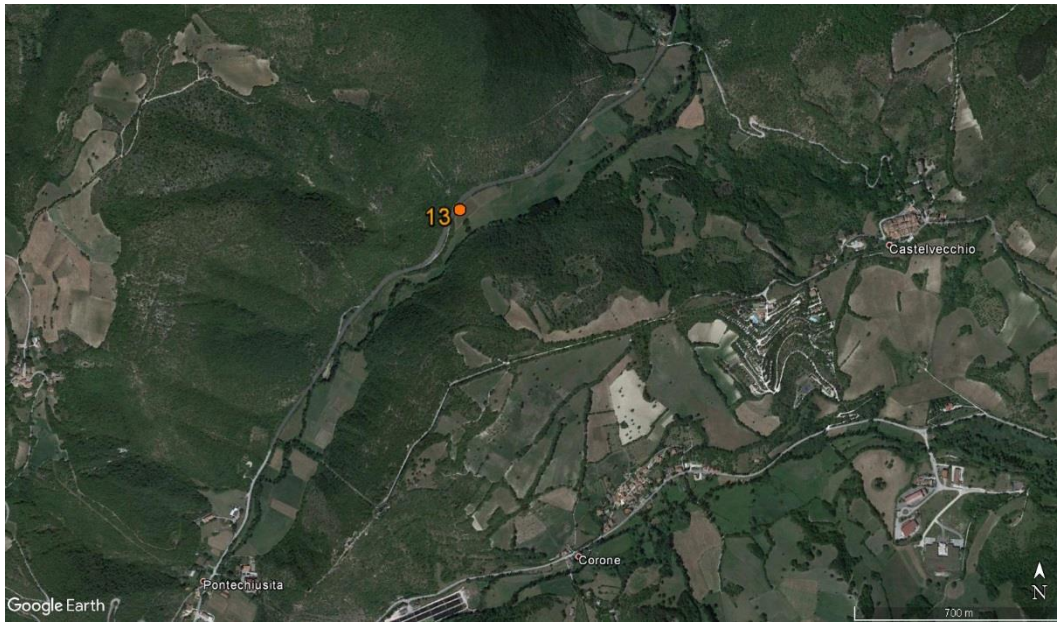


Figure 4.81. Location of the rockfalls in Pontechiusita along SP209.



Figure 4.82. Rockfalls along the SP209 between Triponzi and Visso.

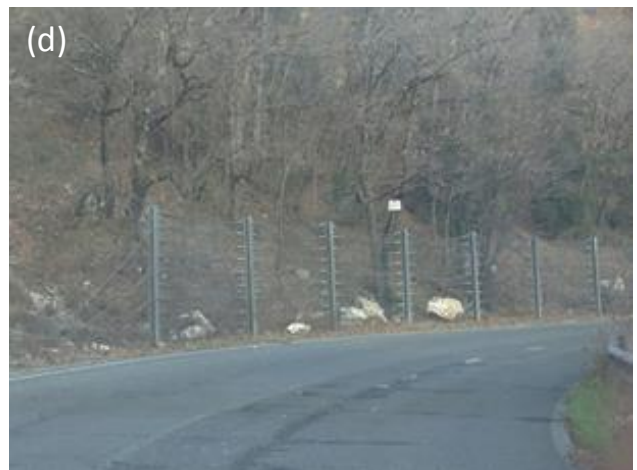


Figure 4.83. Slope protection damaged by boulders and rock-blocks.



Figure 4.84. Debris occurred on the right bank of the Nera river along SP209 (lat 42.9157N, lon 13.0456E).

4.3.2 Rockfalls between Piedipaterno and Cerreto

We observed several rock failures along the highway SS685 (also known as Tre Valli Umbre) between the villages of Piedipaterno and Borgo Cerreto (Figure 4.85). These features, shown in Figure 4.86, are mainly isolated rock falls having a volume ranging from a dozen of cubic centimeters to a few of cubic meters. The geology of the site is characterized by the presence of calcareous rock formations known as red flakes (*scaglia rossa*), and screes constituted by broken rock fragments variously sized. The IFFI landslide inventory (Figure 4.1b) classifies this area as subjected to widespread rock falls and slumps. We did not observe damages on the slope protections (i.e. rockfall nets, dynamic rockfall barriers or catch fences) present along the road.

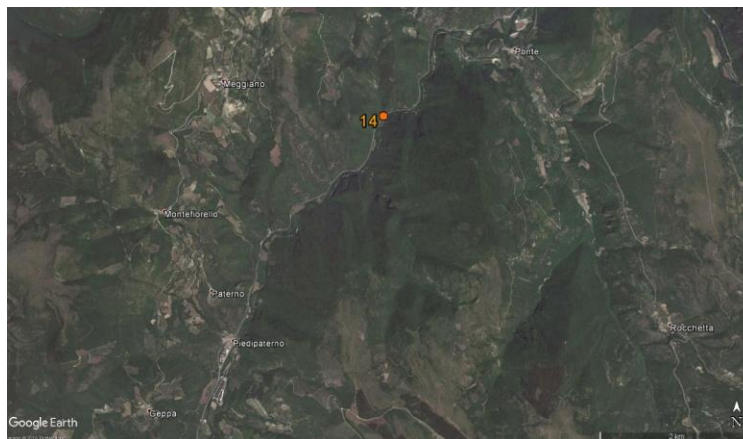


Figure 4.85. Location of the rockfalls between Piedipaterno and Cerreto along highway SS685.



Figure 4.86. Rockfalls between Piedipaterno and Cerreto along highway SS685.

4.3.3 Landslide along SP746 road between Cittareale and Norcia

Along the SP746 road between Cittareale and Norcia a localized landslide was observed (Figure 4.87). The landslide was located in the vicinity of the *Calcareous Breccia* failure site as reported by earlier GEER report (see GEER 2016). The landslide occurred in the carbonate sequence named Corniola as from the geological map of the Umbria region (<http://www.regione.umbria.it/paesaggio-urbanistica/cartografia-geologica-per-google-earth>). From a general inspection of the area, no damage to the road was observed however the debris from the road was already cleared during our visit (Figure 4.88) so that a minimum level of damage can be assigned. The overall mass movement was confined to ~50-70 m. Along the mass movement site, a retaining structure was present that appears to have limited damage. The wall itself was undamaged (Figure 4.89). Other nearby locations presented some rock falls although such rock falls were confined to rockfall protection nets and no road obstructions were observed (Figure 4.89). In case of absence of rockfall protection nets, debris including boulders were observed beside the pavement (Figure 4.89).

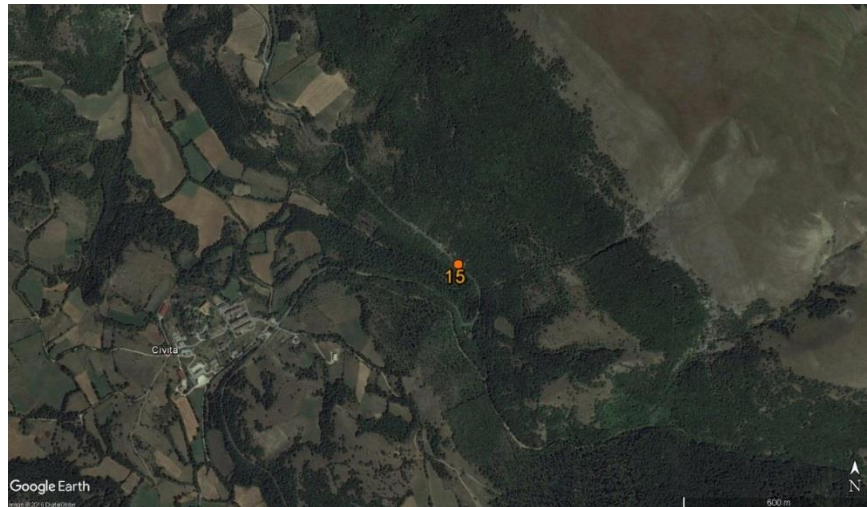


Figure 4.87. Location of the landslide between Cittareale and Norcia along the SP746.

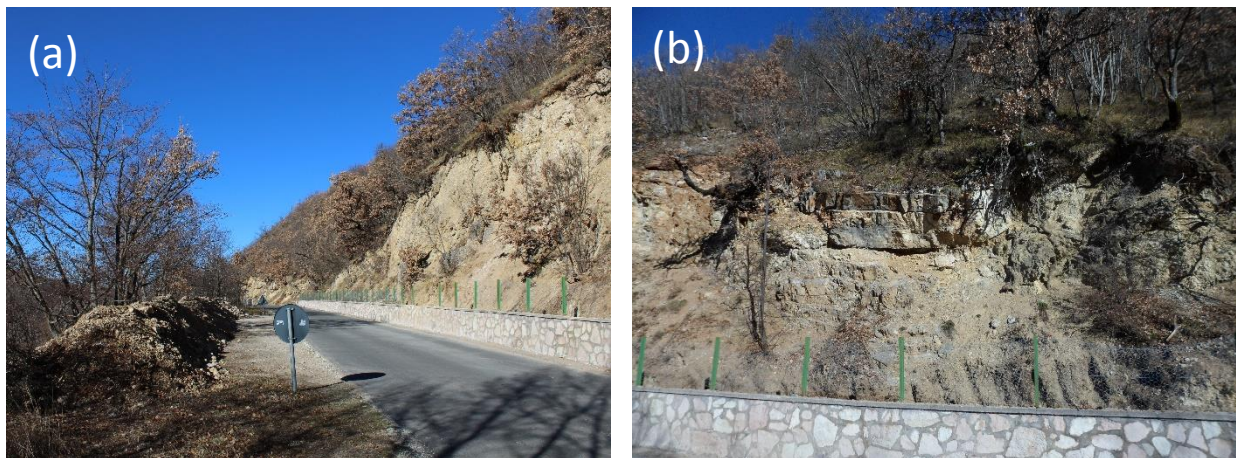


Figure 4.88. Landslide between Cittareale and Norcia along the SP746: (a) General view of the area; (b) Zoom on the crown and main body of the scarp.

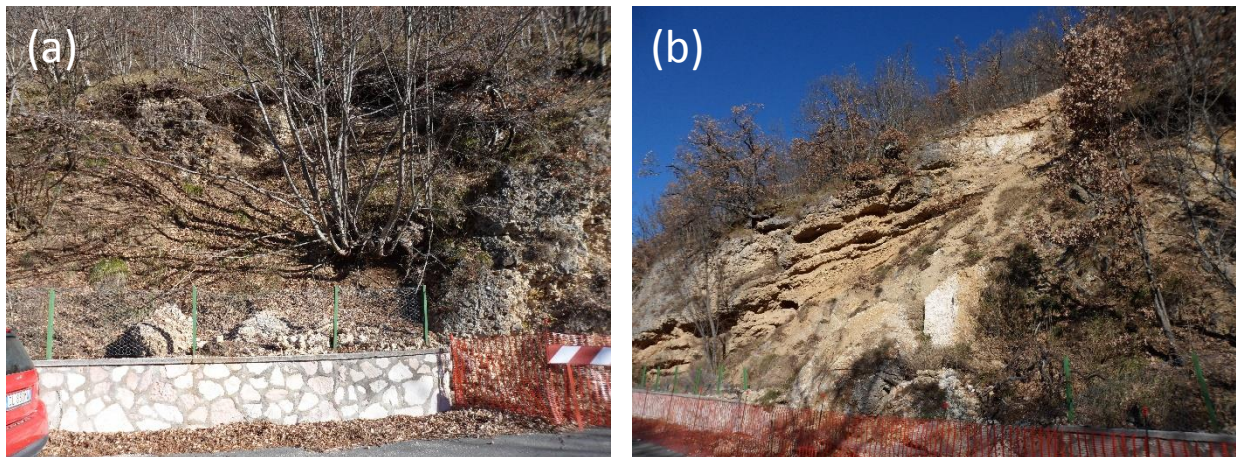




Figure 4.89. Failure in calcareous breccia between Cittareale and Norcia along the SP746: from (a) to (e) view of the all facade; (f) rockfall on the road.

4.3.4 Landslide along road Ortolano-Campotosto

We observed a shallow landslide along the road of Ortolano-Campotosto (Figure 4.90). Figure 4.91 shows the extension of this feature. Along the whole longitudinal extension of the landslide, there is a cut and fill road. The landslide has a spatial extension, along the road of 100 m, with observed maximum vertical offsets of 3-5 m. According to the official geologic map of Italy (sheet 139, 1:100,000 scale; http://193.206.192.231/carta_geologica_italia/tavoletta.php?foglio=139, last accessed April 29, 0217) and the ISPRA geologic map (sheet 349, 1:50,000 scale; http://www.isprambiente.gov.it/Media/carg/349_GRANSASSO/Foglio.html, last accessed April 29, 0217), the formation in this area comprises highly fractured sandstones and marly-clayey strata. The sandstone stratum, is buried by a weathered soil cover, which was affected by the observed landslide feature.

On the exposed surface of the landslide we observed silty clay with traces of sand, gravel, and cobbles. Figures 4.92-4.96 show several cracks on the road, fissures and minor scarps on the cut slope, and minor slide features on the fill slope. We did not observe major damages on the slope protections (i.e. rockfall nets) present along the road (Figure 4.97)



Figure 4.90. Location of the landslide along the road Ortolano-Campotosto.

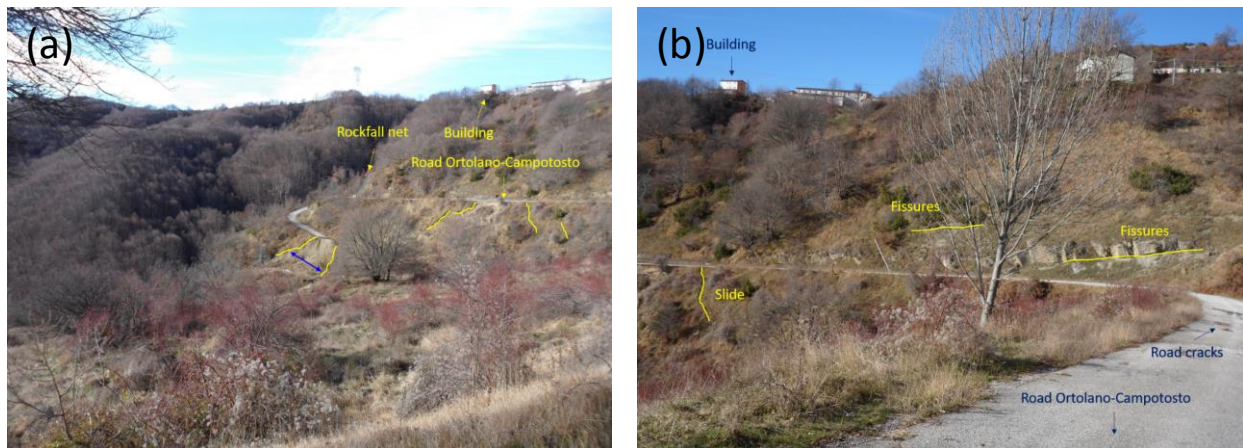


Figure 4.91. (a) Overview of the whole longitudinal extent of the landslide area; (b) close up view of the landslide-related features from the road Ortolano-Campotosto.

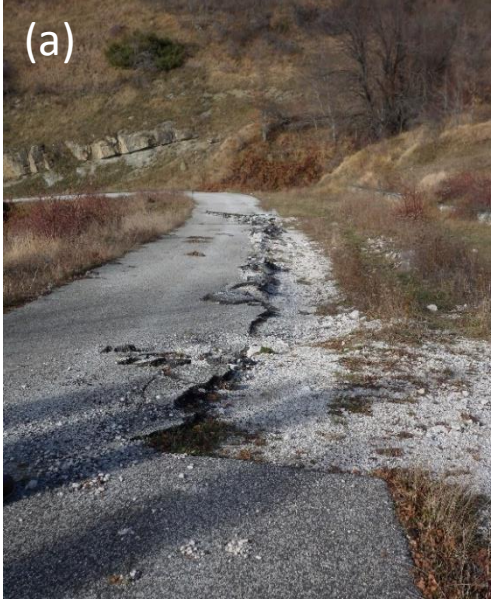


Figure 4.92. Cracks along the road.



Figure 4.93. A slide observed on the fill slope.

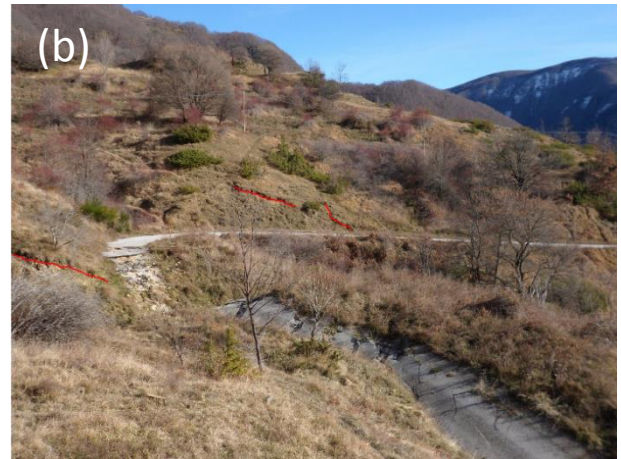


Figure 4.94. Fractures on the cut slope.

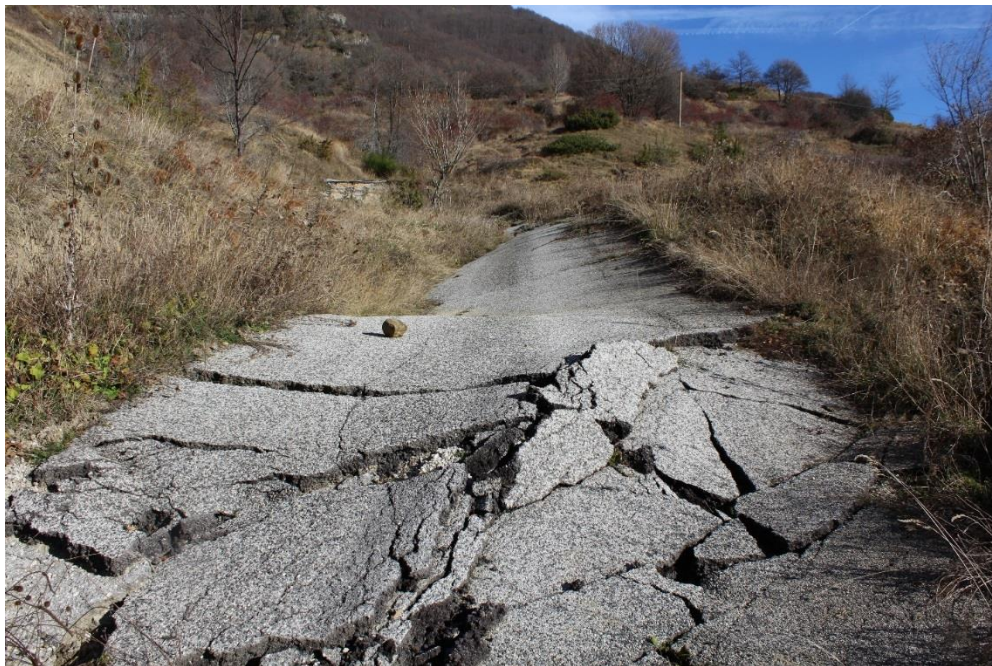


Figure 4.95. Damages along the road.



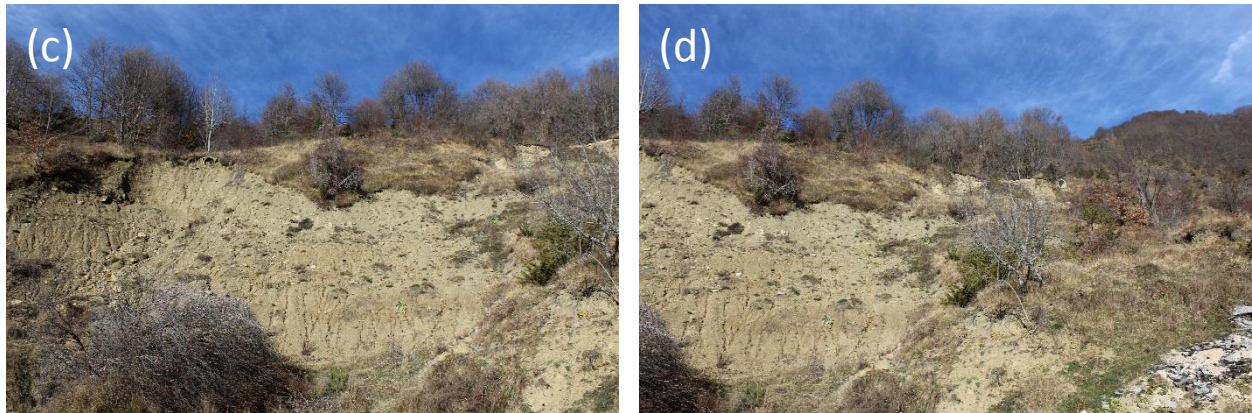


Figure 4.96. Minor scarps observed on the cut slope side of the road.



Figure 4.97. Rock-net protection with captured debris.

4.3.5 Rockfalls along SP476 (between Piedivalle and Preci)

We observed several rock failures along highway SP476 between the villages of Piedivalle and Preci (Figure 4.98). The geology of the area is characterized by alluvial deposits, and *scaglia* and *maiolica* limestones. The IFFI landslide inventory does not classify this area as susceptible to landslides. Between Piedivalle and Preci, along SP476 we have observed several minor rockfalls (Figure 4.99). At the time of the GEER reconnaissance mission the entire road had been cleared and was open to traffic. This road is important for post-earthquake emergency and post-emergency activities, because it is the only primary road that goes north of Norcia towards Preci and Visso. However, many secondary roads were still closed (Figure 99d). We did not observe

damage to slope protections (i.e. rockfall nets, dynamic rockfall barriers or catch fences) present along the road.



Figure 4.98. Location of the rockfalls along SP476 (between Piedivalle and Preci).

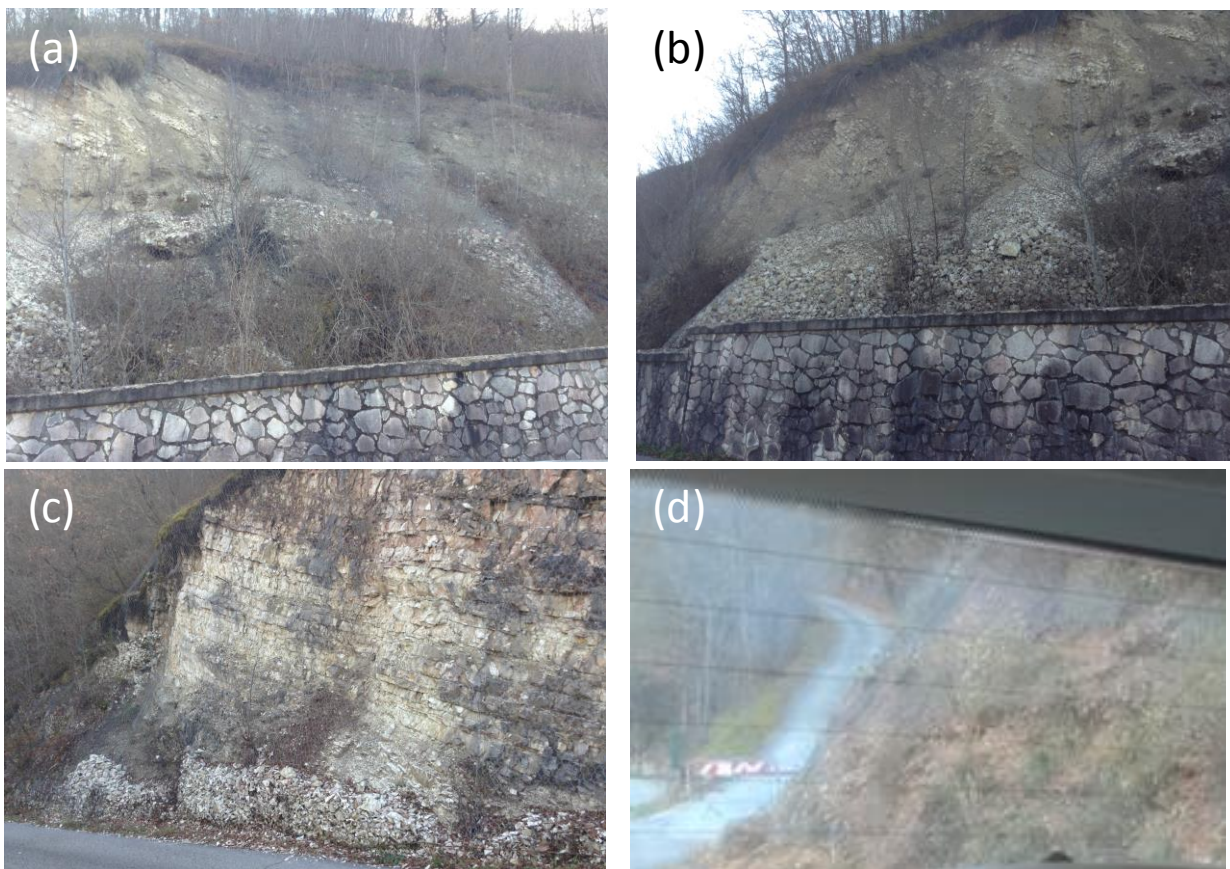


Figure 4.99. Observed rockfalls along SP476 (between Piedivalle and Preci).

4.3.6 Landslide below the village of Tino

While attempting to reach the landslides at Pescia, the GEER team tried to use a small road parallel to SS4 that winds through the foothills of Mt. Vettore. Soon after turning off of SS4, we found the road unpassable due to a landslide that followed the August 2016 and the 26 October 26 events. It is possible, however that this landslide was triggered by a Magnitude 5.0 aftershock

that occurred on November 30, 2017 as the landslide was not reported immediately after the October 30 earthquake. However, the road is small and only leads to villages indirectly so lack or reporting may have been simple omission. This small landslide occurred at the location of a heavily vegetated steep hillside where local highway officials have long had problems with minor rockfall. Rockfall netting had been installed in the exact area of the landslide some years prior and extends only a few meters beyond the extents of the landslide. Thus, the GEER team infers that the landslide occurred on a marginally stable slope. Figure 4.100 shows the location of the landslide and the small road. Main highway SS4 is located only a few hundred meters to the east across a thick wood and a small pond.

Figures 4.101 and 4.102 show the landslide. Several of the boulders from the landslide measured 2 m and appeared to be heavily weathered. Rock was limestone or dolomite (limited time at the site to assess rock type did not allow for more precise identification). Soil cover over the rock was thin (less than 30cm). The slide debris consisted of large amounts of vegetation, as would be expected given the heavy forestation of the slope. No seepage was observed at the bottom of the slide or within the slide mass. To the south and the north of the landslide the slopes are flatter (15° to 20°), while at the location of the slide, the inclination is approximately 34° as measured via a clinometer. Landslide width was estimated at 11 m.

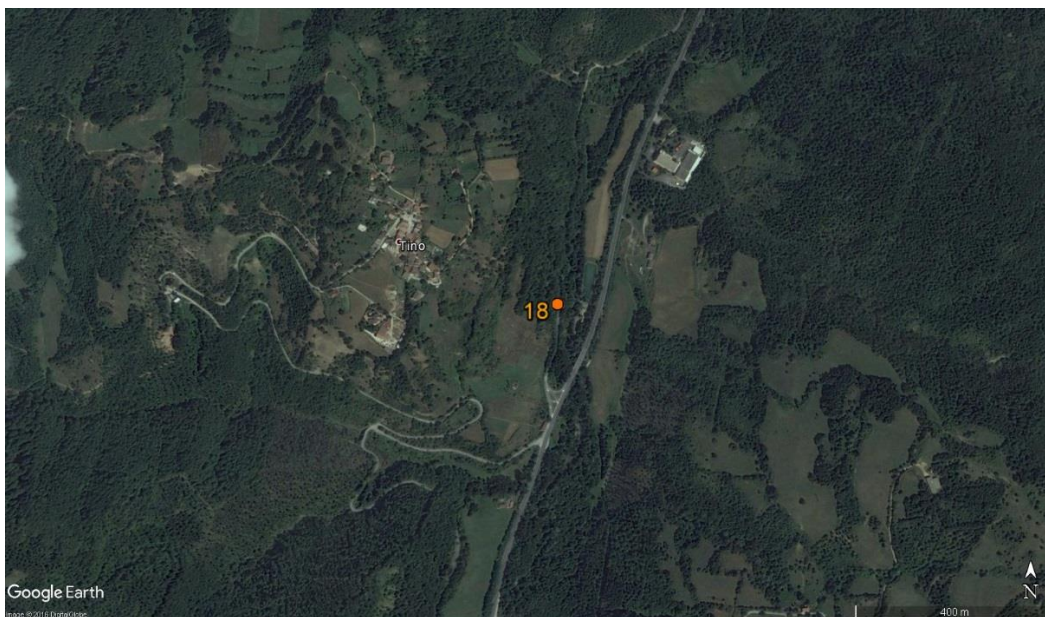


Figure 4.100. Location of the Landslide below the village of Tino on small road parallel to highway SS4.



Figure 4.101. Landslide debris covering the roadway. Boulders range in size up to 2 meters. Also pictured is rockfall netting used by local officials for minor rockfall control on the slope.



Figure 4.102. Landslide debris and head scarp. Also pictured is rockfall netting.

4.3.7 SP477 Road embankment fill damage

The fill embankment for Road SP477 running across the south face of Mt. Vettore was damaged in the 30 October event, occurring at the same location as the Mt. Vettore fault surface rupture (Figures 4.103 and 4.104). No reports of slope instability at this location were made following the 24 August event nor the 26 October event. Road embankment damage was parallel to the roadway, in the direction of the slope.

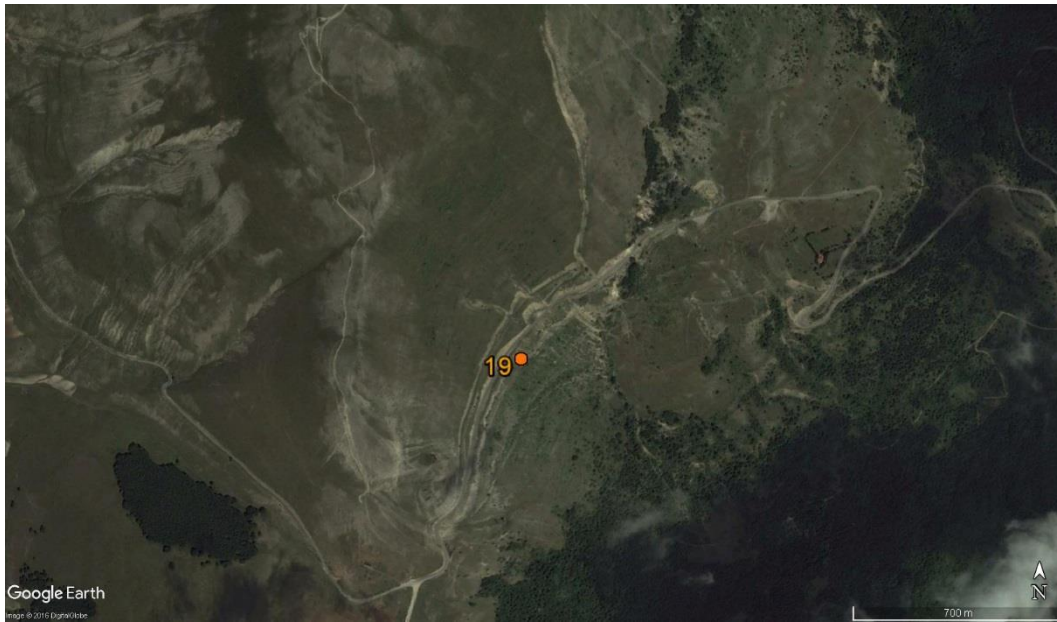


Figure 4.103. Location embankment fill damage area next to fault trace zone along SP477 road, Mt Vettore.



Figure 4.104. 3D SfM model of embankment fill damage area next to fault trace zone along SP477 road, Mt Vettore. Fill that has experienced 15 to 20cm lateral displacement circled in yellow. Observed fault rupture trace shown in red.

We visited the fault rupture and observed the embankment slope damage after documenting surface fault rupture offset. At the location of the SP477 road, strike displacements on the Mt. Vettore fault (in the direction of the embankment displacement down slope) were observed to be zero. Therefore, the GEER team concluded that the roadway embankment damage was from slope displacements rather than lateral fault rupture. Lateral displacement of the slope was estimated at 15cm to 20cm. Cracking parallel to the road along the top of the embankment is seen in Figures 4.105 and 4.106. The total height of the embankment slope was measured at 25-35 m from 3D SfM model (Chapter 2) for the south face of Mt. Vettore. The embankment fill

slope is approximately 20° to 30°, while the slope of Mt. Vettore near the embankment fill is 15° to 20°. Slopes were also measured from 3D SfM model for the location. Embankment material appeared to be a compacted mixture of low plasticity clay soil, granular native limestone aggregates and chert fragments from roadway construction.



Figure 4.105. Road embankment damage along SP477 road, Mt Vettore (Location 19, viewing North). Note fault trace across road and black (new) bitumen repairs following previous (24 August 2016) earthquake.



Figure 4.106. Road embankment damage along SP477 road, Mt Vettore (Location 19, viewing west).

5 Mud Volcanoes

Ernesto Ausilio, Roberto Cairo, Maria Giovanna Durante, Giuseppe Lanzo, Paolo Zimmaro

5.1. Initial Report and Field Reconnaissance

Mud volcanoes are a typical expression of sedimentary volcanism, usually associated with thick overpressured sequences (i.e. pore fluid pressure exceeds the hydrostatic pressure). Argillaceous sediments are often the source of the ejected material (Yassir, 1989). Mud volcanoes typically emit saline waters and hydrocarbons. Erupted water is usually alkaline with pH values ranging between 5-9 (Yassir, 1989; and references therein). Overpressure buildup mechanisms include, but are not limited to, sedimentary or tectonic loading, deep fluid migration, and aquathermal processes. Overpressured fluids typically flow along morphological discontinuities or geological structures such as fault planes, anticline axes, or preexisting deformations (Mazzini, 2009). As a result, mud volcanoes are usually present in active tectonic areas, and they are often triggered by large earthquakes (e.g. Manga and Brodsky, 2006; Mellors et al., 2007; Manga et al., 2009). Manga et al. (2009) show that pre-existing mud volcanoes are more sensitive to earthquakes than quiescent systems. Mud volcanoes play a critical role in natural ecosystems as they contribute to the global atmospheric methane budget (Etioppe and Milkov, 2004; Kopf, 2003).

To establish whether an eruption is triggered by an earthquake, several authors proposed various methodologies based on empirical time- or space-windows. Linde and Sacks (1998) and Mellors et al. (2007) define an eruption as earthquake-triggered if it occurs within ~ 100 km of the epicenter of large earthquakes ($M > 5.5$). Manga et al. (2009) consider, as earthquake-triggered eruptions occurred within 2 days from the earthquake event, using data compiled by Bonini (2009).

After the **M6.5** 30 October 2016 earthquake, new eruptions were detected at Monteleone di Fermo and Santa Vittoria in Matenano, in the province of Fermo (Marche region). Figure 5.1 shows the location of the observed mud volcanoes in the villages of Monteleone di Fermo and Santa Vittoria in Matenano (located 38 and 44 km, respectively, from the epicenter of the **M6.5** 30 October 2016 earthquake). The first organization to investigate these phenomena and to release a report on the subject was INGV on 3 November 2016 (<https://ingvterremoti.wordpress.com/2016/11/11/sequenza-sismica-in-italia-centrale-i-vulcanelli-di-fango-in-provincia-di-fermo/>, last accessed 23 March, 2017; hereafter INGV, 2016). On the basis of this prior research, the GEER reconnaissance team visited the area, providing further documentation and testing of the phenomenon.

5.2. Mud Volcanoes in Monteleone di Fermo

The village of Monteleone di Fermo is known as the *Land of Mud Volcanoes* as they are a regularly occurring phenomenon. Figure 5.2 shows a tour sign located in the area of Santa

Maria in Paganico in the town of Monteleone di Fermo. There are six mud volcanoes located along the Ete Vivo river. The mud volcanoes located in Monteleone di Fermo are induced by the emission of pressurized gas coming from underground deposits of organic material, natural gas, and hydrocarbons.

We inspected two mud volcanoes that erupted within one day from the **M6.5** 30 October earthquake event (Figure 5.3): (1) Santa Maria in Paganico (Figures 5.4a-b) and (2) Valle Corvone (Figures 5.4c-d-e-f). In both cases, we observed fresh deposits of ejected material. Both eruptions, are located within 45 km from the epicenter. . During our reconnaissance activities, both mud volcanoes showed a reduced activity, with a small emission of water. We inspected the sites about one month after the INGV reconnaissance mission. We did not detect any new activity or variations in the soil surface conditions in the inspected area as shown in Figure 5.5. As shown in Figure 5.4c-d-e-f, the material erupted by the mud volcano located in Valle Corvone covered a wide area involving both the river and the pavement of the road. This mud volcano is characterized by radial fractures 140 cm long, 38 cm wide and 80 cm deep. This eruption partially blocked the Ete river's course (Figure 5.4f).

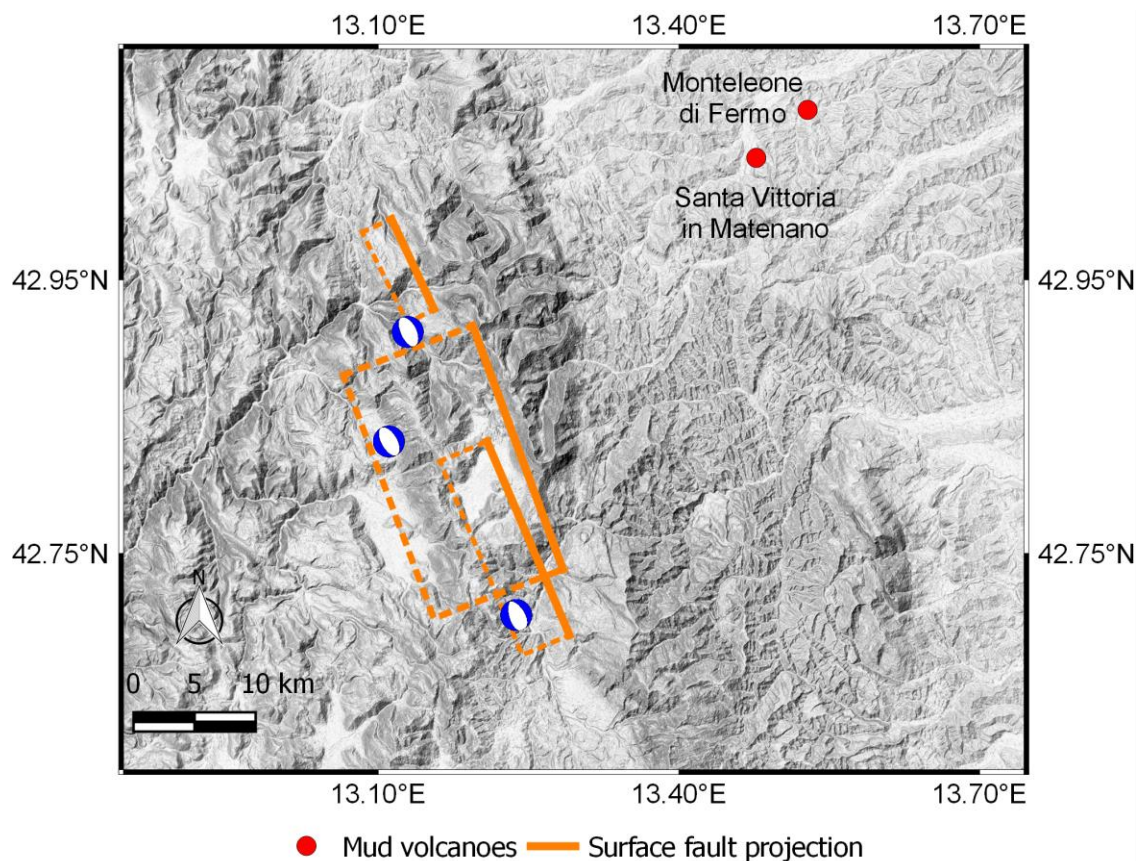


Figure 5.1. Location of the observed mud volcanoes.



Figure 5.2. Tour sign indicating mud volcanoes sited in Monteleone di Fermo.

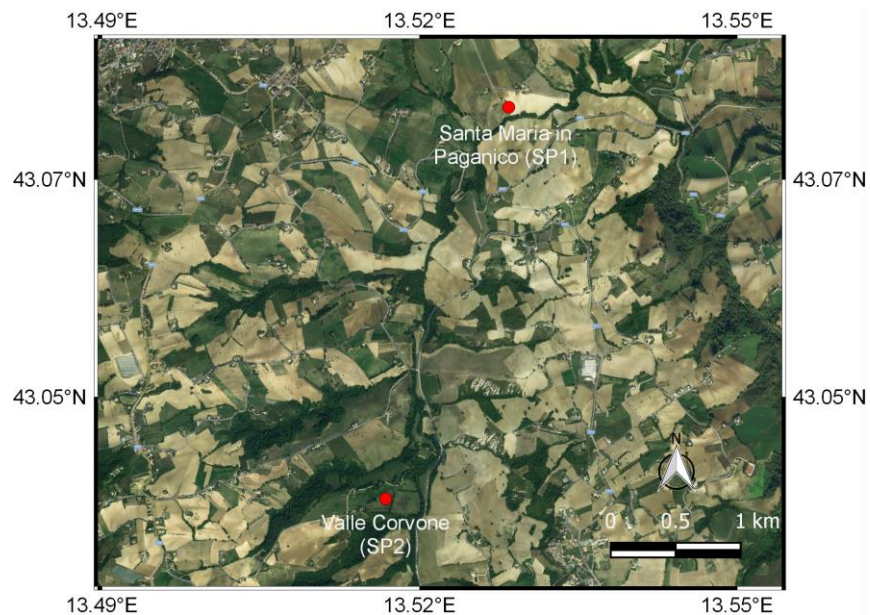


Figure 5.3. Location of the observed mud volcanoes in Monteleone di Fermo.

Figure 5.4b shows the sampling activities performed in Santa Maria in Paganico. We sampled soil and water erupted from the volcano in Santa Maria in Paganico (SP1), and soil in Valle Corvone (SP2). Both samples were taken on 13 December, 2016. We performed conductivity, alkalinity, and chemical analyses on the water erupted from the volcano in Santa Maria in Paganico (SP1); sieve analysis, along with Atterberg limits on soil ejected by both volcanoes (SP1 and SP2). The erupted water presents a value of conductivity of $791 \mu\text{S}/\text{cm}$ and a pH of 7.97. Moreover, the chemical analysis revealed the presence of potassium (K^+), sodium (Na^+) e magnesium (Mg^{2+}). The water appears to be slightly alkaline and with the presence of alkaline-earth materials. No metal elements have been found. These values are consistent with typical ranges observed in other mud volcanoes globally.

Figure 5.6 shows the particle size distribution for samples SP1 (Santa Maria in Paganico) and SP2 (Valle Corvone). The soil in sample SP1 is constituted of 57.4% brown silt, 31.6% clay and 11.0% sand. The fine-grained soil exhibits a liquid limit $LL = 47.5\%$, a plastic limit $PL = 17.8\%$, and a plasticity index $PI = 29.7\%$. The plasticity chart (Figure 5.7a), shows that the soil of sample SP1 can be classified as inorganic clay (CL) or organic silts and clays of low plasticity (OL). For SP1, the activity of clay is 0.94 and is therefore defined as normal (Figure 5.7b). The values of the Atterberg limits are representative of clayey soils for SP1. For SP2, the silt fraction is 66.2%, the sand fraction is 23.7%, and the clay fraction is 10.1%. The Atterberg limits for SP2 are $LL = 30.7\%$, $PL = 18.7\%$, the plasticity index is equal to 11.9% and the fine-grained soil can be classified as inorganic clay (CL) or organic silts and clays of low plasticity (OL). The activity of clay for SP2 is normal (Fig. 5.7b). The Atterberg limits for SP2 are typical of silty soils





Figure 5.4. (a) overview of the mud volcano in Santa Maria in Paganico; (b) sampling activities in in Santa Maria in Paganico; (c) crack originated by the mud volcano in Valle Corvone, (d) mud volcano in Valle Corvone, (e) details of a crack in Valle Corvone, (f) close-up view of the material ejected in the Ete Vivo river (Valle Corvone).

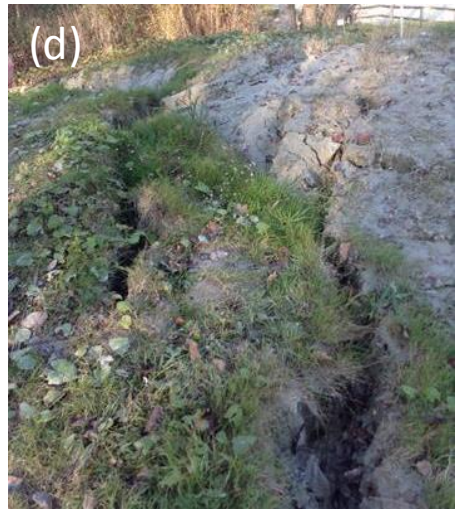
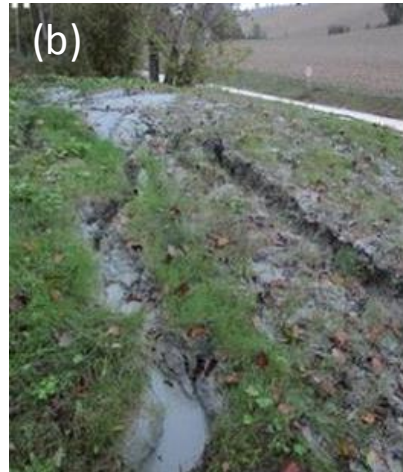


Figure 5.5. (a) and (b) photos of the mud volcano in Valle Corvone taken by INGV in November 2016 (INGV, 2016); (c) and (d) photos of the mud volcano in Valle Corvone taken from a common perspective by GEER in December 2016.

5.3. Mud Volcanoes in Santa Vittoria in Matenano

The nearby location of Santa Vittoria in Matenano presented both reactivation of a mud volcano formed 15 years ago and since dormant, as well as newly-formed mud volcanoes. Two volcanoes formed in Contrada San Salvatore, the flow of which covered a wide area and produced large deformations of the neighboring soil. INGV (2016) reconnaissance immediately following the event pointed out the level of carbon dioxide emission from the soil to be within normal ranges. Low temperatures were measured; which is a characteristic feature of the phenomenon.

We inspected the newly formed volcano that erupted within one day from the **M6.5** 30 October earthquake event. Figure 5.8 shows the location of this eruption. Figure 5.9 shows photos taken during our reconnaissance. During our reconnaissance activities, the eruption showed a reduced activity, with a small emission of water. We inspected the site about one month after the INGV reconnaissance mission. We observed a substantial increase in the erupted material compared to the INGV reconnaissance (Figure 5.9).

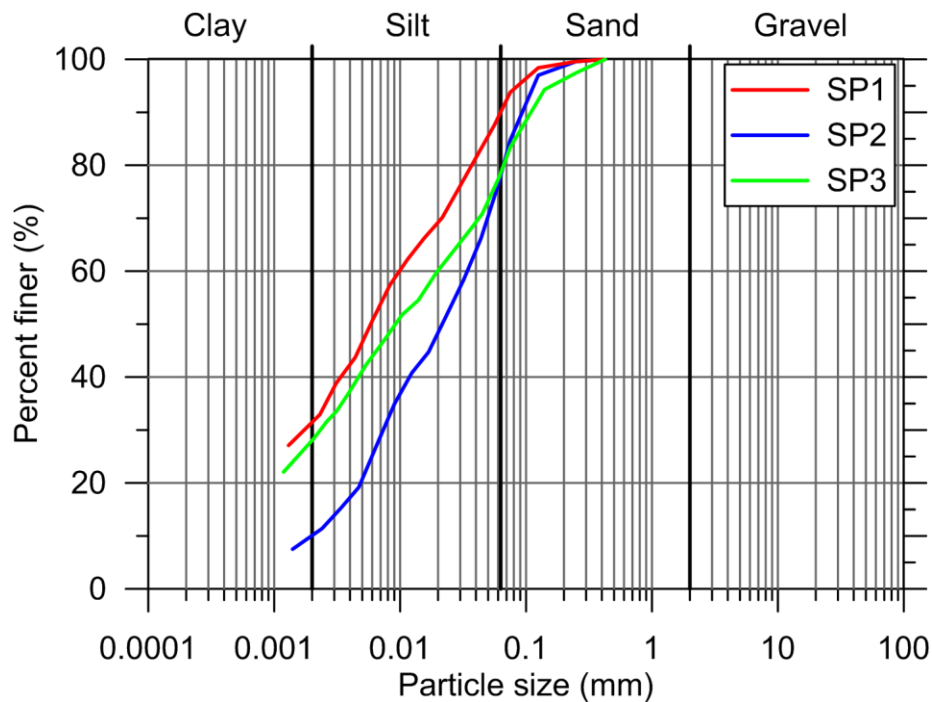


Figure 5.6. Particle size distributions of the mud volcano soils in Monteleone di Fermo and Santa Vittoria in Matenano.

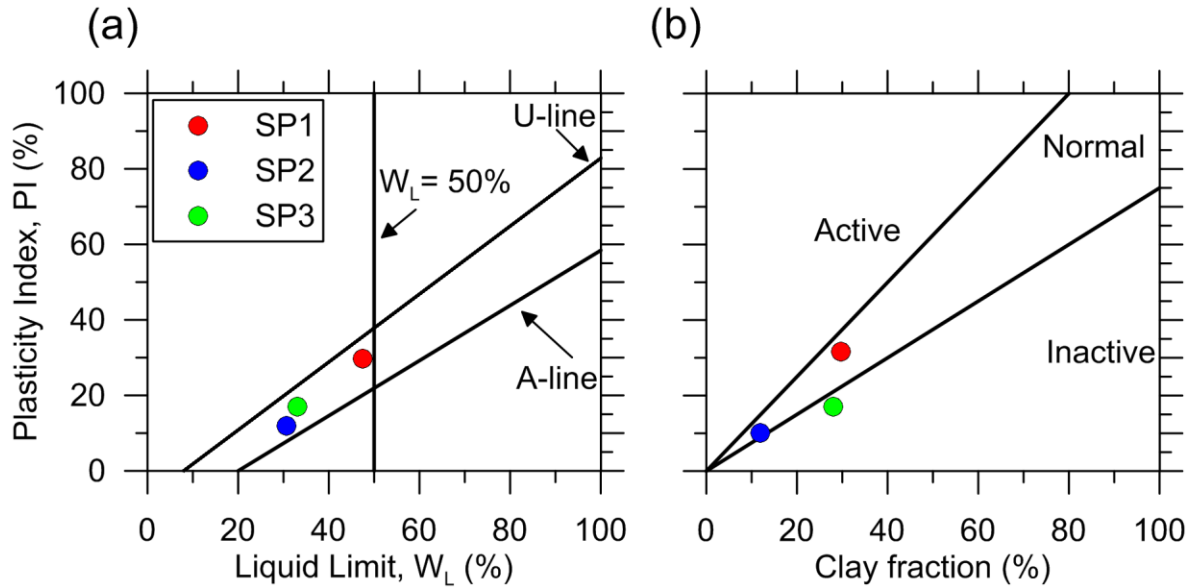


Figure 5.7. (a) Plasticity chart and (b) activity chart of the mud volcano soils in Monteleone di Fermo and Santa Vittoria in Matenano.

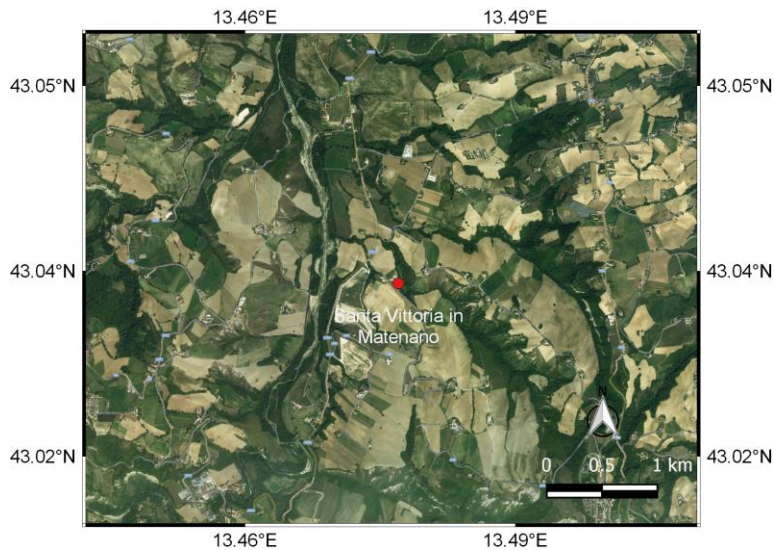


Figure 5.8. Location of the inspected mud new volcano in Santa Vittoria in Matenano.

We sampled soil erupted from the volcano in Santa Vittoria in Matenano (SP3). This sample was taken on 16 November, 2016. On this sample, we performed sieve analysis, along with Atterberg limits. Figure 5.6 shows the particle size distribution for samples SP3. It is consistent with those observed for the mud volcanoes in Monteleone di Fermo. The fine-grained soil exhibits a liquid limit $LL = 33.0\%$, a plastic limit $PL = 16.0\%$, and a plasticity index $PI = 17.0\%$. The plasticity chart (Figure 5.7a), shows that the soil of sample SP3 can be classified as inorganic clay (CL). The clay can be classified as inactive (Figure 5.7b).

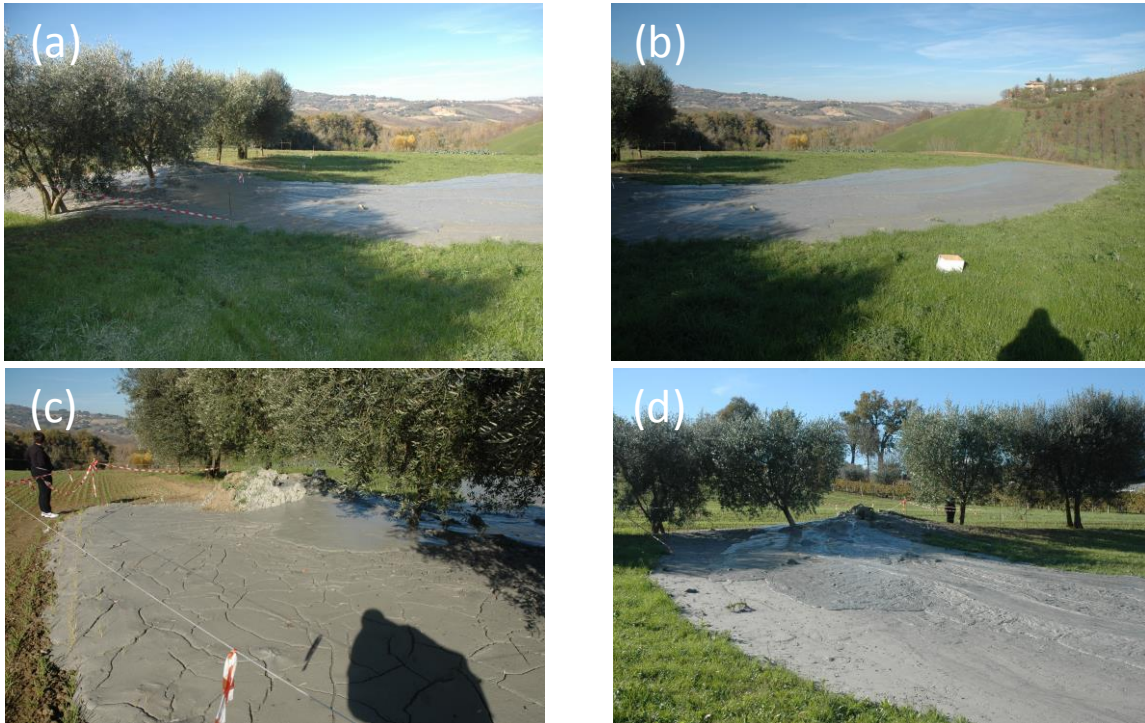


Figure 5.9. Overview of the mud new volcano in Santa Vittoria in Matenano.

5.4. Earthquake-triggered eruptions and correlations between earthquake magnitude and distance

Manga et al. (2009) and Delle Donne et al. (2010) proposed empirical relationships for earthquake-induced eruptions, based on earthquake magnitude and distance (Figure 5.10). The limit curve of Manga et al. (2009) is based on an empirical database of 29 mud volcano eruptions that occurred following earthquakes with magnitudes $M=4.5-9.3$ at epicentral distances of $R_{epi}=4-900\text{km}$. Delle Donne et al (2010) based their relationship on a larger dataset of 68 data points derived for $M=4.5-9.5$ events and $R_{epi}=10-10000\text{km}$. The two limiting curves have similar shapes. Mazzini and Etiope (2017) argue that for large magnitude events, eruptions can be triggered at very long distances. Furthermore, Mazzini and Etiope (2017) point out that many data points lie above the threshold curve developed by Manga et al. (2009), also for relatively small magnitude events. As a result, they believe that the model by Delle Donne et al. (2010) should be generally preferred. Figure 5.10 shows all data points used by Manga et al. (2009) and Delle Donne et al. (2010), along with their limiting curves. Also shown in Figure 5.10 are the earthquake-triggered eruptions observed in this study. The data points related to the Central Italy earthquake are consistent with the general trend, and they lie below both limiting curves.

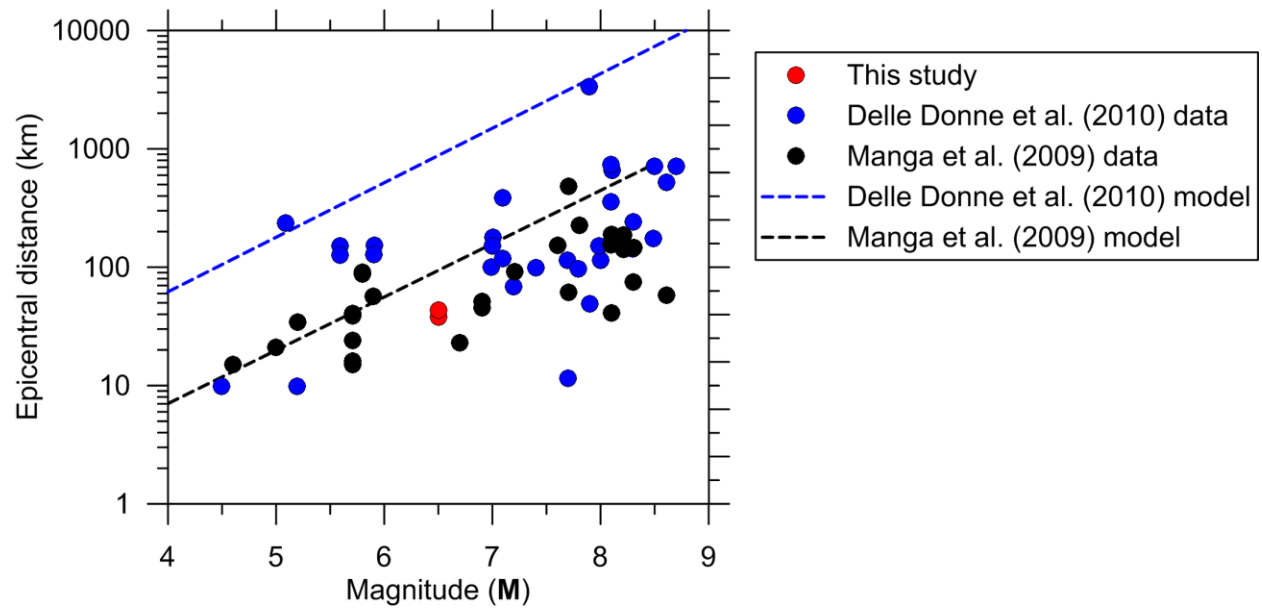


Figure 5.10. Earthquake magnitude versus epicentral distance for earthquake-triggered mud volcanoes, along with limiting curves from Delle Donne et al (2010, blue dashed curve), and Manga et al. (2009, black dashed curve). Red dots represent data collected in this study, blue dots are data points from Delle Donne et al. (2010), black dots are data points from Manga et al. (2009).

6 Performance of buildings and damage patterns

Principal authors: Sebastiano Foti, Alessandro Pagliaroli, Anastasios Sextos, Paolo Zimmaro

Contributing authors: Ernesto Ausilio, Francesca Bozzoni, Roberto Cairo, Maria Chiara Capatti, Massimina Castiglia, Filiberto Chiabrando, Paolo Dabove, Raffaele De Risi, Francesca Dezi, Vincenzo Di Pietra, Luigi Di Sarno, Maria Giovanna Durante, Tony Fierro, Kevin Franke, Dipendra Gautam, Silvia Giallini, Zurab Gogoladze, Giuseppe Lanzo, Paolo Maschio, Luciano Mignelli, Michele Mucciacciaro, Federico Passeri, Brandon Reimschiessel, Filippo Santucci de Magistris, Antonio Sgobio, Stefania Sica, Armando L. Simonelli, Fiorenzo Staniscia, Lorenzo Teppati Lose, Giovanna Vessia

As was done in reconnaissance following the August 2016 event sequence, following the October 2016 events the GEER team evaluated building damage patterns for villages in broad region affected by both August and October events. In analyzing this data, we benefitted from previously collected geological and topographical information that can provide insight into factors contributing to damage patterns. Aside from the data collected during the reconnaissance itself, the information sources used in this analysis is essentially identical to those described in GEER (2016). In this chapter, we utilize this information without detailed descriptions of geologic setting, terrain, etc., which are provided in the earlier report.

As before, we utilize aerial images from Orthohotos, 3D texture models from drones (detailed in Chapter 4), detailed ground surveys, and general qualitative ground surveys. The scale of the reconnaissance performed following the October events was more limited than that following the August events, with GEER in a lead role with participation by researchers sharing affiliations with Reluis Center for Microzonation and its applications, and the Hellenic Association of Earthquake Engineering. We have shared our results with EERI, which we understand is planning work in mid-2017.

Structural damage is mapped according to a standard classification scheme that is described in Section 5.2 of GEER (2016). We have adopted informal descriptions of occupied areas, with hamlets being the smallest (part of town or village separated from village center), villages (an organized civic body with a local government), and town/cities (same as villages, but larger populations).

An important aspect of the October 2016 event reconnaissance is that in many cases we re-visiting areas previously inspected. Other areas, typically north of the August 2016 epicenter, were visited for the first time in the present work. This chapter is organized to distinguish these two situations, with Section 6.1 being re-visits and Section 6.2 being newly inspected areas. As was done in GEER (2016), for the newly inspected areas we have areas with detailed structure-by-structure inspections with quantitative mapping and ‘quick-checks’ in which damage rates are estimated.

Using the procedure described in Section 3.5, we have estimated ground motions (PGA) at each of the locations discussed in this chapter during both the 24 August 2016 and 30 October 2016 mainshocks with the results shown in Table 6.1. The ground motions were estimated for a representative site condition of $V_{s30} = 580$ m/s.

Table 6.1. Inspected villages/hamlets and estimated ground motions.

Village/Hamlet	Lat	Lon	PGA (g)		
			M6.1 24 August	M5.9 26 October	M6.5 30 October
Norcia	42.793451	13.094357	0.30	0.29	0.41
Accumoli	42.695330	13.245280	0.56	0.07	0.45
Amatrice	42.628994	13.289674	0.66	0.08	0.50
Arquata del Tronto	42.772300	13.294900	0.42	0.10	0.28
Pescara del Tronto	42.752500	13.268611	0.51	0.10	0.38
Tufo	42.735344	13.252867	0.53	0.10	0.46
Montegallo	42.840571	13.332968	0.24	0.12	0.25
Visso	42.929300	13.087700	0.25	0.44	0.38
Ussita	42.943300	13.138200	0.22	0.46	0.38
Tolentino	43.209143	13.284525	0.09	0.10	0.11
San Severino	43.230767	13.174877	0.07	0.12	0.12
Camerino	43.134666	13.067698	0.07	0.16	0.20
Pievebovigliana	43.081049	13.110066	0.09	0.20	0.23
Pieve Torina	42.994077	13.046987	0.17	0.47	0.34
Sellano	42.887913	12.925088	0.13	0.07	0.20
Fiume	43.042051	13.001034	0.10	0.24	0.26
Pie del Colle	42.844373	13.101296	0.33	0.48	0.39
Cessapalombo	43.108327	13.257325	0.08	0.11	0.12
Preci	42.880697	13.039657	0.22	0.30	0.35
Piedivalle	42.866786	13.060767	0.25	0.37	0.36
Caldarola	43.139880	13.224710	0.08	0.12	0.13
Castello di Campi	42.853729	13.100582	0.32	0.51	0.39
Colfiorito	43.026044	12.889921	0.20	0.39	0.28
Casavecchia Alta	42.998463	13.06213	0.17	0.47	0.32
San Lorenzo in Colpolina	43.086043	13.12436	0.08	0.18	0.21
Borgo Cerreto	42.815225	12.915500	0.11	0.06	0.15
Serravalle	42.785714	13.022231	0.15	0.13	0.28
Popoli	42.752389	13.107219	0.26	0.17	0.59
San Pellegrino	42.757561	13.149619	0.38	0.19	0.66
Villa Sant'Antonio	42.943274	13.083696	0.25	0.44	0.36
Borgo San Giovanni	42.925066	13.085469	0.25	0.44	0.38
Polverina	43.091576	13.117553	0.08	0.18	0.22
Pie la Rocca	42.833900	13.113102	0.38	0.41	0.41

6.1 Revisits

6.1.1 Norcia

Ground Surveys

As shown in Table 6.1, Norcia experienced stronger estimated ground motions during the 30 October event (PGA = 0.41 to 0.48 g) than in the 24 August event (PGA = 0.30 to 0.36 g).

Norcia's buildings were not severely affected by the first event in August 2016. After the multiple October events, several structures suffered moderate-to-significant of damage or collapse. Figure 6.1 shows the evolution of damage between the two inspections. The distribution of Damage States among the buildings inspected in the red-zone of Norcia is shown in Figure 6.2. These figures show that the structural damage in Norcia was much more severe in the October events than in the earlier August events.

Even though the majority of the building stock is masonry, there is no disproportional damage observed between the first and the sequence of seismic events (Figure 6.1). This is because, unlike Amatrice (Section 6.1.3), the initial damage state of most buildings after the August earthquake was D0, hence the structures had adequate strength to resist the subsequent earthquakes. By focusing more carefully on Figure 6.2, it is also evident that the few structures that suffered damage during the first event, indeed presented a disproportional level of damage increase shifting from DS3 to DS5. Based on the above comparative assessment it can be concluded that masonry structures are particularly prone to failure under cascading seismic events provided that one event in the sequence initiates non-catastrophic damage, a fact that highlights the importance of quick visual inspection and reliable retrofit.

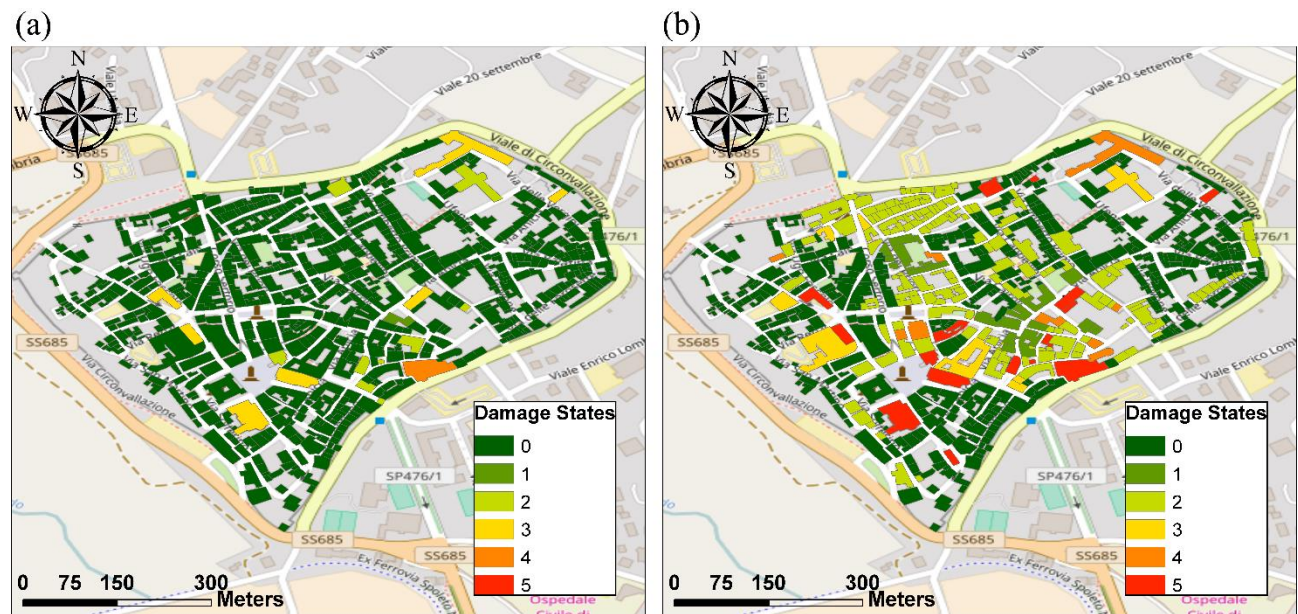


Figure 6.1. Evolution of damage after (a) the 24 August earthquake, and (b) the October events.

Apart from the wider assessment, a side-by-side comparison of significant structures with multi-epoch surveys is made. Figure 6.3 depicts the locations of the buildings presented. Figure 6.4 illustrates one of the churches that were slightly damaged by the first seismic event, but completely collapsed subsequently. Many historical churches in Norcia experienced the same kind of damage evolution. Figure 6.5 shows one exceptional case of a typical residential masonry building where the evolution of damage was rather moderate (damage state shifting from DS2 to DS3). Conversely, Figure 6.6 shows a residential building with irregular masonry construction. This group of buildings experienced an abrupt damage evolution, with an out-of-plane mechanism and increased in-plane damage. Finally, Figure 6.7 depicts the out-of-plane failure of an historical monastery leading to partial loss of support of the roof. Notably, the wall failure was concentrated at a level higher to that of the seismic retrofit, thus highlighting that local interventions should not be only localized on the ground level but also take into consideration the reduced axial load and weak diaphragm action of the masonry walls at higher levels.

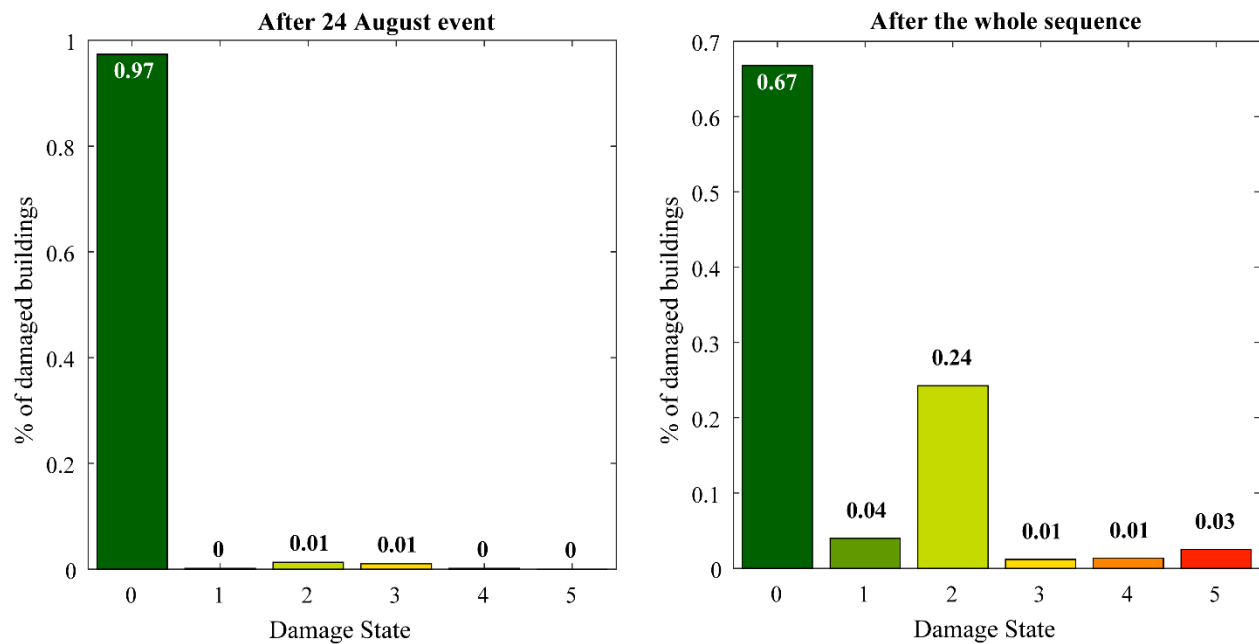


Figure 6.2. Percentage of damaged structures (a) in the aftermath of first event and (b) after the whole sequence.

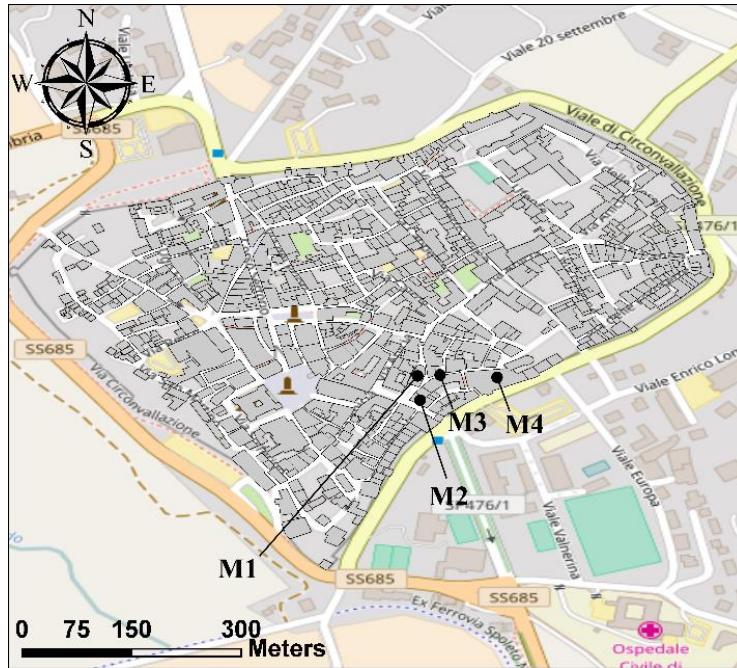


Figure 6.3. Structures shown in detail in the following. (M stands for Masonry).

(a)



(b)



Figure 6.4. Building M1.

(a)



(b)



Figure 6.5. Building M2.

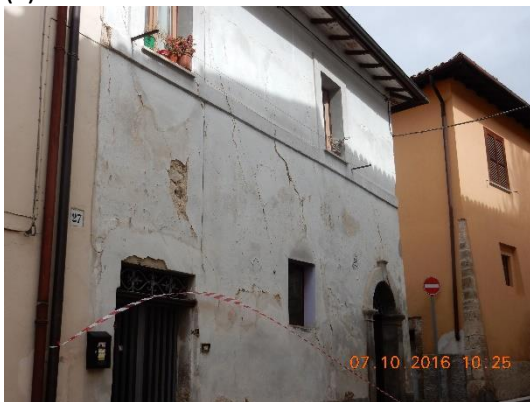
(a)



(b)



(c)



(d)



Figure 6.6. Building M3.



Figure 6.7. Building M4.

UAV imaging

During the GEER mission in Norcia, unmanned aerial vehicle (UAV) imaging was performed by vertically elevating the UAV above two points in the city at the locations shown in Figure 6.8. Images were taken at the horizontal azimuths shown in the Figure. Figure 6.9 to Figure 6.14 show these images. Video footage can be found at <https://www.youtube.com/watch?v=7vOVZOEuBMg>, last accessed April 18, 2017).

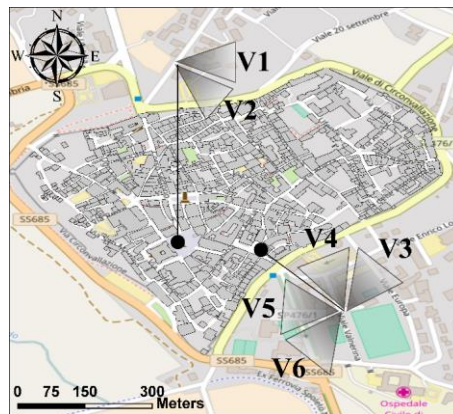


Figure 6.8. Visual angles investigated during UAV flights.



Figure 6.9. UAV image V1.



Figure 6.10. UAV image V2.



Figure 6.11. UAV image V3.



Figure 6.12. UAV image V4.



Figure 6.13. UAV image V5.



Figure 6.14. UAV image V6.

On-site damage assessment versus NASA JPL ARIA Damage Proxy Maps

Section 4.1.2 of GEER (2016) describes damage proxy maps developed by NASA JPL as part of the Advanced Rapid Imaging and Analysis (ARIA) project. After major earthquakes, the ARIA project releases damage proxy maps (DPMs). These DPMs are produced comparing interferometric SAR coherence maps from before and after an extreme event (e.g. Fielding et al., 2005; Yun et al., 2011). The effectiveness of the DPMs has been tested for the rapid evaluation of earthquake-induced landslides and rockfalls after the 2015 **M**7.8 Gorkha Earthquake. In particular, Yun et al. (2015) show that the extent of several observed earthquake-related instability phenomena in the Himalayas were well captured by the DPMs. The resolution of these maps for the August 2016 event damage was too low to enable comparisons to our field observations of building damage, although comparisons of landslide areas was undertaken. The image quality improved markedly for Norcia following the October 2016 event sequence. As a result, detailed structure-by-structure comparisons of ARIA maps vs field observations is now practical and is undertaken here.

After the 30 October **M**6.5 earthquake, a detailed DPM for the city center of Norcia was released (aria-share.jpl.nasa.gov/events/20161030-Italy_EQ/DPM/, last accessed 26 February, 2017). This DPM has a relatively limited spatial extent, but high resolution. Figure 6.15 shows the DPM produced after the 30 October event, superimposed on the map of the city center of Norcia, along with all structures that have been classified, through on-site visual inspection, as completely collapsed (for which a damage level D5 has been assigned), and selected D4 structures.

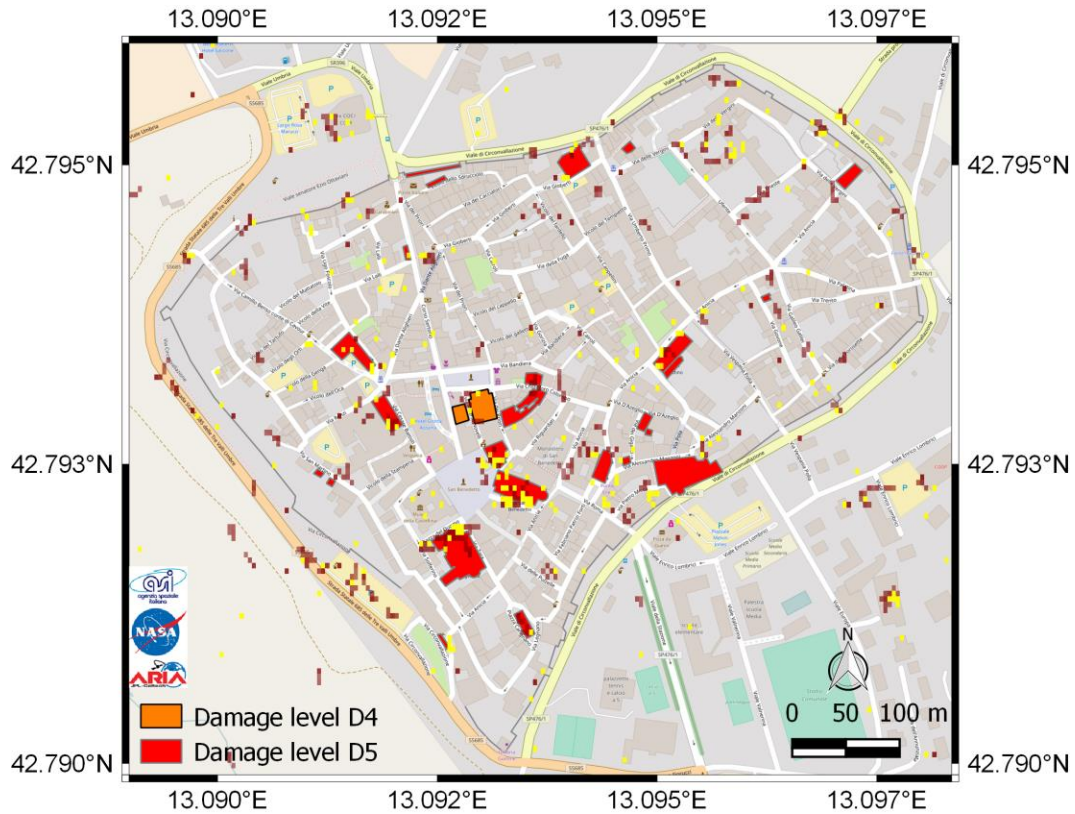


Figure 6.15. Damage proxy map of Norcia, along with all structures with assigned damage level D5, and selected structures with assigned damage level D4.

We analyze 22 structures assigned damage levels D5 and D4; within this group is the full inventory of D5 structures as identified in our field inspections. Figure 6.16 shows the spatial distribution of these structures, along with their identification numbers.

In order to provide a sense for the damage in Norcia at these sites, Figure 6.17 shows representative pictures taken during the on-site inspection performed following the 30 October **M6.5** earthquake event. By comparing the locations of these mapped structures and damage zones per the ARIA imaging, we find good agreement. For all structures with assigned damage level D5, the DPM shows a concentration of red and dark red zones, representing areas in which substantial deformations occurred.

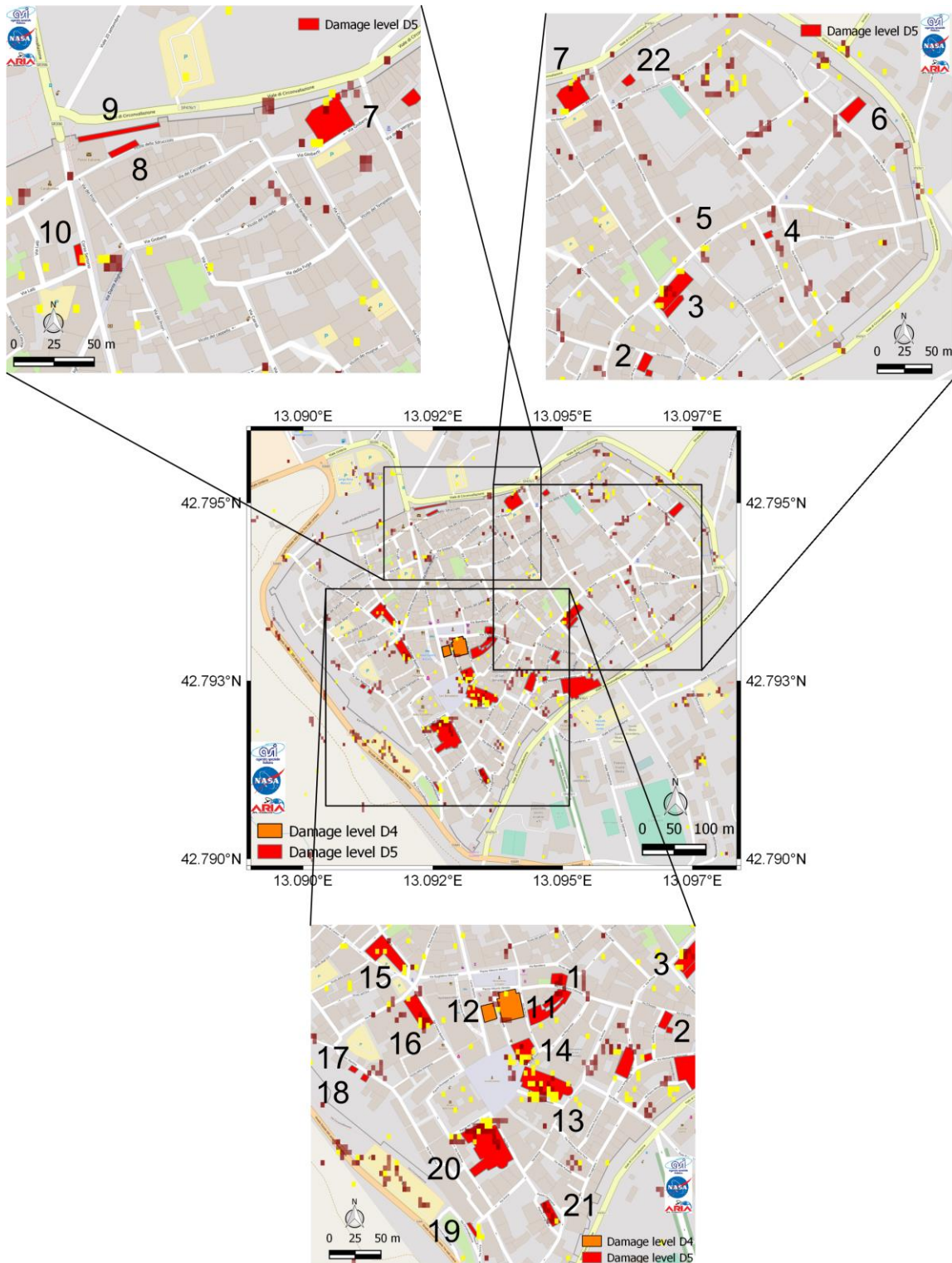


Figure 6.16. Zoom-in of the damage proxy map of Norcia, along with the identification numbers of all structures with assigned damage level D5 from field inspections and available high-quality on-site information and photos.



N. 1 Via Cristoforo Colombo



N. 2 Via Massimo D'Azeglio



N. 3 – Via Anicia S. Agostino church – Piazza Margherita



N. 4 Via Govone



N. 5 –Corner between Via Polla Vespasia – Via Anicia



N. 6 Chiesa del Crocifisso nearby Piazza Palatina



N. 7 Church in Via Cappellini – Piazza Nazario Sauro



N. 8 Collapsed wall



N.9 Medieval walls



N. 10 Corso Sertori



N. 11 Teatro Civico



N. 12 Corso Sertori



N. 13 San Benedetto Cathedral



N. 14 Bell tower



N. 15 San Francesco church



N. 16 Via Cesare Battisti



N. 17 Via San Martino (1)



N. 18 Via San Martino (2)



N. 19 Medieval wall



N. 20 Duomo



N. 21 Collapsed church (1)



N. 22 Collapsed church (2)

Figure 6.17. Pictures of all structures with assigned damage level D5 in the city center of Norcia, along with their identification numbers.

6.1.2 Accumoli

As shown in Table 6.1, Accumoli experienced slightly weaker estimated ground motions during the 30 October event (PGA = 0.45 g) than in the 24 August event (PGA = 0.56 g).

Accumoli was one of the most damaged villages after the 24 August main shock (GEER 2016). During the September reconnaissance, significant additional damage was observed, with widespread partial collapses throughout the village. The eastern part of the village, around the main square (Piazza San Francesco), was the most heavily damaged area, with partial collapses

of the police station and the small church. Moreover, the retaining wall along the eastern side of the village experienced significant relative movements, most likely associated to the instability of the slope below.

The seismic sequence in October caused total devastation of the village. As shown in Figure 6.18, the vast majority of the buildings that were damaged during the August earthquake, eventually collapsed. The evolution of damage after multiple seismic events is also evident as also depicted in Figure 6.19, where a drastic shift from low (DS0/DS1) to high (DS4/DS5) damage states is clearly observed.

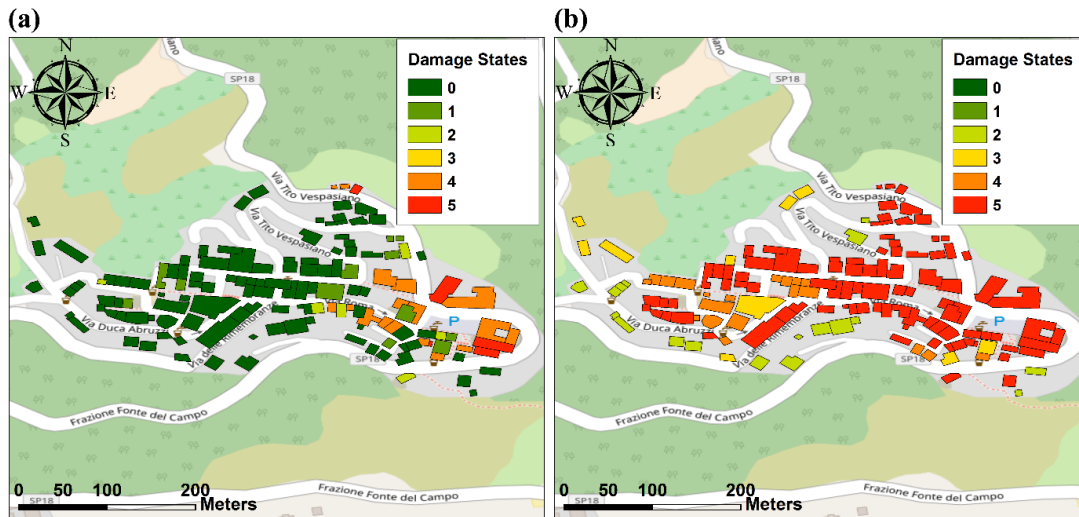


Figure 6.18. Evolution of damage after (a) the first seismic event and (b) the sequence of events.

At the time of the visual inspection by the GEER team, the only accessible walking route was the one connecting the village entrance to the main square, because of the major building damage and collapse in the surrounding areas (Figure 6.20). As a result, a detailed inspection was feasible only within the eastern part of the village, the western part being inspected by means of UAVs. Figure 6.21, Figure 6.22, and Figure 6.23 illustrate the upper part of the village with a colored scale distinguishing three main zones of distinct level of damage.

In general, Modified Mercalli intensities in the lower part of Accumoli are XII (total destruction). The overall view of the highest part from Piazza San Francesco has dramatically changed and most of the structures have collapsed. Significant widespread damage corresponding to D4/D5 states is assigned as a whole to that area based also on aerial pictures. Few standing buildings survived the sequence of events with minor damage and are highlighted in green as mapped in Figure 6.18).

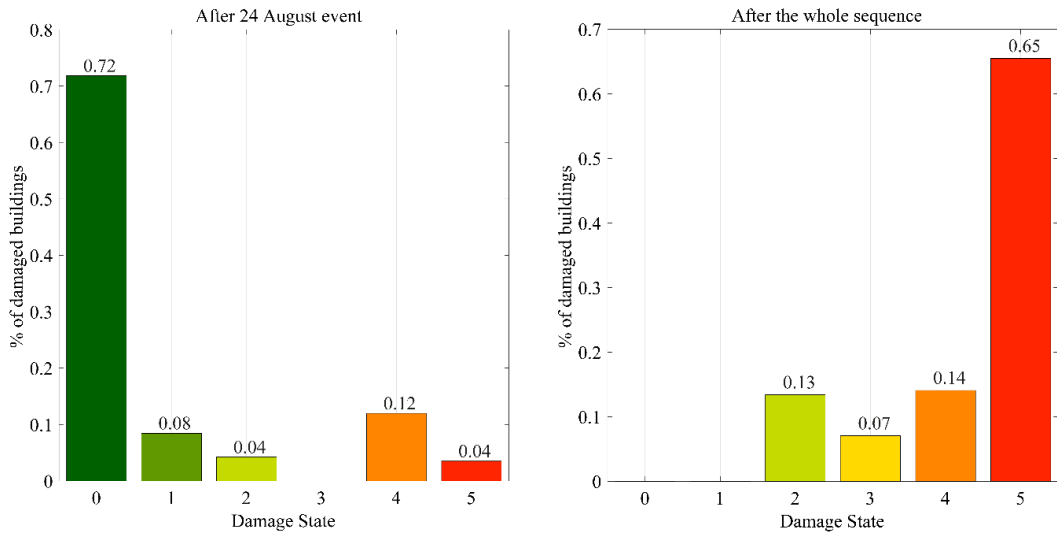


Figure 6.19. Percentage of damaged structures (a) after the first event and (b) after the whole sequence.



Figure 6.20. (a) Access route to the lowest (easternmost) portion village (V1). (b) Piazza San Francesco (V2).

The current orthophoto of the village is presented in Figure 6.24 with the location and orientation of pictures depicting multi-epoch damage states for individual structures. Further details are summarized in Table 6.2 to document the photographed structures and to compare the damage levels detected after the September and December visual inspections. Figure 6.25 shows photos presented in Table 6.2.



Figure 6.21. Aerial view, east-west direction (V3).



Figure 6.22. Aerial view, west-east direction (V4).



Figure 6.23. Aerial view, south-north direction (V5).

Table 6.2. Summary of pictures and structures inspected in Accumoli. (*pictures that show the comparison between September (left) and December (right) inspection).

Picture	DATUM	Description	Position		September Damage Level	December Damage Level
			Lat.	Long.		
V1	WGS-84	Pedestrian route crossing the village	42.694972°	13.248886°	D3	D5
V2	WGS-84	Piazza San Francesco entrance	42.694601°	13.248556°	D3	D5
V3	-	Air view east-west direction	-	-	D1-2	D5
V4	-	Air view west-east direction	-	-	D1-2	D4
V5	-	Air view south-north direction	-	-	D1-2	D3/4
P01*	WGS-84	Church	42.694073°	13.249509°	D4	D5
P02*	WGS-84	Town hall	42.694304°	13.249263°	D3	D5
P03*	WGS-84	Police Station (view from the square)	42.694325°	13.249507°	D3	D5
P04*	WGS-84	Western (view from the square)	42.694215°	13.248842°	D2	D5
P05*	WGS-84	Northern view from the square (bar)	42.694428°	13.249379°	D3	D5
P06*	WGS-84	Small square in front of the church	42.694073°	13.249509°	D2	D5
P07	WGS-84	Panoramic view of the square	42.694215°	13.248842°	D2	D5

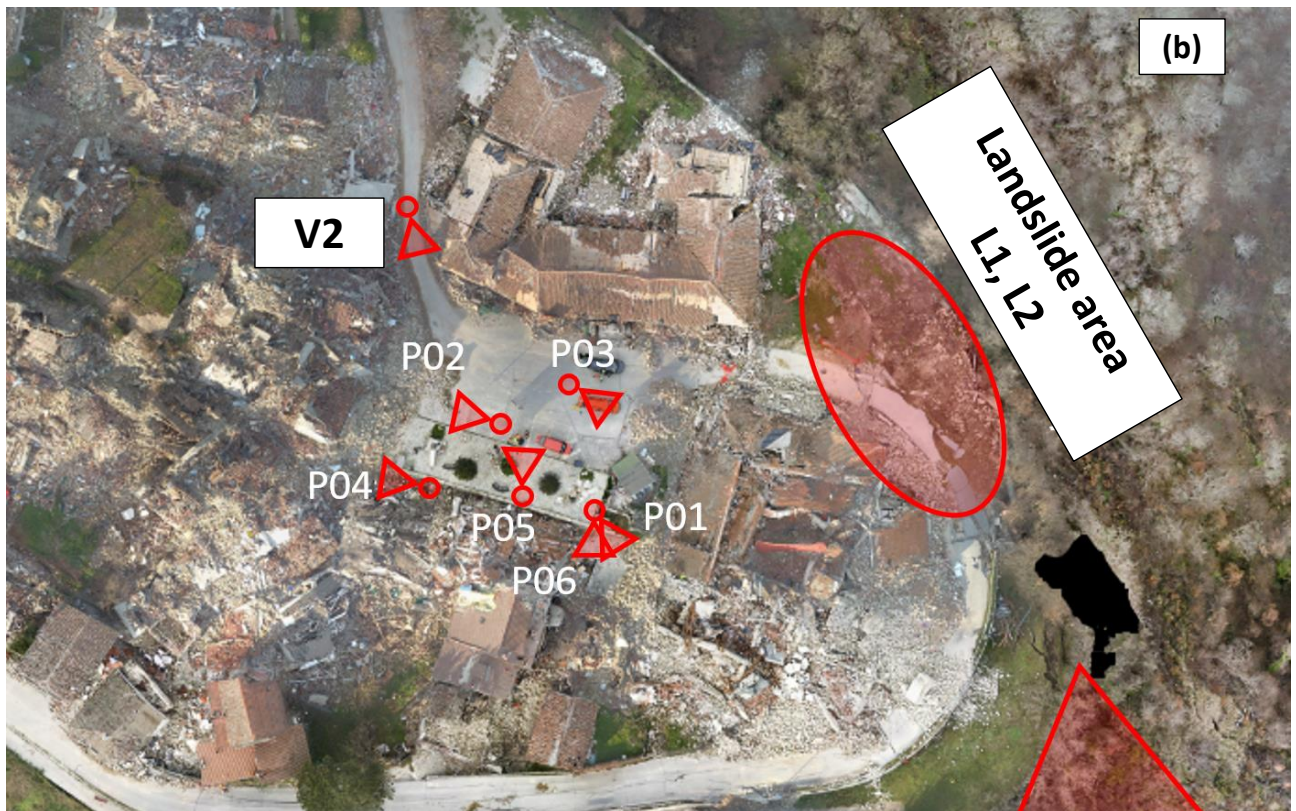
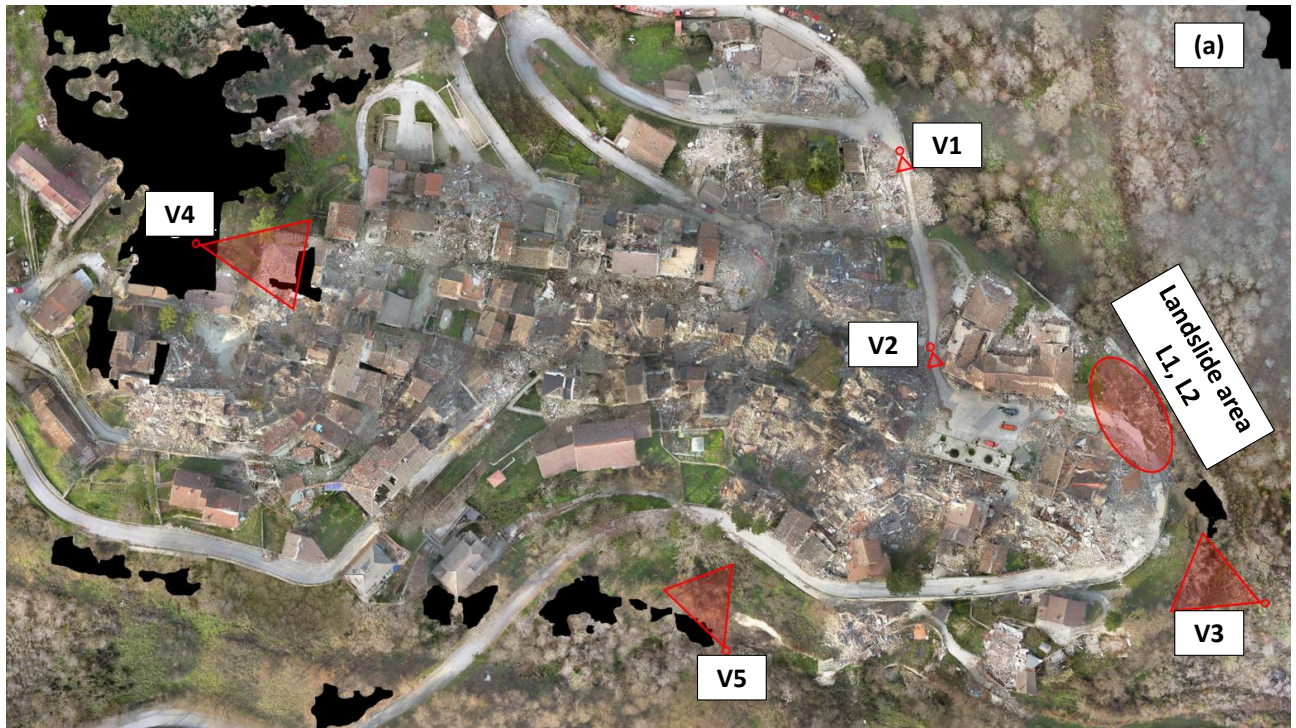


Figure 6.24. Ortho-images captured on December: (a) overview; (b) zoom on Piazza San Francesco.

(August event)



(Multiple events)



P01 (Church)

(August event)



(Multiple events)



P02 (Town hall)

(August event)



(Multiple events)



P03 (Police station, square side)

(August event)



(Multiple events)



P04 (Western view from square)

(August event)



(Multiple events)



P05 (Northern view from square, bar on the background)

(August event)



(Multiple events)



P06 (Small square in front of the church)



P07 (Panoramic view of Piazza San Francesco)

Figure 6.25. Representative pictures taken in Accumoli during the GEER survey (see Table 6.2).

The accumulation of damage across seismic events is also evident by comparing the panoramic view of the village after the September and December field missions (Figure 6.26 and Figure 6.27). More precisely, it is seen that the retaining wall completely overturned, causing disruption of the adjacent road. It is noted that it was not possible to take the pictures from the same position, hence, colored circles are used to indicate the corresponding spots.



Figure 6.26. Representative pictures of landslide in eastern part of village (September 2016).



Figure 6.27. Representative pictures of landslide in the eastern part of village (December 2016).

6.1.3 Amatrice

As shown in Table 6.1, Amatrice experienced weaker estimated ground motions during the 30 October event (PGA = 0.50 g) than in the 24 August event (PGA = 0.66 g).

Amatrice's buildings were severely affected by August event sequence (Section 5.3.2 of GEER 2016). Many buildings that remained standing after the August events had only a small residual capacity, and then collapsed during September and October events. Figure 6.28 shows the multi-epoch damage evolution. This is also reflected in the histograms of red zone damage statistics in Figure 6.29, which show that the percentage of D5 structures increased from 23% to 42%. We distinguish performance of different structural systems qualitatively for a number of characteristic buildings, the locations of which are shown in Figure 6.30.

UAV imaging

During the GEER mission in Amatrice, UAV imaging was performed near building S1. The UAV elevated above a fixed point and photographed across an azimuthal range. **Error! Reference source not found.** shows five angles cropped from online footage (<https://www.youtube.com/watch?v=djF5fkUrYkk>., last accessed April 17, 2017). Figure 6.32 to Figure 6.36 show these images.

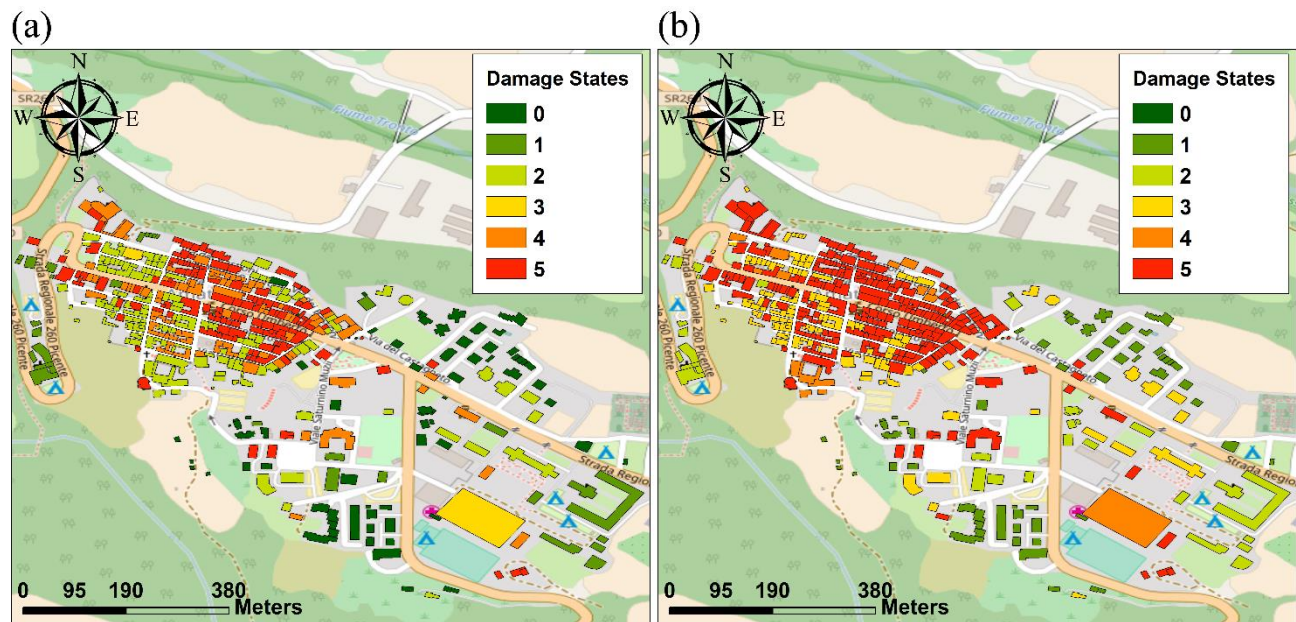


Figure 6.28. Evolution of damage after (a) the first seismic event and (b) the sequence of events.

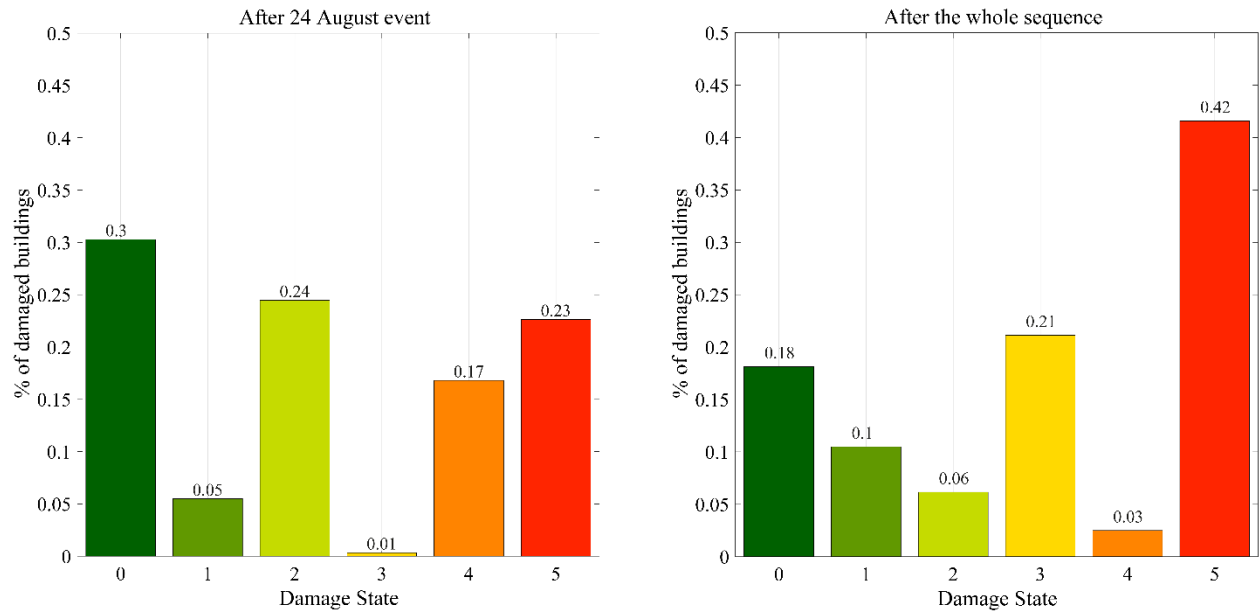


Figure 6.29. Percentage of damaged structures (a) in the aftermath of first event and (b) after the whole sequence.

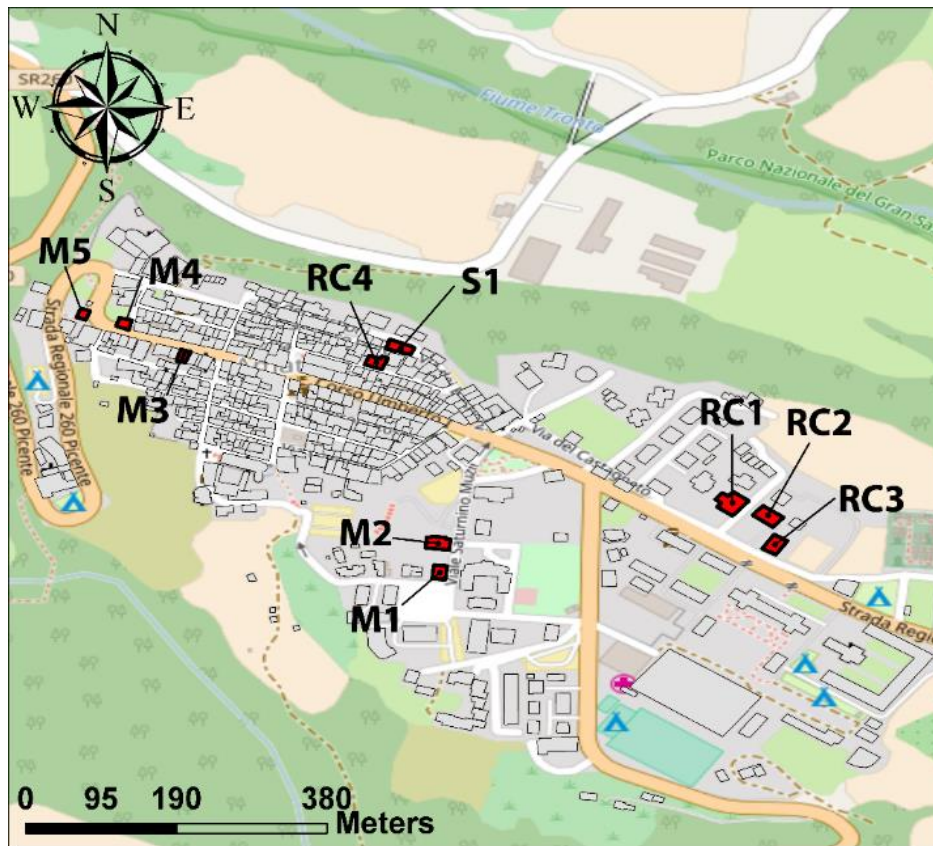


Figure 6.30. Overview of the location and structural system of the buildings that are documented in the following. (RC: Reinforced Concrete, M: Masonry, and S: Steel buildings).

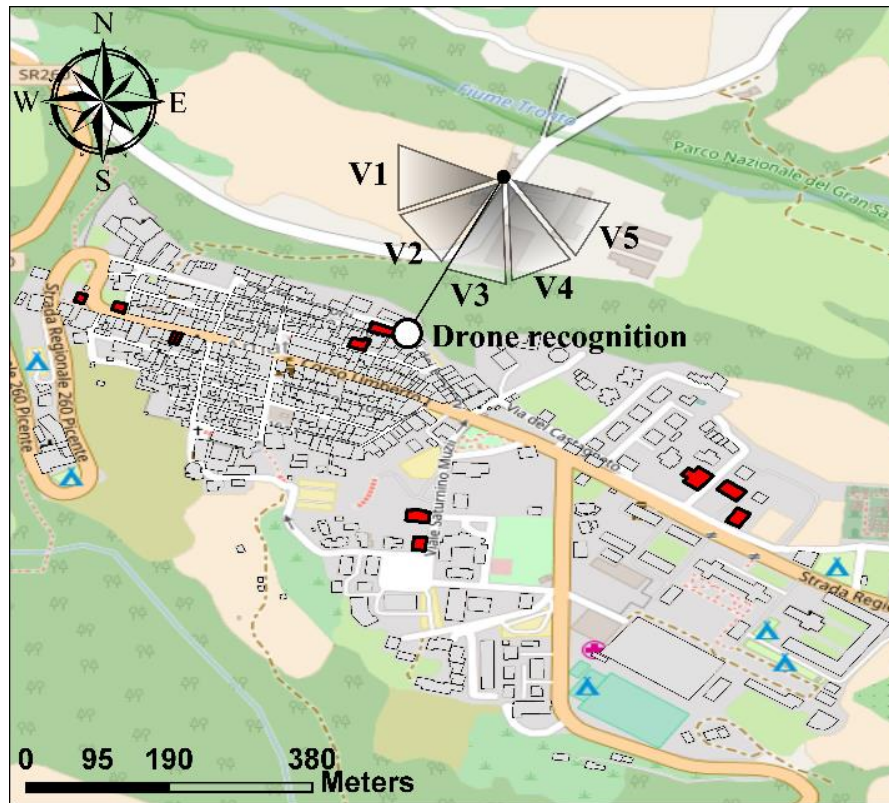


Figure 6.31. Visual angles investigated during the UAV flight.



Figure 6.32. UAV image V1.



Figure 6.33. UAV image V2.



Figure 6.34. UAV image V3.



Figure 6.35. UAV image V4.



Figure 6.36. UAV image V5.

Reinforced Concrete Structures

Figure 6.37 illustrates building RC1 in the aftermath of the first event (a,c) and after the October sequence (b,d). It evident that the infill panel has failed out-of-plane after the seismic sequence (but not after the first main shock), whereas the shear failure at the top of the right column has been clearly pronounced. Figure 6.38 depicts building RC2, a dual shear wall – moment resisting frame built with the older Italian seismic code (The Italian National Annex DM 1996, Norme Tecniche per le Costruzioni, 1996; NTC96). Similar out of plane failure of the,

initially diagonally cracked, infill panel is again observed as a result of shaking from multiple events. A detail of beam-column joint damage is illustrated in Figure 6.39 for building RC3. We observe cyclic degradation of column top, spalling of concrete, and minor longitudinal rebar buckling in the absence of adequate transverse reinforcement. Finally, building RC4 in Figure 6.40 experienced only minor damage after the August event but suffered out-of-plane failure of the majority of its infill panels subsequently, thus exposing the structure to a potential soft story mechanism. Performance of this type was characteristic of the area.



Figure 6.37. Building RC1.

(a)



(b)



Figure 6.38. Building RC2.

(a)



(b)



Figure 6.39. Building RC3.

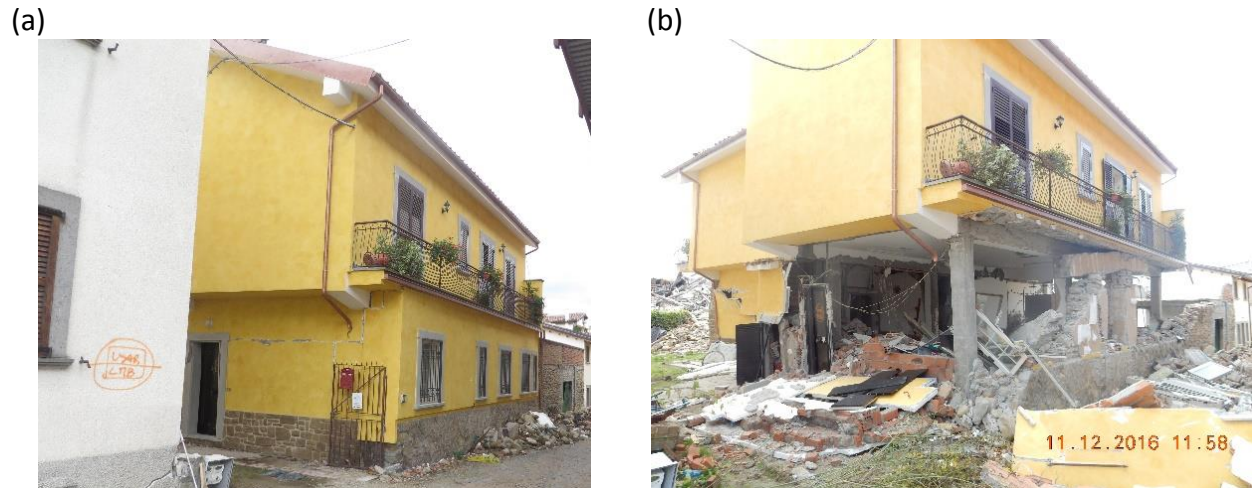


Figure 6.40. Building RC4.

Steel structure

There is only one high-rise steel structure within the Amatrice red zone (Figure 6.41) built in the early 90's with the Italian seismic code of the time (The Italian National Annex DM 1996, Norme Tecniche per le Costruzioni, 1996; NTC96). It consists of a basement, a ground floor and two upper stories, alongside a shorter story on top that serves as a penthouse. Given the intensity of ground motion, its overall performance is deemed relatively satisfactory. Contrarily, Hotel Roma, one of Amatrice's most iconic structures, located a few meters from the steel building, collapsed completely. After the first event, damage was only concentrated to non-structural elements, with small local flange instability at the top of two front columns of the ground floor. At the end of the October event sequence, the building presented permanent deformation along the longer direction, as shown in Figure 6.41. Such permanent deformation is localized at the second level of the building with a visible inter-story drift. Preliminary finite element analyses of the building suggest that the fundamental mode period of the structure is approximately 0.75sec. The mode shape indicates an almost uncoupled translation along the long side, mainly due to the orientation of the steel columns whose strong axis is aligned with the short side of the building.

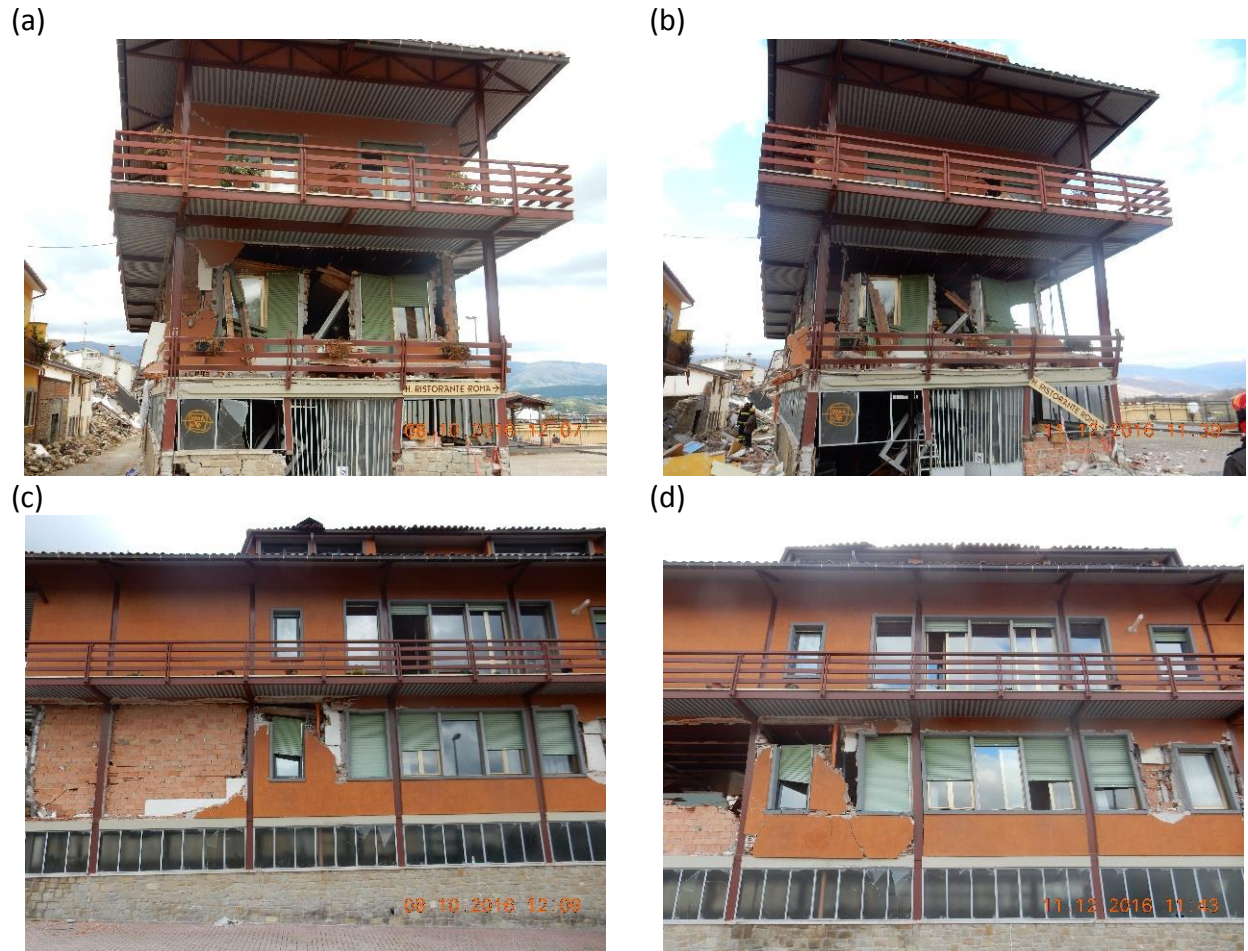


Figure 6.41. Building S1.

Masonry structures

Figure 6.42 shows multi-epoch damage to a masonry building. Damage at the base of the structure is essentially unchanged, but new damage features are observed in the top story. Figure 6.43 shows the local police (“Carabinieri”) station. It is evident that diagonal cracks were extended in both sides of the building after multiple seismic events. Notably, the local retrofit by means of steel ties at the corners of the upper story mitigated further damage and possible collapse.

(a)



(b)



Figure 6.42. Building M1.

(a)



(b)



(c)



(d)



Figure 6.43. Building M2.

Figure 6.44 and Figure 6.45 present two buildings within the Amatrice red-zone, where initial damage of the outer masonry due to the first event evolved to partial collapse after the event sequence. This is also an interesting case in that such partial collapse is not always visible by satellite, thus highlighting the importance of careful on-site ground inspection. The soft-story of another masonry building is illustrated in Figure 6.45. Such a mechanism is presumably due to the higher stiffness of the upper part with respect to the ground floor, and due to the previous shear failures observed at the ground level in the aftermath of the first event. It is also a characteristic case where the evolution of damage in masonry structures under multiple seismic events, as well as the increase of the corresponding damage indeed, is strongly nonlinear. Figure 6.46 shows the complete collapse of a building that was heavily damaged from the first event.



Figure 6.44. Building M3.



Figure 6.45. Building M4.

(a)



(b)



Figure 6.46. Building M5.

Comparative assessment of seismic performance of different structural systems

Overall, notwithstanding the clear evolution of all *local* damage modes of Reinforced Concrete structures as a result of multiple earthquake excitations, a general comment that can be made is that they did not experience the disproportional event-to-event damage increase observed in masonry buildings. In most cases, R/C buildings showed adequate ductility and their global damage at a system level remained approximately within the same Damage State that was reported after the initial visual inspections. On the contrary, masonry buildings suffered, on average, significant and disproportional damage during the sequence of seismic events, due to their low residual capacity and the brittle nature of the failure modes involved, thus quickly shifting from low-to-moderate Damage States (DS1-DS3) to complete collapse (DS5).

6.1.4 Arquata del Tronto

As shown in Table 6.1, Arquata del Tronto experienced weaker estimated ground motions during the 30 October event (PGA = 0.28 g) than in the 24 August event (PGA = 0.42 g).

Arquata del Tronto is a small village of about 1200 inhabitants located in the Ascoli Piceno province. Within the village are numerous hamlets. Observations from several of these hamlets are discussed separately in subsequent sections. As discussed in GEER (2016), Arquata del Tronto was heavily damaged by the 24 August earthquake. This section summarizes the observations performed after the 30 October 2016 event in Arquata del Tronto and in the adjacent hamlet of Borgo. Details about the geology of the area are discussed in GEER (2016). Figure 6.47 shows the location of representative pictures taken during the reconnaissance to illustrate degrees of damage in Arquata del Tronto and Borgo.

The photographs in Figure 6.48 show Arquata del Tronto after the August and October events, from which a substantial damage increase is evident following the 26 and 30 October earthquakes. Conversely, Borgo did not suffer appreciable cumulated damage, as shown in Figure 6.49 and Figure 6.50. Figure 6.51 shows the collapse of a structure onto the access road for Arquata village. At the time of our November reconnaissance, the village was not accessible and much of the village center was destroyed. The damage level assigned to Arquata del Tronto

(D5) is documented in Figure 6.52. Table 6.3 shows the locations and damage levels for all selected representative structures.



Figure 6.47. Location of representative pictures taken in Arquata del Tronto/Borgo after the 24 August 2016 earthquake (yellow dots), and after the October events (red dots).

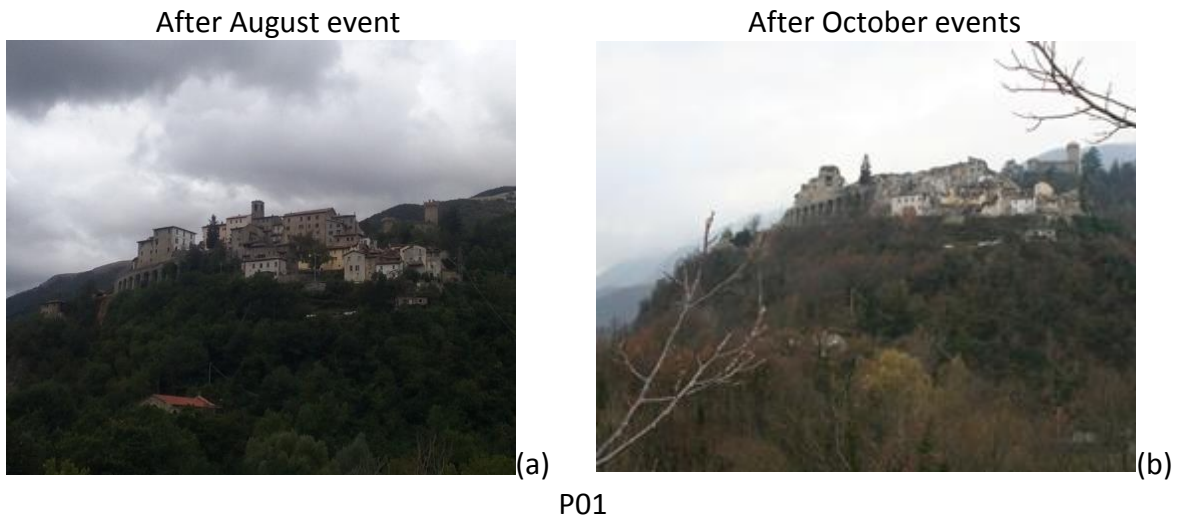


Figure 6.48. Overview of Arquata del Tronto (a) after the 24 August earthquake, and (b) after the October events.

After August event



(a)

After October events



(b)

P03

Figure 6.49. A reinforced masonry building in Borgo (a) after the 24 August earthquake, and (b) after the October events.

After August event



(a)

After October events



(b)

P06

Figure 6.50. A building in Borgo (a) after the 24 August earthquake, and (b) after the October events.



Figure 6.51. Access road to Arquata del Tronto after the October events.



Figure 6.52. Overview of the damage level in Arquata del Tronto after October events.

Table 6.3. Locations of representative pictures with description of reported damage.

Picture	September Damage Level	December Damage Level
P01	Panoramic view of the village. Overall degree of damage D3-D4	Overall degree of damage: D5
P02	D1	
P03	D1	D1-D2
P04	D2	
P05	D2	
P06	D3	D3-D4
P07	D3	
P08	D0	
P10	D4	D5
P11	D4	D5
P12	D5	D5
P13	D5	D5
P14	D4	D5
P15	D2-D3	

6.1.5 Pescara del Tronto

Pescara del Tronto is a hamlet of Arquata del Tronto. As shown in Table 6.1, Pescara del Tronto experienced slightly weaker estimated ground motions during the 30 October event (PGA = 0.38 g) than in the 24 August event (PGA = 0.51 g).

Pescara del Tronto was devastated by the 24 August earthquake (GEER 2016), with nearly half of the structures having collapsed. Figure 6.53 and Figure 6.54 show the evolution of damage from the August (Figure 6.53a and Figure 6.54a) to the October events (Figure 6.53b

and Figure 6.54b). Damage levels in Pescara del Tronto increased as a result of the October events, with approximately 70% of the structures having damage levels D4 or D5 (was 65% following August events).

Figure 6.55 shows locations of selected buildings for which we show photos taken after the August and October events. The cumulative damage is also evident from Figure 6.56. Figure 6.57 shows a photographic overview of the hamlet taken from a common perspective after the August and October events. Figure 6.58 shows screenshots captured from 3D models created from images taken by UAVs. Table 6.4 summarizes locations and damage levels for all selected representative structures.

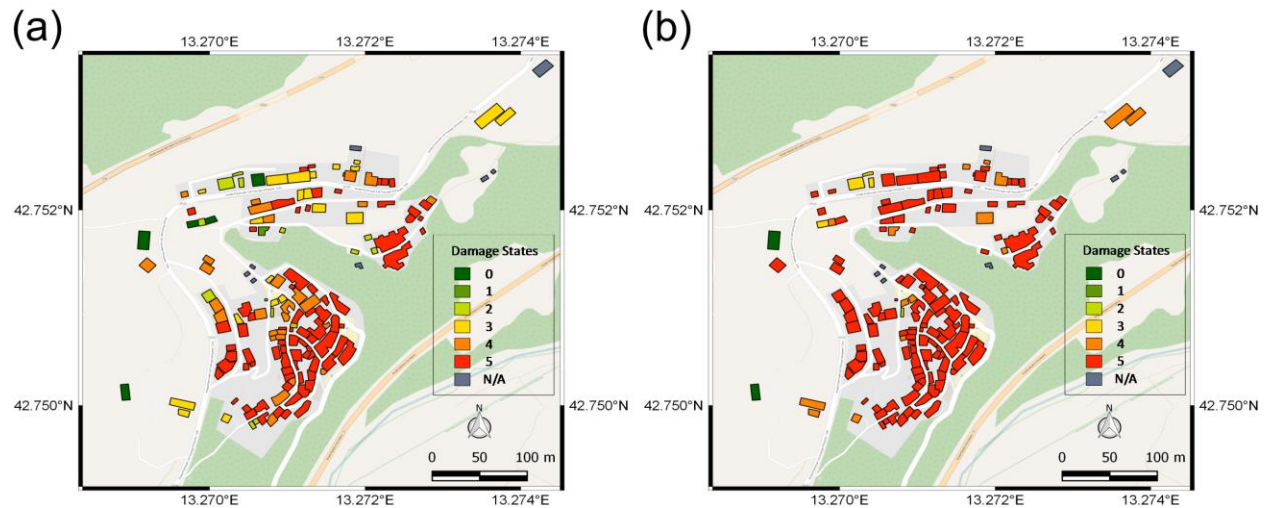


Figure 6.53. Mapped damage levels in Pescara del Tronto: (a) after the 24 August, and (b) the October events.

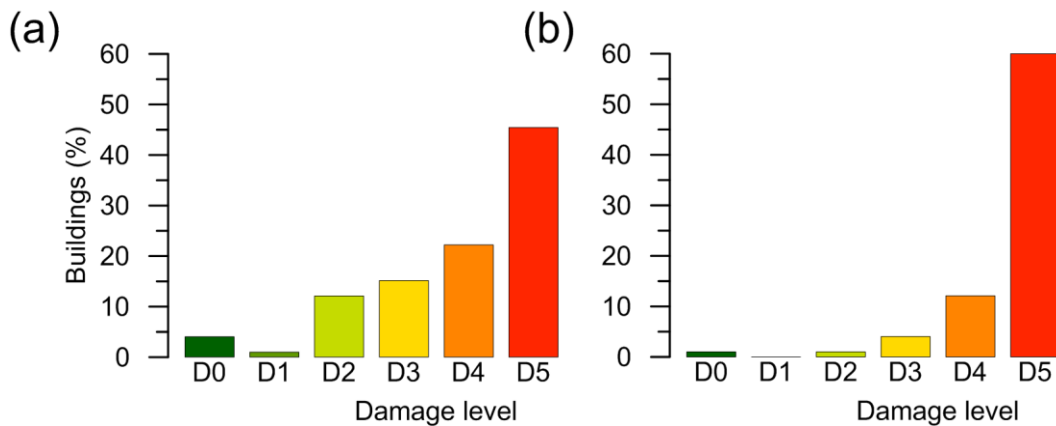


Figure 6.54. Histogram of damage levels in Pescara del Tronto: (a) after the 24 August, and (b) the October events.



Figure 6.55. Location of representative pictures taken in the village after the 24 August (yellow dots) and locations for which we have multi-epoch photos of the same structures (red dots).

After August event



After October events



P01

After August event



After October events



P02

After August event



After October events



P03

After August event



After October events



P06

Figure 6.56. Comparative pictures of selected structures in Pescara del Tronto after the 24 August event, and after the October events.

After August event



After October events



Figure 6.57. Overview of Pescara del Tronto from a common perspective (a) after the 24 August earthquake, and (b) after the October events.

After August event



After October events



Figure 6.58. 3D-model overview of Pescara del Tronto from a common perspective (a) after the 24 August earthquake, and (b) after the October events.

Table 6.4. Locations of representative pictures with description of reported damage.

Picture	September Damage Level	December Damage Level
P01	D3	D5
P02	D3	
P03	D2	D2-D3
P04	D2-D3	
P05	D4	
P06	D5	D5
P08	D5	D5
P09	D4-D5	D5
P10	D4-D5	
P11	D3	D5
P12	D4-D5	
P13	D4-D5	D5

6.1.6 Tufo

Tufo is a hamlet located 5.3 km southwest of Arquata del Tronto. As shown in Table 6.1, Tufo experienced slightly weaker estimated ground motions during the 30 October event (PGA = 0.46 g) than in the 24 August event (PGA = 0.53 g).

The 24 August earthquake produced major damage only to poorly constructed, unretrofitted, and unreinforced masonry buildings (GEER 2016). Damage levels increased markedly from the October events. Figure 6.59 and Figure 6.60 show the evolution of damages from the August (Figure 6.59a and Figure 6.60a) to the October events (Figure 6.59b and Figure 6.60b).

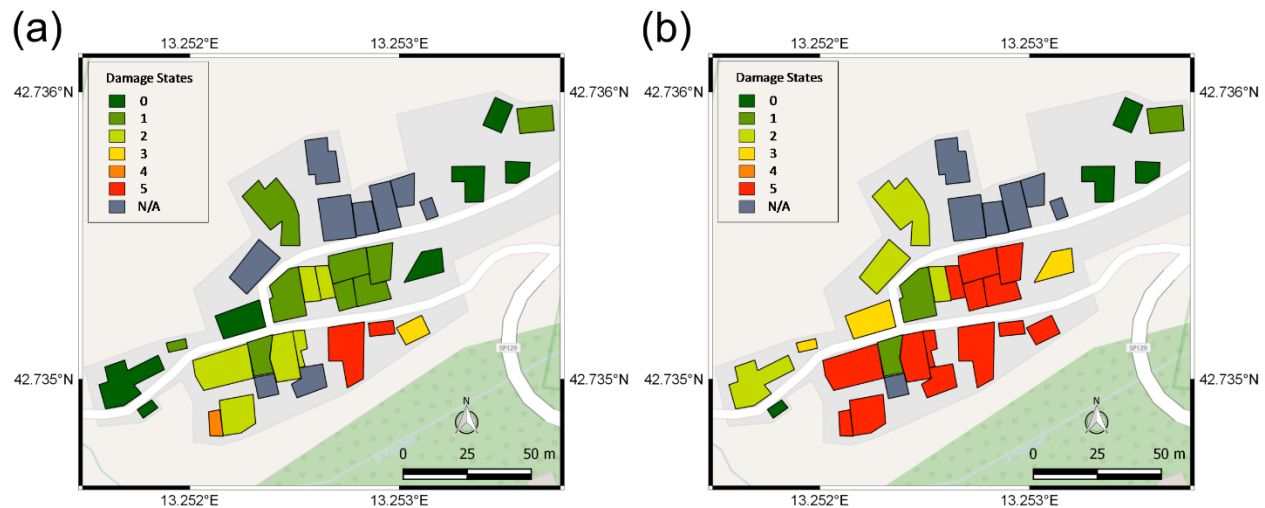


Figure 6.59. Mapped damage levels in Tufo: (a) after the 24 August, and (b) the October events.

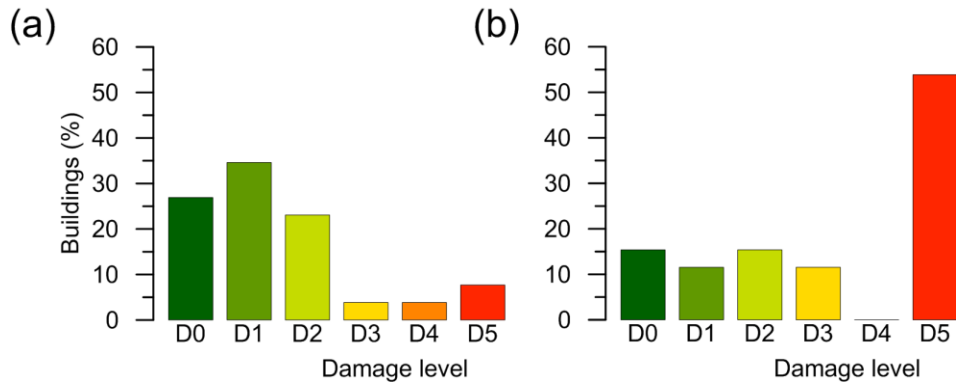


Figure 6.60. Histograms of damage levels in Tufo: (a) after the 24 August, and (b) the October events.

Figure 6.61 shows locations of selected buildings for which we show photos taken after the August and October events. Figure 6.62 shows these pictures, which were taken from a common perspective. Table 6.5 summarizes locations and damage levels for each of the representative structures. Structures M2, M3, and M4 (P1 and P2 in Figure 6.62) are unreinforced masonry buildings. They had damage levels ranging from D1-D3 after the August events and D5 (complete collapse) following the October events. We documented the performance of one reinforced concrete structure (RC1). It had no apparent damage from the August events and damage level D2 after the October events (P3 in Figure 6.62).

An important monument in Tufo is the *Santissima Maria Annunziata Church*. It is a church built in the XVII century that appears to have been recently retrofitted. The church had no apparent damage (D0) from the August events (P4, P5, and P6 in Figure 6.62) and damage level D3 (partial collapse of façade around the rose window; P4 in Figure 6.62) following the October events. Figure 6.62 also shows multiple layers of untied bricks and significant new cracks at corners (P5 and P6), possibly from lack of lateral reinforcement at the corner.

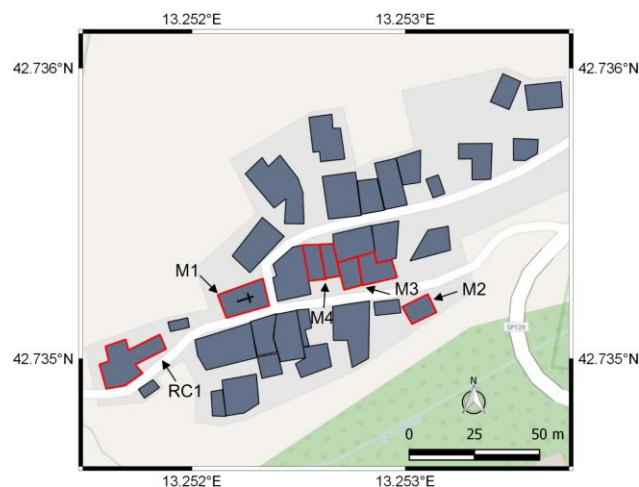


Figure 6.61. Map of the selected representative structures in Tufo.

After August event



After October events



P1

After August event



After October events



P2

After August event



After October events



P3



P4



P5



P6

Figure 6.62. Comparative pictures of selected structures in Tufo after the 24 August event, and after the October events.

Table 6.5. Summary of selected representative structures in Tufo (all pictures show the comparison between September (left) and December (right) inspection).

Picture	DATUM	Description	Location		September Damage Level	December Damage Level
			Lat.	Long.		
P1	WGS-84	Entrance of the historical center (M2-M3)	42.7353°	13.2532°	D3	D5
P2	WGS-84	Masonry buildings (M4)	42.7354°	13.2528°	D1	D5
P3	WGS-84	Reinforced concrete building (RC1)	42.7351°	13.2519°	D0	D2
P4	WGS-84	Santissima Maria Annunziata Church (M1)	42.7351°	13.2522°	D0	D3
P5	WGS-84	Santissima Maria Annunziata Church (M1)	42.7351°	13.2522°	D0	D3
P6	WGS-84	Santissima Maria Annunziata Church (M1)	42.7351°	13.2522°	D0	D3

6.1.7 Montegallo and surrounding hamlets

The village of Montegallo is comprised of 23 dispersed hamlets (Section 5.4.5 of GEER 2016). Here we focus on the hamlets of Astorara, Balzo, Castro, Collefratte, Colleluce, Colle, Piano and Pistrino, which were visited following both the August and October event sequences. As shown in Table 6.1, Montegallo experienced estimated ground motions during the 30 October event of $PGA = 0.25$ g; corresponding values for the 24 August event were $PGA = 0.24$ g. These ground motion estimates do not include possible influences of local site effects.

Damage levels were variable across Montegallo, which is likely a result of variable ground motion levels (mostly as a result of different site effects) and variable construction types and quality. In general, we encountered significant increased damage levels (approximately one class, e.g., D2 to D3) following the October events. A notable exception is Piano, which showed no evidence of damage following either event sequence, despite some examples of apparently poor construction (P14 in Figure 6.63).

Table 6.6 summarizes observed damage patterns for each hamlet. Most of these hamlets were visited (Astorara, Collefratte, Colleluce, Colle, Piano and Pistrino), although Balzo and Castro were assessed from afar due to limited access. In particular, the main access road to Castro was blocked by debris (see Picture P06 below).

Representative pictures of observed damage are reported below and listed in Table 6.7 and shown in Figure 6.63. Multi-epoch photos of the same structures following both event sequences are only available for a limited number of the representative structures.

Table 6.6. Summary of reconnaissance results for Montegalio hamlets.

Hamlet	Structures	Damage description
Astorara	P01*-P02-P03	At the entrance, there are recent buildings with evidence of recent structural retrofitting (D0 level). Many older structures at the back of the village show a D4/5 damage level. At the highest portion of the village a full collapse occurred.
Balzo	P04	General D2/D3 damage level. The village is completely abandoned, while in September after the August main shock it was still populated and with shops and restaurants still in operation.
Castro	P05-P06	Church with a full collapsed apse and the rest of the hamlet with diffused D4/5 damage level. A recent house on the main road with no damage (D0) and still inhabited.
Colle	P07-P08-P09	Similar to Astorara with various levels of structures vulnerability. Recently restored buildings with D0; old masonry buildings with partial or full collapses (D4/D5).
Collefratte	P10-P11*-P12	Very damaged hamlets D3/D3 and a full collapse D5.
Colleluce	P13	Totally D4/5.
Piano	P14*	Generally D0/D1.
Pistrino	P15*-P16*-P17*	The initial part of the village (Pistrino di Sopra) was seriously damaged (D3/D4), whereas the other part (Pitrino di sotto, 1 km from Piano) showed minor problems (D0/D2) except for a collapsed small stones wall.

* Pictures that show the comparison between September (left) and December (right) inspections

Table 6.7. Summary of pictures and structures inspected in Montegalio hamlets.

Picture	Hamlet	DATUM	Position		September damage Level	December damage Level
			Lat.	Long.		
P01*	Astorara	WGS-84	42.837436°	13.31119°	D0-D1	D0-D1
P02	Astorara	WGS-84	42.837222°	13.31055°	-	D0-D1
P03	Astorara	WGS-84	42.837222°	13.31055°	-	D4-D5
P04	Balzo	WGS-84	42.8425°	13.33222°	-	D2-D3
P05	Castro	WGS-84	42.84583°	13.32527°	-	D4-D5
P06	Castro	WGS-84	42.84722°	13.32638°	-	D4-D5
P07	Colle	WGS-84	42.84416°	13.30583°	-	D4-D5
P08	Colle	WGS-84	42.84416°	13.30583°	-	D4-D5
P09	Colle	WGS-84	42.84416°	13.30583°	-	D4-D5
P10	Collefratte	WGS-84	42.83952°	13.31907°	-	D5
P11*	Collefratte	WGS-84	42.83934°	13.31907°	D3	D3
P12	Collefratte	WGS-84	42.83952°	13.31907°	-	D3-D4

Table 6.7 cont. Summary of pictures and structures inspected in Montegallo hamlets.

Picture	Hamlet	DATUM	Position		September damage Level	December damage Level
			Lat.	Long.		
P13	Colleluce	WGS-84	42.83805°	13.30722°	-	D4-D5
P14*	Piano	WGS-84	42.854116°	13.339129°	D0	D0
P15*	Pistrino	WGS-84	42.855579°	13.332649°	D0-D1	D0-D1
P16*	Pistrino	WGS-84	42.855579°	13.332642°	D0-D1	D0-D1
P17*	Pistrino	WGS-84	42.855579°	13.332649°	D0-D1	D0-D1

* Pictures that show the comparison between September (left) and December (right) inspection

After August event



After October events



P01 (Astorara)

After October events



P02 (Astorara)



P03 (Astorara)



P04 (Balzo)



P05 (Castro)



P06 (Castro)



P07 (Colle)



P08 (Colle)



P09 (Colle)



P10 (Collefratte)



P11 (Collefratte)



P12 (Collefratte)

P13 (Colleluce)

After August event

After October events



P14 (Piano)

After August event

After October events



P15 (Pistrino)

After August event



After October events



P16 (Pistrino)



P17 (Pistrino)

Figure 6.63. Representative pictures taken in Montegallo during the GEER survey (see Table 6.6 and Table 6.7).

6.2 Newly inspected areas

6.2.1 Visso

Visso is a village of about 1100 inhabitants located in the Macerata province. Besides the main village, Visso also contains the hamlets of Aschio, Borgo San Giovanni, Croce, Cupi, Fematre, Macereto, Mevale, Molini di Visso, Orvano, Ponte Chiusita, Rasenna, Riofreddo, Villa Sant'Antonio. We performed reconnaissance only in the main town.

Visso is located 4 km northwest of the epicenter of the **M5.9** 26 October 2016 event and 10 km north of the **M6.5** 30 October earthquake. As shown in Table 6.1, Visso experienced

estimated ground motions during the 26 October event of $PGA = 0.44$, corresponding values for the 30 October and 24 August events are $PGA = 0.38$ and 0.25 g respectively.

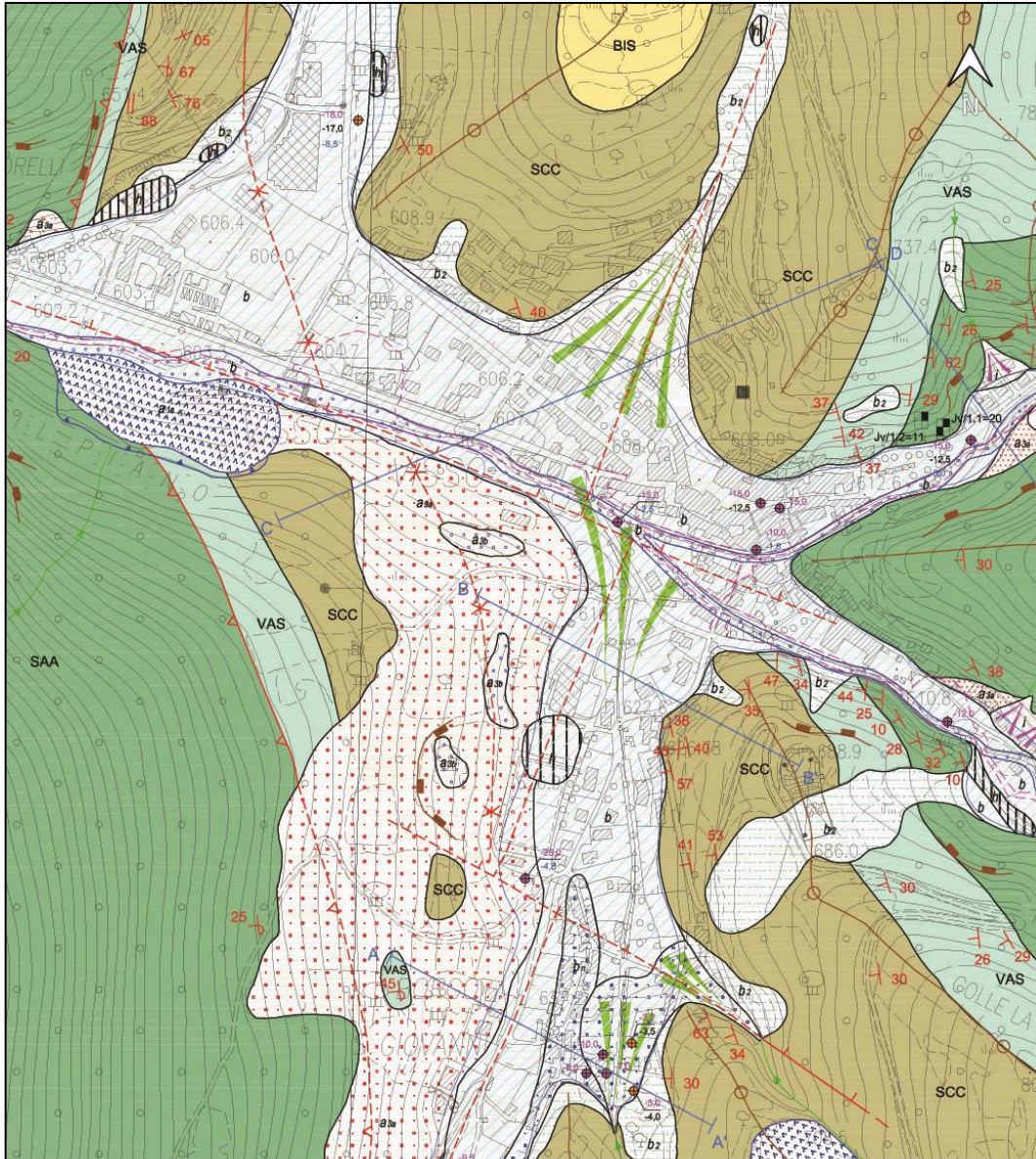
The village was reported to have suffered intensity IX MCS during the 1 December 1328 Valnerina earthquake ($M=6.5$) and VII-VIII MCS during the 12 May 1730 Valnerina earthquake ($M=6$) (Rovida et al. 2016).

From a morphological viewpoint, Visso is located in a depressed area of the Sibillini Mountains, at the Umbria-Marche regional boundary, where the thrust-and fold belt of the Central Apennines involves a Meso-Cenozoic multilayered sedimentary sequence composed of limestones, marly limestones, marls and flysches (e.g. Calamita et al., 1994). Thrust sheets are incorporated to form an east-verging tectonic wedge that was definitively uplifted at the Lower Pliocene. The compressive structures are reworked and dissected by normal fault systems, mainly striking NW-SE. Quaternary normal faults led to the formation of morphological depressed areas and the evolution of intramountain basins. (Gaudiosi et al., 2016). In the studied area of Visso, the tectonostratigraphic setting includes the Cretaceous Miocene basinal succession made of, from bottom to top (Figure 6.64), the Scaglia Rossa Fmt (SAA), Scaglia Variegata Fmt (VAS) and Scaglia Cinerea Fmt (SCC), (also known as Scaglia Formation), the Bisciario Fmt (BIS) and the Marne con Cerrognia Fmt (not shown in Figure 6.64).

These formations are organized in a monoclinial architecture striking from NNW-SSE to N-S, and dipping to W with low-to-moderate angles (see also the regional geological cartography available at <http://www.ambiente.marche.it/Territorio>). Quaternary continental deposits cover all the basinal succession. The latter consist of alluvial deposits, eluvio-colluvial deposits, and widespread slope deposits. The maximum thickness of the continental sedimentary deposits occurring in the central part of Visso village is about 40 m (Figure 6.64).

Locations of representative structures inspected in Visso by the GEER team are reported in Figure 6.65, while details (WGS-84 coordinates, damage level of buildings, other notes) are given in Table 6.8.

The pictures are presented in Figure 6.66. The historical center consists mainly of unreinforced masonry structures (some of which have been recently retrofitted), 2-3 stories in height. Outside of the historical center, modern reinforced concrete structures were encountered (see P01-P02).



LEGEND

- BIS** Bisciario Formation.
Aquitanian-Burdigalian.
- SCC** Scaglia Cinerea Formation.
Upper Eocene-Aquitanian.
- VAS** Scaglia Variiegata Formation.
Middle Eocene-Upper Eocene
- SAA** Scaglia Rossa Formation.
Late Cretaceous-Middle Eocene
- FUC** Marne a Fucoidi Formation.
Aptian-Albian.

GEOLOGICAL ELEMENTS

- Strata
- Trace of geological section

- Anthropic layer. Holoc.
- Active landslide. Holoc.
- Inactive landslide. Pleist.-Holoc.
- Debris flow deposit. Upper Pleist.-Holoc.
- Debris flow deposit. Pleist.
- Alluvial deposit. Holoc.
- Alluvial terraces. Pleist.-Holoc.
- Eluvio-colluvium deposit.
Pleist.-Holoc.
- Mixture: alluvial fan and debris
flow deposit. Holoc.



(a)

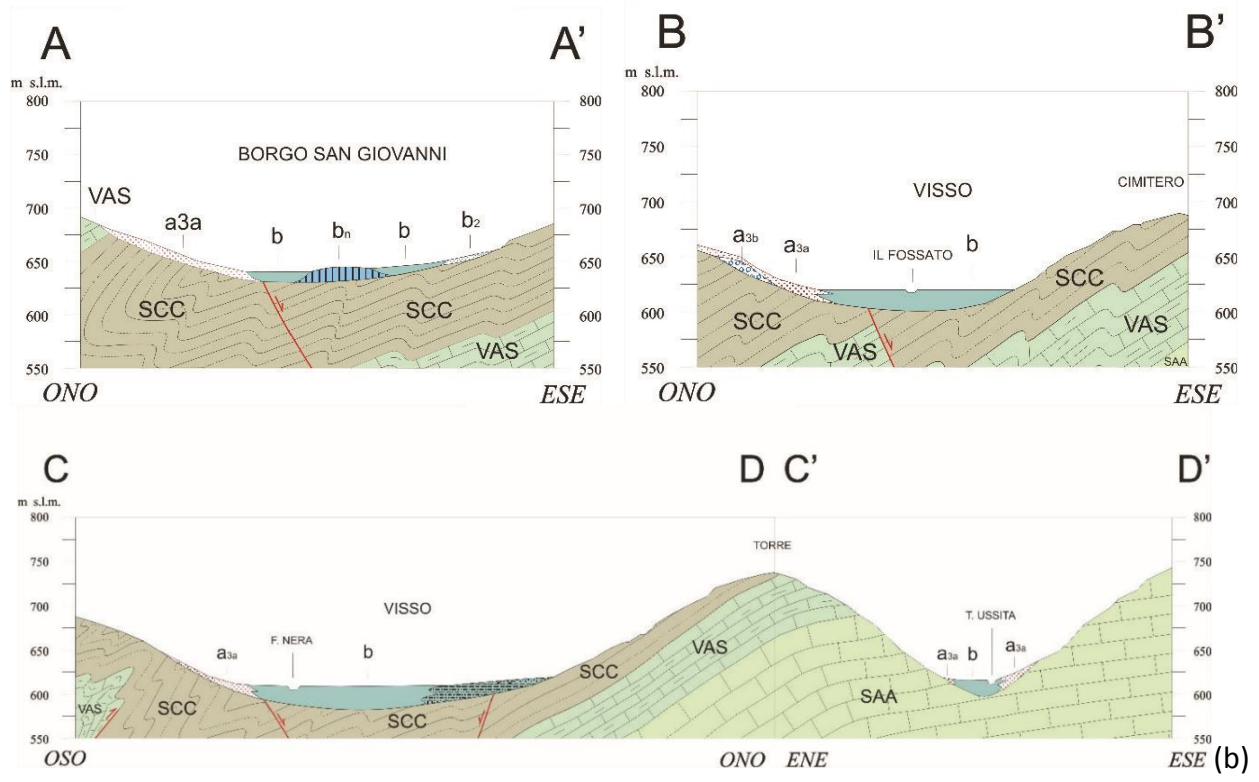


Figure 6.64. Geological map (a) and cross-sections (b) of the Visso village area (Regione Marche, 2012)



Figure 6.65. Locations of representative structures inspected in the Visso village (see Table 6.8 for details).

Table 6.8. Locations of representative structures with damage descriptions.

Visso				
Picture	Datum	Location		Damage Level / notes
		Lat	Long	
P01	WGS-84	42.933162°	13.082982°	D2/D3
P02a	WGS-84	42.931833°	13.083941°	D3
P02b	WGS-84	42.931833°	13.083941°	D3
P03	WGS-84	42.931775°	13.085806°	D5
P04	WGS-84	42.931675°	13.085514°	D4
P05	WGS-84	42.931780°	13.086362°	D3
P06	WGS-84	42.931513°	13.085827°	D3
P07	WGS-84	42.931193°	13.086627°	D5
P08	WGS-84	42.931358°	13.087140°	D3/D4
P09	WGS-84	42.931451°	13.087402°	D3/D4
P10	WGS-84	42.931493°	13.087173°	D4
P11	WGS-84	42.930915°	13.087582°	D3/D4
P12	WGS-84	42.930899°	13.088604°	D4
P13	WGS-84	42.931320°	13.088029°	D1
P14	WGS-84	42.931400°	13.088317°	D1
P15	WGS-84	42.931441°	13.088427°	D2/D3
P16	WGS-84	42.929789°	13.089711°	Scaglia Rossa outcropping
P17	WGS-84	42.930484°	13.088355°	D3/D4
P18a	WGS-84	42.930618°	13.087851°	D3/D4
P18b	WGS-84	42.930618°	13.087851°	D3/D4
P19	WGS-84	42.930221°	13.087917°	D3
P20	WGS-84	42.930042°	13.088132°	D3
P21	WGS-84	42.929836°	13.087886°	D3/D4
P22	WGS-84	42.929783°	13.088463°	D1
P23	WGS-84	42.930057°	13.088793°	D3
P24	WGS-84	42.929911°	13.088493°	D2
P25	WGS-84	42.929883°	13.089065°	D1
P26	WGS-84	42.929676°	13.089440°	D2
P27	WGS-84	42.930756°	13.089196°	D3/D4



P01



P02a



P02b



P03



P04



P05



P06



P07



P08



P09



P10



P11



P12



P13



P14



P15



P16



P17



P18a



P18b



P19



P20



P21



P22



P23



P24



P25



P26



P27

Figure 6.66. Representative pictures taken in Visso during the survey (see Table 6.8).

The village was significantly damaged by the October events. However, the degree of damage to buildings is spatially variable. A tentative damage zonation map is reported in Figure 6.67. Damage levels as high as D3-D4 are concentrated in the historical center, especially the portion founded on the quaternary continental deposits (alluvial deposits, eluvio-colluvial deposits, and widespread slope deposits). Minor damage (D1-D2) was encountered in the portion founded on the SCC rock (Scaglia Cinerea Formation). In the NW portion (outside the historical center), we encountered D2-D3 on average. This part of the village is located on quaternary deposits. However, the relatively minor vulnerability of buildings was probably responsible for the minor damage observed in this part of the historical center.

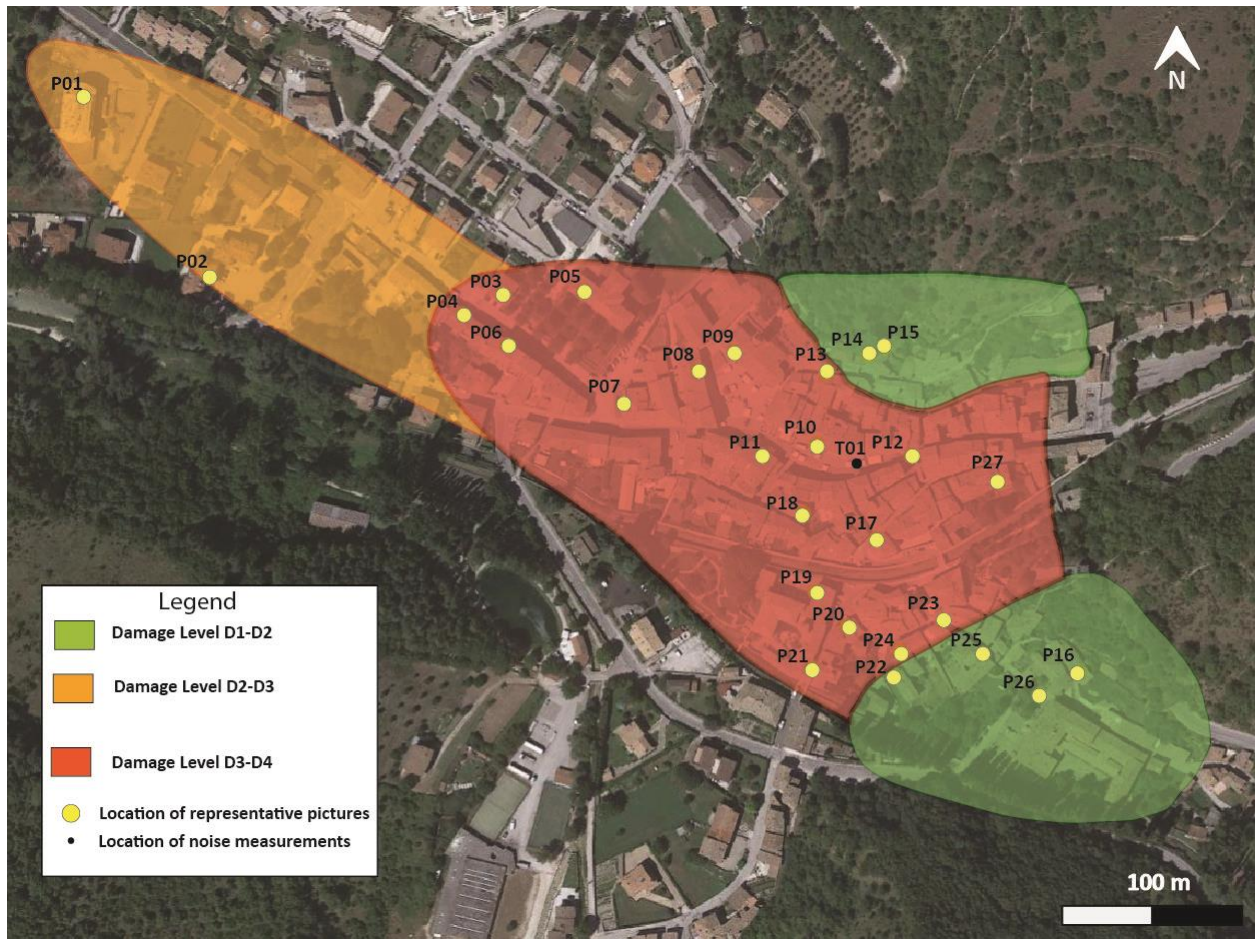


Figure 6.67. Damage zonation within the villages of Visso village.

Microtremor noise measurements (location T01 in Figure 6.67) were carried out during the survey in the most damage zone of the historical center. A portable Tromino tomograph was employed and the total duration of each measurement was approximately 15 minutes. Horizontal-to-vertical (H/V) spectral ratios were computed by using the geometrical mean of horizontal components. Moreover, in order to investigate preferential directions of the amplification (i.e., polarization of ground motion), H/V ratios were computed by rotating the horizontal component between 0° and 180° (directional or polar HVSR). Both H/V and polar H/V

are reported in Figure 6.68. We observe no large H/V peaks at T1, suggesting the lack of a site condition producing a strong resonant site response.

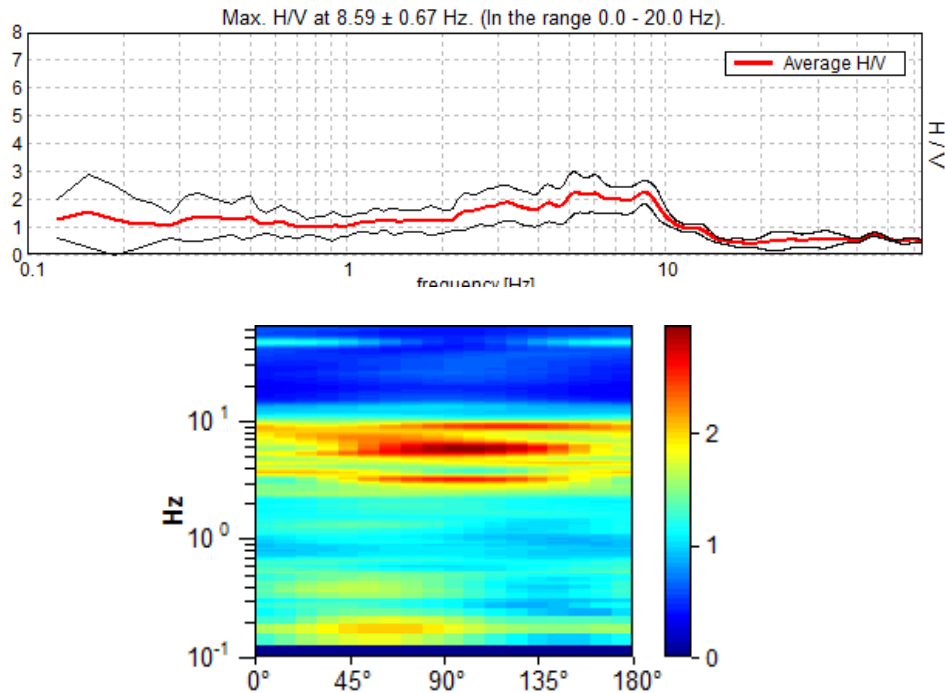


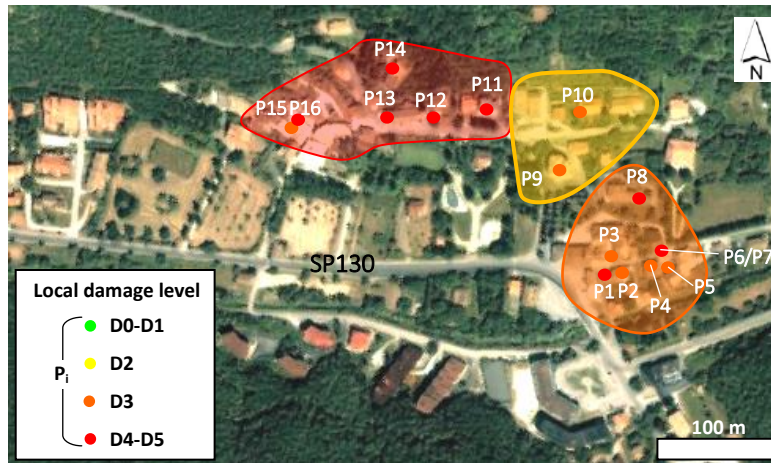
Figure 6.68. Noise measurement T01 results in terms of H/V spectral ratio (up) and H/V polar plots (bottom).

The damage in Visso was likely related both to the presence of some vulnerable buildings in the historical center and to stratigraphic amplification effects related to the presence of quaternary soils resting on Scaglia rock formation (see also preliminary conclusions by Gaudiosi et al., 2016).

6.2.2 Ussita

Ussita is a small village of about 450 inhabitants located in the Macerata province. Ussita consists of 13 small hamlets, including Fluminata (the administrative center), Pieve, Vallazza, Tempori and Sasso. Ussita is crossed by the Ussita creek (tributary of Nera River). Most of the buildings in the historical center are of masonry construction. As shown in Table 6.1, Ussita experienced estimated ground motions during the 26 October event of $PGA = 0.46$ g, $PGA = 0.38$ g during the 30 October event, and $PGA = 0.22$ g during the 24 August event.

Figure 6.69 shows locations of representative structures inspected in Ussita and maps damage zones within the village. Damage levels were generally between D3 and D4. Figure 6.70 shows pictures of selected structures in the area of Ussita that experienced the higher level of damage.



OVERALL DAMAGE LEVELS:

- D3: Overall, major damage to non-structural elements and limited to significant damage to load bearing elements can be identified.
- D3-D4 - Heterogeneous area, which seems to be always characterized by high damages to non structural elements, often by damages to load bearing elements and in some cases also by local collapse.
- D4-D5 - Strip characterized by structures interested by huge damage to load bearing elements and local collapse.

Figure 6.69. Locations of representative structures inspected in Ussita, and damage zonation within the village.





Facade: 2011 (Google Maps)

December 2016

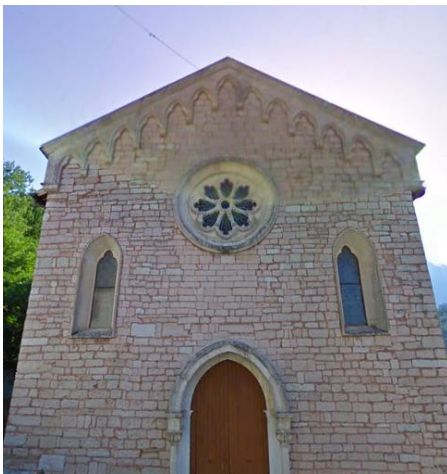


Figure 6.70. Representative pictures taken in Ussita (P13)

6.2.3 Tolentino

Tolentino is a town of about 20000 inhabitants, located in the province of Macerata in the Marche region, in the middle Chienti valley. Tolentino comprises more than 40 hamlets and it is one of the most populated towns in the earthquake area. As shown in Table 6.1, Tolentino experienced estimated ground motions during the 26 October event of $PGA = 0.10$ g, $PGA = 0.11$ g during the 30 October event, and $PGA = 0.09$ g during the 24 August event. Historically the Tolentino area was involved in many important seismic events, in particular in 1690, 1941, 1781, 1943, 1972 and 1997.

The area is a crucial point for the San Nicola da Tolentino Church and Monastery (Figure 6.71), which represent an iconic monument for the catholic community of the region. It is a Roman Catholic Church and minor basilica that is part of the Augustinian monastery in Tolentino. The church is a former cathedral of the Roman Catholic Diocese of Tolentino, suppressed in 1586. It contains architecture and art from the 14th through the 17th century. The imposing marble façade of the church was constructed over the centuries, and was completed in the 17th century. The most relevant portion is an important decorated chapel of the Giotto's

school. The façade is presently the most critical part of the structure, since the 30 October earthquake triggered a relative movement at the highest part of the façade. Moreover, there are plans for the installation of a permanent seismic monitoring system by Politecnico di Torino and Nagoya City University.

Geologically the mountainous area close to Tolentino is mainly composed of calcareous deposits, very resistant to erosion, which then originate steep slopes like those along the Chienti valley upstream of Pievefavera. More easily eroded sediments, such as marl, clay and sandstone, form the hilly area (Regione Marche, 2012). Tolentino is underlain by the Camerino geological formation, which is a mixture of chalky-sulphurous 30-40 m thick layers. The area shows blackish clays and bituminous laminated marl, reddish-brown limestone, microcrystalline gypsum in thin layers and laminated gypsum. In the same area calcareous marl, marl gray-greenish clay, sometimes with reddish bands at the base of thickness about 200 meters are also encountered. The geological map in Figure 6.72 and the Italian *Carg* Project define two main formations for Tolentino:

Chalky-sulphurous: Outcropping from Villa Martinozzi (Valley of the Potenza River) and just west of Tolentino and sits directly on the *Schlier*. It has similar characteristics to those of the same unit outcropping in the southern part of the Aliforni-S. Severino basin; here the level of re-sedimented chalks is missing. There are also stromatolitic limestones, sometimes with traces of bioturbation.

Laga, post-evaporitic part: It consists of a turbidite sequence predominantly pelitic-sandstone, containing three arenaceous-pelitic horizons. The first consists of an alternation of clays and silty clay marl gray-blue color, thin to medium layers, and sandstones in thin to medium layers with sand-clay ratio less than one. Sandstones of yellowish fine-grained and medium, in tabular layers medium to thick, and marl gray-blue silty clays represent the arenaceous-pelitic horizons. Under the second horizon, the guide volcano-derived level is located of variable thickness between 0.5 m and 3 m, consisting of 3-4 layers of blended whitish volcanic ash. This area forms the new fore deep turbidite post-evaporite. The overall characteristics are similar to those seen in the pre-evaporitic.

Tolentino was deeply damaged during the freedom battles conducted by the Italian resistance movement against the Nazi army after the World War II. For this reason, the town was almost totally reconstructed except for the center that was likely protected by the citizens (especially the San Nicola church). Figure 6.73 outlines three zones with different building types: (1) ancient town center (red), (2) industrial (yellow), and (3) contemporary-residential (blue). In the town center, masonry one or multi-stories structures are very common and retrofitting was adopted for many of them. The industrial part is located on the downhill and it is the most recent part of the town. The residential area is the typical postwar housing with a widespread use of the first reinforced concrete technologies of the 1960s and 1970s. Here also many 5-6 stories apartment buildings are diffused. Figure 6.73 also shows in green the locations

of the detailed inspection areas and the numbering of the following pictures described in Table 6.9.

Table 6.9 lists the locations of representative structures photographed and documented in the GEER reconnaissance. Figure 6.74 shows these structures. The town-center was partially damaged, especially Piazza della Libertà (main square of the town), where most of the buildings were strengthened with structural supports.

The San Nicola church is out of service and not accessible to the public as a result of diffused damage to the façade and the unstable wood decorated roof. The adjacent convent is a complex and heterogeneous building made by different and subsequent enlargements. For this reason, there are different states of damage inside the huge complex, depending on the structural type (masonry or reinforced concrete).

Very interesting is the Viale Vittorio Veneto-Viale Martin Luther King-Via Kennedy area. In this neighborhood, an evident site effect was observed, since diffused building damages are observed much more prominently than in the other parts of the town. In particular, the buildings along the eastern side of Martin Luther King road are recent reinforced concrete frames 5-to-8 floors above ground from the 1980s. Most of these buildings were seriously damaged and abandoned at the time of the reconnaissance. On the other side of the road, smaller buildings (most of them 3 floors above ground) suffered much less damage and were apparently in use at the time of the reconnaissance.

At the roundabout connecting Viale Vittorio Veneto e Viale Martin Luther King a retaining wall next to a rail bridge was seriously damaged. In particular, the wall was secured by huge concrete blocks in order to maintain the stability of the back private garden.



Figure 6.71. San Nicola da Tolentino church, façade (left) and interior part (right) (before earthquake events).

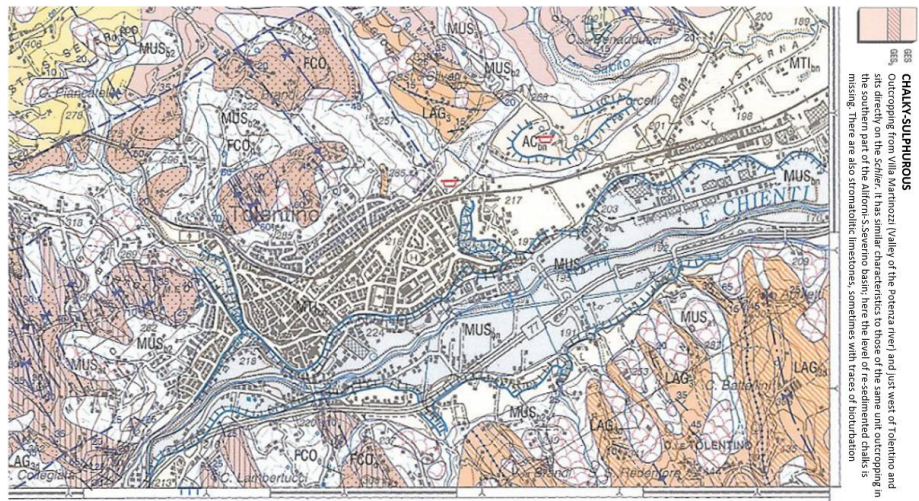


Figure 6.72. Geological map of the Tolentino area.

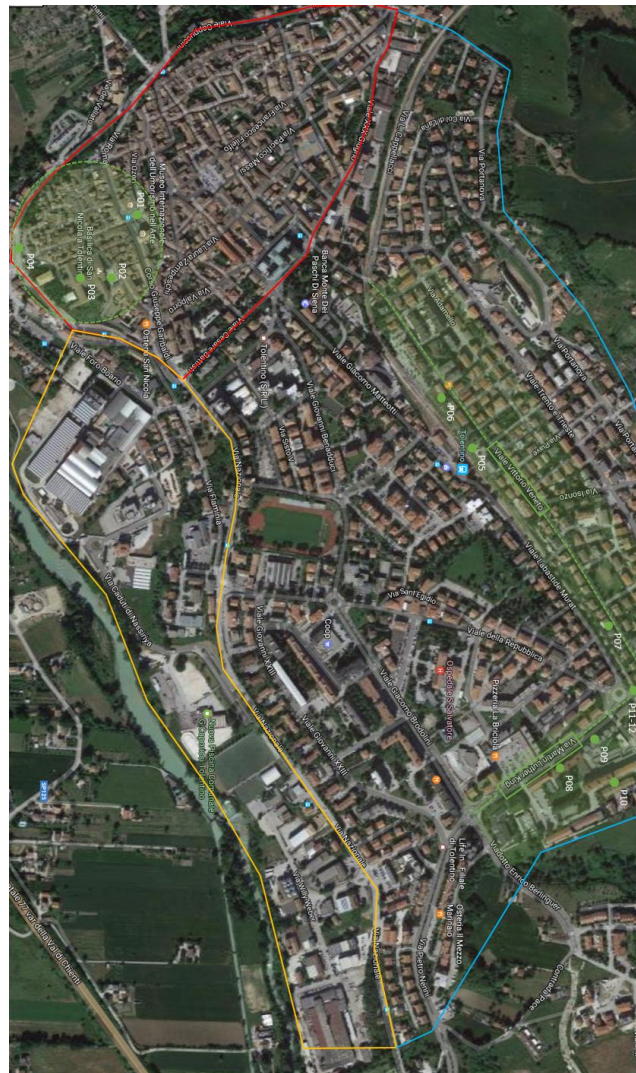


Figure 6.73. Tolentino reconnaissance map: in green the most damaged zones.



P01 (Piazza della Libertà)



P02a-b-c Basilica di San Nicola (Saint Nicholas Church)



P02d-e-f Basilica di San Nicola (Saint Nicholas Church)



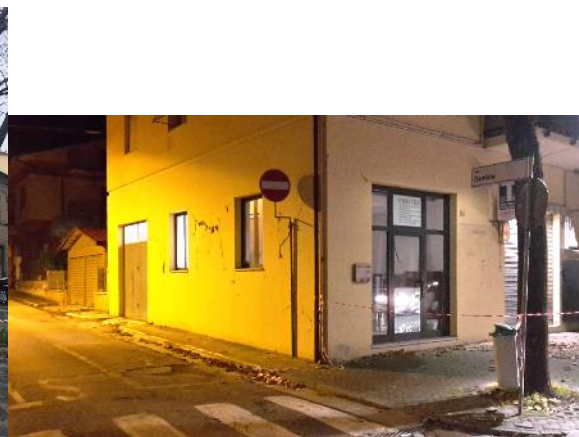
P03a-b Cloister of the Basilica di San Nicola (Saint Nicholas Church)



P03c-d-e Monastery of the Basilica di San Nicola (Saint Nicholas Church)



P04 (Via Filzi)



P05 (Viale Vittorio Veneto)



P06-P07 (Viale Vittorio Veneto)



P08-P09 (Via Martin Luther King)



P10 (Via Kennedy)



P11 (Retaining wall)



P12 (Damaged rail bridge)

Figure 6.74. Representative pictures taken in Tolentino during the GEER survey (see Table 6.9).

Table 6.9. Summary of pictures and structures inspected in Tolentino.

Picture	DATUM	Description	Location		October Damage Level
			Lat.	Long.	
P01a	WGS-84	Piazza della libertà (town hall)	43.20851°	13.28464°	D1-2
P01b	WGS-84	Piazza della libertà (bell tower)			
P02a	WGS-84	San Nicola Church (facade)	43.21344°	13.28864°	D2
P02b	WGS-84	San Nicola church (lateral facade)			
P02c	WGS-84	San Nicola Church (chapel)			
P02d	WGS-84	San Nicola church (damaged nave column)			
P02e	WGS-84	San Nicola church (damaged entrance wall)			
P02f	WGS-84	San Nicola church (retaining nest above the main altar)			
P03a	WGS-84	Monastery (retrofitted main tower)	43.20748°	13.2862°	D2
P03b	WGS-84	Monastery (damaged cloister walkway)			
P03c	WGS-84	Monastery (damaged room)			
P03d	WGS-84	Monastery (damaged room)			
P03e	WGS-84	Monastery (damaged room)			
P04	WGS-84	Viale Filzi	43.20673°	13.2849°	D1-2
P05	WGS-84	Viale Vittorio Veneto	43.21416°	13.28944°	D2

Table 6.9 cont. Summary of pictures and structures inspected in Tolentino.

Picture	DATUM	Description	Location		October Damage Level
			Lat.	Long.	
P06	WGS-84	Viale Vittorio Veneto	43.21399°	13.28918°	D2
P07	WGS-84	Viale Vittorio Veneto	43.21694°	13.29416°	D2
P08	WGS-84	Via Martin Luther King	43.21505°	13.29764°	D3
P09	WGS-84	Via Martin Luther King	43.21555°	13.2975°	D3
P10	WGS-84	Via Kennedy	43.21722°	13.29777°	D3
P11	WGS-84	Retaining wall	43.21874°	13.29686°	D3
P12	WGS-84	Damaged rail bridge	43.21874°	13.29686°	D2

6.2.4 San Severino

San Severino Marche is a village (municipality) in the Province of Macerata in the Italian region Marche, located about 50 kilometers southwest of Ancona and about 25 kilometers southwest of Macerata. It is an important center in Macerata County and it is roughly 8 km from Tolentino (Figure 6.75), on the opposite side of the Potenza River. It is populated by about 12000 inhabitants and it comprises more than 40 hamlets: Agello, Aliforni, Berta, Biagi, Cagnore, Carpignano, Case Bruciate, Casette, Castel San Pietro, Cesolo, Chigiano, Colleluce, Collicelli, Colmone, Colotto, Corciano, Cusiano, Elcito, Gagliannuovo, Gaglianvecchio, Granali, Isola, Maricella, Marciano, Monticole, Orpiano, Palazzata, Parolito, Patrignolo, Pitino, Portolo, Rocchetta, San Mauro, Sant'Elena, Serralta, Serripola, Serrone, Stigliano, Taccoli, Ugliano and Villanova. As shown in Table 6.1, San Severino experienced estimated ground motions during the 26 October event of $PGA = 0.12$ g, $PGA = 0.12$ g during the 30 October event, and $PGA = 0.07$ g during the 24 August event.

The artistic heritage of San Severino Marche is remarkable and strongly linked to the period of maximum independence of the municipality and the first decades of church government. The numerous Gothic churches located in the city and in the territory and the works left by the local school of painting belong to that period. At the beginning and the end of the fifteenth century, brothers Salimbeni and Lorenzo d'Alessandro were the leaders of that important school of painting. The most important and known square is Piazza del Popolo (Figure 6.76).

San Severino Marche was hardly damaged by the October 2016 event sequence, which is notable given its proximity to Tolentino (both villages have essentially identical estimated ground motions). As a result of the October earthquake events, more than 500 buildings collapsed, with 1500 displaced people without any accommodation. Especially in the Uvaiolo neighborhood, (one of the four red zones of the village) more than 40 buildings were scheduled for demolition by the Italian Firefighters Department (CNVVF).

The local geology is similar to Tolentino and three formations are most frequent in the territory of San Severino Marche: Schlier, chalky-sulphurous formation (as in Tolentino) and the Laga formation. The first is characterized by marl, calcareous marl and marl clay grayish 100-250 m thick. The second is made up of clay and blackish bituminous marl, laminated, reddish brown in color, microcrystalline gypsum in thin layers and laminated gypsum overall thickness of 30-40 m. The third formation is divided into pre-evaporitic, pelitic-sandstone, sandstone, arenaceous-pelitic typologies. An excerpt of the geological map with the legend is provided in Figure 6.77.

Table 6.10 lists the locations of representative structures photographed and documented in the GEER reconnaissance. Figure 6.78 shows the locations of these structures, while Figure 6.79 shows a close-up view of the Uvaiolo neighborhood. Figure 6.80 shows photographs of these structures.

Major attention during the reconnaissance was paid to Via Mazzini and Via Rossini neighborhoods, since evident site effects were detected. The first is located on a rise and is parallel to another very damaged road (Via Monti Sibillini). The latter is very close to the Potenza River and the structures were likely built up on the ancient riverbed. Close to Via Rossini there is Villa Collio, a restaurant-villa that was severely damaged. Furthermore, a quick inspection of two towers located on the village hill was carried out (Torre Smeducci and the old Cathedral Tower), as there are plans for the installations of a permanent monitoring system by Politecnico di Torino and Nagoya City University.

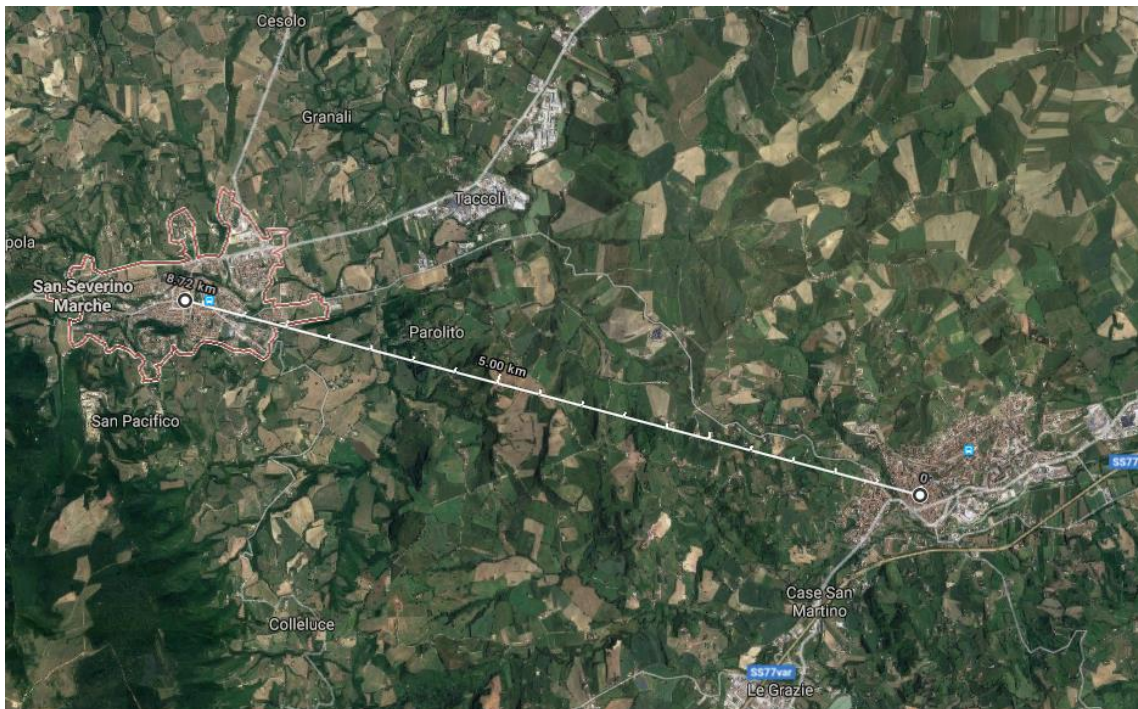


Figure 6.75. Relative position and distance between San Severino Marche and Tolentino.



Figure 6.76. Piazza del Popolo, San Severino Marche (before seismic events).

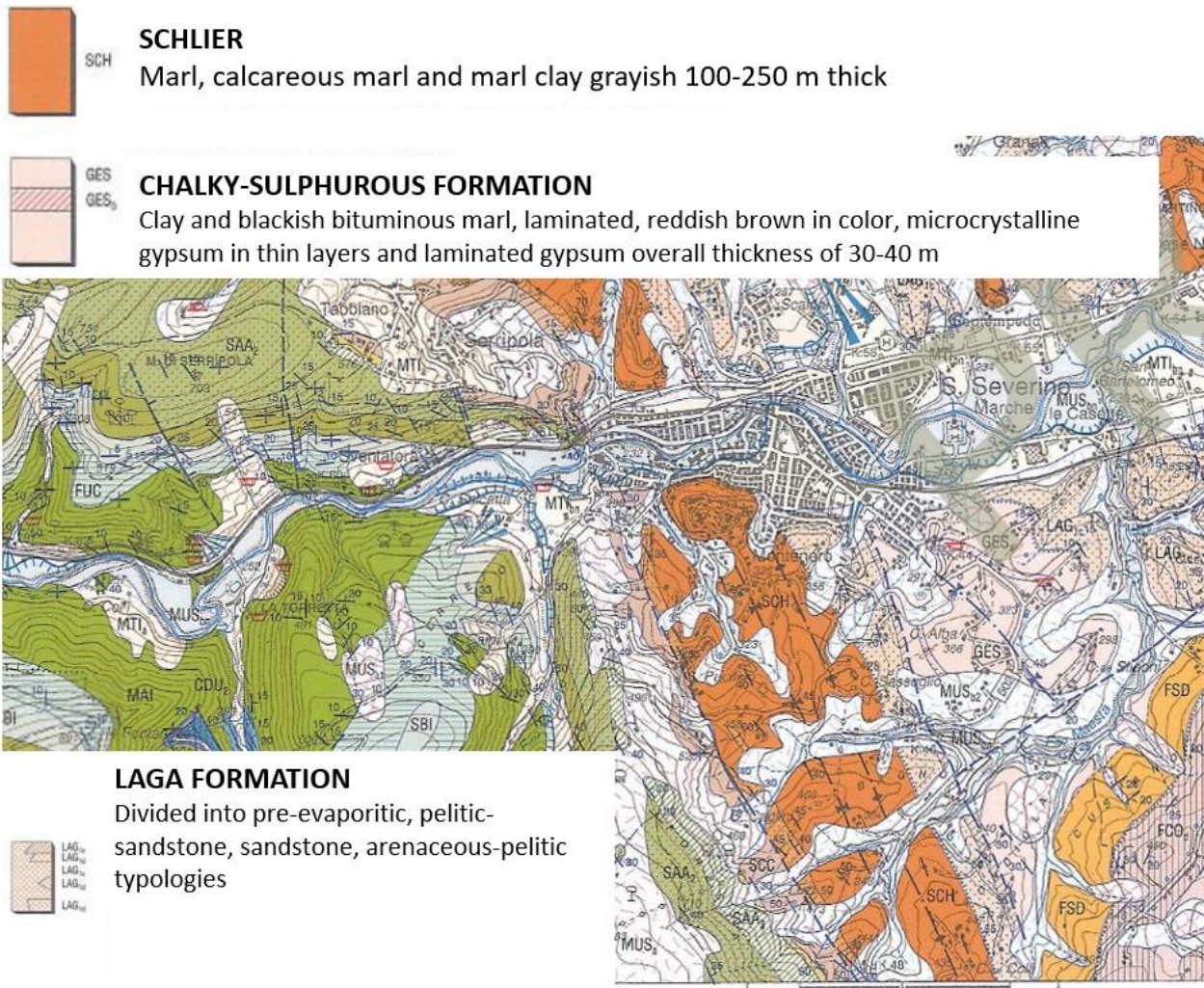


Figure 6.77. Geological map of the San Severino area.



Figure 6.78. Summary reconnaissance map for San Severino Marche.

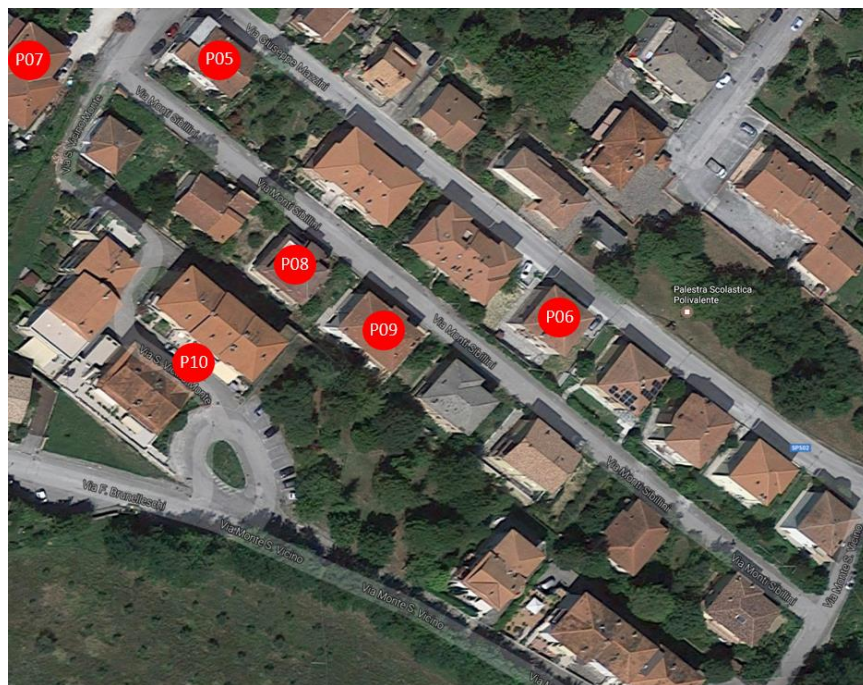


Figure 6.79. Summary reconnaissance map for San Severino Marche (zoom on the Uvaiolo neighborhood).



P1



P2



P3



P4



P5a



P5b



P6a



P6b



P6c



P7



P8



P9



P10



P11



P12



P13



P14

Figure 6.80. Representative pictures taken in San Severino Marche during the GEER survey (see Table 6.10).

Table 6.10. Summary of pictures and structures inspected in San Severino Marche.

Picture	DATUM	Description	Position		October Damage Level
			Lat.	Long.	
P01	WGS-84	Via Mazzini 76	43.22710°	13.18678°	D1-D2
P02	WGS-84	Via Mazzini 84	43.22605°	13.18883°	D2-D3
P03	WGS-84	Via Mazzini 86	43.2259°	13.1890°	D2
P04	WGS-84	Via Mazzini 91	43.2257°	13.1893°	D2
P05a	WGS-84	Via Mazzini 94	43.2255°	13.1897°	D4
P05b	WGS-84	Via Mazzini 94	43.2255°	13.1897°	D4
P06a	WGS-84	Via Mazzini 115	43.2249°	13.1907°	D4-D5
P06b	WGS-84	Via Mazzini 115	43.2249°	13.1907°	D4-D5
P06c	WGS-84	Via Mazzini 115	43.2249°	13.1907°	D4-D5
P07	WGS-84	Intersection Mazzini-Monti Sibillini	43.2255°	13.1897°	D2
P08	WGS-84	Via Monti Sibillini 6	43.2250°	13.1899°	D2
P09	WGS-84	Via Monti Sibillini 15	43.2248°	13.1902°	D2-D3
P10	WGS-84	Via Monte San Vicino	43.2246°	13.1898°	D0
P11	WGS-84	Via Rossini 1	43.2336°	13.1845°	D4
P12	WGS-84	Via Padre Giuseppe Zampa 30	43.2326°	13.1863°	D2
P13	WGS-84	Villa Collio	43.2369°	13.1841°	D2
P14	WGS-84	Smeducci Tower	43.2258°	13.1760°	D0

6.2.5 Camerino

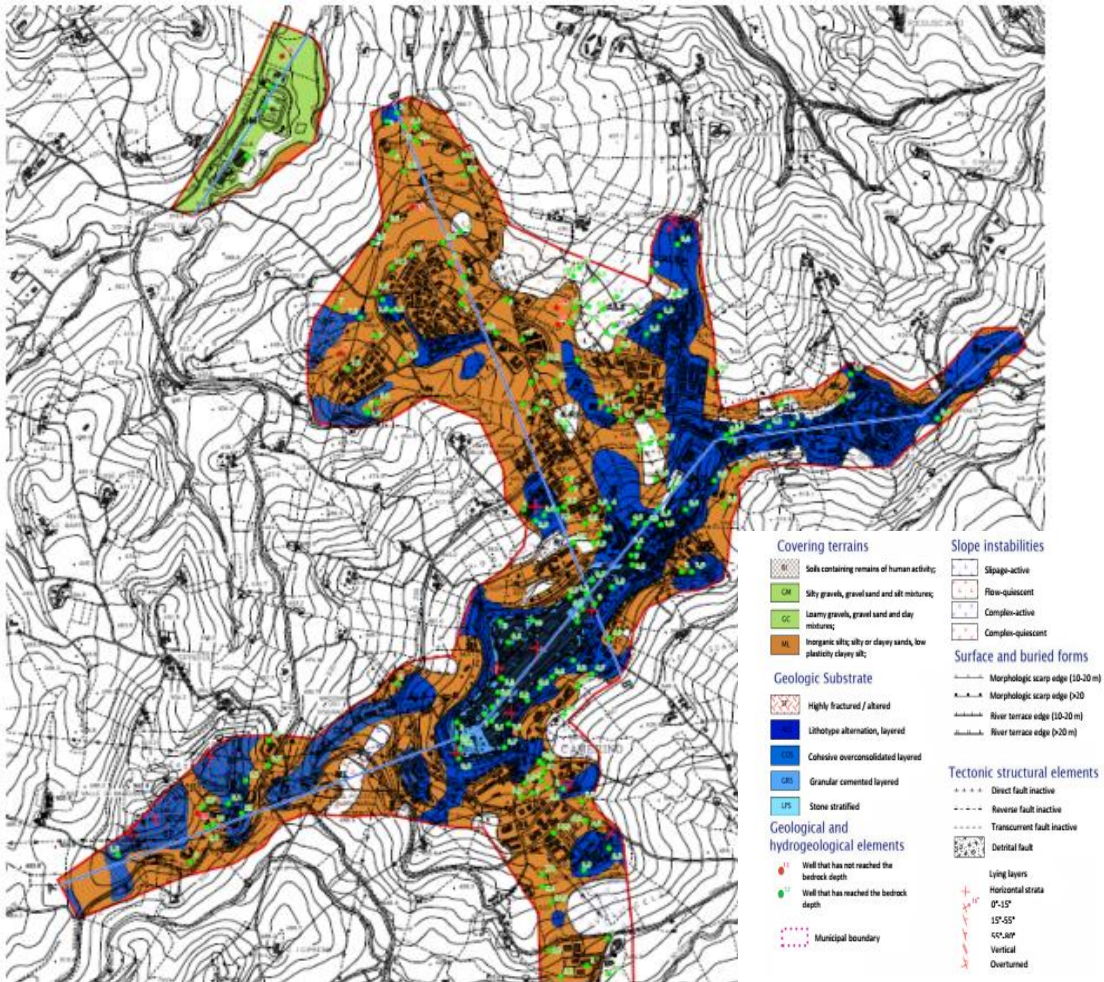
Camerino (43.134666, 13.067698) is a village of about 7000 inhabitants located in the province of Macerata. Apart from the main village, Camerino has 43 hamlets: Arnano, Baregnano, Calcina, Campolarzo, Canepina, Capolapiaggia, Cappuccini, Casale, Colle, Costa San Severo, Letegge, Mecciano, Mergnano San Pietro, Mergnano San Savino, Morro, Nibbiano, Paganico, Palentuccio, Parrocchia Palente, Piegusciano, Polverina, Pontelatrave, Pozzuolo, Raggiano, Sabbietta, Sabbietta di Sopra, Sabbietta di Sotto, San Luca, San Marcello, Sant'Erasmo, Santa Lucia, Sellano, Selvazzano, Sentino, Sfercia, Statte, Strada, Torrone, Tuseggia, Valdiea, Valle San Martino, Valle Vegenana and Varano di Sotto. Our reconnaissance activity focused on the historic center. As shown in Table 6.1, Camerino experienced estimated ground motions during the 26 October event of $PGA = 0.16$ g, $PGA = 0.20$ g during the 30 October event, and $PGA = 0.07$ g during the 24 August event.

Geological bedrock in the area consists of alternation of layered soils, mainly composed of arenaceous and pelithic-arenaceous lithofacies, sometimes with clayey-calcareous marl, called “Scaglia cinerea” and “Schlier”. The above formations are locally covered by eluvio-colluvial soils, made of silt or low-plasticity clay, or alluvial soil in the valley. The historic center is placed

on the arenaceous formation referred to as “Formazione delle Arenarie di Camerino” (Figure 6.81).

The village was reported to have been damaged during the seismic sequence of 1279 and 1328 and the Reatin earthquake of 1703, which destroyed Norcia. The strongest earthquake in Camerino was in 1799. An excerpt of the historical seismicity as reported in the CPTI database by INGV is reported in Figure 6.82.

(a)



(b)

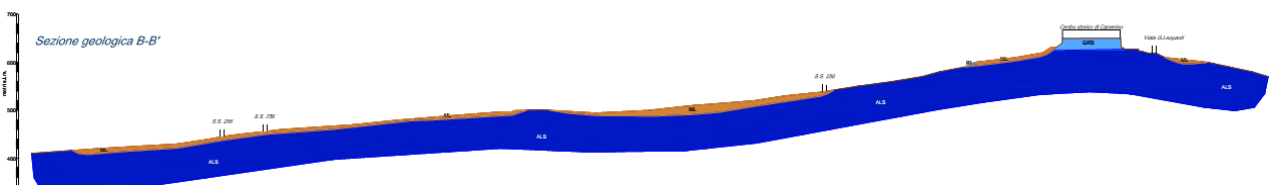


Figure 6.81. Geological map of Camerino (a) and cross section BB' (b) (Regione Marche, 2012).

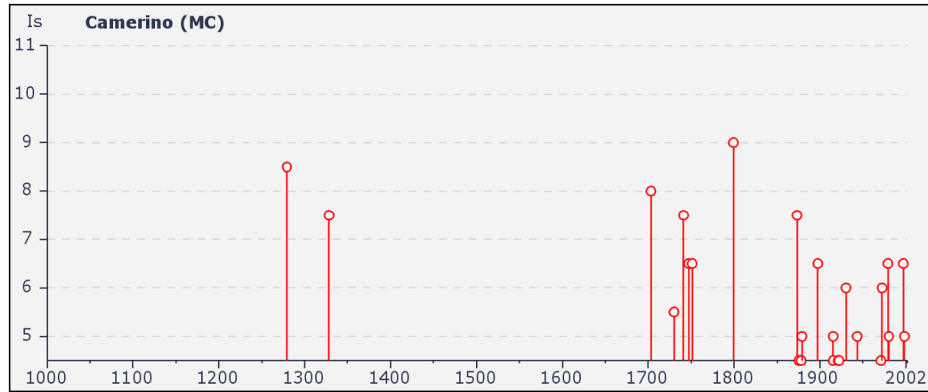


Figure 6.82. Historical earthquakes occurred in Camerino (CPTI-INGV).

Figure 6.83 and Table 6.11 show locations of representative buildings inspected in the historic center of Camerino, including the red zone. Figure 6.84 shows photographs of these representative structures, which include both masonry and reinforced concrete dwellings two to four stories in height. The average damage level in the inspected zone was D2.



Figure 6.83. Locations of the representative structures inspected in Camerino (including red zone) (see Table 6.11 for details).

Table 6.11. Locations of representative structures with damage descriptions.

Picture	DATUM	Location		October Damage Level
		Lat.	Long.	
P01	WGS-84	43.135994	13.068003	D0
P02	WGS-84	43.135741	13.067888	D1
P03	WGS-84			
P04	WGS-84	43.135960	13.068939	D1
P05	WGS-84	43.135602	13.068546	D2
P06	WGS-84	43.135548	13.068208	D1
P07	WGS-84	43.135506	13.067865	D1
P08	WGS-84	43.135373	13.067644	D1
P09	WGS-84	43.135123	13.067159	D1
P10	WGS-84	43.134963	13.067013	D1
P11	WGS-84	43.135038	13.067331	D1
P12	WGS-84	43.134792	13.067035	D1
P13	WGS-84	43.134883	13.066948	D1
P14	WGS-84	43.134697	13.066760	D1
P15	WGS-84	43.134601	13.066622	D1
P16	WGS-84	43.134589	13.066787	D1
P17	WGS-84	43.134287	13.066866	D1
P18	WGS-84			
P19	WGS-84			
P20	WGS-84	43.134461	13.066458	D1
P21	WGS-84	43.134261	13.066439	D1
P22	WGS-84	43.134685	13.065791	D1
P23	WGS-84	43.134871	13.065710	D1
P24	WGS-84	43.134946	13.065849	D2
P25	WGS-84			
P26	WGS-84			
P27	WGS-84			
P28	WGS-84			
P29	WGS-84			
P30	WGS-84	43.135224	13.065621	D2
P31	WGS-84	43.134340	13.065885	D1
P32	WGS-84			
P33	WGS-84	43.134232	13.065760	D1
P34	WGS-84	43.134087	13.065607	D1
P35	WGS-84	43.133977	13.065722	D1
P36	WGS-84	43.133901	13.065422	D1
P37	WGS-84	43.133760	13.065284	D1
P38	WGS-84	43.132951	13.064639	D1
P39	WGS-84	43.132966	13.065040	D2
P40	WGS-84	43.132579	13.064910	D0
P41	WGS-84			
P42	WGS-84	43.132345	13.064641	D1

Table 6.11 cont. Location of representative structures with damage descriptions.

Picture	DATUM	Location		October Damage Level
		Lat.	Long.	
P43	WGS-84			
P44	WGS-84			
P45	WGS-84	43.131907	13.064037	D4
P46	WGS-84			
P47	WGS-84			
P48	WGS-84	43.131885	13.063674	D2-D3
P49	WGS-84			
P50	WGS-84			
P51	WGS-84	43.132024	13.063564	D1
P52	WGS-84	43.132091	13.063757	D1
P53	WGS-84	43.132374	13.063907	D1
P54	WGS-84	43.132246	13.064093	D2
P55	WGS-84	43.132351	13.064252	D1
P56	WGS-84	43.131747	13.062434	D2
P57	WGS-84	43.131631	13.063391	D4
P58	WGS-84	43.131555	13.063705	D1
P59	WGS-84			
P60	WGS-84	43.131457	13.062811	D1
P61	WGS-84			
P62	WGS-84	43.130020	13.060464	D0-D1
P63	WGS-84	43.129763	13.060739	D1
P64	WGS-84	43.139449	13.070221	D0
P65	WGS-84			
P66	WGS-84	43.137732	13.068879	D4
P67	WGS-84	43.138131	13.068340	D0



P01



P02



P03



P04



P05



P06



P07



P08



P09



P10



P11



P12



P13



P14



P15



P16



P17



P18



P19



P20



P21



P22



P23



P24



P25



P26



P27



P28



P29



P30



P31



P32



P33



P34



P35



P36



P37



P38



P39



P40



P41



P42



P43



P44



P45



P46



P47



P48



P49



P50



P51



P52



P53



P54



P55



P56



P57



P58



P59



P60



P61



P62



P63



P64



P65



P66



P67

Figure 6.84. Representative pictures taken in Camerino (see Table 6.11 for details).

6.2.6 Pievebovigliana

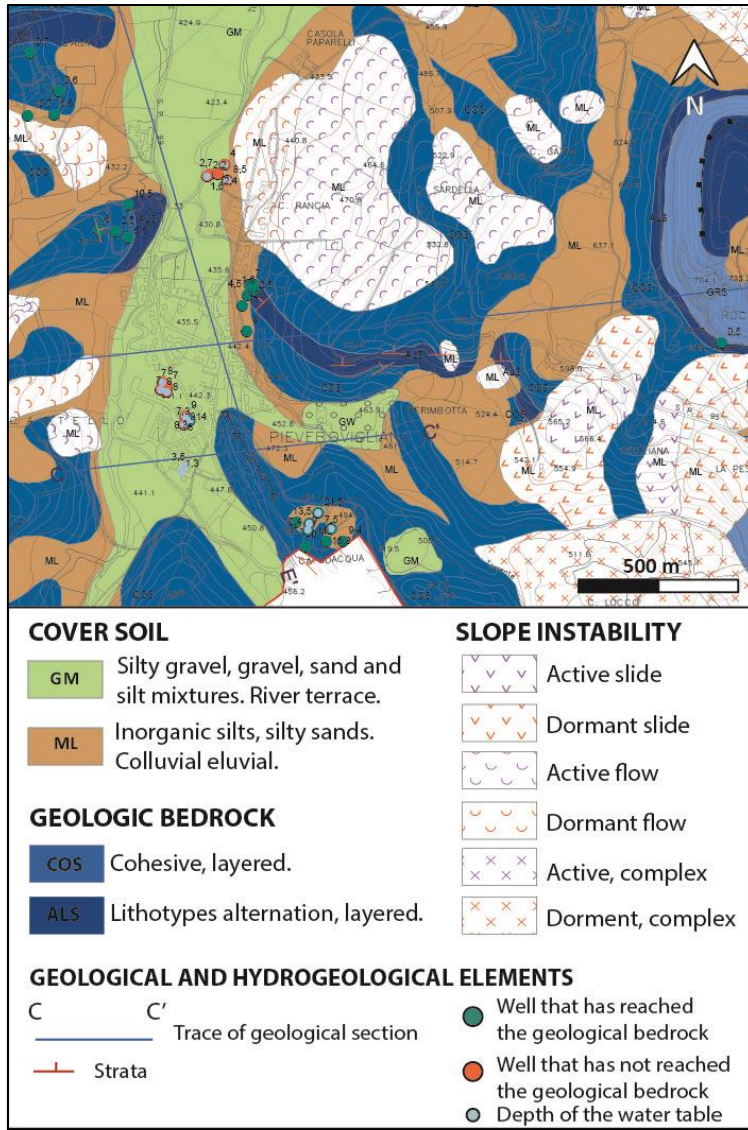
Pievebovigliana is a municipality in the Province of Macerata (Marche), located about 70 km southwest of Ancona and about 40 km southwest of Macerata, within the Monti Sibillini National Park. As shown in Table 6.1, Pievebovigliana experienced estimated ground motions during the 26 October event of $PGA = 0.20\text{ g}$, $PGA = 0.23\text{ g}$ during the 30 October event, and

PGA = 0.09 g during the 24 August event. According to historical documents (Rovida et al., 2016), the village suffered a maximum macroseismic intensity of VII-VIII MCS during the 4 December 1832 Appennino umbro-marchigiano earthquake ($M=5.4$) while an I=VII is reported for the 28 July 1799 Appennino umbro-marchigiano earthquake ($M=6.2$).

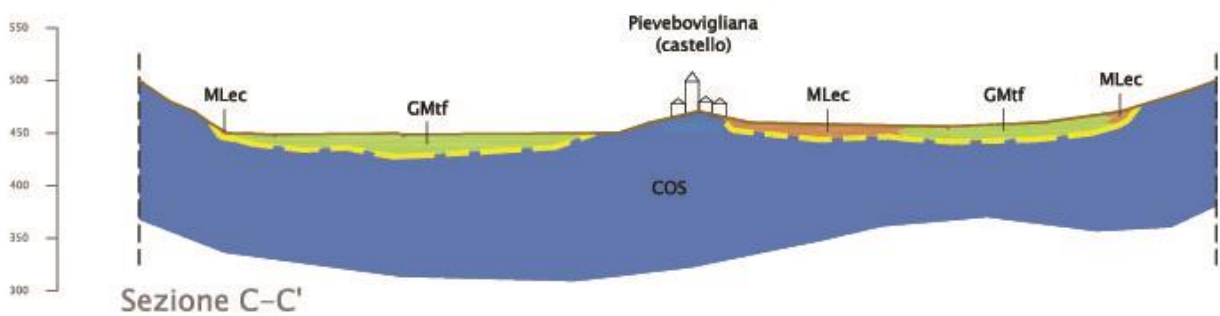
The area is characterized by the well-known Umbria-Marche Succession and, from a structural viewpoint, the area represents a connecting point between limestone/marly limestones ridges at west and the depressed area in the eastern sector. Alteration of clayey marls, limestones and Marly limestones characterize this area. The regional geological cartography, available at <http://www.ambiente.marche.it/Territorio>), are represented by lithologic units of Scaglia Cinerea (SCC), Bisciaro (BIS), Schlier (SCH) and alternation of arenaceous, pelitic-arenaceous and pelitic lithotypes, called « Molasse ». In the geologic-geotechnical map (Figure 6.85) SCC and SCH formations are indicated as COS (Cohesive and layered bedrock), while BIS and Molasse as ALS (bedrock characterized by a layered lithotypes alternation). Regarding the cover soils, they are represented by holocene alluvial terraced deposits of Musone River Synthem, MUSbn in the regional geological cartography, and by holocenic colluvial/eluvial deposits, MUSb2 in the regional geological cartography. The first are mostly made of coarse soils (silty gravel, mixture of gravel, sand and silt) with a shear wave velocity (V_s) of about 400 m/s (Regione Marche, 2014), the second are made of inorganic silt, silty fine sand and clayey fine sands, silt and clay of low plasticity. These latter deposits are characterized by a shear wave velocity (V_s) of about 300 m/s.

Locations of representative photos taken in Pievebovigliana by the GEER team are reported in Figure 6.86. The pictures are presented in Figure 6.87. The historical center consists mainly of un-reinforced old masonry structures, 2-3 stories in height. Some of these structures have retrofitted. Outside of the historical center, isolated modern masonry and reinforced concrete structures were found (see P17-P18). Table 6.12 shows details and damage levels for the inspected structures.

Pievebovigliana was significantly damaged by the October events. However, the degree of damage to buildings is quite variable across the village. A preliminary damage zonation is reported in Figure 6.88. Damage levels as high as D3-D4 are concentrated in the southern portion (area of Castello or S. Maria Assunta church) built on a slight ridge oriented NNW-SSE that is comprised of Scaglia-Cinerea bedrock. Topographic site effects may have impacted structural performance in this area. The northern and central portions of the village generally have damage levels D2 to D2-D3. These areas are mainly located on alluvial terraced deposits. Minor damage was observed along the western portion of the village; the northern part of this area, located on alluvium, has relatively modern buildings (see P17) while the southern area is on bedrock at the toe of the Scaglia-Cinerea ridge.



a)



b)

Figure 6.85. (a) Geological map of Pievebovigliana village and (b) geological section showing the main stratigraphical relationships (Regione Marche, 2014).

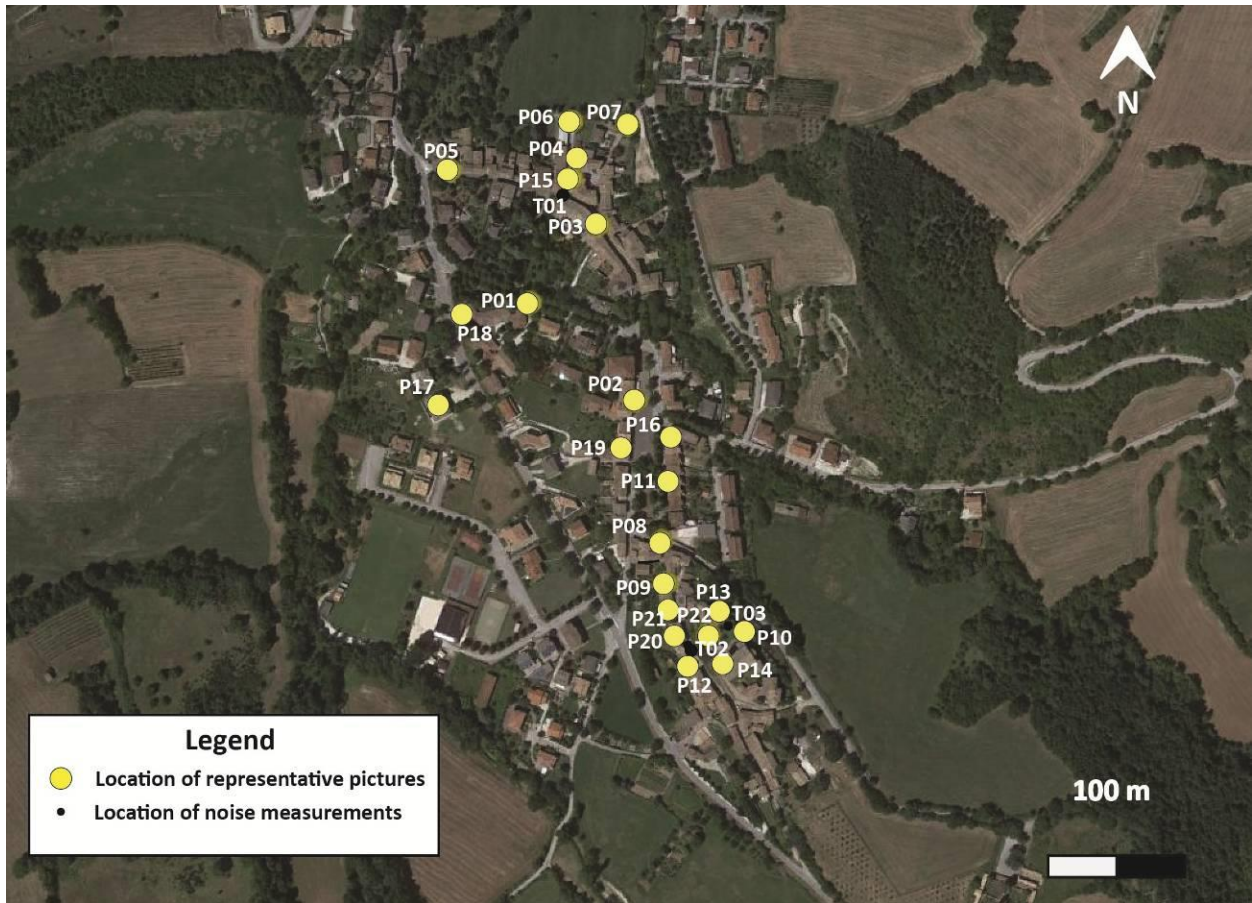


Figure 6.86. Locations of representative structures inspected in Pievebovigliana (see Table 6.12 for details).



P01



P02



P03



P04a



P04b



P05



P06



P07



P08



P09



P10



P11



P12



P13



P14



P15



P16



P17



P18a



P18b



P19



P20



P21



P22

Figure 6.87. Representative pictures in Pievebovigliana during the survey (see Table 6.12).

Table 6.12. Locations of representative structures with damage descriptions

Pievebovigliana				
Picture	Datum	Location		Damage Level
		Lat	Long	
P01	WGS-84	43.062787°	13.083464°	D3
P02	WGS-84	43.061945°	13.084577°	D3
P03	WGS-84	43.063389°	13.084261°	D3
P04	WGS-84	43.063783°	13.083991°	D3
P05	WGS-84	43.063783°	13.083991°	D3
P06	WGS-84	43.063899°	13.082638°	D2
P07	WGS-84	43.064250°	13.084019°	D3-D4
P08	WGS-84	43.064200°	13.084639°	D2-D3
P09	WGS-84	43.060806°	13.084796°	D2
P10	WGS-84	43.060468°	13.084825°	D3-D4
P11	WGS-84	43.060045°	13.085259°	D1-D2
P12	WGS-84	43.061275°	13.084864°	D1-D2
P13	WGS-84	43.059584°	13.085267°	D3-D4
P14	WGS-84	43.060023°	13.085500°	D2-D3
P15	WGS-84	43.059860°	13.085446°	D3
P16	WGS-84	43.063751°	13.084271°	D3
P17	WGS-84	43.061613°	13.084808°	D1
P18a-P18b	WGS-84	43.063833°	13.082469°	D2-D3
P19	WGS-84	43.061650°	13.084506°	D2
P20	WGS-84	43.060083°	13.084933°	D1
P21	WGS-84	43.060303°	13.085108°	D1
P22	WGS-84	43.059975°	13.085269°	D3

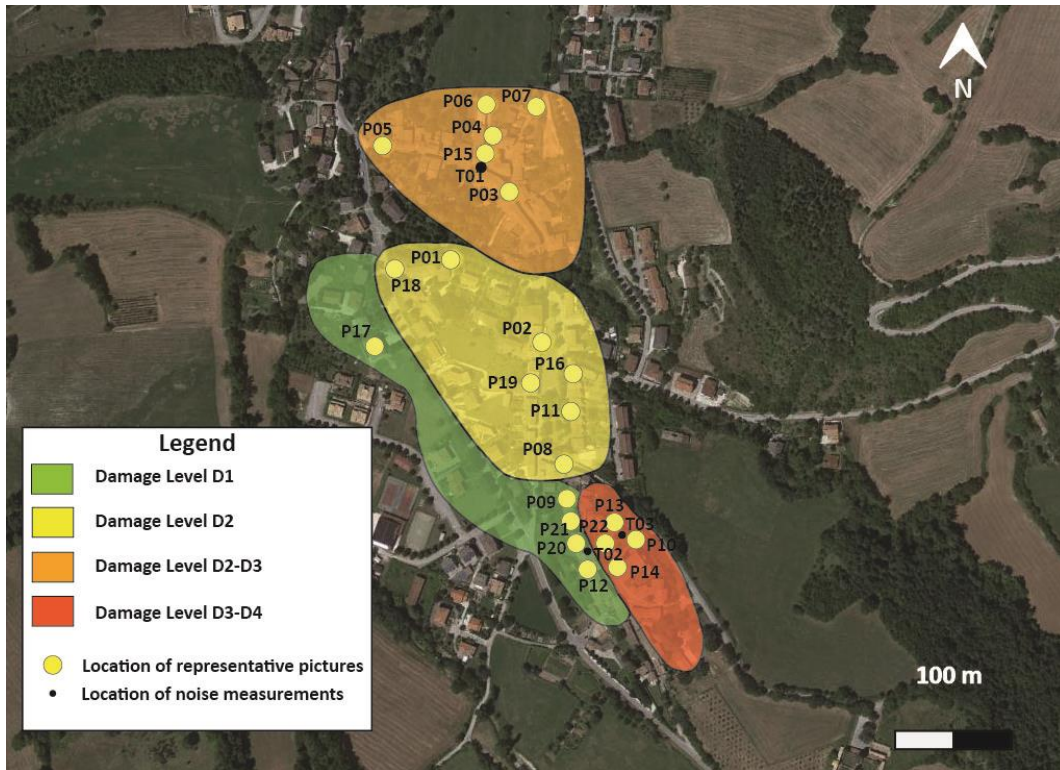
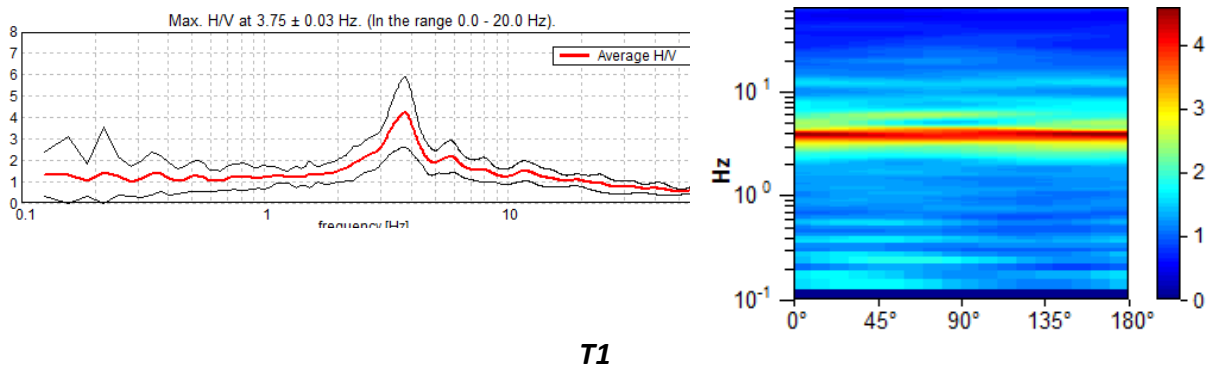


Figure 6.88. Damage zonation within the villages of Pievebovigliana village.

Three microtremor noise measurements (T01-T02-T03 in Figure 6.88) were carried out during the survey in the most damaged zone of the historical center. The same instrument and data acquisition procedures described for Visso were employed here. Average horizontal-to-vertical (H/V) spectral ratios and polar H/V are reported in Figure 6.89. The data indicate relevant H/V peaks in the 3-5 Hz range. The highest peak in T01 can be related to the resonance of alluvial soils on bedrock while peaks in T02 and T03, slightly lower in amplitude and strongly polarized, are probably influenced by the topographic feature present in southern portion of village.



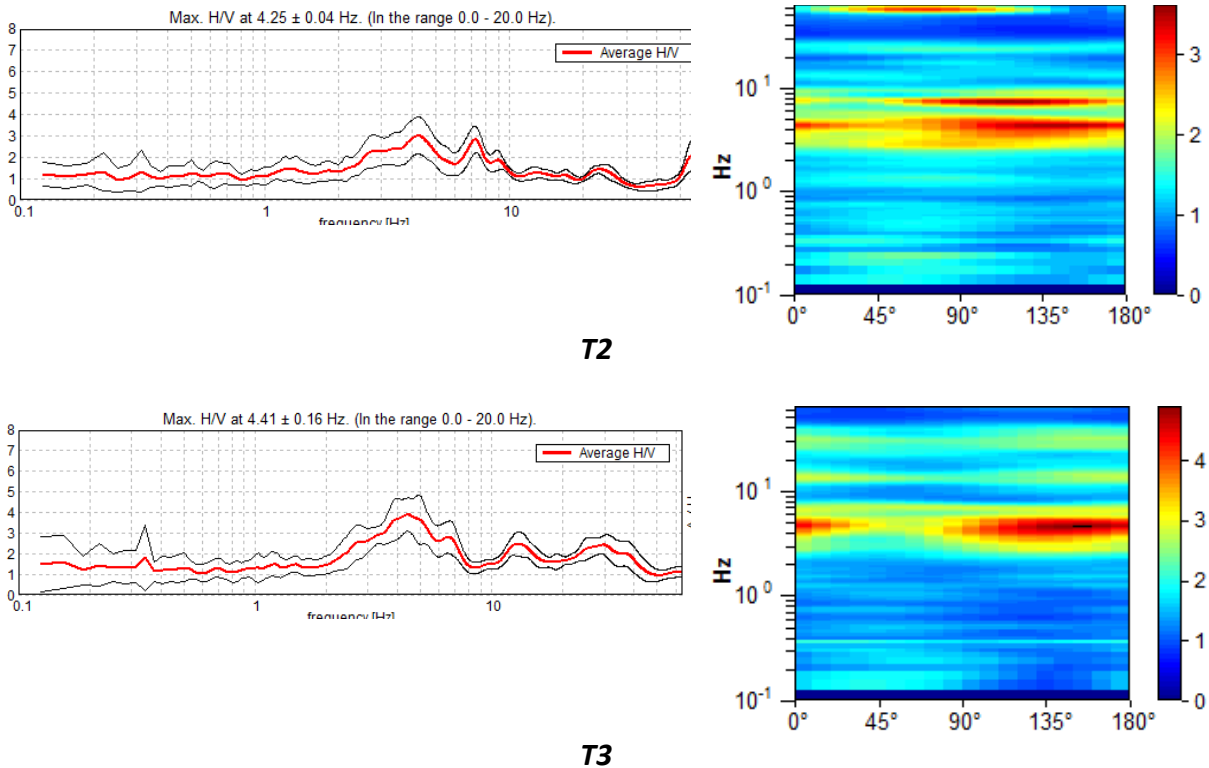
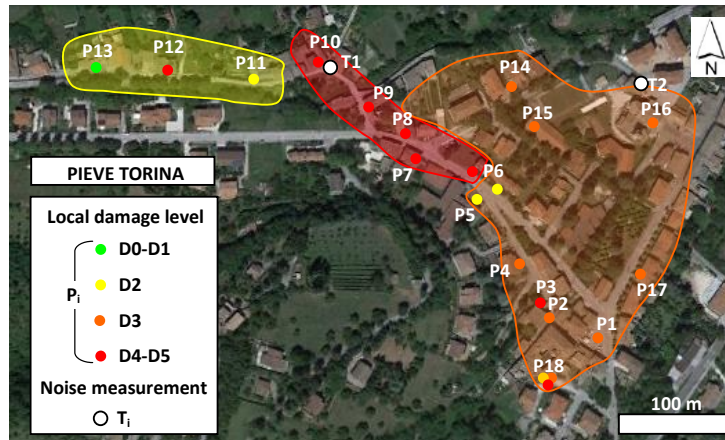


Figure 6.89. Noise measurements results in terms of H/V spectral ratio (on the left column) and H/V polar plots (on the right).

6.2.7 Pieve Torina

Pieve Torina is a village of about 1500 inhabitants located in the Macerata province. In addition to the main village it has the following hamlets: Antico, Appennino, Capecchiara, Capodacqua, Capriglia, Casavecchia Alta, Fiume, Giulo, Le Rote, Lucciano, Piè Casavecchia, Piccollina, Seggiole, Tazza, Torricchio, Vari. GEER reconnaissance occurred in the main village and a few additional hamlets described in other sections below. This section concerns the main village only. As shown in Table 6.1, Pieve Torina experienced estimated ground motions during the 26 October event of $PGA = 0.47$ g, $PGA = 0.34$ g during the 30 October event, and $PGA = 0.17$ g during the 24 August event.

Pieve Torina is crossed by the Sant'Angelo creek. Most of the buildings are masonry structures. Figure 6.90 shows the locations of representative structures inspected and a preliminary damage zonation. Figure 6.91 shows details of a building complex, and a damaged structure located in the center of the village. Two microtremor noise measurements (T01-T02 in Figure 6.90) were carried out during the survey in the most damaged zone of the town. Figure 6.92 shows noise measurements results in terms of H/V spectral ratio and H/V polar plots. Both measurements show a peak at about 10 Hz. This value is compatible with the high level of damage observed for one-two stories buildings (usually characterized by similar values of fundamental frequency), indicating possible double resonance phenomena.



OVERALL DAMAGE LEVELS:

- D1-D2 - With the exception of complete collapse of pre-existing ruins, the area seems to be characterized by limited damages to non structural elements.
- D3 - Heterogeneous area, in terms of structural typology and damage extent; overall, major damage to non structural elements and limited to significant damage to load bearing elements (with local collapse in some points) can be identified.
- D4-D5 - Strip characterized by structures interested by huge damage to load bearing elements and local collapse.

Figure 6.90. Locations of representative structures inspected in Pieve Torina, and damage zonation within the village.



Figure 6.91. Representative pictures taken in Pieve Torina.

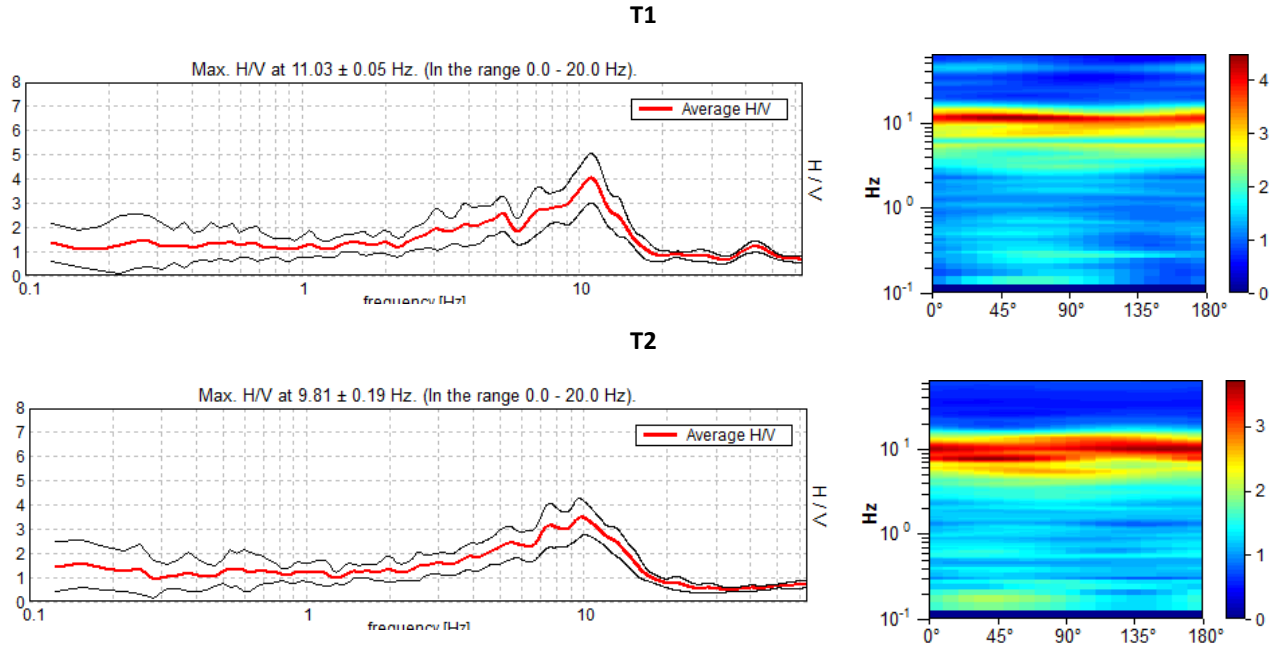


Figure 6.92. Noise measurements results in terms of H/V spectral ratio (on the left column) and H/V polar plots (on the right).

6.2.8 Fiume

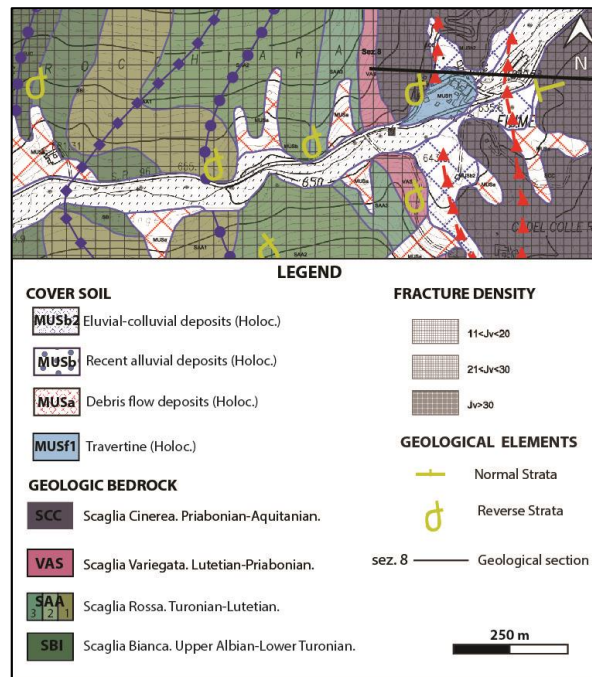
Fiume is part of the municipality of Pieve Torina, in the province of Macerata, in Marche region. The village is 3.70 kilometers (2.3 mi) from the Pieve Torina main village. As shown in Table 6.1, Fiume experienced estimated ground motions during the 26 October event of $PGA = 0.24$ g, $PGA = 0.26$ g during the 30 October event, and $PGA = 0.10$ g during the 24 August event.

The west part of the hamlet is built on Holocene travertine, travertine plaques and calcium-carbonate-encrusted. These materials are indicated as MUSf1 in Figure 6.93 and on regional geological cartography, available at <http://www.ambiente.marche.it/Territorio>. In some cases, these materials are tender and crumbly ($V_s=500-700$ m/s, Regione Marche, 2012). The Eastern part of the hamlet, is built on Holocene eluvial colluvial deposits, consisting mainly of silty sandy clay intercalated with marl and limestone fragments (thickness higher than 3 m with estimated maximum of about 10 m); recent alluvial deposits, mainly made of silts and sandy clay intercalated with marl and limestone (MUSb); and debris flow deposits, mainly limestone debris and gravels with silty-sandy matrix (MUSa) (Figure 6.93). The geologic bedrock of the study area is represented by the Scaglia Cinerea Formation, that represents a cohesive bedrock, finely bedded and highly fractured (SCC in Figure 6.93). Scaglia Cinerea is made of grey clays and calcareous marls with marly limestones intercalations (estimated $V_s = 700-800$ m/s).

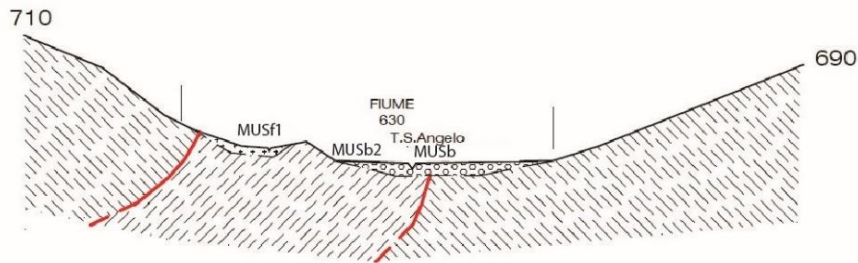
Locations of representative structures inspected in Fiume by the GEER team are reported in Figure 6.94, while details (WGS-84 coordinates, damage level of buildings) are given in Table 6.13. Pictures of these structures are presented in Figure 6.95. Buildings in the village consist of un-reinforced old masonry structures, 2-3 stories in height, some of which appear to have been retrofitted.

Fiume was significantly damaged by the October events. However, the degree of damage to buildings is strongly variable across the village (Figure 6.94). In particular, the eastern portion, founded on colluvial and alluvial deposits resting on bedrock, experienced high levels of damage (D3, see pictures P01-P02) whereas the western portion located on travertine rock had negligible damage (see P03).

Two microtremor noise measurements (T01-T02 in Figure 6.94) were carried out during the survey in the damage zone. The same instrument and data acquisition procedures described for Visso were employed. Average horizontal-to-vertical (H/V) spectral ratios and polar H/V are reported in Figure 6.96. Both measurements show a large H/V peak around 4 Hz that is likely related to stiffness contrast between soil cover and underlying bedrock.



(a)



(b)

Figure 6.93. (a) Geological map of Fiume (Pieve Torina) village and (b) EW Geological cross-section (Regione Marche, 2012).

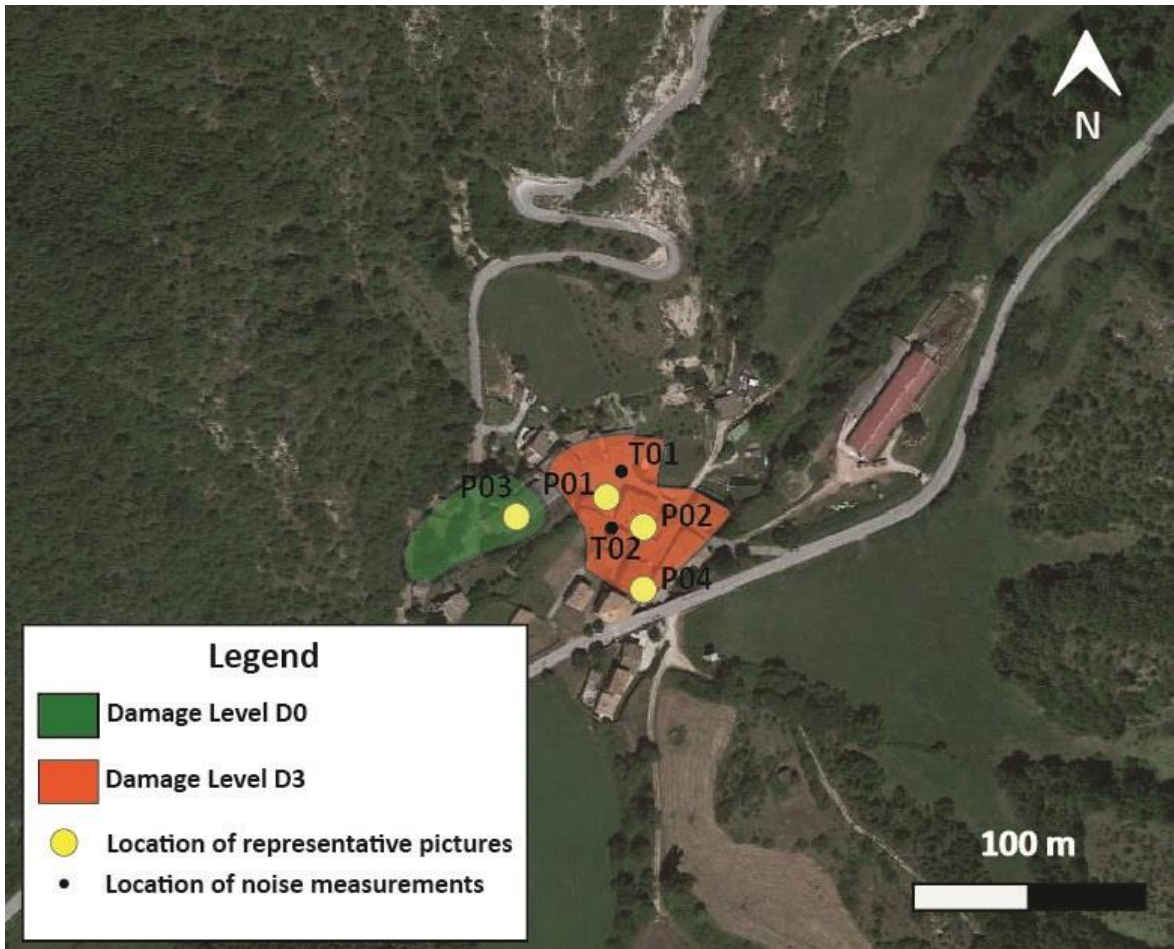


Figure 6.94. Locations of representative structures inspected in Fiume (Pieve Torina) and damage zonation (see Table 6.13 for details).

Table 6.13. Locations of representative structures with damage descriptions.

Fiume (Pieve Torina)				
Picture	Datum	Location		Damage Level
		Lat	Long	
P01a,b	WGS-84	43.042201°	13.001130°	D3
P02	WGS-84	43.042146°	13.001298°	D3
P03	WGS-84	43.042172°	13.000544°	D0/D1
P04	WGS-84	43.041870°	13.001228°	D3



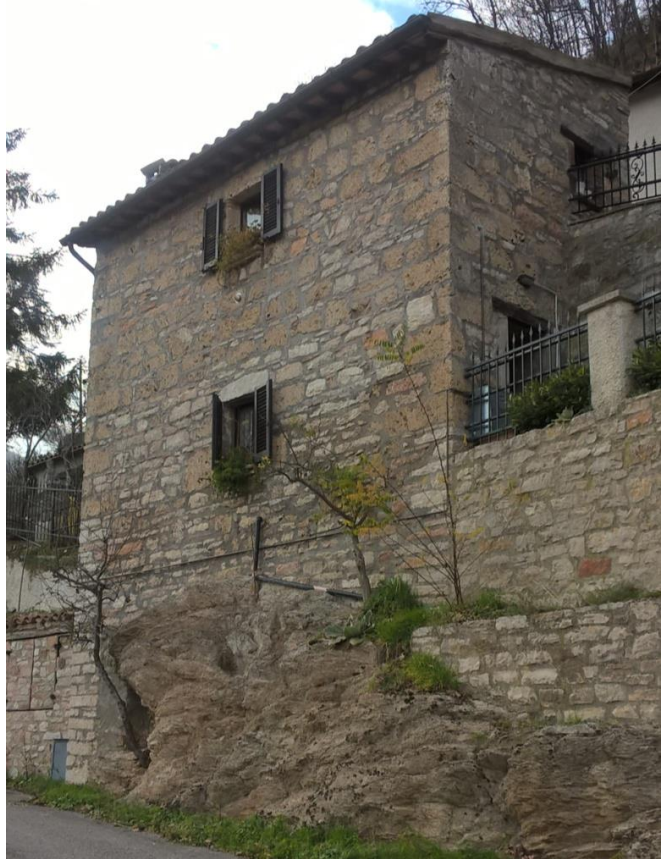
P01a



P01b



P02



P03



P04

Figure 6.95. Representative pictures taken in Fiume (Pieve Torina) during the survey (see Table 6.13).

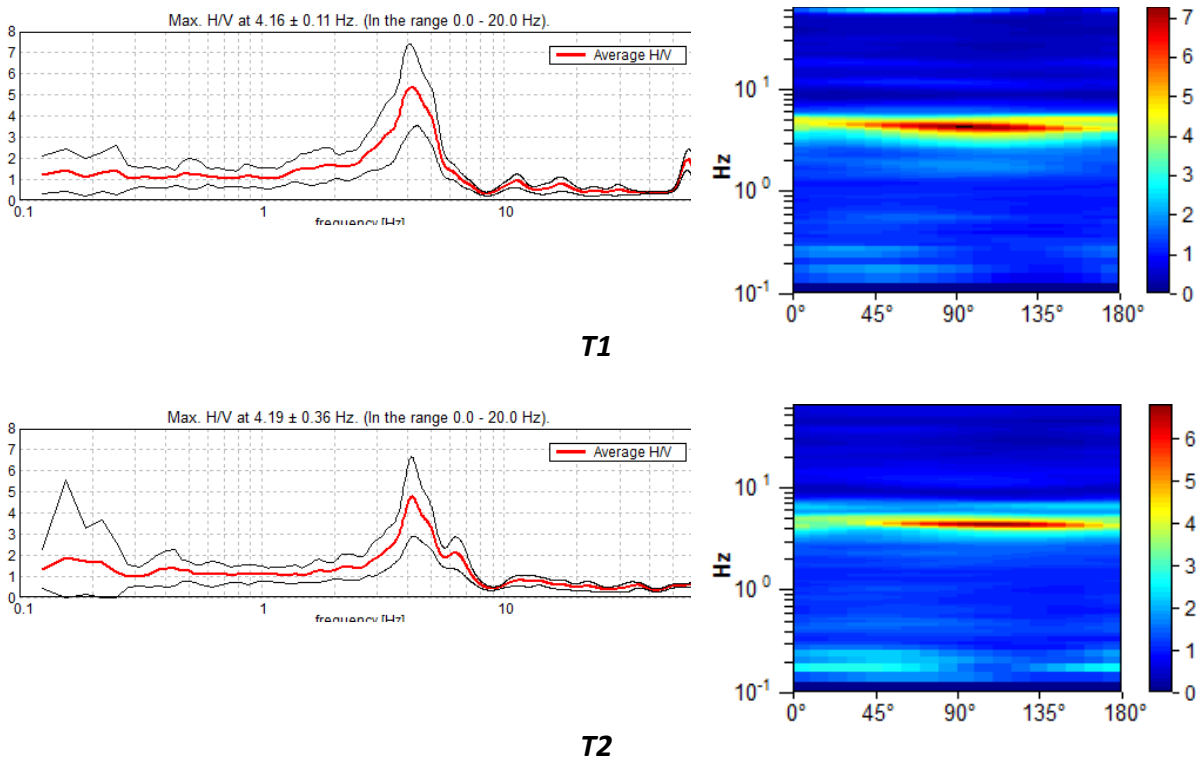


Figure 6.96. Noise measurements results in terms of H/V spectral ratio (on the left column) and H/V polar plots (on the right).

6.2.9 Casavecchia Alta

Casavecchia is part of the municipality of Pieve Torina, in the province of Macerata, Marche region. Casavecchia hamlet is located about 5 kilometers from Pieve Torina. Table 6.1 shows estimated ground motion levels.

The upper part of Casavecchia hamlet (called Casavecchia Alta) is built on a synclinal ridge, an elongated hill underlain by a syncline whose core is formed by marl and calcareous marl, belonging to the Schlier Formation ($V_s = 700\text{-}800$ m/s) with a high fracturation value ($J_v > 30$); that can be considered as a cohesive and layered bedrock. About 20-60 m below the Schlier, there is the Bisciario Formation. This latter consists of alternations of limestone, flint and marly limestone with calcareous marl and flint nodules. Bisciario Formation is characterized by a J_v index between 21 and 30, and a $V_s > 800$ m/s (Regione Marche, 2012b). The lower part of the village (Piè Casavecchia), located at the toe of the ridge, is founded on both Schlier Formation and alluvial terraced deposits (Figure 6.97).

Locations of representative structures inspected in Casavecchia Alta and Piè Casavecchia by the GEER team are reported in Figure 6.98, while details (WGS-84 coordinates, damage level of buildings) are given in Table 6.14. The pictures are presented in Figure 6.99.

The village consists essentially of un-reinforced old masonry structures, 2-3 stories in height. It was significantly damaged by the October events, being the damage level slightly higher in

the upper part (Casavecchia Alta) where several partial and full collapses took place (see P03-P04) with respect to Piè Casavecchia (P01-P02).

A noise measurements (T01 in Figure 6.98) was carried out during the survey in the upper part. The same instrument and data acquisition procedures described for Visso survey were employed. Average horizontal-to-vertical (H/V) spectral ratios and polar H/V plot are reported in Figure 6.100. A broad band H/V peak appears at 2-6 Hz polarized in the direction of about 60°, i.e. perpendicular to the axis of the ridge, thus indicating possible topographic site effects (Pagliaroli et al., 2015).

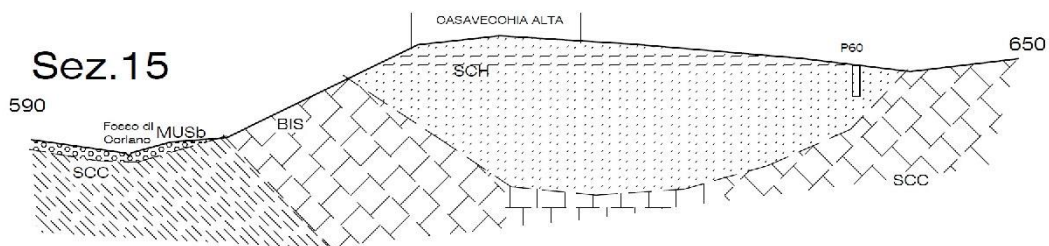
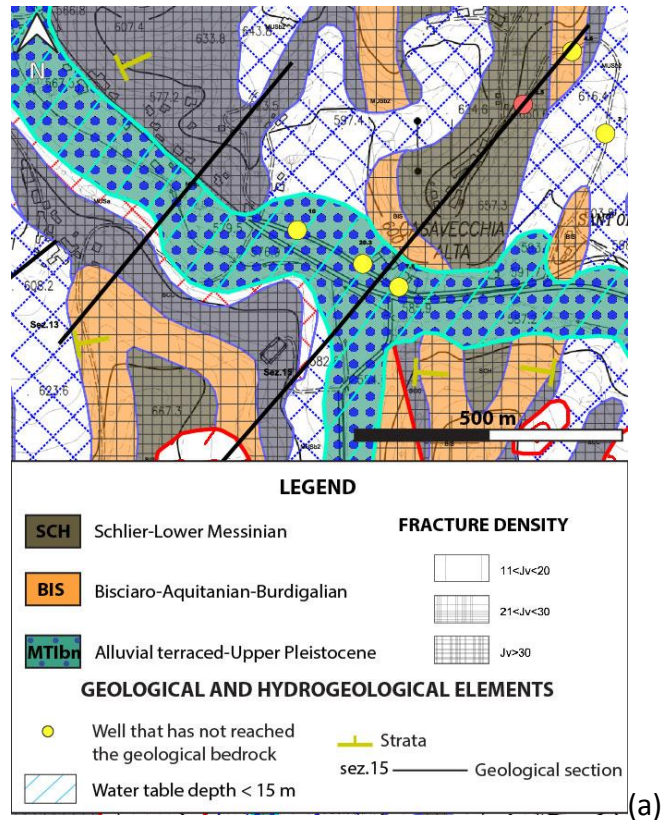


Figure 6.97. (a) Geological map of Casavecchia Alta village, and (b) Geological cross-section (Regione Marche, 2012b).

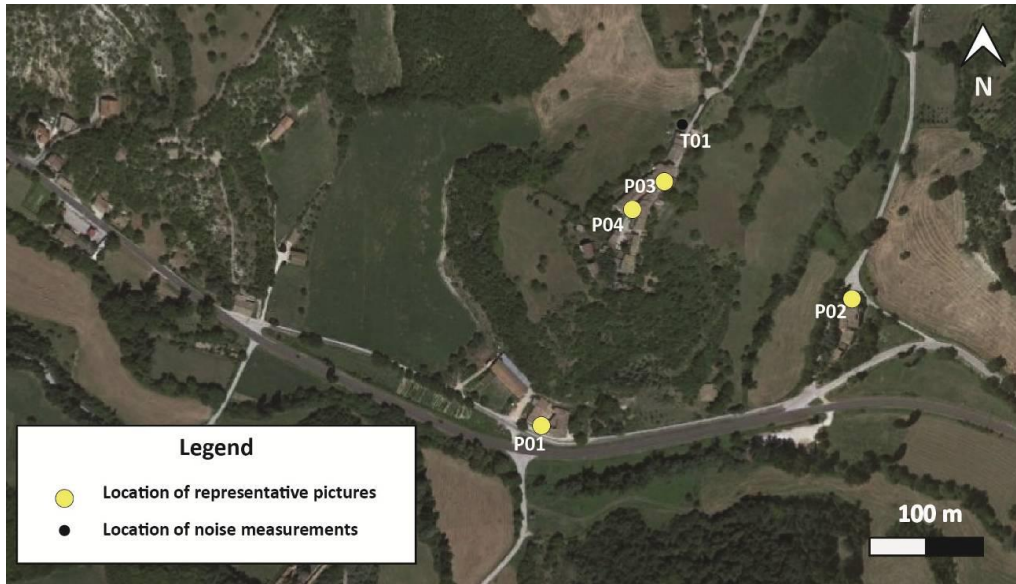


Figure 6.98. Locations of representative structures inspected in Casavecchia (see Table 6.14 for details).

Table 6.14. Locations of representative structures with damage descriptions.

Casavecchia Alta / Piè Casavecchia				
Picture	Datum	Location		Damage Level
		Lat	Long	
P01	WGS-84	42.996714°	13.060456°	D3-D4
P02	WGS-84	42.997693°	13.064266°	D2-D3
P03	WGS-84	42.998803°	13.062181°	D4-D5
P04	WGS-84	42.998500°	13.061722°	D4-D5



P01



P02



P03



P04

Figure 6.99. Representative pictures taken in Casavecchia during the survey (see Table 6.14).

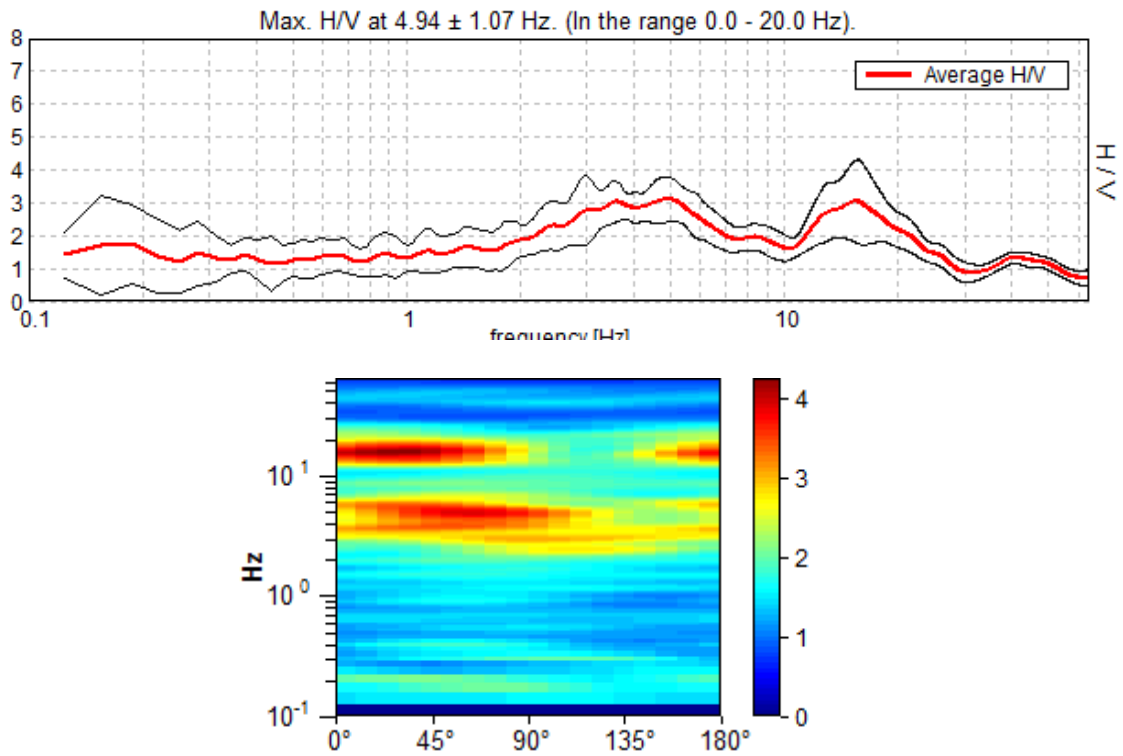


Figure 6.100. Noise measurement T01 results in terms of H/V spectral ratio (up) and H/V polar plots (bottom).

6.2.10 Sellano

Sellano and related hamlets are located about 15-20 km W from the epicenters of seismic events of October. GEER reconnaissance occurred in the main village and several hamlets, identified below. As shown in Table 6.1, Sellano experienced estimated ground motions during the 26 October event of $PGA = 0.07$ g, $PGA = 0.20$ g during the 30 October event, and $PGA = 0.13$ g during the 24 August event.

Locations of representative structures inspected by the GEER team are reported in Figure 6.101, while details (WGS-84 coordinates, damage level of buildings) are given in Table 6.15. The pictures are presented in Figure 6.102.

No or negligible damage was observed in the hamlets of Terne and Villamagina (on average D0-D1). Slightly higher damage (D1-D2) was reported in the upper part of Sellano (area of Santa Maria Assunta and Municipio, see P04 and P06).

A noise measurement was carried out during the survey in the upper part of Sellano (close to P06 in the Municipio square), about 30 m from a slope. The same instrument and data acquisition procedures described for Visso survey were employed. Average horizontal-to-vertical (H/V) spectral ratios and polar H/V plots are reported in Figure 6.103. A broad band peak can be identified at about 3-5 Hz that is clearly polarized in the direction of about 90° , which is roughly orthogonal to the strike of the adjacent slope.

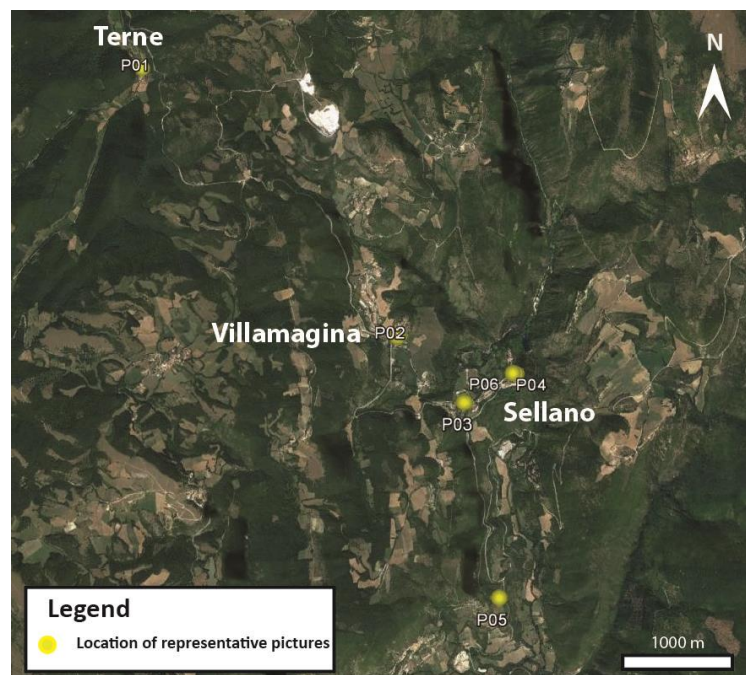


Figure 6.101. Locations of representative structures inspected in Sellano and surrounding hamlets (see Table 6.15 for details).

Table 6.15. Locations of representative structures with damage descriptions

Sellano/Terne/Villamagina				
Picture	Datum	Location		Damage Level
		Lat	Long	
P01	WGS-84	42.915280°	12.884264°	D0
P02	WGS-84	42.891653°	12.913796°	D0
P03	WGS-84	42.886215°	12.921222°	D0
P04	WGS-84	42.888617°	12.927153°	D2
P05	WGS-84	42.870454°	12.924667°	D0-D1
P06	WGS-84	42.888828°	12.926805°	D1



P01



P02



P03



P04



P05



P06

Figure 6.102. Representative pictures taken in Sellano and surroundings during the survey (see Table 6.15).

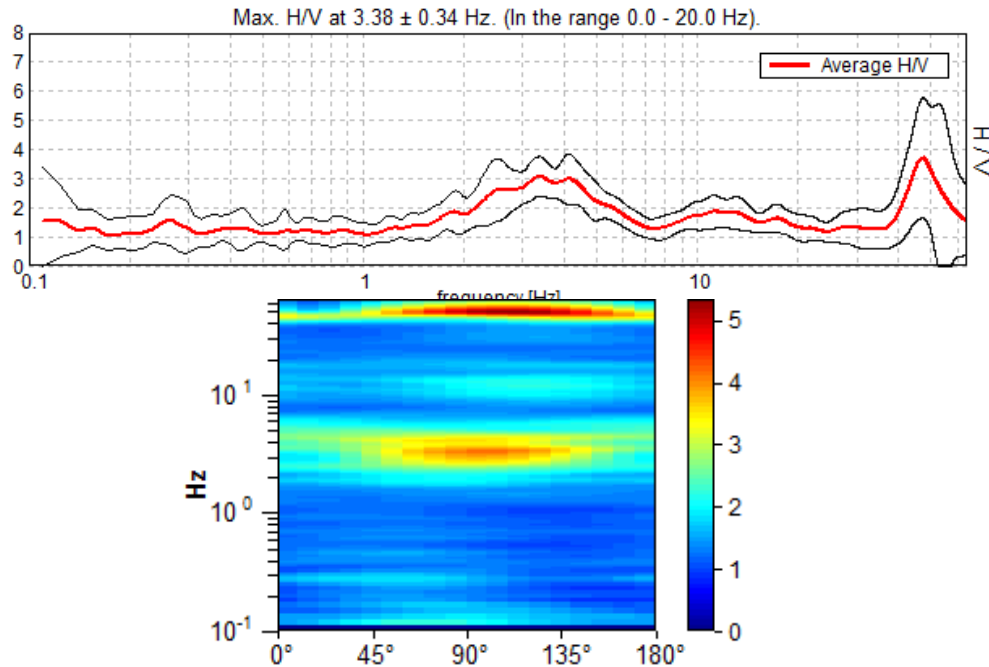


Figure 6.103. Noise measurement results in terms of H/V spectral ratio (top) and H/V polar plots (bottom) (Sellano, Municipio square, 42.888828°- 12.926805°).

6.2.11 Pié del Colle

The town of Norcia includes a cluster of hamlets, one of which (Pié del Colle) was visited in GEER reconnaissance. Pié del Colle is about 5.6 km from the Norcia center. As shown in Table 6.1, Pié del Colle experienced estimated ground motions during the 26 October event of $PGA = 0.48$ g, $PGA = 0.39$ g during the 30 October event, and $PGA = 0.33$ g during the 24 August event.

Figure 6.104 and Table 6.16 show locations and details of representative buildings inspected in Pié del Colle. Figure 6.105 shows representative structures, which include unreinforced masonry and reinforced concrete buildings. Damage was observed to both types of structures, although among reinforced concrete structures the principal damage was collapse of interior tiles from frames. Typical damage levels were between D2 and D3.



Figure 6.104. Locations of the representative structures inspected in Ancarano piè del colle (see Table 6.16 for details).

Table 6.16. Location of representative structures with damage descriptions.

Picture	DATUM	Location		Damage Level	Notes
		Lat.	Long.		
P01	WGS-84	42.844373	13.101296	D2	
P02	WGS-84	42.844211	13.101267	D2	
P03	WGS-84	42.844400	13.101682	D1	
P04	WGS-84	42.844270	13.101787	D1	
P05	WGS-84	42.844039	13.101900	D1	
P06	WGS-84	42.844130	13.102034	D1	
P07	WGS-84	42.844310	13.102489	D1	
P08	WGS-84	42.844148	13.103076	D1	
P09	WGS-84	42.844152	13.103284	D4	
P10	WGS-84	42.844152	13.103527	D0	
P11	WGS-84	42.844028	13.103713	D5	
P12	WGS-84	42.844166	13.103785	D2	
P13	WGS-84	42.844177	13.103916	D5	
P14	WGS-84	42.843939	13.103436	D3	
P15	WGS-84	42.843826	13.103548	D0	
P16	WGS-84	42.843215	13.102244	D2	
P17	WGS-84	42.843167	13.102265	D2	



P01



P02



P03



P04



P05



P06



P07



P08



P09



P10



P11



P12



P13



P14



P15



P16



P17

Figure 6.105. Representative pictures taken at Ancarani pié del Colle (see Table 6.16 for details).

6.2.12 Cessapalombo

Cessapalombo is a small village of about 540 inhabitants located in the province of Macerata at 454 m a.s.l. In addition to the main village there are 7 hamlets: Case Colbottoni, Case Meschine, Invernale, La Valle, La Villa, Monastero, Trebbio. GEER reconnaissance occurred in the main

village of Cessapalombo. As shown in Table 6.1, Cessapalombo experienced estimated ground motions during the 26 October event of $PGA = 0.11\text{ g}$, $PGA = 0.12\text{ g}$ during the 30 October event, and $PGA = 0.08\text{ g}$ during the 24 August event.

Geological bedrock in the area consists of alternation of layered soils (ALSzz), mainly composed of arenaceous and pelithic-arenaceous lithofacies. In the main village of Cessapalombo, the above formation is covered by alluvial soils (GM) made of gravels and sands, locally in silty clayey matrix (ML) (Figure 6.106). In the mountainous region, calcareous and marly formations may be found (Monte Codardo, Monte Pretella, Monte di Bozzi, etc.). At the base of the mountains, several fans may be recognized with some villages risen just upon fans (f.e., La Villa and La Valle).

Figure 6.107 shows historical seismicity of Cessapalombo (CPTI-INGV database). The village was heavily damaged during the seismic event of July 28, 1799 (also known as the Camerino earthquake).

Table 6.17 summarizes locations and details of the representative inspected buildings, while Figure 6.108 shows locations of these buildings. Figure 6.109 shows pictures of representative structures in the village. The average damage level in the main village is approximately D1 to D2.

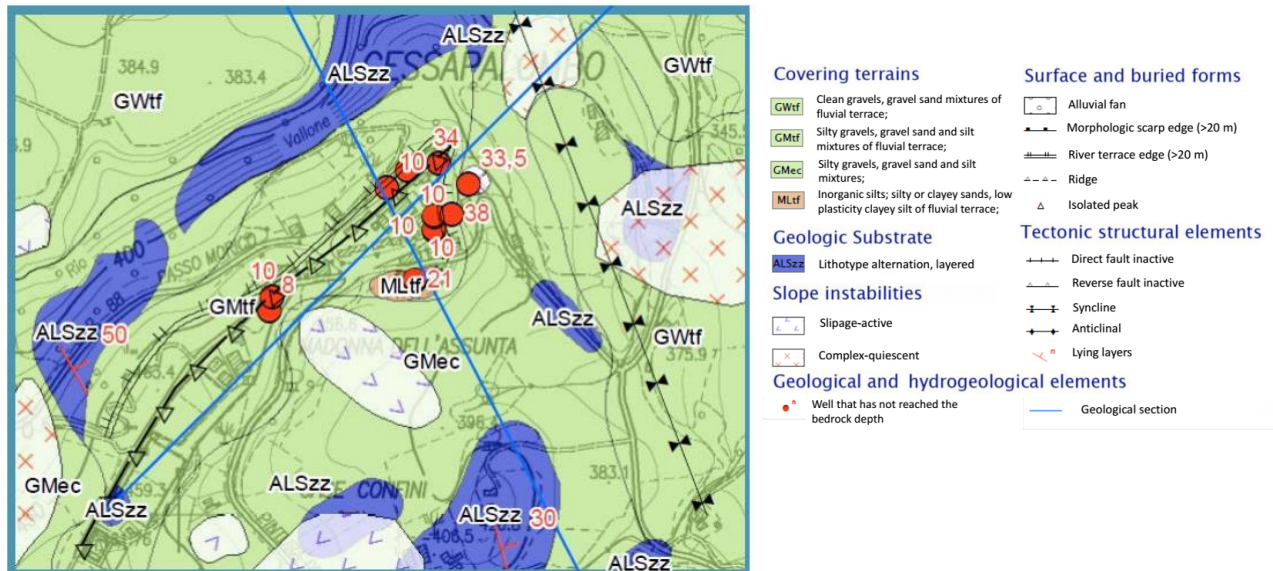


Figure 6.106. Geological map of Cessapalombo main centre (Regione Marche, 2012).

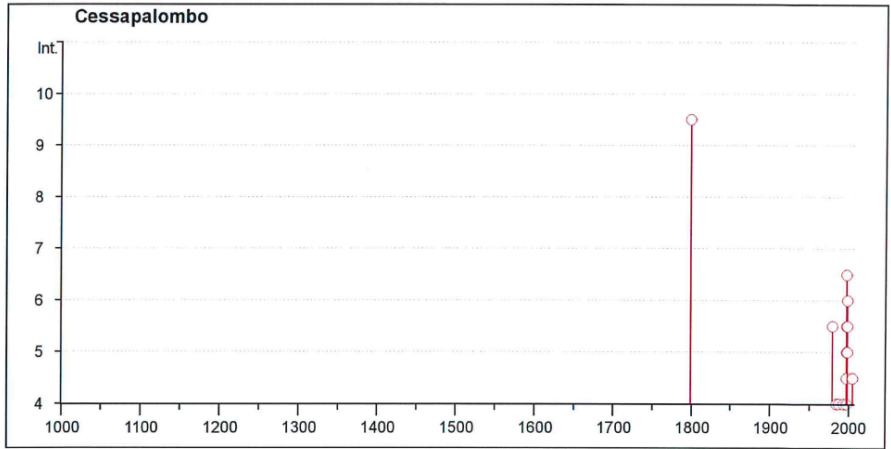


Figure 6.107. Historical earthquakes felt in Cessapalombo (CPTI- INGV).



Figure 6.108. Locations of the representative structures inspected in Cessapalombo (see Table 6.17 for details).

Table 6.17. Location of representative structures with damage descriptions.

Picture	DATUM	Location		Damage Level	Notes
		Lat.	Long.		
P01	WGS-84	43.108198	13.258378	D5	
P02	WGS-84	43.108592	13.258880	D2	
P03	WGS-84	43.108566	13.257992	D1	
P04	WGS-84				
P05	WGS-84	43.108643	13.258125	D1	
P06	WGS-84	43.108739	13.258286	D1	
P07	WGS-84				
P08	WGS-84				
P09	WGS-84				
P10	WGS-84				
P11	WGS-84	43.108772	13.258107	D1	
P12	WGS-84	43.108713	13.257500	D0	
P13	WGS-84	43.108522	13.257597	D3-D4	
P14	WGS-84	43.108463	13.257340	D1	
P15	WGS-84	43.109235	13.258417	D2	



P01



P02



P03



P04



P05



P06



P07



P08



P09



P10



P11



P12



P13



P14



P15

Figure 6.109. Representative pictures taken at Cessapalombo (see Table 6.17 for details).

6.2.13 Preci

Preci (42.880697, 13.039657) has about 750 inhabitants and is located in the province of Perugia. Apart from the main village, it has several hamlets: Abeto, Acquaro, Belforte, casali Belforte, Case sparse, Castelvechio, Collazzoni, Collescille, Corone, Fiano, Montaglioni, Montebufo, Poggio di croce, Piedivalle, Roccanolfi, Sacco Vescio, San Lazzaro, Todiano, Villa del

Guado. Ground motion levels are reported in Table 6.1. The main village was lightly damaged. Figure 6.110 shows the location of representative pictures taken in Preci, while Figure 6.111 shows a church with damage level D1.



Figure 6.110. Locations of the representative structures inspected in Preci.



P01



P02



P03



P04

Figure 6.111. Representative pictures of church in Preci (Lat = 42.881418, Lon = 13.036290).

6.2.14 Piedivalle

The hamlet of Piedivalle (42.866786, 13.060767) belongs to the municipality of Preci and is about 2.5 km from the Preci center. Its elevation is 611 m a.s.l. and it has 35 inhabitants. Estimated ground motions are given in Table 6.1. We inspected three structures at the location shown in Figure 6.112. The building photographs are shown in Figure 6.113. The masonry structures have damage level D1.



Figure 6.112. Locations of the representative structures inspected in Piedivalle.



P01



P02



P03



P04

Figure 6.113. Representative pictures taken at Piedivalle.

6.2.15 Caldarola

Caldarola (43.13988, 13.22471) is a small village of about 1850 inhabitants located in the province of Macerata. Table 6.1 shows the ground motions levels. Figure 6.114 shows the locations of inspected buildings, Figure 6.115 shows the building photos. Table 6.18 shows details for inspected buildings. Buildings are both unreinforced masonry and reinforced concrete. Damage levels vary from D0 to D1.



Figure 6.114. Locations of the representative structures inspected in Caldarola (see Table 6.18 for details).

Table 6.18. Location of representative structures with damage descriptions.

Picture	DATUM	Location		Damage Level	Notes
		Lat.	Long.		
P01	WGS-84	43.136801	13.226607	D1	
P02	WGS-84	43.137202	13.225963	D0	
P03	WGS-84	43.137617	13.226234	D1	
P04	WGS-84	43.137827	13.225873	D1	
P05	WGS-84	43.138038	13.226472	D2	
P06	WGS-84	43.138212	13.226377	D0	
P07	WGS-84	43.138370	13.226287	D0	
P08	WGS-84	43.138488	13.226146	D0	
P09	WGS-84	43.127572	13.220054	D3	
P10	WGS-84	43.127735	13.219258	D3	
P11	WGS-84				



P01



P02



P03



P04



P05



P06



P07



P08



P09



P10



P11

Figure 6.115. Representative pictures taken at Caldarola (see Table 6.18 for details).

6.2.16 Castello di Campi

The village of Castello di Campi (42.853729, 13.100582) belongs to the municipality of Norcia and is about 11 km from the center of Norcia. It has 172 inhabitants according to the ISTAT census of 2001. Table 6.1 shows the ground motions levels. Figure 6.116 shows the locations of inspected buildings, Figure 6.117 shows the building photos. Table 6.19 shows details for inspected buildings. Observed buildings are unreinforced masonry. Damage levels vary from D2 to D3.

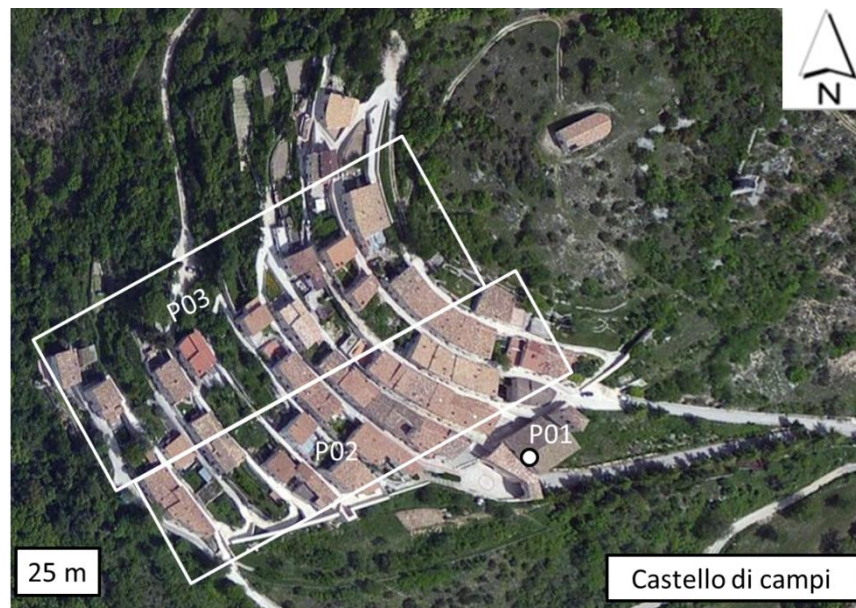


Figure 6.116. Locations of the representative structures inspected in Castello di Campi (see Table 6.19 for details).

Table 6.19. Location of representative structures with damage descriptions.

<i>Picture</i>	<i>DATUM</i>	<i>Location</i>		<i>Damage Level</i>	<i>Notes</i>
		<i>Lat.</i>	<i>Long.</i>		
<i>P01</i>	<i>WGS-84</i>	<i>42.853422</i>	<i>13.101411</i>	<i>D4</i>	
<i>P02</i>	<i>WGS-84</i>	<i>42.853480</i>	<i>13.100616</i>	<i>D2-D5</i>	
<i>P03</i>	<i>WGS-84</i>	<i>42.853819</i>	<i>13.100276</i>	<i>D2-D5</i>	



P01



P02



P03

Figure 6.117. Representative pictures taken at Castello di Campi (see Table 6.19 for details).

6.2.17 Colfiorito

Colfiorito village consists essentially of masonry structures, 2-3 stories in height. Some structures were retrofitted following the 1997 earthquake. No or negligible damage was observed (on average D0-D1). Table 6.1 lists ground motion levels.

Coordinates and damage level of representative buildings inspected during the survey are given in Table 6.20 while corresponding pictures are presented in Figure 6.118.

Table 6.20. Locations of representative structures with damage descriptions

Colfiorito				
Picture	Datum	Location		Damage Level
		Lat	Long	
P01	WGS-84	43.026700°	12.890759°	D1
P02	WGS-84	43.028375°	12.891436°	D0
P03	WGS-84	43.026766°	12.890206°	D0



P01



P02



P03

Figure 6.118. Representative pictures taken in Colfiorito during the survey (see Table 6.20)

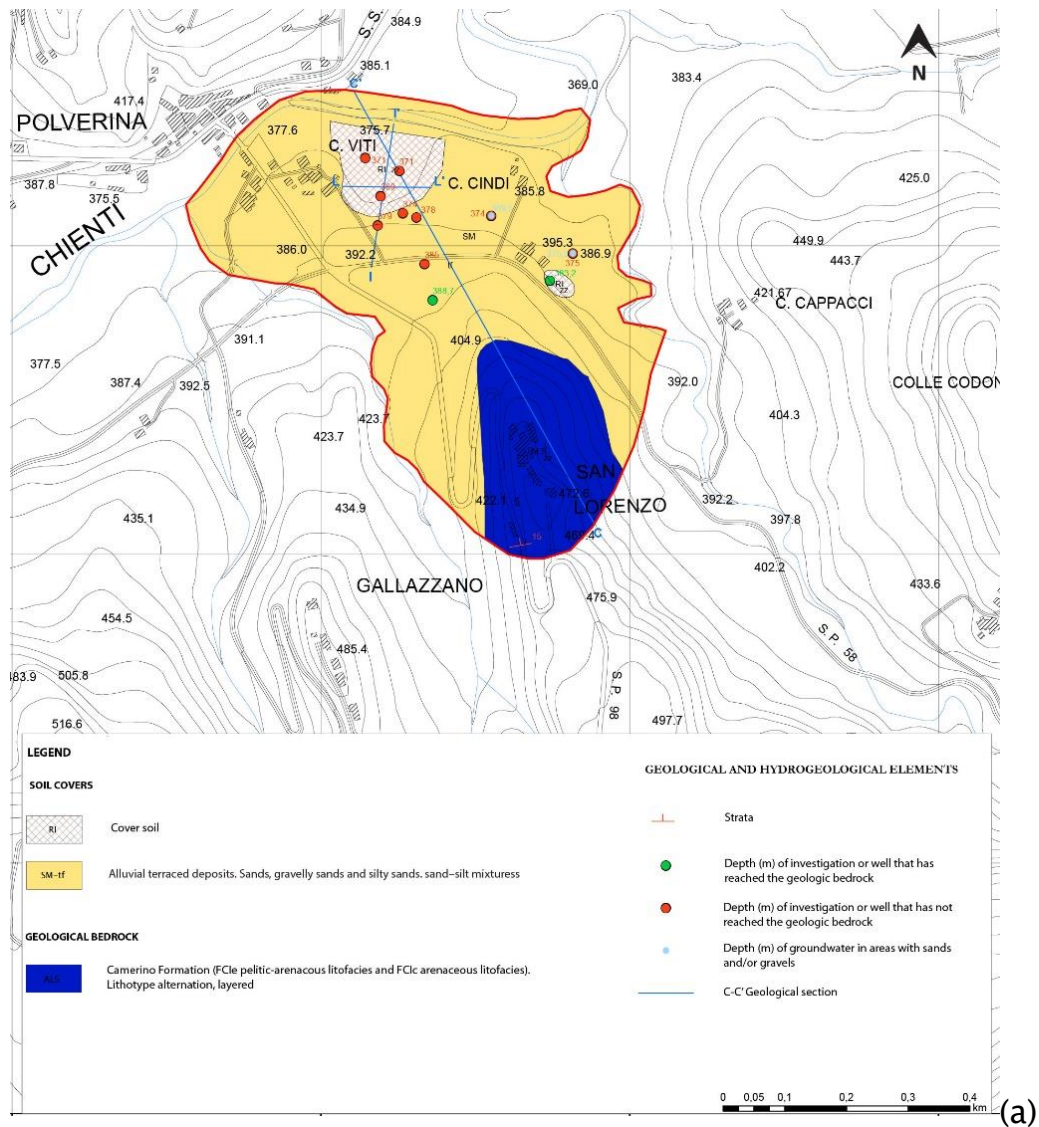
6.2.18 San Lorenzo in Colpolina

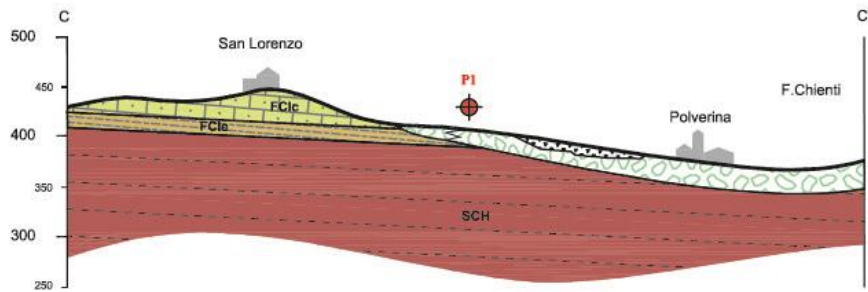
San Lorenzo in Colpolina is part of the municipality of Fiastra, in the province of Macerata, Marche Region. The hamlet is 6.2 kilometers from Fiastra of which it is part. Table 6.1 shows estimated ground motion levels.

As one can see from Figure 6.119 (modified from Regione Marche, 2012), San Lorenzo in Colpolina is built on a ridge elongated NNW-SSE and constituted by pelitic-arenaceous and arenaceous lithofacies of Camerino Formation, that consists of foredeep turbidites, locally present in different silicoclastic lithofacies, having different lateral and overlapping relationships. In particular, in the study area there are outcrops of the pelitic-sandstone, and sandstone lithofacies; Tortonian-Messinain. In the geologic-geotechnical map Camerino Formation is

indicated as ALS, bedrock characterized by a layered lithotypes alternation according to the Italian standard of seismic microzonation (available at <http://www.protezionecivile.gov.it>). The hamlet is located on a general synclinorium, with nucleus made up of terrigenous turbiditic formation, while its sides are made up of pelitic terms belonging to the Schlier Formation (SCH in Figure 6.119). The Quaternary continental deposits mainly consist of alluvial soils (SM-tf), attributable to the alluvial phases Chienti River.

Locations of representative structures inspected in San Lorenzo in Colpolina by the GEER team are reported in Figure 6.120, while details (WGS-84 coordinates, damage level of buildings) are given in Table 6.21. The pictures are presented in Figure 6.121.





(b)

Figure 6.119. (a) Geological map of San Lorenzo in Colpolina village, and (b) Geological cross-section (Regione Marche, 2012).

The village consists essentially of un-reinforced masonry structures, 2-3 stories in height. Some structures are retrofitted. The damage at the top of the ridge was quite high (D3-D4 on average) with several partial collapses (see P01- P03-P04).

A noise measurements (T01 in Figure 6.120) was carried out during the survey on the ridge on to which San Lorenzo is founded. The same instrument and data acquisition procedure described for Visso survey were employed. Average horizontal-to-vertical (H/V) spectral ratios and polar H/V plot are reported in Figure 6.122. A peak can be identified at about 3 Hz polarized in the direction of about 100°, i.e. perpendicular to the axis of the ridge, thus indicating possible topographic site effects (Pagliaroli et al., 2015).

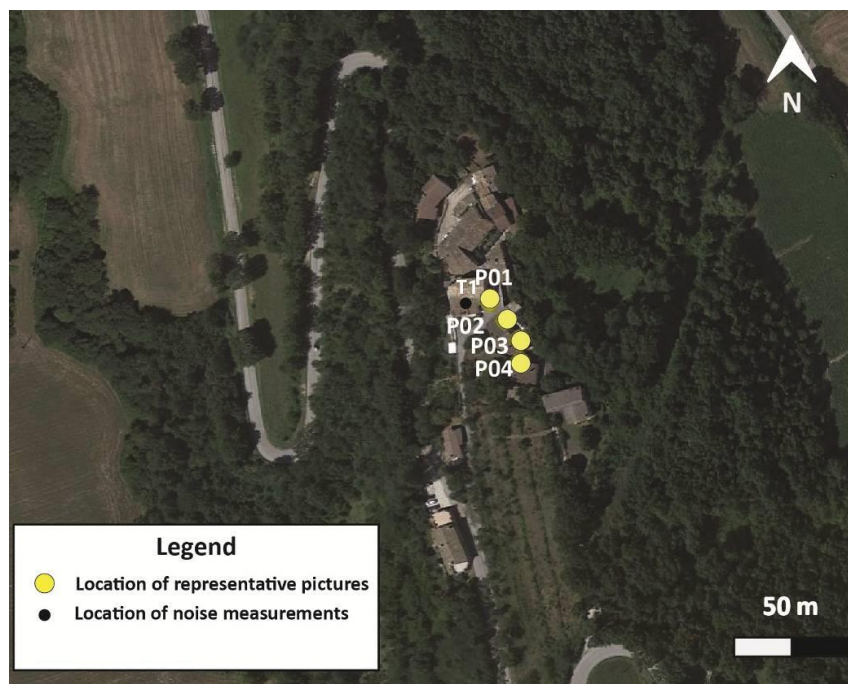


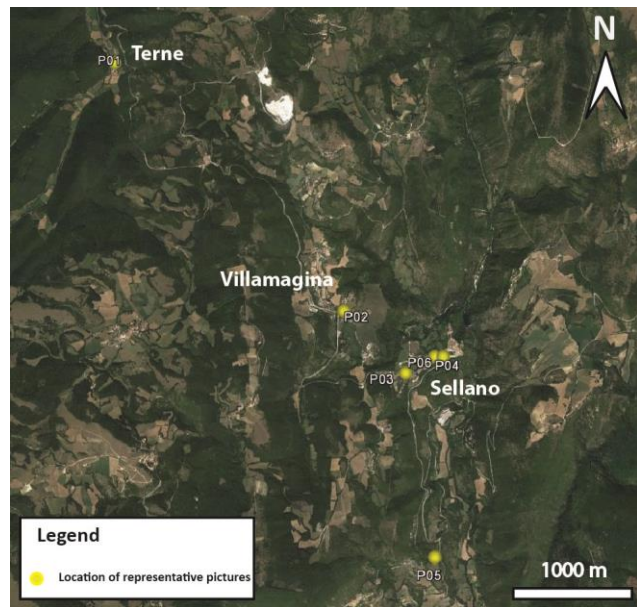
Figure 6.120. Locations of representative structures inspected in San Lorenzo in Colpolina (see Table 6.21 for details).

Table 6.21. Locations of representative structures with damage descriptions.

San Lorenzo in Colpolina				
Picture	Datum	Location		Damage Level
		Lat	Long	
P01	WGS-84	43.086690°	13.124509°	D5
P02	WGS-84	43.086511°	13.124582°	D3-D4
P03	WGS-84	43.086319°	13.124638°	D4
P04	WGS-84	43.087064°	13.124486°	D4



P01



P02



P03



P04

Figure 6.121. Representative pictures taken in San Lorenzo in Colpolina during the survey (see Table 6.21).

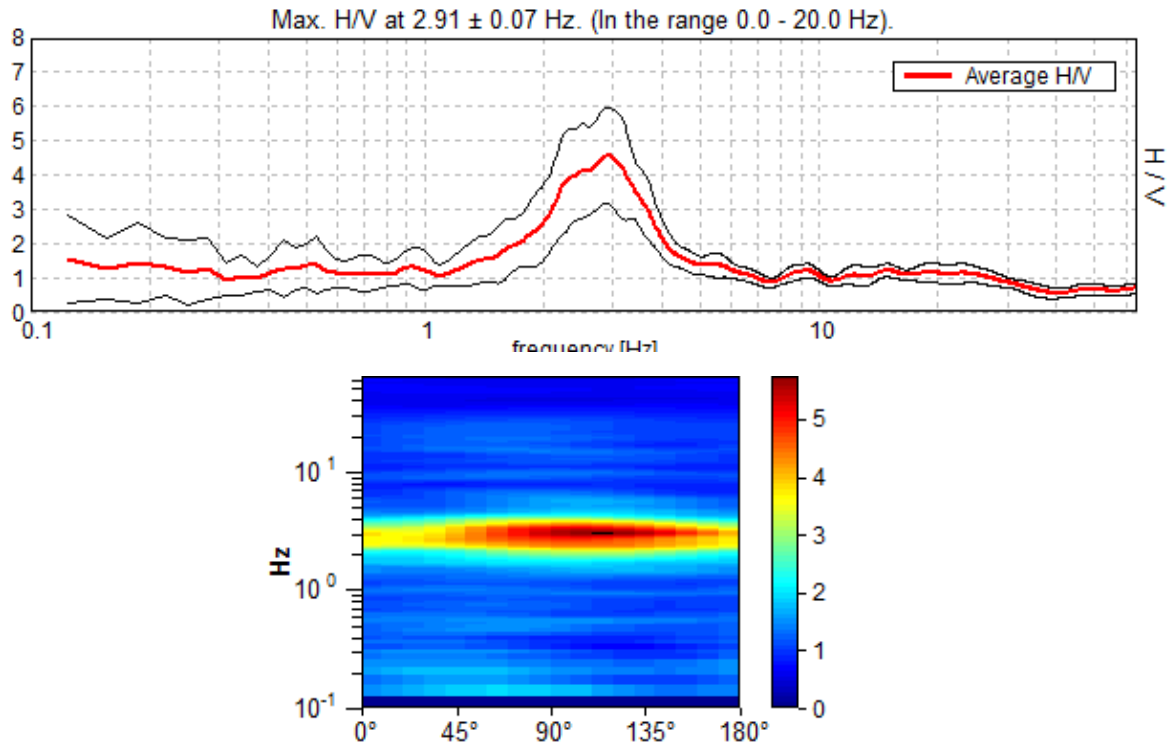


Figure 6.122. Noise measurements results in terms of H/V spectral ratio (top) and H/V polar plots (bottom).

6.2.19 Serravalle

Serravalle is a hamlet part of the municipality of Norcia, in the province of Perugia, Umbria region. Serravalle is located about 6 kilometers from Norcia and it has a population of 25 people. Ground motion levels are reported in Table 6.1 The hamlet was not damaged by the earthquake and the generalized damage level was D0 (Figure 6.123, Table 6.22).



P01



P02



P03

Figure 6.123. Representative pictures taken in Serravalle during the GEER reconnaissance (see Table 6.22).

Table 6.22 Locations of representative structures with damage descriptions

Serravalle				
Picture	Datum	Location		Damage Level
		Lat	Long	
P01	WGS-84	42.785802	13.022287	D0
P02	WGS-84	42.785816	13.022504	D0
P03	WGS-84	42.785852	13.022981	Do

6.2.20 Popoli

The small village of Popoli is located 4.67 km far from Norcia. Before the 24 August 2016 earthquake, 47 people lived there. There were 51 buildings, 43 of which for residential use. The majority of the structures are one or two-story masonry buildings, constructed before 1919. In the last 30 years, only seven buildings were built. Others structural types are also present (wooden and steel structures). Before the 24 August event, 32 buildings were assessed in excellent conditions, 7 in good conditions and 4 in poor conditions due to aging effects and lack of maintenance (http://italia.indettaglio.it/ita/umbria/perugia_norcia_popoli.html, last accessed 21 April, 2017). The village is located in a valley floor consisted of alluvial deposits, susceptible to seismic amplification phenomena. Ground motion levels are reported in Table 6.23 Figure 6.124 shows the damage proxy map after the 30 October earthquake. Red zones mark zones seriously damaged (damage level D5). Figure 6.125 shows buildings with different

level damage ranging from D0 to D5. Only poorly constructed masonry buildings experienced major damage.



Figure 6.124. Damage proxy map of Popoli (http://aria-share.jpl.nasa.gov/events/20161030-Italy_EQ/DPM/, last accessed 21 April, 2017).



P01



P02



P03



P04



P05



P06

Figure 6.125. Representative pictures taken in Popoli during the GEER reconnaissance (see Table 6.23).

Table 6.23. Locations of representative structures with damage descriptions

Picture	DATUM	Location		Damage Level
		Lat.	Long.	
P01	WGS-84	42.751381	13.106139	D1
P02	WGS-84	42.751381	13.106139	D1
P03	WGS-84	42.751800	13.105000	D3
P04	WGS-84	42.751700	13.105700	D2/D3
P05	WGS-84	42.751572	13.106256	D4/D5
P06	WGS-84	42.751300	13.106075	D0

6.2.21 San Pellegrino

The village of San Pellegrino is located 5.93 km far from Norcia. Before the 24 August event, 156 people lived there. There were 140 residential buildings, and two buildings were used for commercial purposes. The overwhelming majority of the structures was formed by two-story masonry buildings, constructed between 1946 and 1990, and just a few reinforced concrete buildings. Before the 24 August earthquake, 11 residential buildings were in excellent conditions, 128 in good conditions, and 1 was in poor conditions due to aging effects and lack of maintenance (http://italia.indettaglio.it/ita/umbria/perugia_norcia_sanpellegrino.html). The geology of San Pellegrino is characterized by the presence of screes or alluvial cone and alluvial deposits. San Pellegrino was heavily damaged after the 24 August 2016 seismic events. Ground motion levels are reported in Table 6.1 Figure 6.126 shows the damage proxy map produced after the 30 October event. Red and yellow zones localized the wide area heavily damaged.

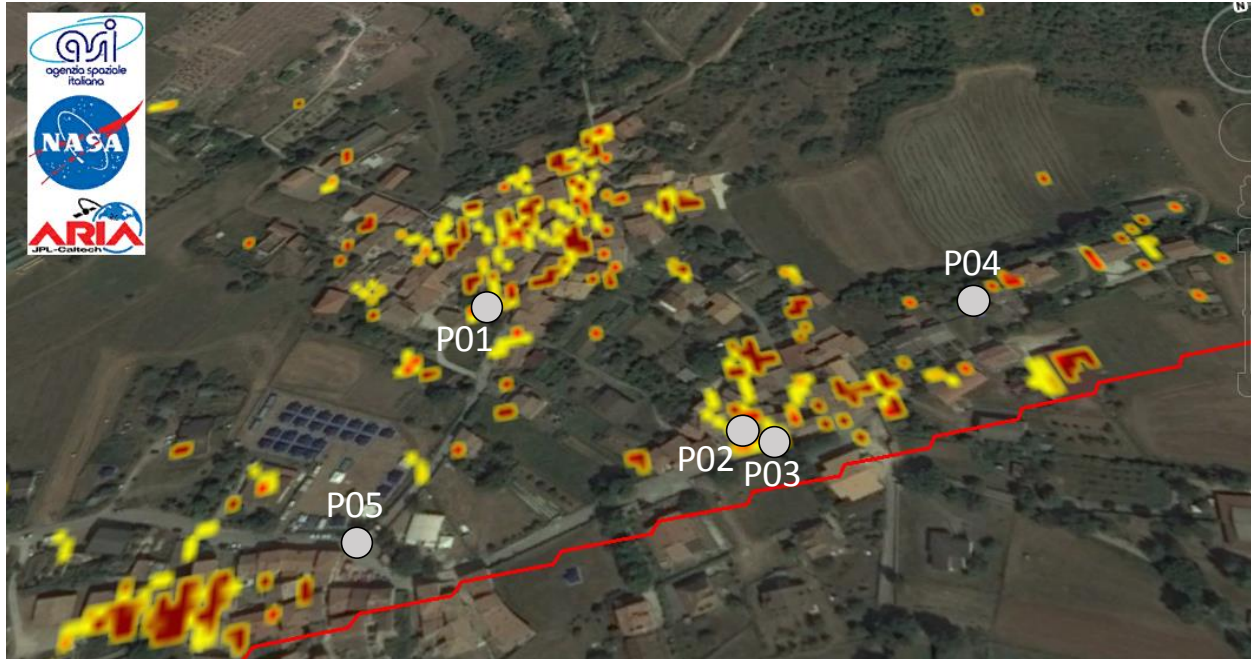


Figure 6.126. Damage proxy map of San Pellegrino (http://aria-share.jpl.nasa.gov/events/20161030-Italy_EQ/DPM/) along with the identification numbers of the structures with assigned damage level D5.

During our reconnaissance following the 30 October event, we observed extensive damages in almost all the masonry structures (classified as D3-D5) located mainly in the historical center of the town, which was in part not accessible. Some pictures of the damaged buildings in the historical center are shown in Figure 6.127 (source Repubblica.it, last accessed 21 April, 2017). In the new part of the town damages were concentrated on non-structural components of some of the reinforced concrete buildings recently constructed (classified as D2). Figure 6.128 shows multi-epoch pictures (before August and after 30 October, 2017) of selected locations. Table 6.24 summarizes the overall damage level observed in these locations.





Figure 6.127. Damaged constructions in the oldest part of San Pellegrino (<http://video.repubblica.it/dossier/terremoto-30-ottobre/terremoto-centro-italia-la-distruzione-a-san-pellegrino-di-norcia-dal-drone/257495/257761>).



P01. Montesanto street



P02. San Pellegrino Church



P03. War memorial



P04. Francesco Crispi Street



P05. Pasquale Severini Square

Figure 6.128. Pictures of the structures with assigned damage level D5 in San Pellegrino, before and after the October earthquake, along with their identification numbers.

Table 6.24. Locations of representative structures with damage descriptions.

<i>Picture</i>	<i>Damage Level</i>
<i>P01</i>	<i>D4</i>
<i>P02</i>	<i>D4</i>
<i>P03</i>	<i>D5</i>
<i>P04</i>	<i>D3/D4</i>
<i>P05</i>	<i>D4/D5</i>

7 Performance of Bridges

Principal authors: Luigi Di Sarno, Maria Giovanna Durante, Jonathan P. Stewart

Contributing authors: Ernesto Ausilio, Roberto Cairo, Stefania Sica, Michele Mucciacciaro, Paolo Zimmaro

GEER and the Consortium ReLuis inspected 12 bridges following the 24 August 2016 earthquake. The outcomes of the survey are presented in Chapter 6 of GEER (2016). Most of the reinforced concrete (RC) and composite bridges that were inspected did not experience significant seismically-induced damage. Conversely, the masonry bridges suffered extensive damage during the August events that affected roadway operations. The latter damaged bridges were re-visited following the October seismic sequences. An additional small masonry bridge along SP477 was also checked. The earthquake reconnaissance showed that the investigated masonry bridges suffered substantial additional damage during the October seismic sequence. The locations of surveyed masonry bridges is shown in Figure 7.1; further details are given in Table 7.1.

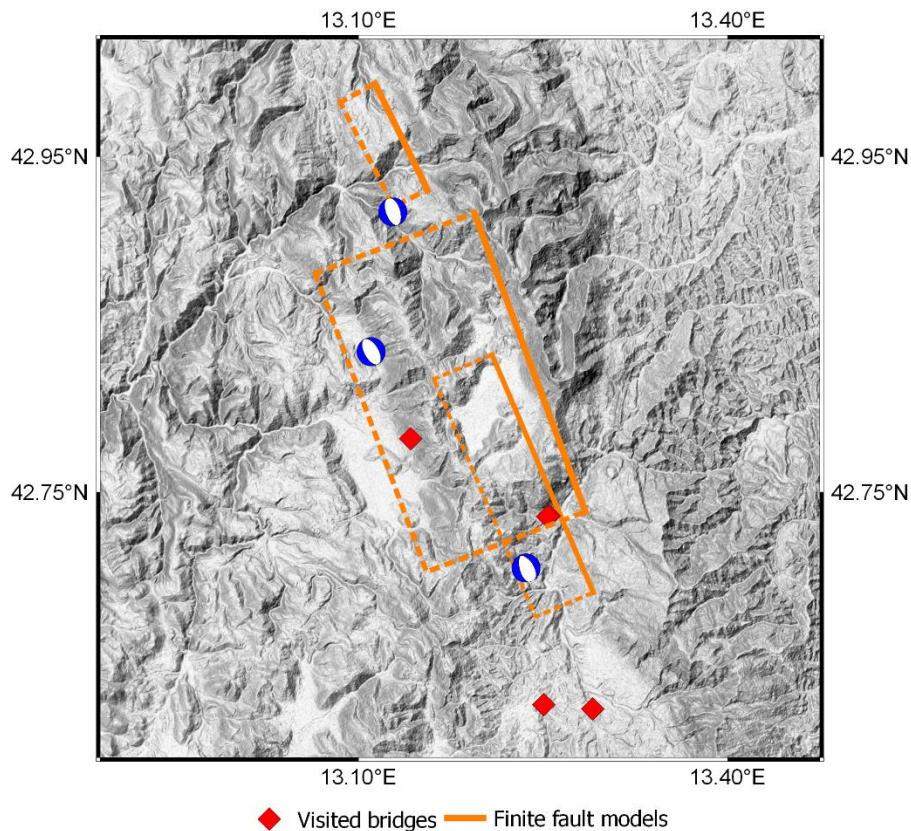


Figure 7.1. Map of epicentral region showing locations of bridge sites visited by the GEER team following the October 2016 seismic sequence.

Table 7.1. Details of bridges inspected following October 2016 seismic sequence.

	Type of bridge	Longitude [deg]	Latitude [deg]
SP477 – Castelluccio - Norcia	Masonry	13.142383	42.782073
Roman-era SP129 Trisungo-Tufo (1 span)	Masonry	13.254862	42.735981
Roman-era SP129 Trisungo-Tufo (3 spans)	Masonry	13.253655	42.73538
SR260 Ponte a Tre Occhi - Amatrice	Masonry	13.290176	42.620668
SR260 Ponte a Cinque Occhi - Amatrice	Masonry	13.250428	42.623178

The inspected masonry bridges include:

- Single arch bridge along road SP477, located between Castelluccio e Norcia villages (Figure 7.2);
- Two arch bridges along the Roman-era road SP129 Trisungo-Tufo, located near the village of Tufo (Figures 7.3 and 7.4);
- Ponte a Tre Occhi (Three eyes), located along the SR260 road in Amatrice (Figure 7.5);
- Ponte a Cinque Occhi (Five eyes) located along the internal road connecting SS4 (exit of Casale Nibbi) and SR260, in the direction of Amatrice (Figure 7.6).

Figure 7.2 shows damage observed on the single arch masonry bridge along road SP477. The bridge did not appear seriously damaged, but several cracks were observed, especially in the road carriage. Transversal and longitudinal cracks along the road surface were documented (Figure 7.2a), with a measured maximum opening in the longitudinal direction of about 6 cm. From the visual inspection, the transversal cracks close to the road-bridge connection appear more recent when compared to those in the longitudinal direction. Longitudinal cracks also formed in road fill adjacent to the bridge (Figure 7.2b). Minor additional cracking was observed within the bridge arch (Figures 7.2c and 7.2d). Figure 7.2e (from Google earth) shows a photo of the bridge in December 2011, when no roadway cracks are evident. Because this bridge was not inspected in the reconnaissance performed following the August 2016 sequence, we cannot identify which events produced the observed effects.

Figure 7.3 shows comparative pictures (taken after the 24 August and the October events) of the 1-span masonry bridge along the Trisungo route (along road SP129). The bridge presents additional cracks following the October events in the interior part of the arch (Figure 7.3b). The

width of the crack in the longitudinal direction (Figure 7.3d) has increased with respect to that observed in the first reconnaissance (Figure 7.3c). However, there was no additional spalling of masonry elements as had been observed following the first event.

Figure 7.4 shows the response of the second arch along the Trisungo route (3 spans bridge) after the different events (24 August and October 2016). The incremental damage was significant: part of central arch, already damaged after the first event (Figures 7.4a and 7.4c), collapsed as a result of the October earthquakes (Figures 7.4b and 7.4d).

The Ponte a Tre Occhi (Three eyes) near Amatrice (Figure 7.5) also experienced additional damage, consisting mainly of spalling of outer-layer masonry elements located along abutment areas (not involving the three arches) (Figure 7.5b). At the time of the reconnaissance (December 2, 2016) repairs had been carried out on one of the two abutments (Figure 7.5c), while the bridge masonry and structure appeared to have not yet been repaired (Figure 7.5d).

The Ponte a Cinque Occhi (Five eyes) along the internal road connecting SS4 (from the Casale Nibbi exit) to SR260 along Scandarello lake suffered additional damage during the October strong motions. The damage was concentrated in the arches and the piers as shown in Figures 7.6a and 7.6b. The bridge was retrofitted, as a rapid intervention, in early December 2016 with fiber-reinforced mortar and steel mesh (see Figures 7.6c and 7.6d). The latter intervention was aimed at restoring the structural capacity to the piers and the abutments. Construction was also carried out on the carriage way (bridge deck) and drainage ducts were installed.



(a)



(b)



(c)



(d)



(e)

Figure 7.2. Bridge along SP477 (42.782073 deg, 13.142383 deg): road surface cracks (a); longitudinal cracks along the road side (b); cracks between the bridge arch and the main structure (c-d); view of the bridge on December 2011 (e).



(a)



(b)



(c)



(d)

Figure 7.3. Roman-era bridge along the Trisungo route (1 span bridge - Tufo area – Arquata del Tronto - N42.735981, E13.254862): view of the arch (a, b) and the road cracks (c, d) after the 24 August event (photo on September 7 2016 (a, c)) and after the 30 October event (photo on December 13 2016 (b, d)).



(a)



(b)



(c)



(d)

Figure 7.4. Roman-era bridge along the Trisungo route (3 spans bridge - Tufo area – Arquata del Tronto - N42.73538, E13.25365): (c) after the 24 August event (photo on September 7 2016) and (d) after the 30 October event (photo on December 13 2016).



(a)



(b)



(c)



(d)

Figure 7.5. Ponte a Tre Occhi (42.620668 deg, 13.290176deg): (a) after the 24 August event (photo on September 7 2016) and (b,c,d) after the 30 October event (photo on December 13 2016), repairing works (c) and bridge masonry collapse (d).



(a)



(b)



(c)



(d)

Figure 7.6. Ponte a Cinque Occhi (42.623178 deg, 13.250428deg): increased sub-vertical cracks to the piers after the 30 October event at the top (a) and bottom (b) of the piers (photo on November 20 2016) and structural retrofitting of the bridge (c and d) (photo on December 15 2016).

8 High-Value Case Histories

Jonathan P. Stewart, Paolo Zimmaro

Earthquake engineering and engineering seismology are disciplines that are experience-driven to a substantial extent. Post-earthquake reconnaissance, for example as recorded in this report and in GEER (2016) for the 2016 Central Italy earthquake sequence, provides the means by which we develop this experience and document it for use by the broader community. In the case of man-made structures and systems, we examine the effectiveness of our methods and practices. In many cases data gathered during reconnaissance is not from engineered systems but from natural systems (e.g., ground motions, ground failure, etc.); such data plays a fundamental role in the development of engineering methods for seismic risk forecasting (e.g., ground motions, ground failure hazards).

GEER (2016) presented the results of extensive reconnaissance activities undertaken over approximately a one month period following the mainshock event on 24 August 2016. This report builds upon that earlier document, with a focus on the effects of events on 26 and 30 October 2016.

As a GEER team, our objective was reconnaissance related to ground failures (surface rupture, landslides, other ground deformations), soil-structure interaction (e.g., retaining wall failures), and indicators of local site response effects (such as damage patterns). However, for both the August and October events, our mission broadened to include documentation of structural performance for a variety of reasons including: (1) it supported our mission of evaluating damage patterns; (2) the structural performance data was indeed perishable, and as the principal reconnaissance team in many of the visited areas, we felt a duty to document our observations. As a result, the reader can find in this report and in GEER (2016) elements of traditional GEER reports combined with considerable detail on structural performance, particularly in relation to building damage patterns and bridge performance.

Looking collectively at the observations made in both reconnaissance exercises, we suggest the following data as likely to be especially impactful in future research:

1. Earthquake probabilities: When a large earthquake occurs, there are two schools of thought regarding its effect on the risk of subsequent large events. One is that stress release lowers earthquake rates relative to the long-term (Poisson) rate until stresses can again build-up on the fault. Another is that stress release on one portion of the fault may increase stress on adjoining portions of the same fault segment or adjacent segments. This would tend to increase earthquake rates (and hence short-term probabilities) relative to the long-term rate. This subject is of substantial practical significance for regional risk assessment. As shown in Figure 1.1, the August 2016 and October 2016 events occupy a gap along the NW striking Apennine chain between the locations of the 1997 Umbria-Marche and 2009 L'Aquila events. The occurrence of this cluster of

earthquakes suggest that latter (probability increasing) mechanism occurred and may continue into the future.

2. Faults as seismic sources: The portions of the Apennines affected by these earthquakes have numerous fault segments, many of which are well expressed at the ground surface (Chapter 2 of GEER 2016). Despite this, seismic source models used for Italian hazard studies in many cases do not take into consideration known attributes of these segments, often relying instead on seismic source zones or composite faults. We encourage the use of fault sources for seismic source characterization.
3. Multi-segment rupture: When fault segments are considered as seismic sources, an important question is whether single earthquake events can rupture multiple segments. It appears the 24 August 2016 event ruptured both the Mt. Vettore and Laga Mountains faults (GEER 2016), whereas multiple discontinuous segments of the Mt. Vettore fault ruptured during the 30 October 2016 event (Chapter 2).
4. Surface fault rupture: The data on surface faulting from this event sequence, which was observed following all three mainshocks (24 August, 26 and 30 October) will be a valuable resource for statistical models of surface rupture characteristics of normal fault earthquakes.
5. Ground motions: For the most part, the ground motions arising from this event sequence are compatible with expectation from ground motion models that are customized for known fast-attenuation features in Italy. Hence, to a large extent, the event itself and the ground shaking that it produced were not a surprise. The ground motions generated by these events will significantly extend the world-wide inventory of normal fault ground motions in tectonically active regions, as used for the example in NGA-West projects (e.g., Bozorgnia et al. 2014).
6. Landslides: While landslide effects were relatively modest in the August 2016 events, the effects were severe from the October events (Chapter 4). The geometry of the landslide source zones, as well as depositional areas, are well-documented with 3D models from UAVs and LiDAR. The geology of these areas is also documented. Two aspects of these case histories are of interest in future work: (1) the occurrence of landslides in some events but not others (predictive models should be able to forecast both) and (2) the landslide fall/runout distances.
7. Masonry structure fragility: Data on structural performance during earthquake events, including accumulation of damage from event-to-event, can be used to develop empirical fragility curves. Such relations are used for seismic vulnerability and risk assessment. Several Italy-specific models have been published including Sabetta et al. (1998) (using data for 50,000 structures examined following the 1980 Irpinia and 1984 Abruzzo earthquakes) and Rota et al. (2008) (using data for 150,000 structures from various events between 1980 and 2002). Features of the data collected in this event sequence include: (1) good constraint on ground motion characteristics due to multiple near-field sensors; (2) mapping that documents structural performance according to a common classification scheme at high resolution within major villages and broadly across many villages and

hamlets over the breadth of the strongly shaken region; and (3) multi-epoch mapping of the same structures following the August 2016 events and the October 2016 events, which documents damage accumulation (or lack thereof). We anticipate that fragility models will be re-evaluated in consideration of the data from these events.

8. Retrofit effectiveness: Lack of retrofit in masonry structures, combined with strong shaking, too often led to high collapse rates. Where present and well implemented, retrofit typically saved structures (and their occupants) from collapse, even across multiple events. The effectiveness of various retrofit measures, or lack thereof, can be investigated using the data collected here and in GEER (2016).

References

- Abrahamson N. A., W.J. Silva, R. Kamai, 2014. Summary of the ASK14 ground motion relation for active crustal regions. *Earthquake Spectra*, **30**, 1025-1055.
- Ancheta T. D., R. B. Darragh, J. P. Stewart, E. Seyhan, W.J. Silva, B. S.-J. Chiou, K.E. Wooddell, R. W. Graves, A. R. Kottke, D. M. Boore, T. Kishida, J. L. Donahue, 2014. NGA-West2 database. *Earthquake Spectra*, **30** (3):989–1005
- Antonini G., F. Ardizzone, M. Cardinali, M. Galli, F. Guzzetti, P. Reichenbach, 2002. Surface deposits and landslide inventory map of the area affected by the 1997 Umbria-Marche earthquakes. *Boll. Soc. Geo! It.*, Volume speciale n. **I**, 843 -853.
- Baker J.W., 2007. Quantitative classification of near-fault ground motions using wavelet analysis. *Bull. Seismol. Soc. Am.*, **97** (5), 1486-1501.
- Bindi D., F. Pacor, L. Luzi, R. Puglia, M. Massa, G. Ameri, R. Paolucci, 2011. Ground motion prediction equations derived from the Italian strong motion database. *Bull Earthq Eng*, **9**: 1899-1920.
- Bonini M., 2009. Mud volcano eruptions and earthquakes in the Northern Apennines and Sicily, Italy. *Tectonophysics*, **474**: 723-735.
- Boore D.M., J. P. Stewart, E. Seyhan, G.M. Atkinson, 2014. NGA-West 2 equations for predicting PGA, PGV, and 5%-damped PSA for shallow crustal earthquakes. *Earthquake Spectra*; **30**: 1057-85.
- Bozorgnia Y., N.A. Abrahamson, L. Al Atik, T.D. Ancheta, G.M. Atkinson, J.W. Baker, et al., 2014. NGA-West2 Research Project. *Earthquake Spectra*, **30**: 973-87.
- Calamita F., G. Cello, G. Deiana, W. Palthnieri, 1994. Structural styles, chronology rates of deformation, and time-space relationships in the Umbria-Marche thrust system (central Apennines, Italy). *Tectonics*, **13**, 4, 873-881.
- Campbell K.W., Y. Bozorgnia, 2014. NGA-West2 ground motion model for the average horizontal components of PGA, PGV, and 5% damped linear acceleration response spectra. *Earthquake Spectra*, **30**, 1087-1115.
- Chiaraluce L., A. Amato, M. Cocco, C. Chiarabba, G. Selvaggi, M. Di Bona, D. Piccinini, A. Deschamps, L. Margheriti, F. Courboux, M. Ripepe, 2004. Complex Normal Faulting in the Apennines Thrust-and-Fold Belt: The 1997 Seismic Sequence in Central Italy. *Bulletin of the Seismological Society of America*, **94** (1), 99–116.
- Chiou B.S.-J., R.R. Youngs, 2014. Update of the Chiou and Youngs NGA model for the average horizontal component of peak ground motion and response spectra. *Earthquake Spectra*, **30**, 1117-1153.
- D.M. Lavori Pubblici, 16 Gennaio 1996. G.U. 5-2-1996, N.29, *Norme tecniche per le costruzioni in zona sismica*.

- Delavaud E., F. Cotton, S. Akkar, F. Scherbaum, L. Danciu, C. Beauval, S. Drouet, J. Douglas, R. Basili, M. A. Sandikkaya, M. Segou, E. Faccioli, N. Theodoulidis, 2012. Toward a ground-motion logic tree for probabilistic seismic hazard assessment in Europe. *J Seismol*, **16** (3):451–473
- Delle Donne D., A. J. L. Harris, M. Ripepe, R. Wright, 2010. Earthquake-induced thermal anomalies at active volcanoes: *Geology*, v. **38**, p. 771-774.
- Etiop G., A.V. Milkov, 2004. A new estimate of global methane flux from onshore and shallow submarine mud volcanoes to the atmosphere. *Environmental Geology*, **46** (8), pp. 997–1002.
- Falucci E., S. Gori, F. Galadini, G. Fubelli, M. Moro, M. Saroli, 2016. Active faults in the epi-central and mesoseismal Ml 6.0 24, 2016 Amatrice earthquake region, central Italy. Methodological and seismotectonic issues. *Annals of geophysics*, **59**, Fast Track 5, 2016. DOI: 10.4401/ ag-7266.
- Fielding E.J., M. Talebian, P.A. Rosen, H. Nazari, A. Jackson, M. Ghorashi, R. Walker, 2005. Surface ruptures and building damage of the 2003 Bam, Iran, earthquake mapped by satellite synthetic aperture radar interferometric correlation. *J. Geophys. Res.* **110**, B3, B03302.
- Galadini F., P. Galli, 2003. Paleoseismology of silent faults in the Central Apennines (Italy): the Mt. Vettore and Laga Mts. faults. *Annals of Geophysics*, **46** (5), 815-836.
- Gardner J. K., L. Knopoff, 1974. Sequence of Earthquakes in Southern- California, with Aftershocks Removed, Poissonian. *Bulletin of the Seismological Society of America*, **64** (15), 1363-1367.
- Gaudiosi I., G. Vignaroli, P. Sirianni, S. Giallini, F. Mori, F. Polpetta, R. Razzano, M. Simionato, M. Moscatelli, 2016. Local seismic response studies in the north-western portion of the August 24th, 2016 Mw 6.0 earthquake affected area. The case of Visso village (Central Apennines). *Annals of Geophysics*, **59**, Fast Track 5, 2016; DOI: 10.4401 / ag – 7258.
- GdL INGV sul terremoto di Amatrice, 2016. Primo rapporto di sintesi sul Terremoto di Amatrice Ml 6.0 del 24 Agosto 2016 (Italia Centrale), DOI: 10.5281/zenodo.61121 (in italian).
- GdL INGV sul terremoto in centro Italia, 2016. Summary report on the October 30, 2016 earthquake in central Italy Mw 6.5, DOI: 10.5281/zenodo.166238.
- GEER (2016). Engineering Reconnaissance of the 24 August 2016 Central Italy Earthquake. Version 2, GEER Association Report No. GEER-050B. DOI:10.18118/G61S3Z.
- Gregor N., W. Silva, R. Darragh, 2002. Development of attenuation relations for peak particle velocity and displacement. *A PEARL report to PG&E/CEC/Caltrans*, June 12, 2002.
- Guzzetti F., P. Reichenbach, S. Ghigi, 2004. Rockfall hazard and risk assessment in the Nera River Valley, Umbria Region, central Italy. *Environ Manage*, **34** (2):191-208.
- INGV Report 2016. Sequenza sismica in Italia centrale: i vulcanelli di fango in provincia di Fermo. Available at: <https://ingvterremoti.wordpress.com/2016/11/11/sequenza-sismica-in-italia-centrale-i-vulcanelli-di-fango-in-provincia-di-fermo/>, last accessed 23 March, 2017; in Italian).

INGV Working Group “GPS Geodesy (GPS data and data analysis center)” 2016. Preliminary co-seismic displacements for the October 26 (Mw5.9) and October 30 (Mw6.5) central Italy earthquakes from the analysis of GPS stations, DOI: 10.5281/zenodo.167959.

Jayaram N, JW Baker, 2009. Correlation model for spatially distributed ground-motion intensities, *Earthquake Engineering and Structural Dynamics*, **38** (15), 1687–1708.

Kaklamanos J., L.G. Baise, D.M. Boore, 2011. Estimating unknown input parameters when implementing the NGA ground-motion prediction equations in engineering practice. *Earthq. Spectra*, **27**: 1219-1235.

Kopf A.J., 2003. Global methane emission through mud volcanoes and its past and present impact on the earth's climate. *International Journal of Earth Science*, **92** (5), pp. 806–816.

Kwak D.Y., A. Mikami, S.J. Brandenberg, J.P. Stewart, 2012. Ground motion estimation for evaluation of levee performance in past earthquakes, *Proc. 9th International Conf. on Urban Earthquake Engin./4th Asia Conf. on Earthquake Eng.*, Center for Urban Earthquake Engineering, March 6-8, 2012, Tokyo Institute of Technology, Tokyo, Japan.

Kwak D.Y., J.P. Stewart, S.J. Brandenberg, A. Mikami, 2016. Characterization of seismic levee fragility using field performance data. *Earthquake Spectra*, **32**, 193-215.

Linde A., I.S. Sacks, 1998. Triggering of volcanic eruptions. *Nature*, **395** (6705), pp. 888–890.

Luzi L., R. Puglia, E. Russo, ORFEUS WG5, 2016. Engineering Strong Motion Database, version 1.0. *Istituto Nazionale di Geofisica e Vulcanologia, Observatories & Research Facilities for European Seismology*. DOI: 10.13127/ESM.

Manga M., E. Brodsky, 2006. Seismic triggering of eruptions in the far field: volcanoes and geysers. *Annual Review of Earth and Planetary Sciences*, **34**, pp. 263–291.

Manga M., M. Brumm, M.L. Rudolph M, 2009. Earthquake triggering of mud volcanoes. *Marine and Petroleum Geology*. Volume **26**, Issue 9, Pages 1785–1798.

Mazzini A., 2009. Mud volcanism: Processes and implications. *Marine and Petroleum Geology*. Volume **26**, Issue 9, Pages 1677-1680.

Mazzini A., and G. Etiope, 2017. Mud volcanism: An updated review. *Earth-Science Reviews*. doi: 10.1016/j.earscirev.2017.03.001.

Mellors R., D. Kilb, A. Aliyev, A. Gasanov, G. Yetirmishli, 2007. Correlations between earthquakes and large mud volcano eruptions. *Journal of Geophysical Research*, **112** (B4), p. B04304.

Ministry of the Infrastructures. Norme Tecniche per le Costruzioni. Decreto Ministeriale D.M. 14 gennaio 2008. *Gazzetta Ufficiale della Repubblica Italiana*; 2008;29. In Italian.

Pagliaroli A., A. Avalle, E. Falcucci, S. Gori, F. Galadini 2015. Numerical and experimental evaluation of site effects at ridges characterized by complex geological setting. *Bulletin of Earthquake Engineering*, **13**:2841–2865.

- Piatanesi A., A. Cirella, 2009. Rupture Process of the 2009 Mw6.3 L'Aquila (Central Italy) Earthquake from Nonlinear Inversion of Strong Motion and GPS Data. *Istituto Nazionale di Geofisica e Vulcanologia (INGV)*, Rome, Italy.
- Regione Marche, 2012a. Microzonazione sismica del Comune di Visso. Attuazione art. 11 legge n.77/2009. OPCM n. 3907/2010. Approvato dalla Regione Marche.
- Regione Marche, 2012b. *Microzonazione sismica del Comune di Pieve Torina (MC)*. Attuazione art. 11 legge n.77/2009. OCDPC n. 52/2013. Approvato dalla Regione Marche.
- Regione Marche, 2014. Microzonazione sismica del Comune di Pievebovigliana. Attuazione art. 11 legge n.77/2009. OCDPC n. 52/2013. Approvato dalla Regione Marche.
- Rota M., A. Penna, C.L. Strobbia, 2008. Processing Italian damage data to derive typological fragility curves. *Soil Dynamics and Earthquake Engineering*, **28**, 933-947.
- Rovida A., M. Locati, R. Camassi, B. Lolli, P. Gasperini (eds), 2016. CPTI15, the 2015 version of the Parametric Catalogue of Italian Earthquakes. *Istituto Nazionale di Geofisica e Vulcanologia*. doi:<http://doi.org/10.6092/INGV.IT-CPTI15>.
- Sabetta F., A. Goretti, A. Lucantoni, 1998. Empirical fragility curves from damage surveys and estimated strong ground motion. *Proceedings: Eleventh European Conference on Earthquake Engineering*, Paris, France.
- Scasserra G., J.P. Stewart, R.E. Kayen, G. Lanzo, 2009. Database for earthquake strong motion studies in Italy. *Journal of Earthquake Engineering*, **13** (6), 852-881.
- Stafford P.J., 2012. Evaluation of structural performance in the immediate aftermath of an earthquake: a case study of the 2011 Christchurch earthquake, *Int. J. Forensic Engineering*, **1**: 58–77.
- Stewart J. P., J. Douglas, M. Javanbarg, Y. Bozorgnia, N. A. Abrahamson, D. M. Boore, et al., 2015. Selection of ground motion prediction equations for the Global earthquake model. *Earthq Spectra*, **31**:19–45.
- Stewart J.P., G. Lanzo, A. Pagliaroli, G. Scasserra, G. Di Capua, S. Peppoloni, R. Darragh, N. Gregor, 2012. Ground Motion Recordings from the Mw 6.3 2009 L'Aquila Earthquake in Italy and their Engineering Implications. *Earthquake Spectra*, **28**, 317-345.
- Tinti, E., L. Scognamiglio, A. Michelini, M. Cocco, 2016. Slip heterogeneity and directivity of the ML 6.0, 2016, Amatrice earthquake estimated with rapid finite-fault inversion, *Geophysical Research Letters*, accepted.
- Wooddell K.E., N. A. Abrahamson, 2012. New earthquake classification scheme for mainshocks and aftershocks in the NGA-West2 ground motion prediction equations. *Proceedings, 15th World Conf. Earthquake Engineering*, Lisbon, Portugal.
- Yassir, N., 1989. Mud Volcanoes and the Behaviour of Overpressured Clays and Silts PhD thesis, *Univ. London*.

Yun S., E.J. Fielding, M. Simons, P. Rosen, S. Owen, F. Webb, 2011. Damage proxy map of M 6.3 Christchurch earthquake using InSAR coherence. *Fringe Workshop, Advances in the science and applications of SAR interferometry from ESA and 3rd party missions*. Frascati, Italy, https://earth.esa.int/documents/10174/1567329/Yun_FRINGE2011.pdf.

Yun S., K. Hudnut, S. Owen, F. Webb, M. Simons, P. Sacco, E. Gurrola, G. Manipon, C. Liang, E.J. Fielding, P. Milillo, H. Hua, A. Coletta, 2015. Rapid Damage Mapping for the 2015 Mw 7.8 Gorkha Earthquake Using Synthetic Aperture Radar Data from COSMO–SkyMed and ALOS-2 Satellites. *Seismological Research Letters*, **86** (6), 1549-1556.

Zimmaro P., J.P. Stewart, 2017. Site-specific seismic hazard analysis for Calabrian dam site using regionally customized seismic source and ground motion models. *Soil Dynamics and Earthquake Engineering*, **94**: 179-192.